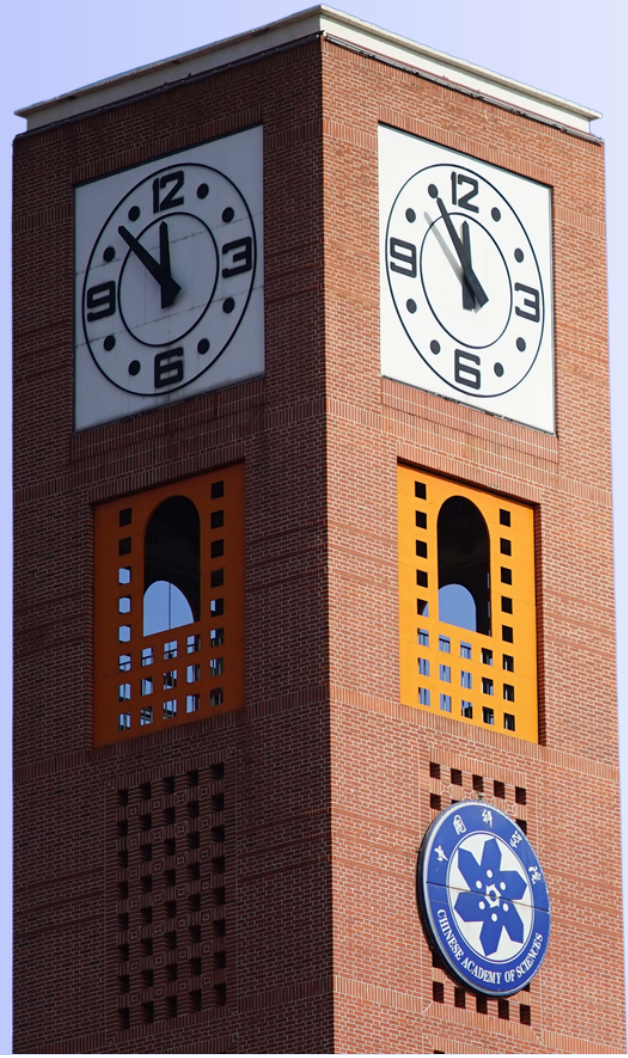


# Development of Gallium Nitride Power MEMS Devices

*Xingyu Zhou*

National Center for Nanoscience and Technology  
University of Chinese Academy of Sciences

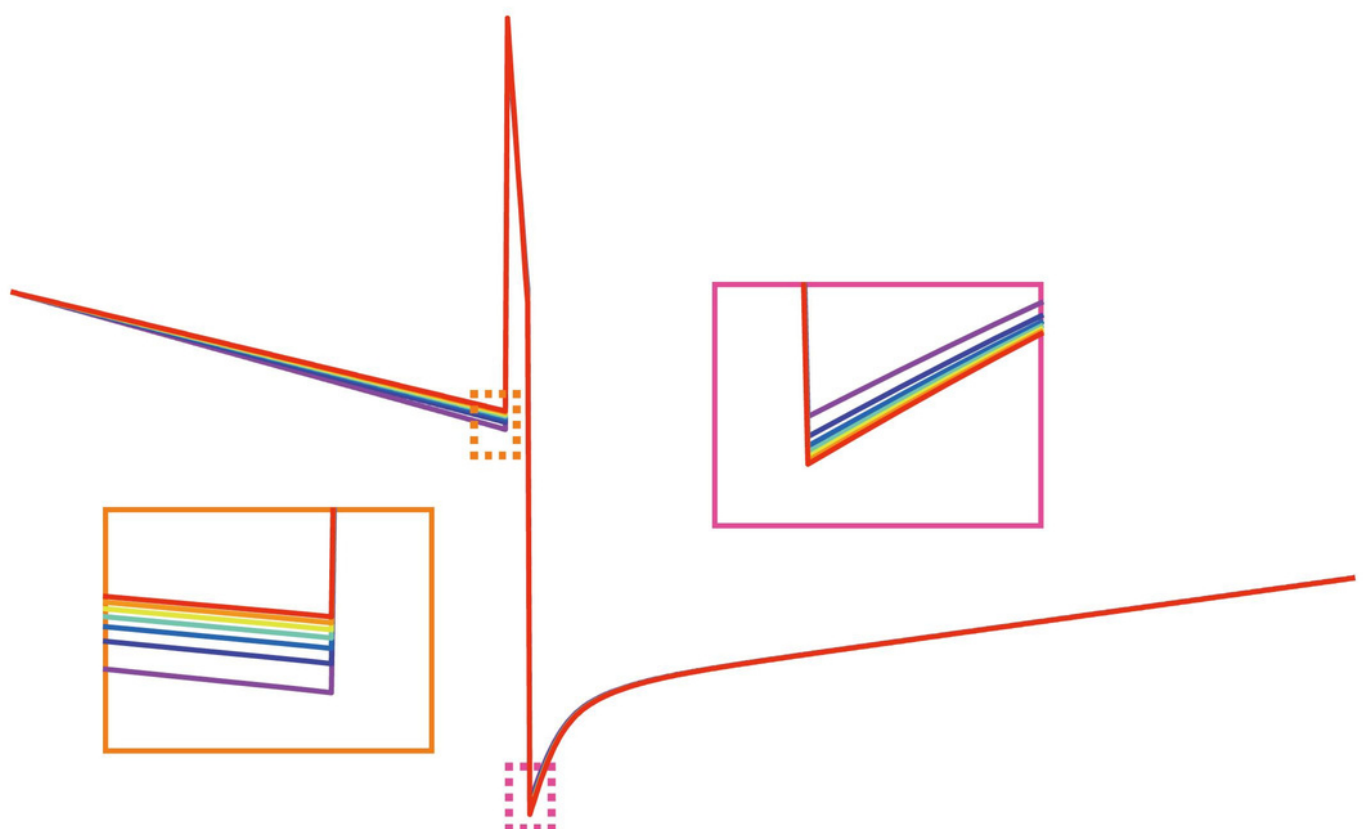
June 21, 2021



Master's Thesis

XINGYU ZHOU

# Development of Gallium Nitride Power MEMS Devices



Master's thesis

XINGYU ZHOU

Development of Gallium Nitride Power  
MEMS Devices

# **Development of Gallium Nitride Power MEMS Devices**



**Xingyu Zhou**

National Center for Nanoscience and Technology  
University of Chinese Academy of Sciences

This thesis is submitted for the degree of

*Master of Natural Science*

Chinese Academy of Sciences

June 2021

# Contents

<b>List of Figures</b>	<b>vii</b>
<b>List of Tables</b>	<b>xii</b>
<b>Declaration</b>	<b>xiv</b>
<b>Acknowledgements</b>	<b>xvi</b>
<b>Publication List</b>	<b>xviii</b>
<b>Abstract</b>	<b>xix</b>
<b>List of Abbreviations and Symbols</b>	<b>xxii</b>
<b>1 Introduction</b>	<b>1</b>
1.1 Introduction to piezotronics effect . . . . .	1
1.1.1 Development and principles of piezotronics effect . . . . .	1
1.1.2 Application prospect of piezotronics effect . . . . .	9
1.2 Piezotronics effects in III-V nitrides . . . . .	10
1.2.1 Crystal structure and polarization properties of III-V nitrides . . . . .	10
1.2.2 Application of piezotronics effect in III-V nitride . . . . .	13
1.3 Introduction to III-V nitride MEMS devices . . . . .	17

1.3.1	Introduction to micro-electromechanical systems (MEMS) . . . . .	17
1.3.2	III-V nitride MEMS devices . . . . .	18
1.3.3	Microstructure of III-V nitrides . . . . .	25
1.4	Outline of the thesis . . . . .	27
<b>Part I Theory</b>		<b>32</b>
<b>2 Theoretical Model of Power MEMS Devices</b>		<b>33</b>
2.1	Polarization effects of III-V nitrides . . . . .	33
2.2	Piezoelectric theory of III-V nitrides . . . . .	37
2.2.1	Piezoelectric constitutive equation . . . . .	37
2.2.2	Piezoelectric polarization charge-strain equation . . . . .	39
2.3	Lattice strain model of AlGaN/AlN/GaN heterojunction . . . . .	40
2.3.1	Biaxial strain model of thin films . . . . .	40
2.3.2	Lattice strain in multilayer thin films . . . . .	41
2.3.3	Piezoelectric polarization charge of GaN AlGaN AlN layer . . . . .	47
2.4	Self-consistent coupling model of strained AlGaN/AlN/GaN heterojunction .	50
2.4.1	The theoretical equations of the model . . . . .	50
2.4.2	A self-consistent numerical method for one-dimensional Schrödinger-Poisson coupling equation . . . . .	53
2.5	The framework of theoretical model . . . . .	55
2.6	Simulation results of theoretical model . . . . .	56
2.7	Summary . . . . .	61
<b>Part II Manufacturing</b>		<b>62</b>
<b>3 Manufacturing Technology of Power MEMS Devices</b>		<b>63</b>
3.1	Fabrication techniques . . . . .	64

3.1.1	GaN-on-Si wafer epitaxial growth . . . . .	64
3.1.2	Wafer dicing . . . . .	66
3.1.3	Cleaning technologies . . . . .	67
3.1.4	Photolithography . . . . .	70
3.1.5	Thin film deposition . . . . .	71
3.1.6	Dry etching . . . . .	75
3.1.7	Rapid thermal processing . . . . .	76
3.2	Characterization techniques . . . . .	77
3.2.1	Semiconductor parameter analyzer . . . . .	77
3.2.2	Scanning electron microscopy (SEM) . . . . .	78
3.2.3	Transmission electron microscopy (TEM) . . . . .	80
3.2.4	Energy dispersive X-ray spectroscopy (EDX) . . . . .	82
3.2.5	High-resolution X-ray diffraction (HRXRD) . . . . .	83
3.2.6	Raman spectroscopy . . . . .	85
3.3	Summary . . . . .	86
<b>4</b>	<b>Process Development and Integration of Power MEMS Devices</b>	<b>87</b>
4.1	Process flow and recipe . . . . .	88
4.1.1	Wafer growth . . . . .	90
4.1.2	Pre-processing . . . . .	91
4.1.3	Mesa preparation . . . . .	92
4.1.4	Metal-semiconductors contact formation . . . . .	94
4.1.5	Magnetic thin film deposition (For MPD) . . . . .	99
4.1.6	GaN cantilever preparation . . . . .	101
4.2	Mechanisms of process-induced performance degradation . . . . .	104
4.2.1	Lattice strain relief and piezoelectric effect . . . . .	105
4.2.2	Lattice defects and Schottky contact degradation . . . . .	106

4.3	Process optimization . . . . .	107
4.3.1	Positive photoresist double coating process . . . . .	107
4.3.2	GaN cantilever ICP-RIE etching process . . . . .	108
4.4	Summary . . . . .	109
<b>Part III</b>	<b>Devices</b>	<b>110</b>
<b>5</b>	<b>Strain-Controlled Power Devices</b>	<b>111</b>
5.1	Background and motivation . . . . .	111
5.2	Design and preparation . . . . .	114
5.2.1	Device structure and characterization . . . . .	114
5.2.2	Fabrication processes . . . . .	116
5.3	Device performance . . . . .	118
5.3.1	Electrical performance . . . . .	118
5.3.2	Strain-power modulation performance . . . . .	121
5.4	Working mechanism . . . . .	127
5.5	Summary . . . . .	129
<b>6</b>	<b>Magnetosensory Power Devices</b>	<b>131</b>
6.1	Background and motivation . . . . .	131
6.2	Design and preparation . . . . .	134
6.2.1	Device structure and characterization . . . . .	134
6.2.2	Fabrication processes . . . . .	138
6.3	Device performance . . . . .	140
6.3.1	Electrical performance . . . . .	140
6.3.2	Magnetic field-power modulation performance . . . . .	142
6.4	Working mechanism . . . . .	146

6.5    Summary . . . . .	153
<b>7    Discussion and Outlook</b>	<b>155</b>
7.1    Conclusions . . . . .	155
7.2    Future work . . . . .	157
<b>Bibliography</b>	<b>159</b>
<b>Appendix A Publication Titles</b>	<b>179</b>
<b>Appendix B Micro/Nano-fabrication Equipment</b>	<b>183</b>
<b>Appendix C MATLAB Code for Theoretical Model</b>	<b>184</b>
<b>Index</b>	<b>190</b>

# List of Figures

Fig. 1.1	Coupling characteristics of piezotronics and piezo-phototonics . . . . .	2
Fig. 1.2	Piezopotential in wurtzite crystal ZnO . . . . .	3
Fig. 1.3	Energy band diagram of piezotronics effect in Schottky contact and p-n junction . . . . .	5
Fig. 1.4	Energy band diagram of piezotronic effect in p-n heterojunction . . . . .	7
Fig. 1.5	Working principle of piezotronics transistor . . . . .	9
Fig. 1.6	The application prospects and future prospects of piezotronics . . . . .	10
Fig. 1.7	The wurtzite crystal structure of GaN material and the polarization characteristics of the Ga and N plane . . . . .	11
Fig. 1.8	Polarization charge in AlGaN/GaN heterojunction with Ga-plane and N-plane polarity . . . . .	13
Fig. 1.9	Piezotronic effect in AlGaN/AlN/GaN heterostructure microwire . . . . .	14
Fig. 1.10	Piezotronics effect in AlGaN/GaN MOS HEMTs and unpassivated HEMTs	15
Fig. 1.11	Piezotronics effect modulated flexible AlGaN/GaN HEMT . . . . .	16
Fig. 1.12	Block diagram for the basic components in MEMS and their interaction .	18
Fig. 1.13	Advantages of group III-V nitrides for the realization of integrated MEMS	20
Fig. 1.14	The AlGaN/GaN resonant body high electron mobility transistor . . . . .	21
Fig. 1.15	An all-GaN integrated microsystem platform wherein GaN MEMS resonators are monolithically integrated with AlGaN/GaN HEMT . . . . .	22

Fig. 1.16 Miniature pressure MEMS sensor based on AlGaN/GaN heterojunction suspended structure . . . . .	23
Fig. 1.17 AlGaN/GaN HEMT MEMS biosensor for detecting cardiac troponin I in a physiological environment . . . . .	24
Fig. 1.18 SEM image of a series of p-GaN microcantilever arrays . . . . .	25
Fig. 1.19 SEM image of a series of p-GaN structures suspended between two half-plane supports . . . . .	26
Fig. 1.20 Structure and SEM image of GaN power MEMS devices . . . . .	27
Fig. 1.21 The outline of the thesis . . . . .	28
Fig. 2.1 Ball and stick model of an ideal GaN crystal with Ga and N-polarity in a relaxed state . . . . .	35
Fig. 2.2 Ball and stick model of a GaN crystal for both Ga and N polarity with a homogeneous in-plane tensile strain . . . . .	36
Fig. 2.3 Ball and stick model of a GaN crystal for both Ga and N polarity with a homogeneous in-plane compressive strain . . . . .	36
Fig. 2.4 Piezoelectric polarization charge distribution of group III-V nitride material $Al_xGa_{1-x}N$ when $P_{PE} < 0$ . . . . .	40
Fig. 2.5 Schematic diagram of biaxial stress model . . . . .	41
Fig. 2.6 Bandgap energy versus lattice constant for III-V nitride semiconductors at room temperature . . . . .	42
Fig. 2.7 Lattice strain of the thin films . . . . .	43
Fig. 2.8 Thin film structure of AlGaN/AlN/GaN heterostructure . . . . .	44
Fig. 2.9 Finite element analysis of GaN cantilever strain under external stress . . . . .	48
Fig. 2.10 Iteration process of Schrodinger-Poisson self-consistent calculation . . . . .	54
Fig. 2.11 Framework diagram of the theoretical model . . . . .	55
Fig. 2.12 Simulation results of MPD with upward magnetic force . . . . .	57

Fig. 2.13 Simulation results of MPD with downward magnetic force . . . . .	57
Fig. 2.14 Simulation results of SPD with downward normal force . . . . .	58
Fig. 2.15 Simulation results of MEMS with the cantilever length of 400 $\mu\text{m}$ under downward force . . . . .	59
Fig. 2.16 Simulation results of MEMS with the cantilever length of 450 $\mu\text{m}$ under downward force . . . . .	60
Fig. 2.17 Simulation results of MEMS with the cantilever length of 500 $\mu\text{m}$ under downward force . . . . .	60
Fig. 3.1 Aixtron CCS 3 $\times$ 2 MOCVD . . . . .	64
Fig. 3.2 The 3-inch GaN-on-Si wafer . . . . .	65
Fig. 3.3 DISCO DAD3350 automatic dicing saw . . . . .	66
Fig. 3.4 PVA TePla IoN 40 plasma cleaner . . . . .	69
Fig. 3.5 SUSS MA6 mask aligner designed for high-resolution photolithography	70
Fig. 3.6 The schematic diagram showing the process of photolithography . . . . .	71
Fig. 3.7 Denton Discovery 635 magnetron sputtering system . . . . .	72
Fig. 3.8 Denton Vacuum Explore 14 electron beam evaporation system . . . . .	73
Fig. 3.9 SENTECH SI 500 inductively coupled plasma reactive ion etching . . . . .	75
Fig. 3.10 LABSYS RTP-1200 rapid thermal processing system . . . . .	76
Fig. 3.11 Keysight B1500A semiconductor device parameter analyzer and I-V characteristics of MPD under external magnetic field modulation . . . . .	77
Fig. 3.12 FEI Nova Nano SEM 450 field-emission scanning electron microscopy .	78
Fig. 3.13 SEM image of fabricated GaN power MEMS devices . . . . .	79
Fig. 3.14 FEI Tecnai F20 cryo-transmision electron microscope . . . . .	80
Fig. 3.15 High-resolution TEM image acquired from the AlGaN/AlN/GaN hetero-stacks . . . . .	81

Fig. 3.16 Principle of EDX and elemental composition of AlGaN/GaN HEMT characterized by EDX . . . . .	82
Fig. 3.17 Bruker D8 DISCOVER high-resolution X-ray diffraction . . . . .	83
Fig. 3.18 The X-ray diffraction spectra of GaN HEMT . . . . .	84
Fig. 3.19 HORIBA LabRAM HR Evolution Raman spectroscopy . . . . .	85
Fig. 3.20 Principle of Raman spectroscopy and Raman spectroscopy of GaN-on-Si wafers . . . . .	86
Fig. 4.1 The schematic diagram of process flow . . . . .	88
Fig. 4.2 Layout of GaN power MEMS devices . . . . .	89
Fig. 4.3 GaN-on-SiC wafer hetero-epitaxial structure . . . . .	90
Fig. 4.4 Photomask of active area . . . . .	93
Fig. 4.5 Photomask of source and drain contact . . . . .	95
Fig. 4.6 Photomask of gate contact . . . . .	97
Fig. 4.7 Electrical performance of fabricated AlGaN/AlN/GaN HEMTs . . . . .	99
Fig. 4.8 Photomask of magnetic film . . . . .	100
Fig. 4.9 Photomask of GaN cantilever . . . . .	102
Fig. 4.10 Electrical performance of fabricated MPD . . . . .	104
Fig. 4.11 Raman spectroscopy of fabricated HEMT and MPD . . . . .	105
Fig. 5.1 Concept of strain-controlled power device (SPD) as inspired by human reflex . . . . .	114
Fig. 5.2 EDX line profiles for the element of Ga (orange), Al (red), and N (purple) .	115
Fig. 5.3 Structure and material characterizations of the SPD . . . . .	116
Fig. 5.4 Etching process flow chart of the SPD . . . . .	117
Fig. 5.5 Fabrication process flow chart of the SPD . . . . .	118
Fig. 5.6 Electrical performance of the HEMT . . . . .	119

Fig. 5.7 Contact characterizations of the SPD . . . . .	120
Fig. 5.8 Electrical performance of the SPD . . . . .	121
Fig. 5.9 Strain-controlled output power characteristics at various gate voltage . .	122
Fig. 5.10 Strain-controlled output power characteristics of SPD . . . . .	124
Fig. 5.11 Reproducible strain-dependent analysis of the SPD . . . . .	125
Fig. 5.12 The reproducibility of the SPD under external strain . . . . .	126
Fig. 5.13 The calculated energy band and 2DEG concentration in AlGaN/AlN/GaN heterojunction under external strains. . . . .	129
Fig. 6.1 Illustration of the magnetosensory power device (MPD) inspired by mag- netoreception in birds . . . . .	133
Fig. 6.2 The fabrication process and characterization of MPD . . . . .	136
Fig. 6.3 The EDX line profiles for the element of Ga (red), Al (green), and N (purple) and energy-dispersive X-ray spectroscopy (EDS) element mapping including Ga, Al, and N acquired from the AlGaN/AlN/GaN hetero-stacks . .	138
Fig. 6.4 Electrical characteristics of the HEMT (before etching) and the as-fabricated MPD . . . . .	141
Fig. 6.5 The contact and leakage characteristics of HEMT and MPD . . . . .	142
Fig. 6.6 The magnetic field-power modulation characteristics of MPD . . . . .	144
Fig. 6.7 The calculated energy band and 2DEG concentration n AlGaN/AlN/GaN heterojunction under magnetic force in +z direction. . . . .	149
Fig. 6.8 The calculated energy band and 2DEG concentration in AlGaN/AlN/GaN heterojunction under magnetic force in -z direction and rotation. . . . .	153

# List of Tables

1.1	Comparison of characteristics of several electromechanical materials . . . . .	19
2.1	Physical parameters of wurtzite structure AlN and GaN . . . . .	46
2.2	Lattice strain of GaN cantilever active region and the corresponding piezoelectric polarization charge density of the films at $0 \sim 24$ mN downward force . .	49
2.3	Lattice strain of GaN cantilever active region and the corresponding piezoelectric polarization charge density of the films at $0 \sim 24$ mN upward force . . . . .	56
5.1	Structure parameters of the HEMT and SPD . . . . .	115
5.2	The calculated result for $n_{2deg}$ -strain relationship under the external force . .	128
6.1	Structural parameters of HEMT and MPD . . . . .	135
6.2	The calculated result for $n_{2deg}$ -strain relationship under the magnetic force in $+z$ direction . . . . .	148
6.3	The fitting curve of the calculated $n_{2deg}$ -strain relationships under the magnetic force in $+z$ direction . . . . .	148
6.4	The calculated result for $n_{2deg}$ -strain relationship under the magnetic force in $-z$ direction . . . . .	151
6.5	The fitting curve of the calculated $n_{2deg}$ -strain relationships under the magnetic force in $-z$ direction . . . . .	151

I would like to dedicate this thesis to my loving parents.

# Declaration

In this revision, the research content of Chapter Six has been officially published in a peer-reviewed journal *Advanced Electronic Materials* under the name "Magnitosensory power devices based on AlGaN/GaN heterojunctions for interactive electronics", and the relevant information of the paper has been updated in the publications list.

Xingyu Zhou

January 2023

This revision newly adds the "Manufacturing" part including the Chapter Three and Four, detailing the manufacturing equipment, process design and process integration of GaN HEMT and power MEMS devices.

Xingyu Zhou

July 2022

This is the self-translated English version of the master's thesis submitted to Degree Awarding Committee, University of Chinese Academy of Sciences. Compared with the Chinese version submitted in June 2021, several modifications need to be briefly explained here. Firstly, in order to more accurately highlight the theme of the thesis, the title has been changed from the original "Research on MEMS Cantilever Devices based on AlGaN/AlN/GaN Heterostructure" to "Development of Gallium Nitride Power MEMS Devices". Secondly, the Chapter Six contains the latest revisions as of April 2022, because its content is extracted from the article that I am revising and submitting as the first author. Please refer to the final published article.

Xingyu Zhou

April 2022

I hereby declare that the thesis I submitted is the result of my independent and permitted collaborative research under the guidance of the supervisor. To the best of my knowledge, this thesis does not include any other individual or collective work that has been published or written except for the content specifically marked and cited in the reference.

Xingyu Zhou

June 2021

# Acknowledgements

The three-year postgraduate study career at UCAS has come to an end. During the time, I received selfless help from my parents, mentors, and classmates. They accompanied me through a pleasant study time, and I gained precious friendship in the journey of life. Here, I would like to express my sincere gratitude to all of them.

First of all, I would like to thank my supervisor, Professor Weiguo Hu, who has brought me a lot from his profound theoretical knowledge and deep insight into the power devices. Professor Hu pointed out the core of the problem in time when I first tried theoretical research, and clarified the direction when I was confused, which helped me successfully complete the theoretical model and gain valuable scientific research experience. I would also like to thank Professor Xiong Pu for his guidance over the past three years, which has greatly broadened my research horizons.

I would like to express my deep gratitude to Professor Jiping Li from Nanjing University of Aeronautics and Astronautics. During the nearly seven years of study, Professor Li gave me very valuable suggestions on my learning attitude, research methods, and living life. She made pertinent and serious criticism to my shortcomings, and encouraged me to persevere in the most difficult times of my life. I grew up with her earnest teachings, and will keep her love in my heart forever.

In the short three years of my master's study, I was accompanied by my colleagues in the laboratory. I would like to thank Dr. Ting Liu, Dr. Chunyan Jiang, Dr. Liang Jing, MSc.

Jiyuan Zhu and Dr. Wei Sha, for their selfless help in my research and living life. We share sorrow and joy together, and think about the puzzles and confusions in learning. Everyone give me new insights and point out the fog in front of me. I sincerely hope that they will reach new heights and achieve success in their future life.

Thanks to Dr. Ruihang Xu from the Institute of Mathematics and Systems Science, Chinese Academy of Sciences for his precious friendship. The acquaintance of Yanqi Lake Campus is the treasure of my life. In the past three years, we encouraged each other to explore artificial intelligence, mathematical optimization, physical modeling and philosophy of science. We also strive to establish a comprehensive understanding of Western science, to obtain truly mature scientific discoveries. "There are very few people in the world who will help us, while bosom friend even fewer". Wang Wei, a Chinese poet living more than 1,000 years ago, has a famous saying in praise of friendship. I sincerely hope that our friendship will last forever. I will never forget our ambitions and will work hard to achieve our dreams.

I am deeply grateful to my parents. They will always be my strongest backing, shield me from the wind and rain, and allow me to study without distractions. The thousands of volumes of books at home have laid the cornerstone of my life. They have not only given me all the love, but also given me the wings of Kunpeng. The former seedlings have become towering trees, and I will definitely live up to their ardent expectations.

# Publication List

## First author journal papers

1. **Xingyu Zhou**, Qilin Hua, Wei Sha, Jiyuan Zhu, Ting Liu, Chunyan Jiang, Qi Guo, Liang Jing, Chunhua Du, Junyi Zhai, Weiguo Hu, Zhong Lin Wang. Magnetosensory power devices based on AlGaN/GaN heterojunctions for interactive electronics. *Advanced Electronic Materials*, 2023,
  - <https://onlinelibrary.wiley.com/doi/full/10.1002aelm.202200941>

## Co-first author journal papers

2. Shuo Zhang‡, Bei Ma‡, **Xingyu Zhou‡** (‡ co-first authors), Qilin Hua, Jian Gong, Ting Liu, Xiao Cui, Jiyuan Zhu, Wenbin Guo, Liang Jing, Weiguo Hu, Zhong Lin Wang. Strain-controlled power devices as inspired by human reflex. *Nature Communications*, 2020, 11(1): 1-9.
  - <https://www.nature.com/articles/s41467-019-14234-7>
3. Jiyuan Zhu‡, **Xingyu Zhou‡** (‡ co-first authors), Liang Jing, Qilin Hua, Weiguo Hu, Zhong Lin Wang. Piezotronic effect modulated flexible AlGaN/GaN high-electron-mobility transistors. *ACS Nano*, 2019, 13(11): 13161-13168.
  - <https://pubs.acs.org/doi/abs/10.1021/acsnano.9b05999>

# **Abstract**

Microelectromechanical system (MEMS) is a multidisciplinary and cutting-edge scientific research field produced and developed on the basis of microelectronics technology. It is a micro device or system that integrates micro sensors, micro actuators, and micro mechanical structures. Traditional MEMS devices are usually based on silicon materials, which are showing more and more environmental limitations and temperature reliability problems. These shortcomings of silicon-based MEMS technology have promoted the research of more biochemically resistant and thermally stable MEMS such as wide-bandgap group III-V nitride semiconductor material MEMS. Group III-V nitride materials have very high mechanical, thermal and chemical stability, as well as excellent high-frequency characteristics. Its high-concentration two-dimensional electron gas (2DEG) is extremely sensitive to mechanical loading and surface chemical modification. In addition, group III-V nitride materials have unique piezotronics effect. These characteristics greatly expand the application of III-V nitride materials in the MEMS field. Based on the piezoelectric effect, this thesis systematically studies the theoretical modeling and fabrication of gallium nitride power MEMS devices based on the AlGaN/AlN/-GaN heterojunction with microcantilever structure. A semi-classical physical model of the power MEMS is established, and a strain-regulated power MEMS device (Strain-controlled Power Device, SPD) and a magnetic field-controlled power MEMS device (Magnitosensory Power Device, MPD) are also prepared, which provides a theoretical framework and novel device structure for the research of III-V nitride power MEMS devices.

The content of this thesis is mainly composed of the following three parts:

### 1. Theoretical model of power MEMS devices

Based on the theory of piezoelectric effect and semiconductor physics, a semi-classical physical model of a MEMS cantilever device based on the AlGaN/AlN/GaN heterojunction is established, and the modulation characteristics of the external stress on the energy band of the heterojunction as well as the electrical performance of the MEMS device are calculated, which provides a theoretical framework for the development of SPD and MPD, and the research guidance for the development and optimization of cantilevered III-V nitride power MEMS devices.

### 2. Manufacturing of power MEMS devices

In this study, the manufacture of GaN power MEMS devices from epitaxial growth wafers to well-functional devices have been systematically studied. Benefiting from the rapid development of III-V compound semiconductor fabrication and characterization equipment. Firstly, the main nanofabrication and characterization equipment is introduced, including epitaxial growth, dry etching, photolithography, thin film deposition, plasma cleaning, Raman spectroscopy, scanning electron microscopy, transmission electron microscopy, etc. Secondly, the corresponding process parameters and their process integration have been developed based on the manufacturing technology and equipment, thus realizing the whole process from GaN wafer to device. Step by step, high-performance GaN HEMTs and GaN power MEMS devices have been successfully fabricated.

### 3. Strain-controlled / Magnetosensory power MEMS devices

In this study, a strain-modulated power MEMS device (Strain-controlled power device, SPD) and a magnetic field-controlled power MEMS device (Magnetosensory power devices, MPD) are designed. The SPD uses external strain to modulate the output power of the device by simulating the reflection process of the human body. Under the external strain of  $0 \sim 16$  mN, the maximum output power density of SPD increases from  $2.30 \times 10^3$  W cm $^{-2}$  to  $2.72 \times 10^3$  W cm $^{-2}$ . The MPD uses an external magnetic field to modulate the output power of the device by simulating the working mechanism of the magnetic induction neuron. Upon the magnetic field of 200 mT, the maximum output power density of the MPD reached 85.8 W mm $^{-2}$ . Under the action of an external magnetic field of  $0 \sim 400$  mT, when the gate voltage is -5 V, the saturation output power density of MPD increases from 18.04 W mm $^{-2}$  to 18.94 W mm $^{-2}$ . Both the SPD's and MPD's gate voltage can control the output power in a larger range, so it combines the two-dimensional control advantages of small-range external strain control and large-range programmable gate voltage control. This research not only provides insights into the interaction between external stimulation and power control of GaN MEMS devices, but also promotes the development of bionic intelligent power MEMS devices.

# List of Abbreviations and Symbols

## Roman Symbols

$c_E$	Elastic coefficient tensor
$D$	Electric displacement vector
$E$	Electric field strength vector
$e$	Linear piezoelectric coefficient
$k$	Dielectric constant tensor
$S$	Strain tensor
$\mathbf{P}$	Electric polarization strength
$\psi_i(x)$	Wave function of the $i$ th subband
$\sigma$	Stress tensor
$\theta$	Rotation angle
$\epsilon(x)$	Dielectric constant AlGaN, AlN and GaN
$\epsilon_0$	Vacuum permittivity
$a$	Lattice constant

$a_{AlGaN}$	Lattice constant of AlGaN
$a_{AlGaN}(strain)$	Lattice constant of strained AlGaN
$a_{AlN}$	Lattice constant of AlN
$a_{AlN}(strain)$	Lattice constant of strained AlN
$a_A$	Lattice constant of the substrate $A$
$a_B(epi)$	Lattice constant of the thin film $B$
$a_{GaN}$	Lattice constant of GaN
$a_{GaN}(strain)$	Lattice constant of strained GaN
$A_m$	Area of magnetic film
$Al_xGa_{1-x}N$	The percentage of AlN in AlGaN
$B$	External magnetic field
$b_{Al_xGa_{1-x}N}$	Bending coefficient of AlGaN
$c$	Lattice constant
$C_{11}$	Elastic constants
$C_{12}$	Elastic constants
$C_{13}$	Elastic constants
$C_{33}$	Elastic constants
$e_{133}$	Piezoelectric Constant
$e_{31}$	Piezoelectric Constant

$e_{311}$	Piezoelectric Constant
$e_{33}$	Piezoelectric Constant
$e_{333}$	Piezoelectric Constant
$E_g$	Bandgap energy
$e_{ijk}$	Nonlinear piezoelectric coefficient of GaN crystal
$E_i$	Energy of the $i$ th subband
$F$	External force
$g_m$	Transconductance
$I_{ds}$	Source-drain current
$k_B$	Boltzmann constant
$m^*$	Effective mass of the electron
$n(x)$	Concentrations of free electrons
$n_{2DEG}$	2DEG concentration
$N_A^-$	Acceptor ion concentration
$N_D^+$	Donor ion concentration
$N_e$	Sum of the electron densities in all the subbands
$n_i$	Density of electrons in the $i$ th subband
$p(x)$	Concentrations of holes
$P_{AlGaN}^{PE}$	Piezoelectric polarization charge density of AlGaN

---

$P_{AlGaN}^{sp}$	Spontaneous polarization charge density of AlGaN
$P_{AlN}^{PE}$	Piezoelectric polarization charge density of AlN
$P_{AlN}^{sp}$	Spontaneous polarization charge density of AlN
$P_{GaN}^{PE}$	Piezoelectric polarization charge density of GaN
$P_{GaN}^{sp}$	Spontaneous polarization charge density of GaN
$P_{interface}$	The density of polarization charges at the interface
$P_{PE}$	Piezoelectric polarization charge density
$P_{Psp}$	Spontaneous polarization charge density
$P_z$	Piezoelectric polarization in the $z$ direction
$q$	Absolute value of the unit charge
$S_{\perp}$	Lattice strains perpendicular to c-plane of GaN crystal
$S_{AlGaN}(strain)$	Strain of strained AlGaN
$S_{AlN}(strain)$	Strain of strained AlN
$S_B$	Stain of the thin film $B$
$S_{GaN}(strain)$	Strain of strained GaN
$S_{xx}, S_x$	Strains in the $x$ direction
$S_{yy}, S_y$	Strains in the $y$ direction
$S_{zz}, S_z$	Strains in the $z$ direction
$T$	Electron temperature

---

$v$	Poisson's ratio
$V(x)$	Potential energy
$V_c(x)$	Conduction band edge potential
$V_{ds}$	Source-drain voltage
$V_{gs}$	Gate voltage
$V_h(x)$	Hartree potential
$V_{xc}(x)$	Exchange-correlated potential
$S_{xx}(GaN)$	Strain of GaN in the $x$ direction
$S_{yy}(GaN)$	Strain of GaN in the $y$ direction
$S_{zz}(GaN)$	Strain of GaN in the $z$ direction

**Acronyms**

2DEG	The two-dimensional electron gas
AlGaN	Aluminium gallium nitride
AlN	Aluminum nitride
FET	Field effect transistor
HEMT	High-electron-mobility transistor
CVD	chemical vapor deposition
DC	Direct current
E-Beam	Electron beam

---

EDX	Energy dispersive X-ray spectroscopy
EUV	Extreme ultraviolet
GaN	Gallium nitride
HAADF-STEM	High-angle annular dark-field scanning transmission electron microscopy
ICP-RIE	Inductively coupled plasma reactive ion etching
MOCVD	Metal organic compound chemical vapor deposition
MOVPE	Metal organic vapor phase epitaxy
MPD	Magnetosensory power device
PVD	Physical vapor deposition
RF	Radio frequency
RTP	Rapid thermal processing
SEM	Scanning electron microscopy
SPD	Strain-controlled power devices
TEM	Transmission electron microscopy
UID	Unintentionally doped
UV	Ultraviolet
XRD	X-ray diffraction

# **Chapter 1**

## **Introduction**

### **1.1 Introduction to piezotronics effect**

The piezoelectric effect is the effect of accumulating electric charge in certain solid materials in response to applied mechanical stress, e.g. crystals, some ceramics and biological substances such as bones, DNA and various proteins [1]. It was discovered in 1880 by brothers Pierre and Jacques Curie [2]. In 1910, German physicist W. A. Wooster published the book "A Text-Book on Crystal Physics", which described 20 natural crystals capable of producing piezoelectric effects, and used tensor analysis to strictly define piezoelectric coefficients for the first time [3]. In 2006, Neil Downey proposed to use piezoelectric material and carbon piezoresistive material to make a FET-like amplifying device, which marked the beginning of piezoelectric effect research in the field of electronics [4]. By combining the semiconductor properties and piezoelectric properties of piezoelectric semiconductor materials, Professor Zhong Lin Wang formally proposed the concepts of "Piezotronics" and "Piezophotonics" in 2007 and explained the basic principles [5]. Figure 1.1 shows the coupling characteristics of piezoelectric electronics and piezoelectric optoelectronics. The coupling between piezoelectric, opti-

cal, and semiconducting properties in piezoelectric semiconductor materials is the basis of piezotronics (piezoelectricity-semiconductor coupling), piezophotonics (piezoelectric-photon excitation coupling), optoelectronics, and piezophotronics (piezoelectricity-semiconductor-photoexcitation) [6]. Since it was formally proposed, this research field has developed rapidly and made a lot of remarkable progress [7–9].

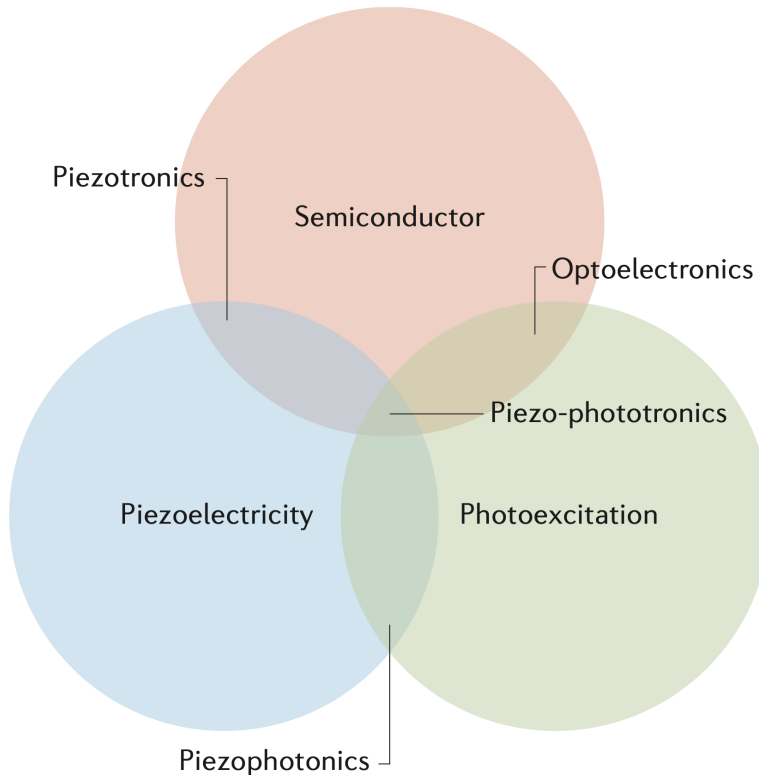


**Fig. 1.1 Coupling characteristics of piezotronics and piezo-photronics [6]**

The research of piezotronics effect mainly focus on the adjust/control the transport of carriers through piezoelectric potential generated by mechanical stress in semiconductor materials with piezoelectric properties. Therefore, according to this effect, the external stress can directly regulated the macroscopic electrical properties of piezoelectric semiconductor materials [10]. Among them, the Wurtzite crystal with hexagonal close-packed structure has good piezoelectric properties due to its non-centrosymmetric structure [11]. Some of these materials have both piezoelectric and semiconductor properties, such as ZnO, GaN, InN and ZnS, etc., so

they are widely used in piezotronics research. Figure 1.2 shows the piezoelectric potential in Wurtzite-structured ZnO nanowires. The  $Zn^{2+}$  cation and  $O^{2-}$  anion in ZnO are tetrahedral coordinated, and the centers of positive and negative ions overlap each other. If stress is applied at the vertices of the tetrahedron, the center of the cation and the center of the anion are displaced relative to each other and an electric dipole moment is created (Figure 1.2a).

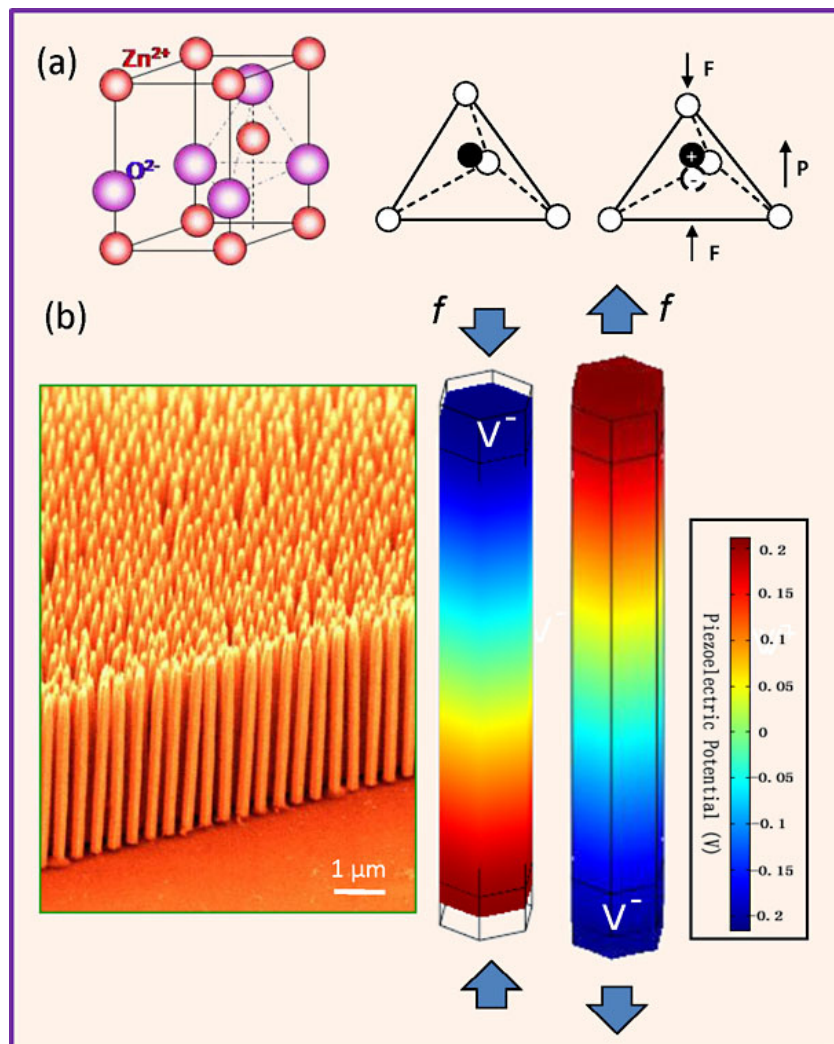


**Fig. 1.2 Piezopotential in wurtzite crystal ZnO [12]**

The accumulation of electric dipole moments generated by all units in the crystal leads to the generation of polarization charges with the same density and opposite polarity at the interface between the two ends of the crystal, resulting in a macroscopic potential along the strain

direction, that is, the piezoelectric potential (Figure 1.2b). For a ZnO nanowire with a length of 1200 nm and a hexagonal length of 100 nm, a pulling force of 85 nN produces a positive potential of approximately 0.4 V between the two ends. When the applied force becomes compressive stress, the piezoelectric potential is reversed. The potential difference remains 0.4 V, and the piezoelectric potential at both ends of the nanowire is the same in magnitude and opposite in polarity. The first systematic study of the piezoelectric potential in ZnO nanowires marked the beginning of the research of piezotronics [13].

In piezoelectric semiconductor materials, the piezoelectric effect can significantly modulate the energy band structure of the material, thereby affecting the electrical properties of the material. Under the action of mechanical stress, piezoelectric polarization charges with opposite polarities are generated at the interface of the material. Piezoelectric polarization charges are distributed within a small depth from the surface of the material, and they are non-mobile ionic charges located near the interface. In this case, due to the finite dielectric constant and limited doping concentration of the crystal, the free carriers can only partially shield the piezoelectric polarization charge, but they cannot completely cancel the piezoelectric polarization charge. The piezoelectric potential formed by the piezoelectric polarization charges at the material interface can significantly change the contact properties of the semiconductor through the built-in electric field, and thus the optical and electrical properties of the semiconductor contact can be directly modulated by external mechanical stress. Among them, Schottky contact, p-n junction, p-n heterojunction are the most common semiconductor contacts in piezoelectric semiconductor materials, so we briefly discuss the piezoelectric effects in these three semiconductor contacts (Figure 1.3).

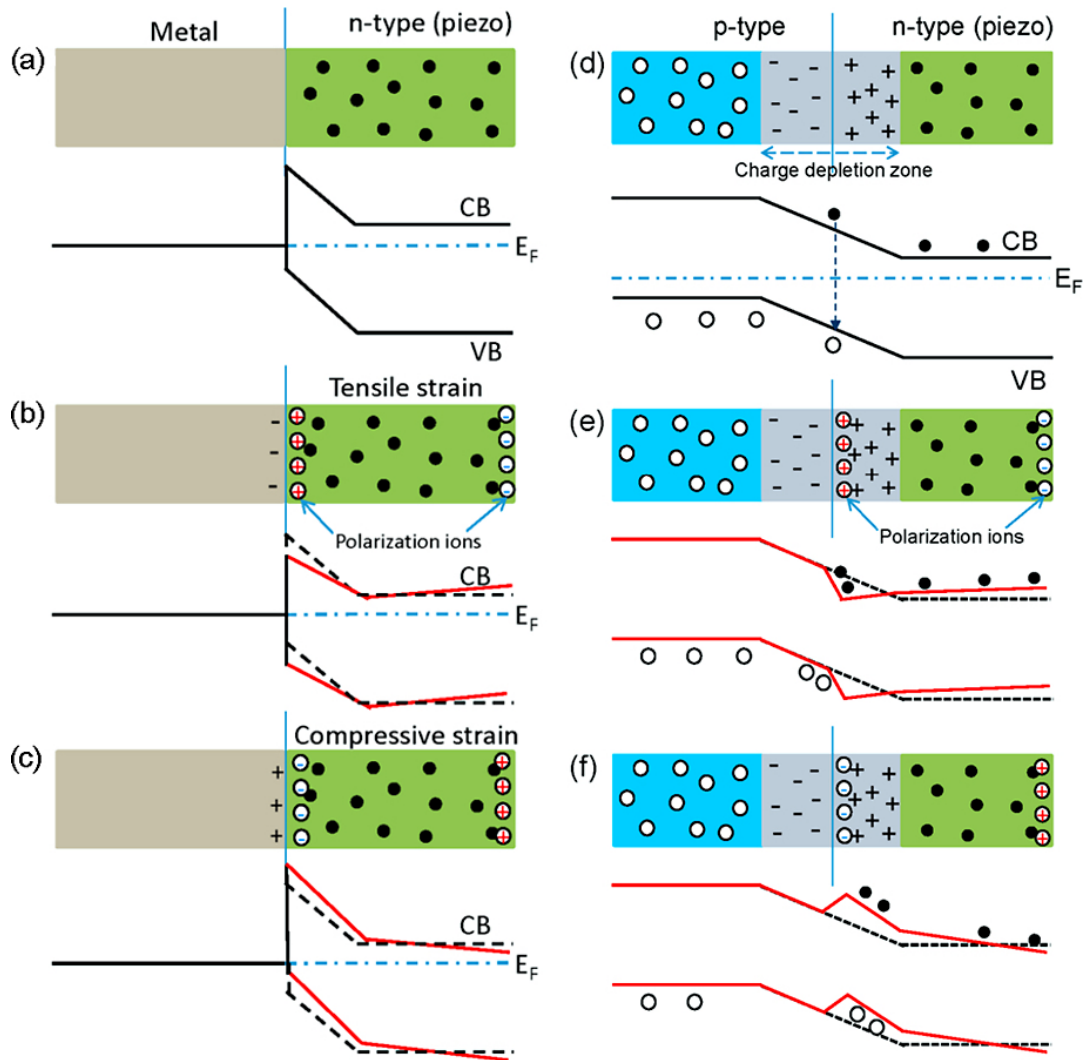


**Fig. 1.3 Energy band diagram of piezotronics effect in Schottky contact (a-c) and p-n junction (d-f) [12]**

In a Schottky contact formed by a metal material and a piezoelectric semiconductor material, strains in different directions can generate piezoelectric polarization charges with opposite polarizations at the interface of the piezoelectric semiconductor material, and a negative piezoelectric polarization charges at the metal-semiconductor material interface can effectively reduce the local barrier height of Schottky contacts, while negative piezoelectric polarization charges further increase the barrier height (Figure 1.3a–c). The height of the Schottky barrier determines the carrier transport properties at the metal-semiconductor material interface, so we

can directly modulate the electrical properties of the Schottky contact by external mechanical stress according to the piezotronics effect.

In a p-n junction composed of the same bandgap material, the interdiffusion and recombination of electrons and holes forms a depletion region in the junction region when the p-type and n-type semiconductors are in contact. The presence of such carrier-free regions can significantly enhance the piezotronics effect, since the piezoelectric polarization charges here are not shielded by locally remaining free carriers. As shown in Figure 1.3d-f, with the strain applied to n-type piezoelectric semiconductor material, a net positive piezoelectric polarization charge will be generated at the depletion region interface if the doping concentration is relatively low. Piezoelectric potential tends to lower the local energy band slightly and introduce a slow slope into the energy band. When the applied strain is in the opposite direction, the negative piezoelectric polarization charge at the interface of the depletion region raises the local energy band. The change of the energy band in the p-n junction can significantly affect the electron-hole recombination rate, which is very beneficial to improve the efficiency of LEDs. In addition, the degree of band tilt also affects the internal carrier mobility. Therefore, the piezotronics effect in the p-n junction can effectively tune its electrical and optical properties by external mechanical stress.

For p-n heterojunctions made of two materials with different band gaps, the piezoelectric polarization charge also significantly affects the band distribution, as shown in Figure 1.4. The black and red curves are used to represent the energy band diagrams of the p-n heterojunction before and after the external strain in the eight cases, from which it can be seen that the transport characteristics of carriers at the interface will be directly modulated by the piezoelectric polarization charge. Take the case shown in Figure 1.4e as an example: the height of the barrier formed at the interface is reduced due to the reduction of the energy band caused by the piezoelectric polarization charge, so that electrons can be transported across the interface

more efficiently. In contrast to Figure 1.4f, the height and width of the potential barrier at the interface increase due to piezoelectric polarization charges, hindering the transport of electrons

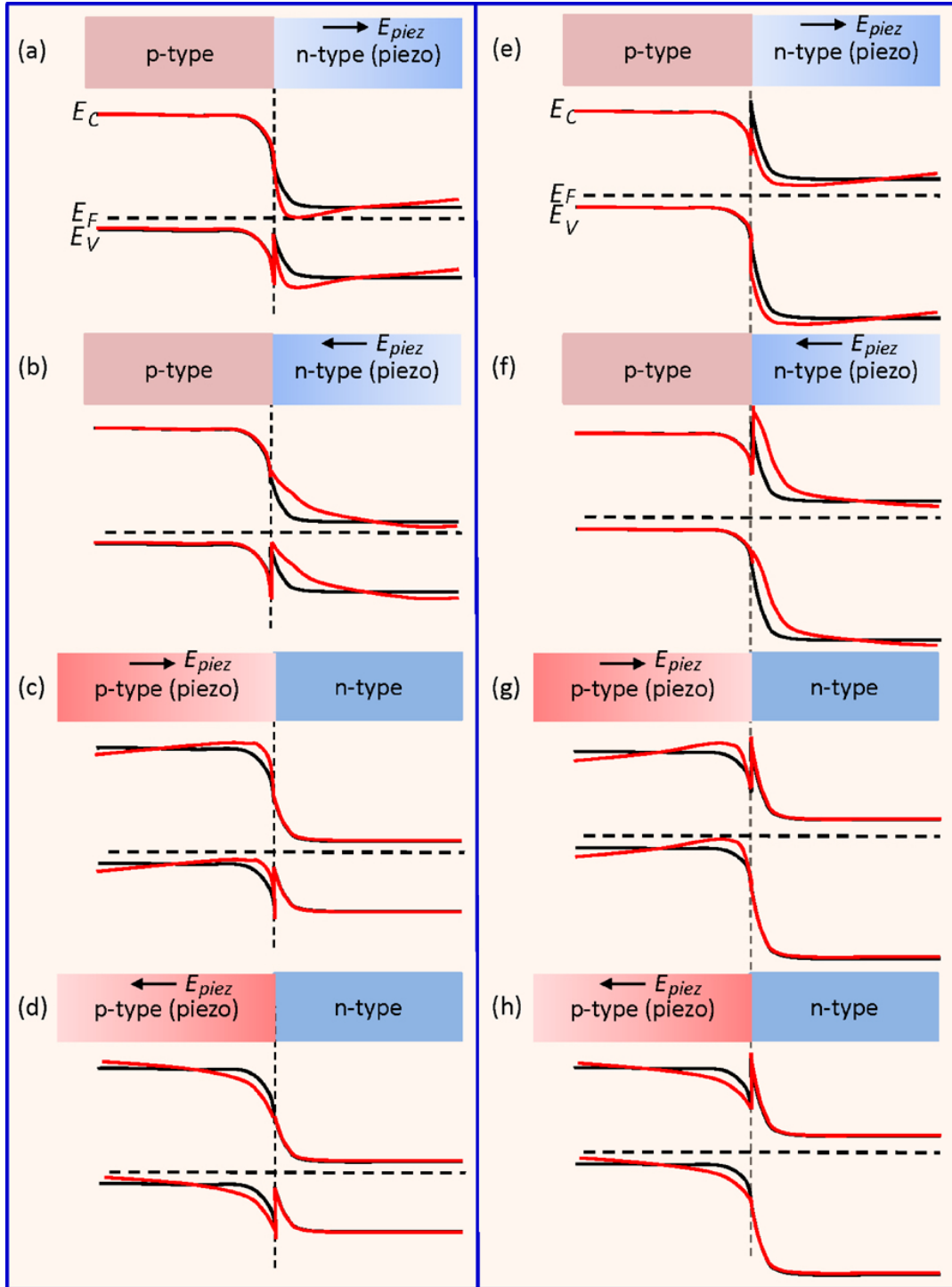


**Fig. 1.4 Energy band diagram of piezotronic effect in p-n heterojunction [12]**

across the interface. For the case shown in Figure 1.4b, the reorganization of the energy band caused by the piezoelectric polarization charge can significantly increase the local trapping of holes and improve the luminous efficiency of the LED. But for the case of Figure 1.4a, the reformation of the energy bands negatively affects the efficiency of the LED. Therefore, based on the piezotronics effect, the external strain in the heterojunction can effectively tune the optoelectronic properties of the material.

Piezotronics transistors can be designed and fabricated based on the modulation properties of piezoelectric polarization charges in piezoelectric semiconductor materials. For a conventional n-channel metal-oxide-semiconductor field-effect transistor MOSFET (Fig. 1.5a), the drain and source are two n-type doped regions, and a thin metal insulating oxide layer is deposited on the p-type region to form the Schottky contact as the gate. The gate voltage  $V_G$  controls the channel width of the transport carriers, so the current flowing from the drain to the source under the source-drain bias voltage  $V_{DS}$  is controlled by the gate voltage  $V_G$ . Similarly, for a single-channel FET (Figure 1.5b) fabricated using semiconducting nanowire materials, the drain and source are two metal electrodes, and the current is regulated by applying a gate voltage on top of the nanowire. A piezotronics transistor is a metal-nanowire-metal structure, such as Au-ZnO-Au or Ag-ZnO-Ag, as shown in Figure 1.5c,d. The basic principle of piezotronics transistor is to generate a piezoelectric potential at the interface of the semiconductor by applying external strain, thereby regulating the local energy band at the contact, and finally realizing the control of the carrier transport characteristics at the metal-semiconductor interface. Therefore, unlike conventional MOSFETs, in piezotronics transistor based on the piezoelectric effect, the externally applied gate voltage that controls the channel width is replaced by a strain-generated piezoelectric potential, thus eliminating the "gate". Piezotronics transistor are a new type of transistors that replace voltage control with external strain/stress control, and have broad application prospects.

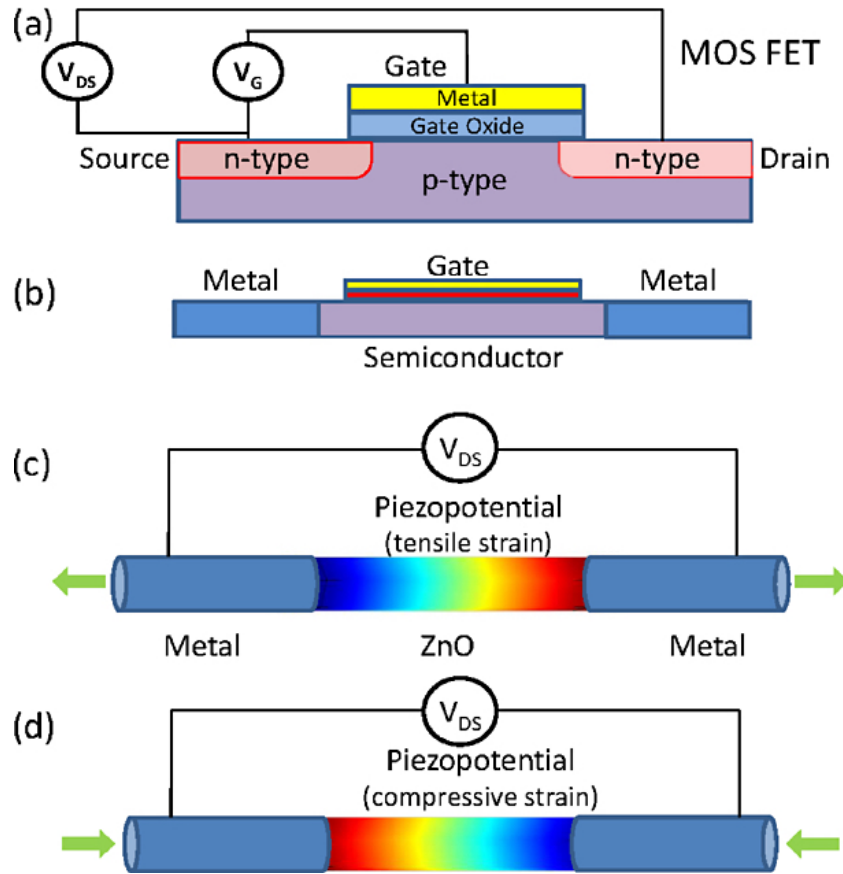


**Fig. 1.5 Working principle of piezotronics transistor. (a) The n-channel MOSFET; (b) The semiconductor nanowire FET; The piezotronics transistor with tensile strain (c) and compressive strain (d) [12]**

### 1.1.2 Application prospect of piezotronics effect

The study of piezotronics effects, ie the study of the coupling properties of piezoelectric and semiconductor properties in piezoelectric semiconductor materials, has given rise to a whole new range of applications. By using piezoelectric potential as the gate voltage to modulate the transport properties of electrons, researchers have fabricated transistors, sensors and smart devices driven and controlled by external stress, including piezoelectric potential gate field effect transistors [14], piezoelectric potential gated diodes [15], strain sensor [16], force/flow sensor [17], hybrid field effect transistor [18], piezoelectric logic gate [19], electromechanical

memory [20], etc. Piezotronics devices have been regarded as a new class of semiconductor devices with important applications in sensors, human-machine interfaces, MEMS, nanorobots, and flexible electronics (Figure 1.6).

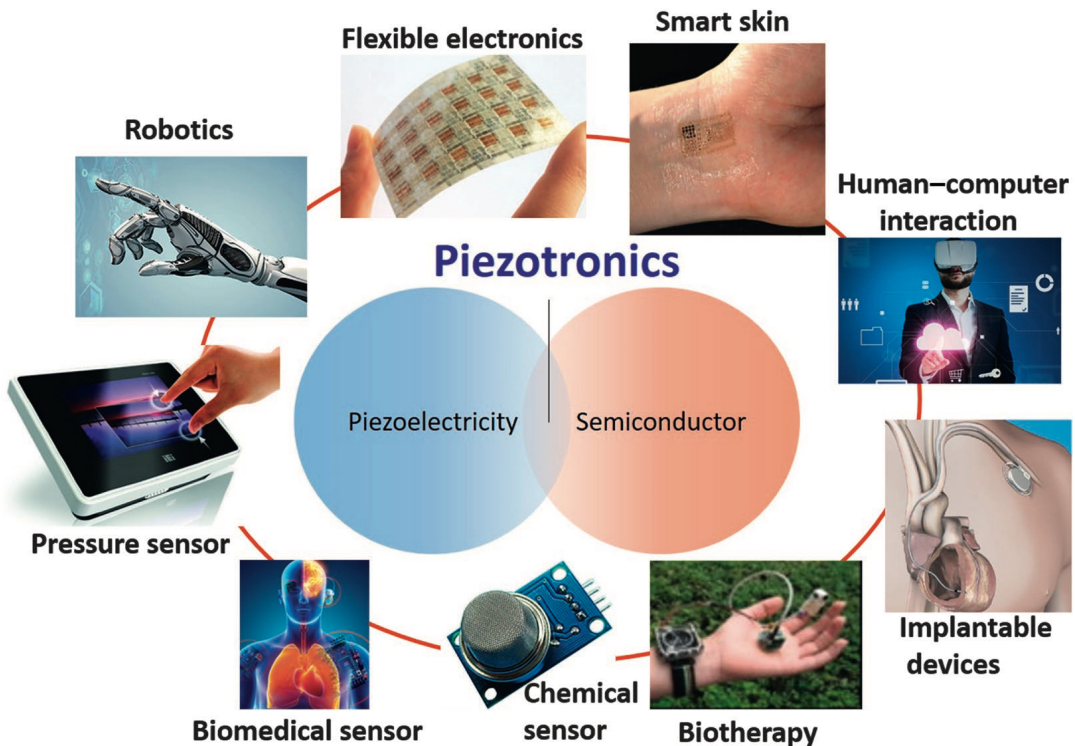


**Fig. 1.6 The application prospects and future prospects of piezotronics [9]**

## 1.2 Piezotronics effects in III-V nitrides

### 1.2.1 Crystal structure and polarization properties of III-V nitrides

Group III-V nitride materials are compound semiconductor materials formed by group III elements Al, Ga, In and group V elements N, such as GaN, InN, AlN and multi-element alloy materials ( $In_xGa_{1-x}N$ ,  $Al_xGa_{1-x}N$ , etc.). There are usually two different lattice structures of hexagonal wurtzite (Wurtzite) and cubic sphalerite (Zinc-blende). Among them, the nitride crystal of wurtzite structure is more stable and is widely used in semiconductor materials. This research focuses on GaN, AlN and  $Al_xGa_{1-x}N$  semiconductor materials.

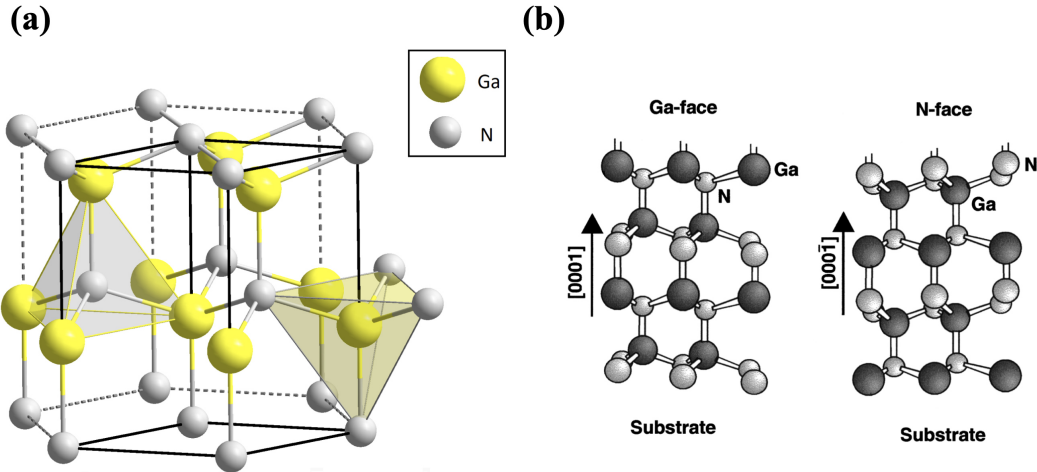


**Fig. 1.7 The wurtzite crystal structure of GaN material and the polarization characteristics of the Ga and N plane**

Figure 1.7a shows the wurtzite structure of GaN crystal. Since the wurtzite structure of GaN crystal belongs to the non-centrosymmetric crystal, the crystal pole axis is the c-axis, and the atomic layers are aligned along the c-axis from two different directions [0001] and [000̄1], thus forming two distinct polar faces. It can be seen from Figure 1.7b that when accumulating from the bottom to the top along the [0001] direction, the top is the Ga atomic plane, which causes the Ga surface polarity to be generated on the surface of the material; when accumulating from the bottom to the top along the [000̄1] direction, the top is the N atomic plane so that the N-plane polarity is generated on the surface of the material [21]. Since the electronegativity of negative ions formed by N atoms is stronger than that of positive ions formed by Ga atoms, a built-in electric field will be generated. The direction of the electric field is from Ga atoms to N atoms along the c-axis. This phenomenon is called Spontaneous Polarization effect of GaN crystal [22, 23]. Generally, the spontaneous polarization direction of Ga-plane polarity GaN crystals is that the surface points to the inside, and the upper surface of the material gathers negative polarized charges and is negatively charged. The spontaneous polarization direction of N-plane polarity GaN crystals is that the interior points to the surface. The upper

surface is positively charged by accumulating positive polarized charges. This phenomenon is more obvious in the Al-N atomic pair, so the same spontaneous polarization effect also exists in the AlGaN compound semiconductor material. In addition, if the GaN lattice is subjected to compressive or tensile deformation due to mechanical stress, it will cause lattice strain within a certain range. At this time, the centers of  $Ga^+$  ions and  $N^-$  ions will be separated to form an electric dipole moment, and the surface of the material will also appear polarization charge. This effect is called Piezoelectric Polarization effect of GaN crystal [22, 23]. Therefore, the GaN crystal is also known as piezoelectric semiconductor material.

GaN and its corresponding Al and In composition compound semiconductor materials have unique material and electrical properties due to piezoelectric effect, such as changing Al composition in AlGaN/GaN heterojunction to adjust the degree of lattice mismatch between AlGaN and GaN so as to generate corresponding piezoelectric polarization charges, thereby modulating the energy band at the heterojunction and forming a two-dimensional electron gas (2DEG) with high density and high electron mobility. The method of modulating the energy band and electrical properties by the polarization effect is called Polarization Engineering [24, 25]. Figure 1.8 shows the strain-induced piezoelectric polarization charge density and the direction of spontaneous and piezoelectric polarization in an AlGaN/GaN heterojunction with Ga- and N-plane polarities. Therefore, III-V nitride compound semiconductor materials couple piezoelectric properties and semiconductor properties, and exhibits significant piezotronics effects [26, 27, 7]. Piezoelectric polarization charges generated at the interface by external strain can modulate the energy band of the heterojunction and the two-dimensional electron gas (2DEG) concentration in the potential well [28]. In recent years, several studies have shown that the strain-induced piezoelectric polarization charge at the AlGaN/GaN heterojunction interface has been used to tune the piezoelectric nanowires [29], LEDs [30–32] and HEMTs [33–35] based on the piezotronics effect.

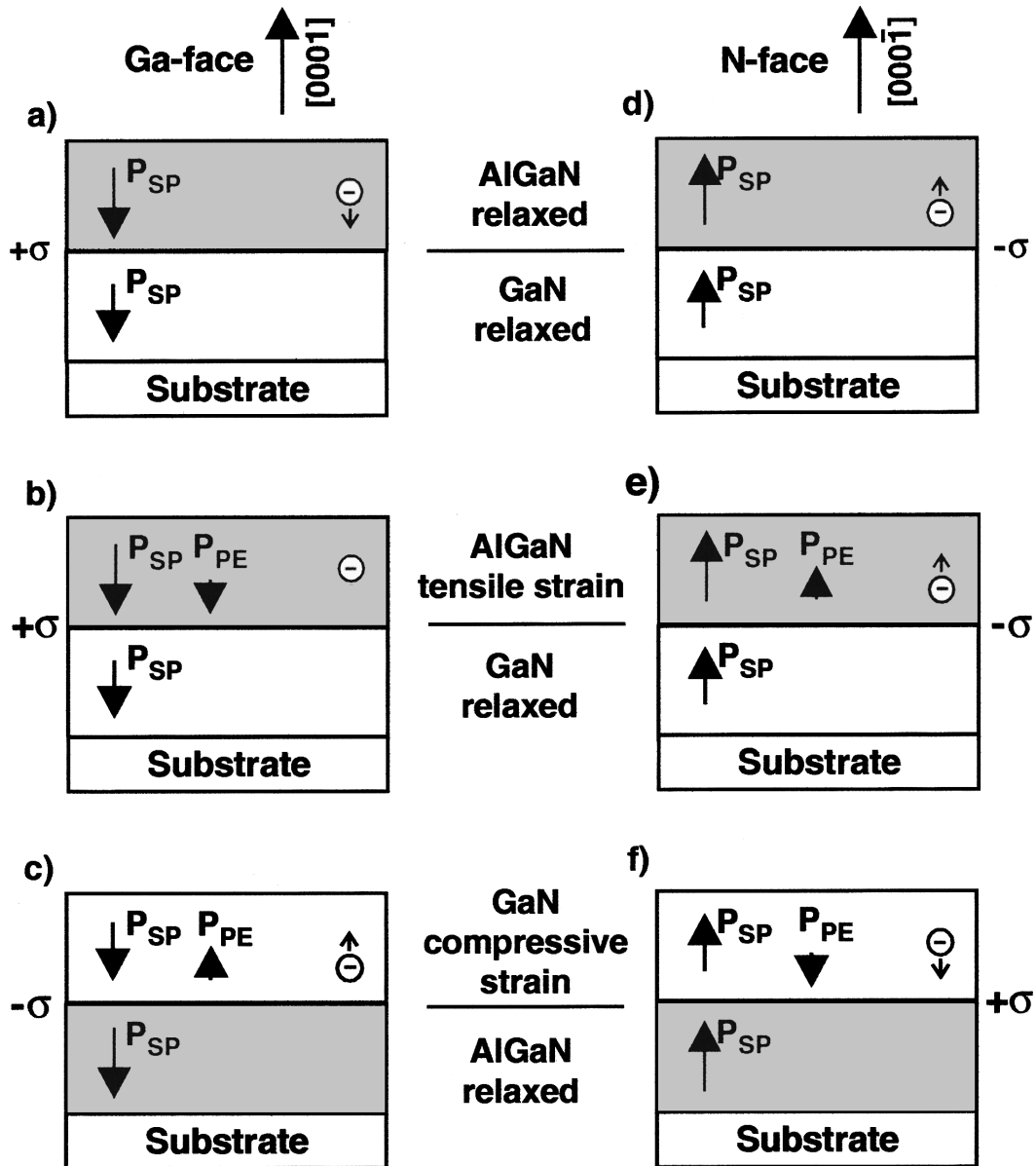


**Fig. 1.8** Polarization charge in AlGaN/GaN heterojunction with Ga-plane and N-plane polarity [36]

### 1.2.2 Application of piezotronics effect in III-V nitride

Piezotronics effects have been widely used in the study of III-V nitrides. Wang et al. were the first to study the piezotronics effect in AlGaN/AlN/GaN heterostructured microwires and applied it as a novel approach to tune the physical properties of heterojunction electron gas

(HEG) [29]. Unlike conventional approaches to tune HEG properties by changing the alloy composition or controlling the thickness of the heterojunction film, this work exploits strain-induced piezoelectric polarization charges to modify the local energy band distribution at the heterojunction, as shown in Figure 1.9. By introducing piezotronics effects into AlGaN/Al-N/GaN heterostructure microwires, the electrical conductivity of HEG increases by 165% at -1.78% compressive strain and decreases by 48% at 1.78% tensile strain at room temperature. This modulation is further enhanced by 890% and 940% under compressive and tensile strains, respectively, due to the enhanced piezoelectric effect at lower ambient temperature of 77 K. This study provides insight into the piezotronics effects of low-dimensional electron gas in heterostructured nanomaterials with potential applications in HEMT and MEMS/NEMS.

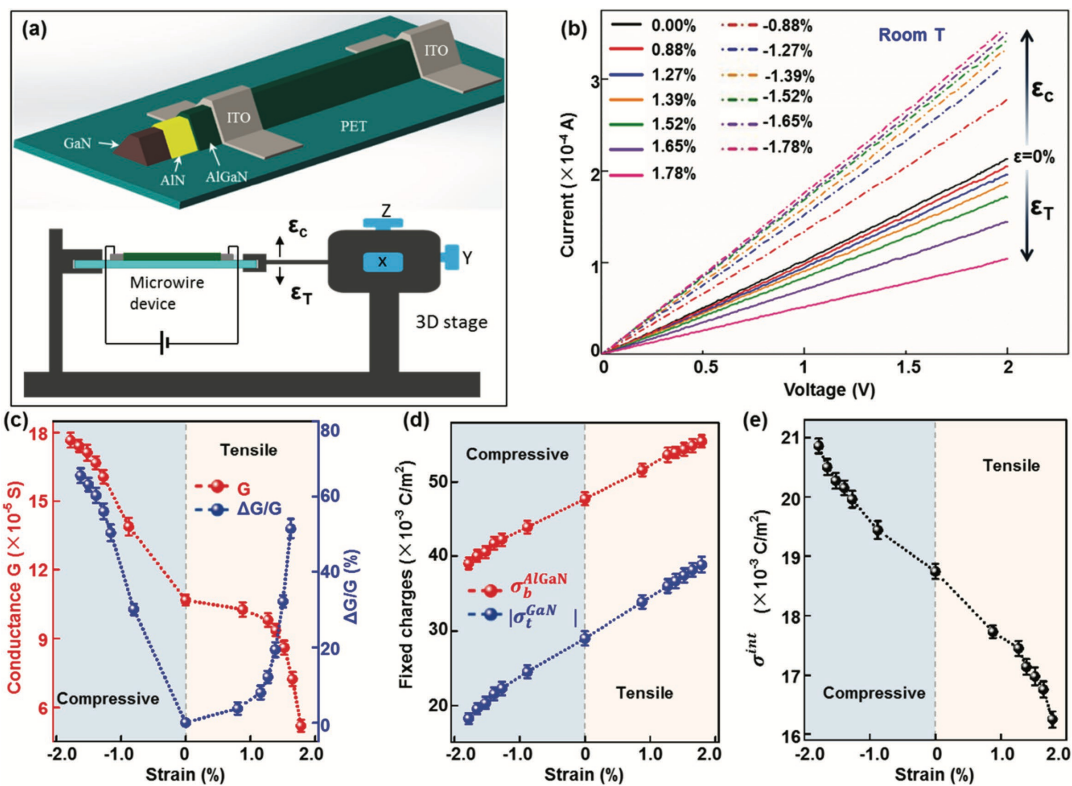


**Fig. 1.9 Piezotronic effect in AlGaN/AlN/GaN heterostructure microwire [29]**

In the work of Liu et al., the piezotronics effect in AlGaN/GaN MOS high-electron mobility-transistors (HEMT) [33, 37] was studied for the first time (Figure 1.10). Traditional AlGaN/

GaN MOS HEMTs adjust the 2DEG concentration at the interface by adjusting the alloy composition or modifying the thickness of the epitaxial layer, which modulates the electrical properties of the HEMT device mainly from the perspective of materials science. This work is the first to use strain-induced piezoelectric polarization charge to change the energy band distribution in AlGaN/GaN heterojunctions, thereby affecting the carrier distribution and 2DEG concentration and modulating the electrical properties of HEMT devices. This study deepens the understanding of piezotronics effects in AlGaN/GaN heterojunction transistors and provides a new idea for the research of piezotronics transistors based on AlGaN/GaN HEMTs.

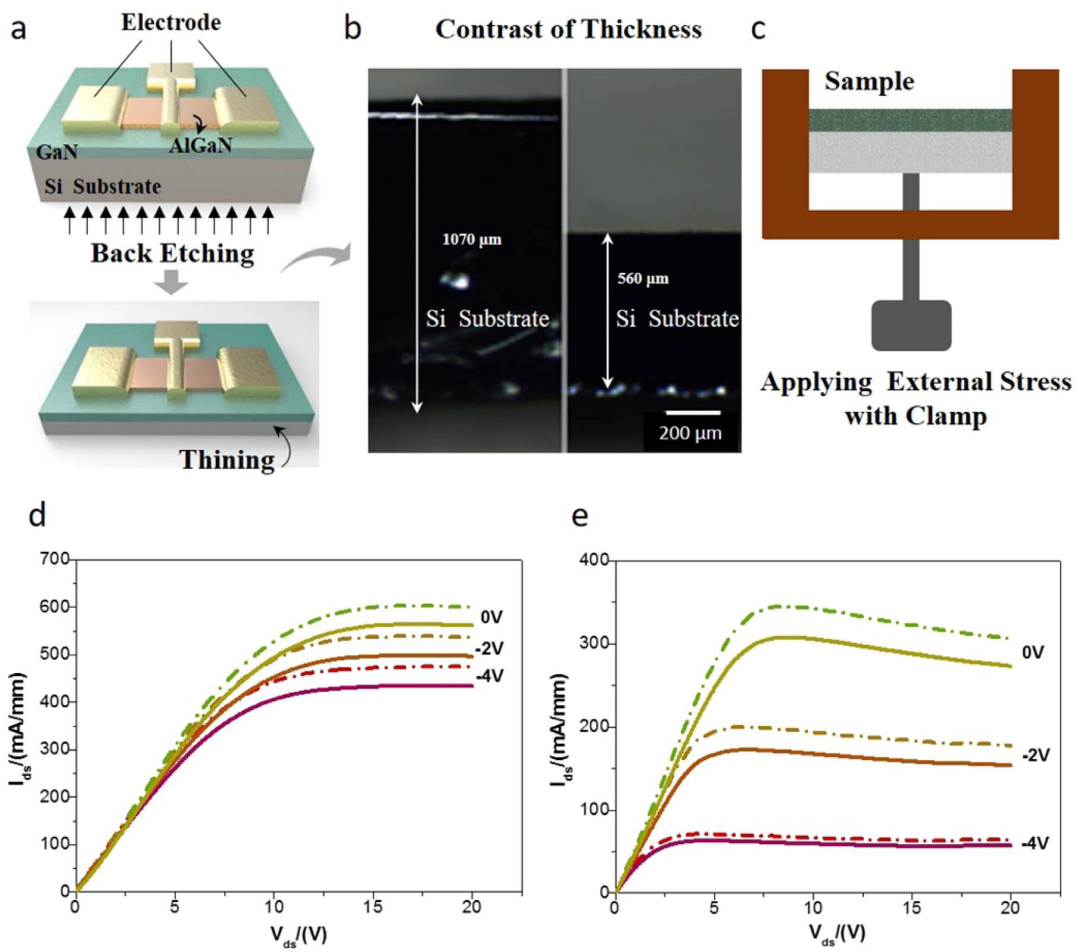


**Fig. 1.10** Piezotronics effect in AlGaN/GaN MOS HEMTs and unpassivated HEMTs [33]

Flexible electronics have received increasing attention due to their wide-ranging applications in fields such as healthcare, robotics, and artificial intelligence. Based on the work of Liu et al., Zhu et al. successfully fabricated flexible AlGaN/GaN HEMTs and studied their electrical properties under bending strain through piezotronics effects (Figure 1.11) [35, 38].

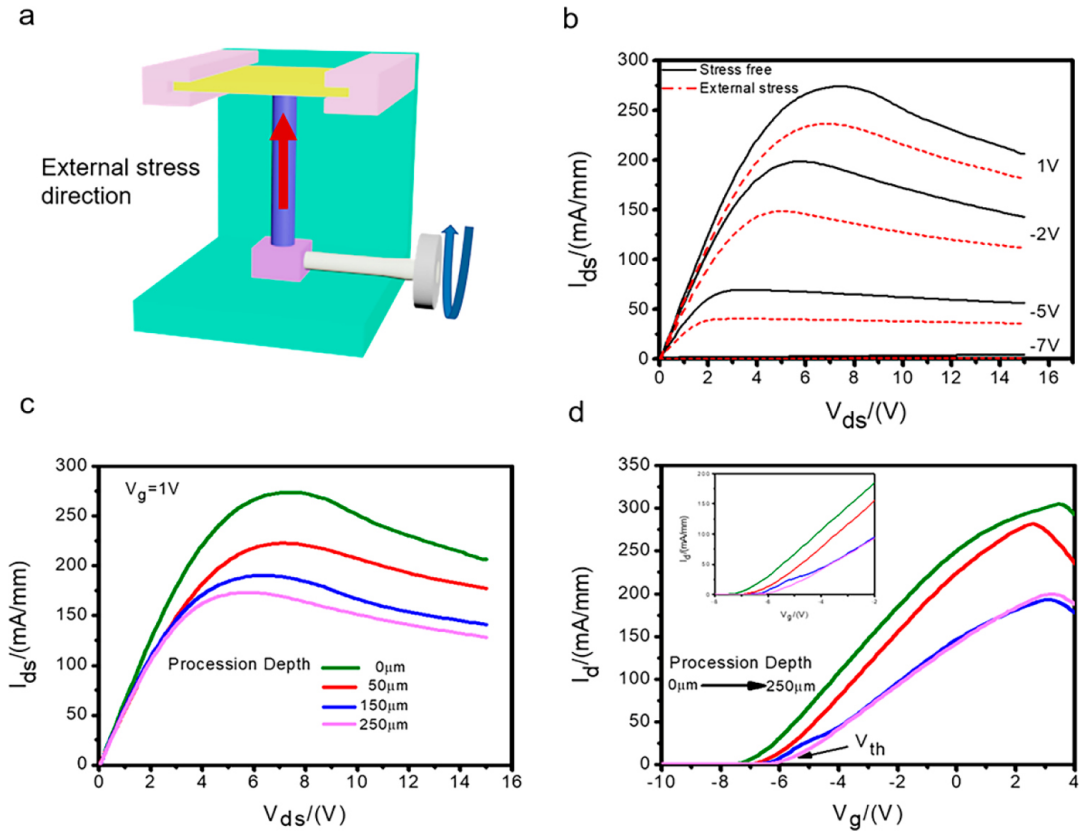


**Fig. 1.11 Piezotronics effect modulated flexible AlGaN/GaN HEMT [35]**

The fabricated flexible AlGaN/GaN HEMT completely removes the rigid silicon substrate and has excellent electrical properties. When the gate voltage  $V_{gs} = 2\text{ V}$ , the maximum saturated drain current density  $I_{ds,max}$  reaches  $290\text{ mA mm}^{-1}$ , The maximum transconductance  $g_{m,max}$  reaches  $40\text{ mS mm}^{-1}$ . At the same time, the flexible HEMT can withstand large bending strains. Based on the piezotronics effect of the AlGaN/GaN heterojunction, mechanical stress was introduced in the experiment to study the electrical properties of the flexible HEMT under strain. The results show that the output current of the flexible HEMT device can be sig-

nificantly modulated by the external strain, and the electrical performance of the device will be degraded if it is subjected to forward bending strain. Flexible HEMT devices modulated by piezotronics effects have broad application prospects in the fields of wearable electronics, smart MEMS, and human-computer interaction.

## 1.3 Introduction to III-V nitride MEMS devices

### 1.3.1 Introduction to micro-electromechanical systems (MEMS)

In the past decade, Micro-electromechanical systems (MEMS) technology has developed from a basic exploratory research to an important mainstream technology that has been widely used in many fields [39–41]. As an industrial technology that integrates microelectronics technology and mechanical engineering, MEMS combines the electrical information processing function and the mechanical sensing function to form a micro-electromechanical integrated system.

MEMS have three main characteristics:

- 1) Combines electrical and mechanical components in order to sense its environment (mechanical sensors).
- 2) Ability to analyze data (electronics) and react to changes in the environment (actuators).
- 3) Devices are typically fabricated by microelectronics and have dimensions on the order of micrometers to millimeters.

Therefore, MEMS can "perceive", "think" and "react", and it is an intelligent micro-integrated system. The system block diagram of MEMS is shown in Figure 1.12.

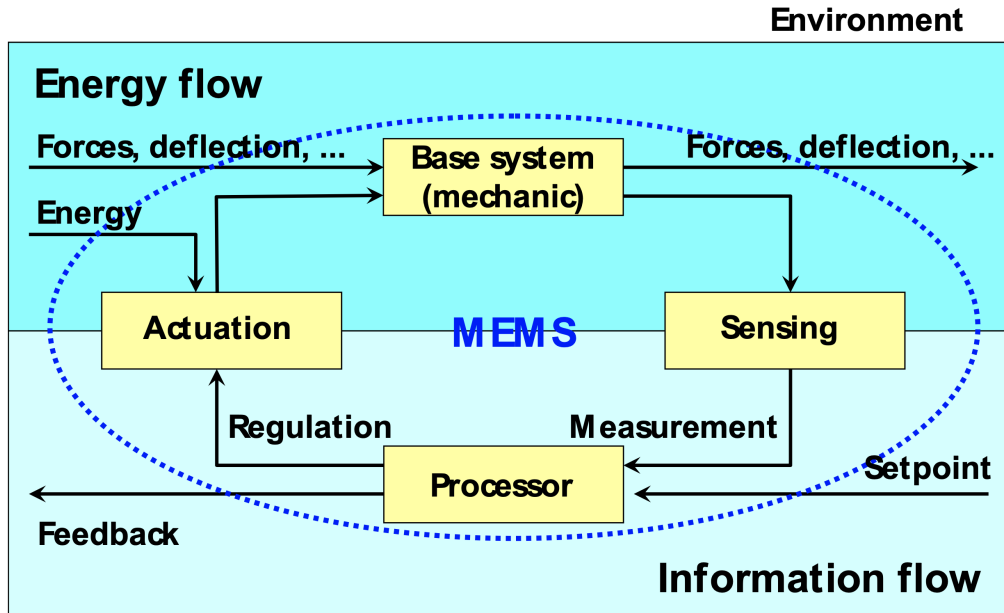


Fig. 1.12 Block diagram for the basic components in MEMS and their interaction [42]

### 1.3.2 III-V nitride MEMS devices

With the rapid development of silicon-based microelectronics technology, the integration of Si-based MEMS devices has rapidly increased, and the system's "response" is faster, more reliable, cheaper, and capable of incorporating more complex functions. Si-based MEMS devices are being used in more and more fields [43], including chemical, biological and physical sensors [44–47], microfluidic sensors [48], radio frequency MEMS [49, 50], micro-opto-electro-mechanical system (MOEMS) [51, 52], Internet of Things, etc., as well as various MEMS-based acceleration, pressure, and flow sensors [53–55] used in the automotive industry. However, Si-based MEMS have shown limitations for sensing in harsh environmental conditions [56], an issue that has received increasing attention over the past few years. First, Si-based MEMS cannot be used for high-temperature applications because Si materials lose mechanical reliability at 500 °C [56]. Second, Si materials are easily attacked by corrosive media and have low biochemical compatibility, which limits its application in the field of biosensing [56].

Therefore, additional protection of the sensing and actuation elements is necessary for chemical and biological Si-based MEMS sensors, which are generally no longer integrated systems. For these reasons, Si-based MEMS allow only very limited applications. These shortcomings of Si-based MEMS technology have stimulated research into MEMS of more biochemically resistant and thermally stable materials such as wide-bandgap semiconductors.

**Table 1.1 Comparison of characteristics of several electromechanical materials [57]**

Material	Elastic Modulus $C_{33}$ (GPa)	Acoustic Velocity (m/s)	Piezoelectric Coefficient $e_{33}$ (C m $^{-2}$ )	$f \times Q$ (Hz)	$K_{eff}^2$ (%)	Ref
Si	165	8415	N/A	$2.5 \times 10^{13}$	N/A	[58]
SiC	605	13100	0.2	$3.5 \times 10^{14}$	0.08	[58–61]
GaAs	118	2470	-0.16	–	0.04	[62, 63]
AlN	390	11000	1.55	$10^{13}$	5.6	[58, 64]
GaN	398	8044	0.65	$5.0 \times 10^{12}$	2	[58, 65–68]

III-V nitride materials are the main representatives of wide-bandgap semiconductors because of unique material properties that exhibit excellent mechanical, electrical, and perceptual properties in MEMS applications (Figure 1.13) [57, 69, 70]. Compared to Si [71], the high Young's modulus of III-V nitrides enables higher frequencies and quality factor in resonant devices of the same geometry (Table 1.1). In addition, materials with high Young's modulus can better maintain the linear relationship between applied load and induced strain. Another major advantage of III-V nitrides is their very high mechanical, thermal, chemical and biological stability [72, 73]. They have no or very low reactivity with molecules in air, and can be applied in reliable environmental sensors. Therefore, III-V nitride materials are very suitable

for MEMS or NEMS applications. Finally, due to the high frequency properties of III-V nitride materials, they can be combined or integrated into MEMS as amplifiers for radio frequency devices. It is worth mentioning that the piezoelectric effect offers completely new possibilities to integrate new functionalities into MEMS devices [74]. The AlGaN/GaN heterojunction interface contains a high concentration of two-dimensional electron gas (2DEG), which is extremely sensitive to both mechanical loading and chemical modifications of the surface, such as (i) the charge on the free, unpassivated gate surface; (ii) mechanical stress that modulates the internal piezoelectric potential; and (iii) external fields such as magnetic fields or electromagnetic radiation. Therefore it is widely used in biochemical sensors [75–81], pressure sensors [82, 83], cantilever sensors [84–86], and many other novel sensors. Compared with Si-based MEMS, MEMS devices based on III-V nitrides have broader development prospects.

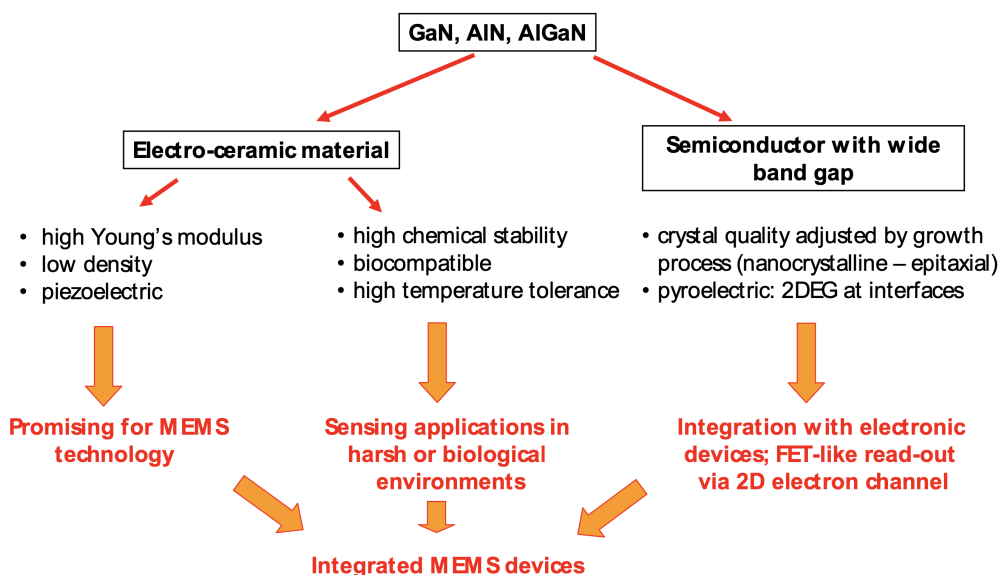


**Fig. 1.13 Advantages of group III-V nitrides for the realization of integrated MEMS [42]**

Based on the excellent properties of III-V nitride materials, the research on GaN-based MEMS devices has made remarkable progress. Azadeh Ansari et al. reported a gigahertz AlGaN/GaN resonant body transistor (RBT) in which mechanical resonance and electrical signals can be modulated simultaneously, as shown in Figure 1.14 [87]. An AlGaN layer with

a thickness of 17.5 nm was used as the piezoelectric transducer layer, and the 2DEG at the AlGaN/GaN interface was used as the bottom electrode as well as the transistor conduction channel. The strain generated by the acoustic wave can effectively modulate the 2DEG concentration of the channel. A quality factor of 250 and an acoustic transconductance of 25  $\mu\text{S}$  are obtained at the resonant frequency of 4.23 GHz, resulting in excellent mechanical and electrical properties.

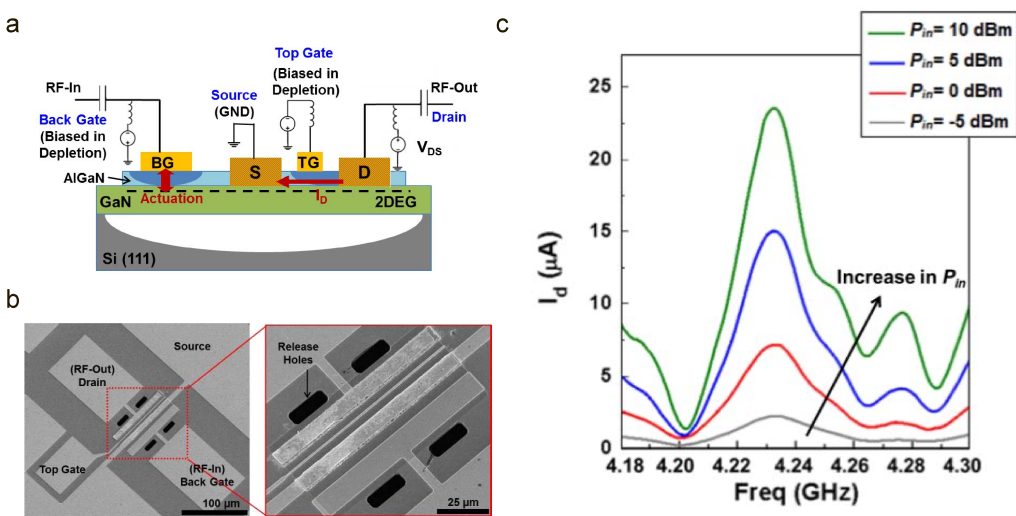


**Fig. 1.14 The AlGaN/GaN resonant body high electron mobility transistor [87]**

The development of all-GaN integrated MEMS has always been the focus of research in the field of GaN-based MEMS. On the basis of the above work, Azadeh Ansari et al. reported an all-GaN integrated microsystem platform integrating high-frequency GaN-based MEMS resonators and AlGaN/GaN HEMTs, as shown in Figure 1.15 [88]. For the first time, stacked high-quality GaN bulk acoustic resonators and AlGaN/GaN HEMTs have been fabricated on silicon substrates, achieving signal tuning over 30 dB using HEMT amplifiers. This work can serve as a starting point for further development of integrated GaN-based MEMS, that is, integrating GaN-based devices (MEMS, HEMT, RBT, etc.) together to build fully GaN integrated MEMS with different architectures and functions.

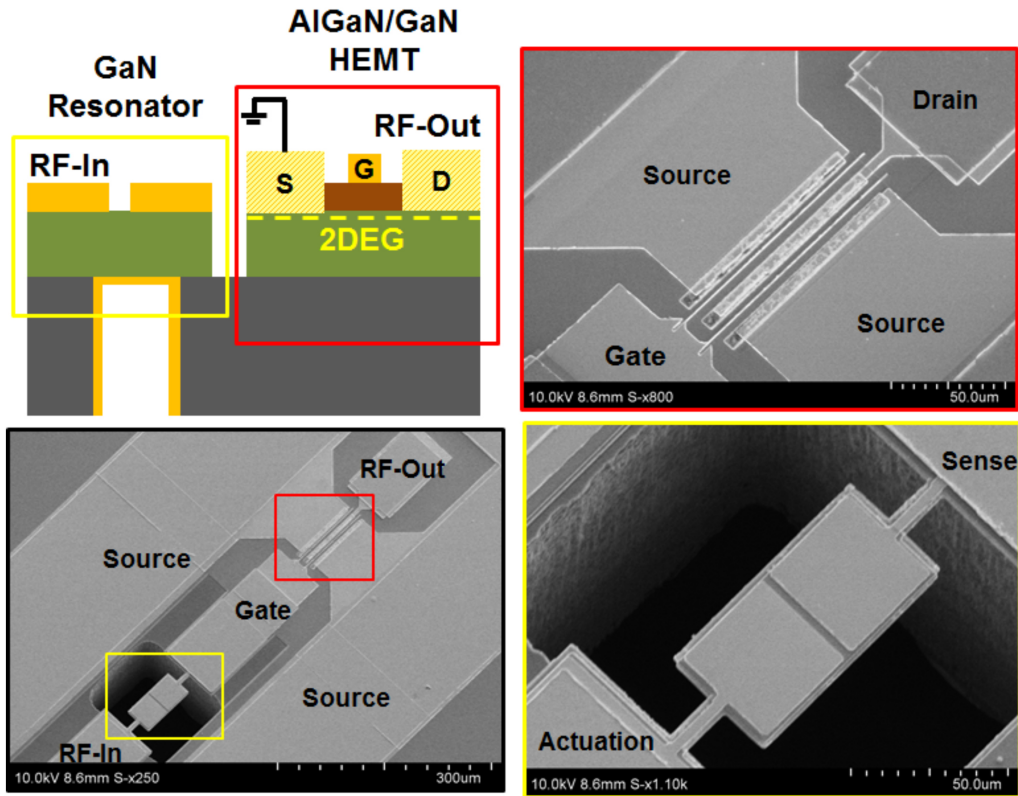


**Fig. 1.15 An all-GaN integrated microsystem platform wherein GaN MEMS resonators are monolithically integrated with AlGaN/GaN HEMT [88]**

Based on the unique piezoelectric effect of III-V nitride materials, Sun et al. reported a miniature pressure MEMS sensor based on a suspended structure of AlGaN/GaN heterojunction (Figure 1.16) [83]. The sensor's drain current can respond quickly when subjected to different pressures (especially in the low pressure range below 600 Pa). Under the operating condition of 100 °C, the dynamic current change percentage of the sensor is 18.75% when the pressure is changed from 96 KPa to 10 Pa, and the power consumption is only 1.8 uW. In the pressure range of 600 Pa to 10 Pa, the maximum sensitivity of the sensor is 22.8%/KPa. Meanwhile, at higher temperature, the thermally induced displacement of the film increases the 2DEG concentration, and the drain current response of the sensor increases accordingly. Therefore, miniature pressure MEMS sensors can be applied to high vacuum and high temperature sensing.

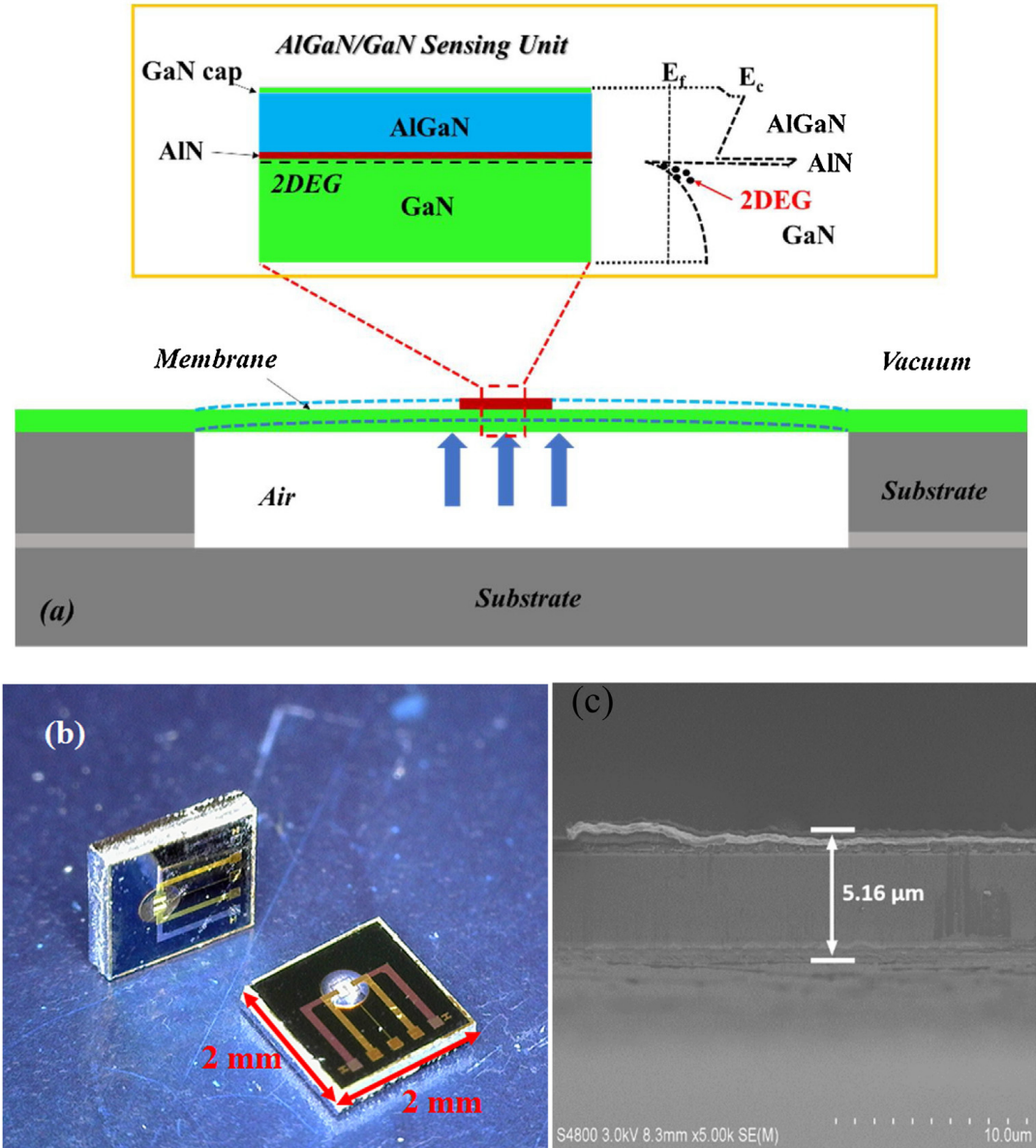


**Fig. 1.16 Miniature pressure MEMS sensor based on AlGaN/GaN heterojunction suspended structure [83]**

III-V nitride MEMS devices are also widely used in the field of biosensing. Indu Sarangadharan et al. reported a highly sensitive AlGaN/GaN HEMT bioMEMS sensor for detecting cardiac troponin I (Figure 1.17) [89]. The unique double-layer gate-controlling mechanism overcomes the shortcomings of charge screening in conventional Si-based MEMS biosensors and enables detection of target proteins in physiological solutions without sample processing

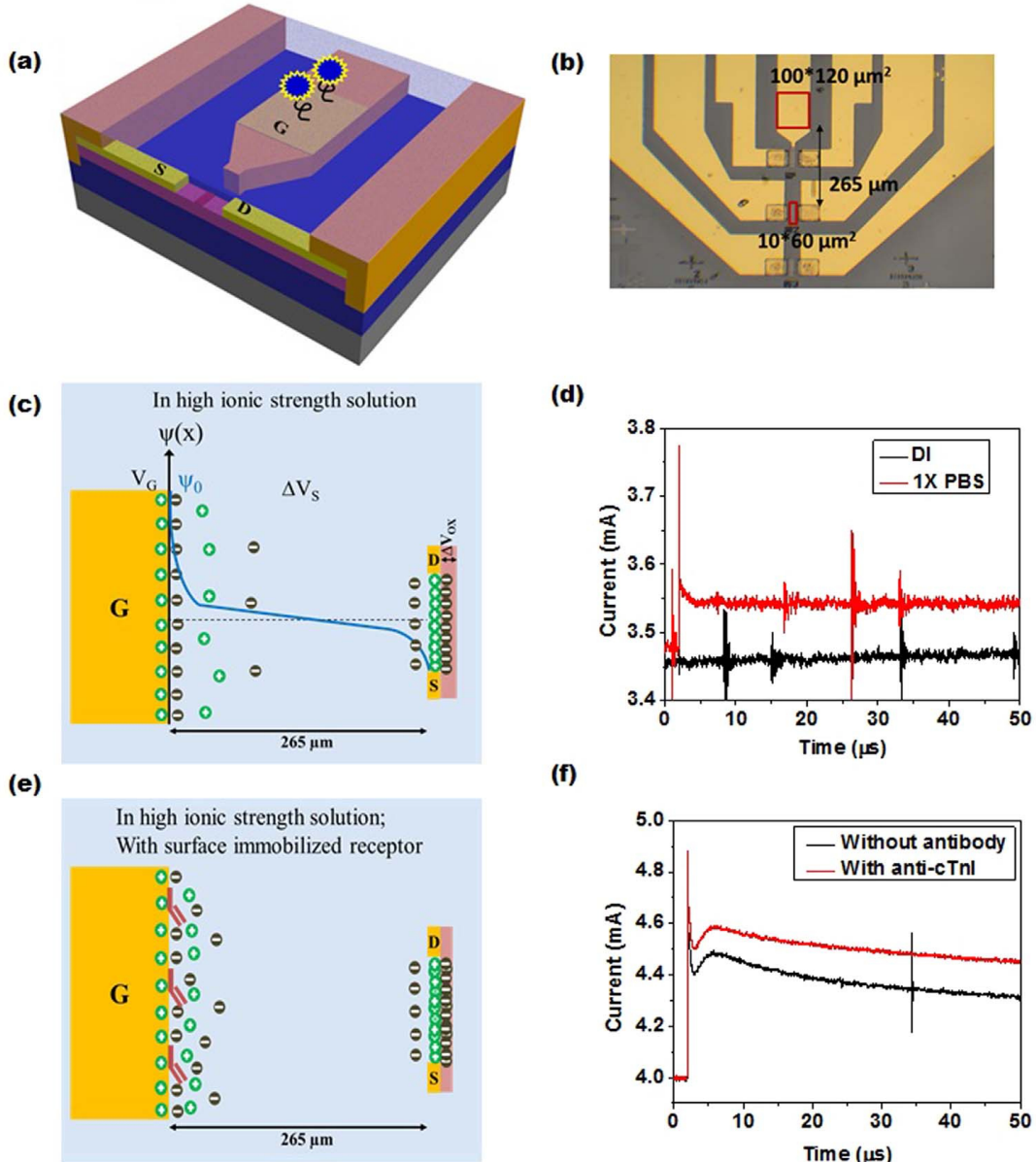


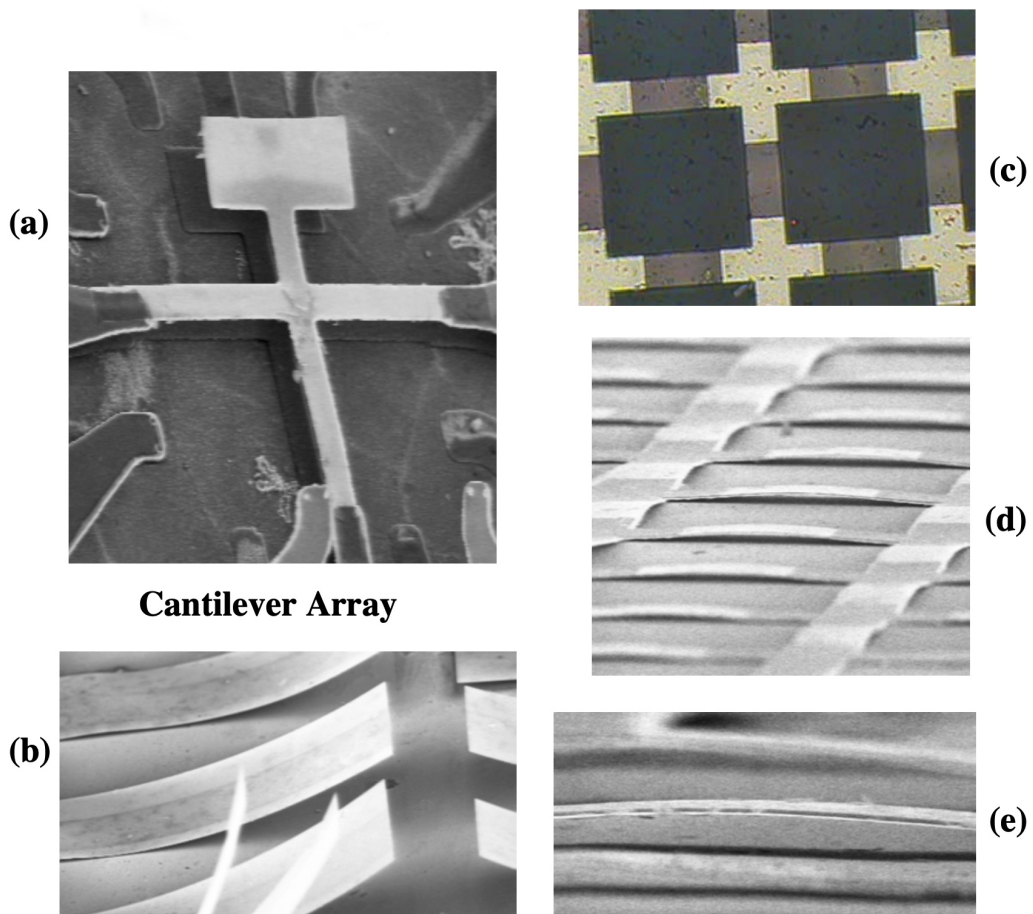
**Fig. 1.17 AlGaN/GaN HEMT MEMS biosensor for detecting cardiac troponin I in a physiological environment [89]**

steps, thus greatly simplifying the biosensor system. Tests using purified protein solutions and clinical serum samples showed that the sensor has high sensitivity, specificity, and a wide dynamic range ( $0.006 \sim 148 \text{ ng/mL}$ ) to quantitatively detect Calcitonin I in serum samples with sample volumes less than  $2 \mu\text{L}$  within 5 minutes. In addition, MEMS chips can be packaged in polymer substrates for easy integration with portable measurement units, which can serve

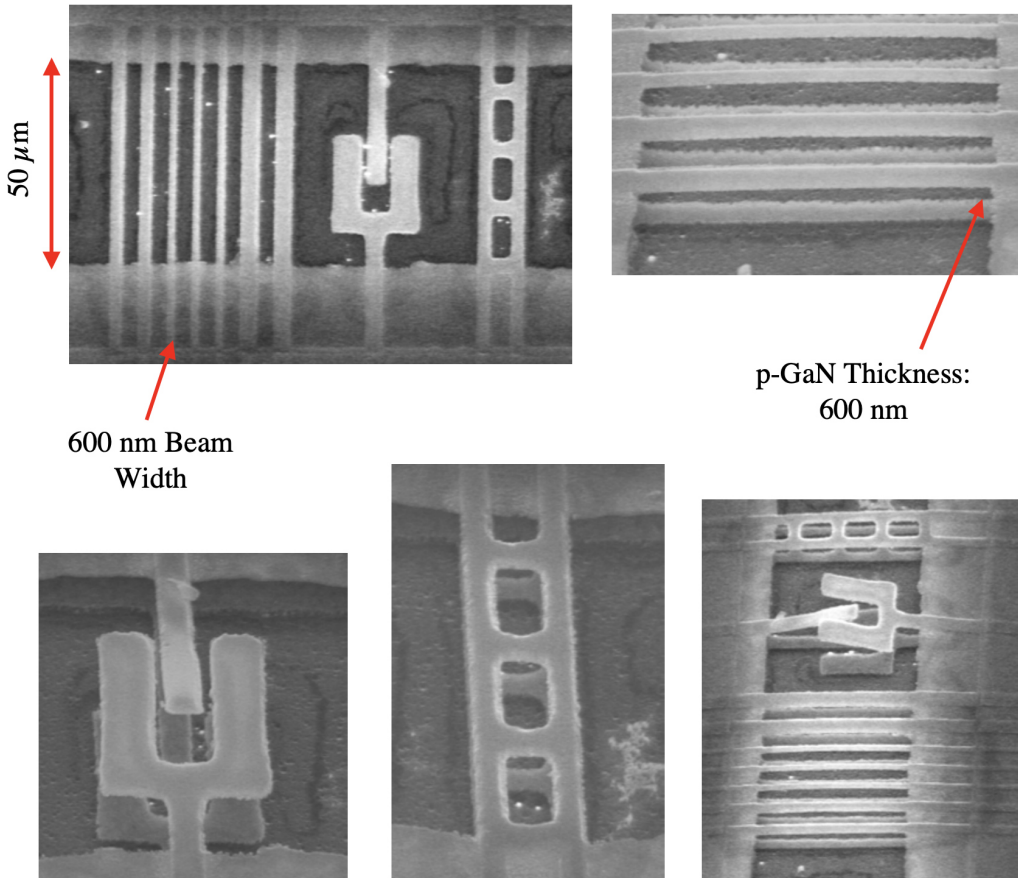
as a fast, inexpensive, and highly sensitive cardiovascular disease detection device with broad applications in point-of-care diagnostics and personal healthcare systems.

### 1.3.3 Microstructure of III-V nitrides

With the deepening of the research on the properties of wide-bandgap semiconductor materials, the preparation technology of III-V nitrides has made significant progress. More complex MEMS devices structures can be prepared by heterojunction epitaxial growth, thin film deposition (epitaxial film and polycrystalline film), inductively coupled plasma (ICP) etching process, and photoelectrochemical (PEC) etching process [69, 90–95].



**Fig. 1.18 SEM image of a series of p-GaN microcantilever arrays [69]**



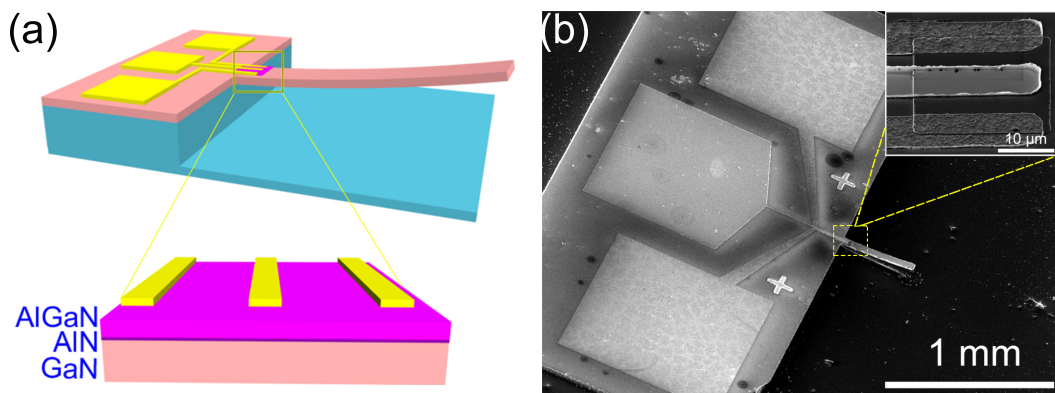
**Fig. 1.19 SEM image of a series of p-GaN structures suspended between two half-plane supports [69]**

Figure 1.18 shows a series of p-GaN microcantilever arrays fabricated by a PEC etch process. The etched p-GaN cantilever relaxes into a uniformly curved shape along the direction away from the substrate. This is because a vertical stress gradient is introduced in the p-GaN layer due to crystal defects during the growth process [69]. Figure 1.19 shows a series of p-GaN structures suspended between two half-support planes fabricated by the PEC process, with a lateral dimension of about 1  $\mu\text{m}$  and a minimum beam width of only 600 nm. The lateral dimension of the device reaches the sub-micron scale, which indicates that GaN-based MEMS devices can be easily extended to the field of nano-electromechanical systems (NEMS). Ad-

vances in III-V nitride preparation technology have greatly promoted the development of new III-V nitride power MEMS devices.

## 1.4 Outline of the thesis

This thesis systematically studies the theoretical modeling and device fabrication of III-V nitride power MEMS based on the cantilever structure of AlGaN/AlN/GaN heterojunction. Figure 1.20 illustrates the structure and SEM image of GaN power MEMS devices. The active area is at the junction of the cantilever and the wafer, which is enlarged in the figure. Due to the design of cantilever structure, the external stimulus from direct strains or non-contact magnetic force will be greatly amplified, thereby introducing the piezoelectric polarization charges in the active area. Based on the piezotronics effect, the piezoelectric polarization charges generated by external stimulus can modulate the energy band at the AlGaN/AlN/GaN heterojunction, thereby effectively adjusting the 2DEG concentration and finally controlling the output current and power density of the MEMS devices.



**Fig. 1.20 Structure and SEM image of GaN power MEMS devices**

The physical framework and mathematical analysis method are presented to model the modulation characteristics of the external stress on the energy band of the AlGaN/AlN/GaN heterojunction and the electrical properties of the MEMS device, which provide theoretical

guidance for the design of III-V nitride power MEMS. On this basis, two types of novel power MEMS devices based on the cantilever structure of AlGaN/AlN/GaN heterojunctions were designed and fabricated, namely, a strain-controlled power MEMS devices (SPD) and a magnetic field-controlled power MEMS devices (MPD), in which external strain and magnetic field can significantly modulate the output power density of MEMS devices due to the micro-cantilever structure.

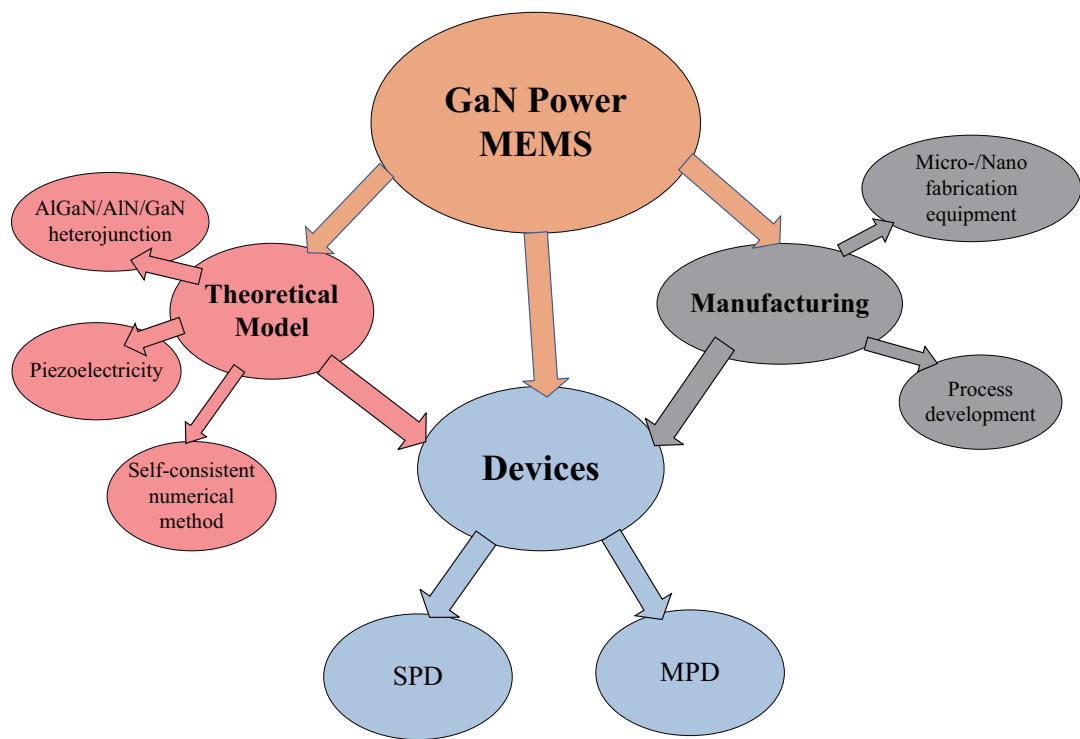


**Fig. 1.21 The outline of the thesis**

The content of this thesis is mainly composed of the following three parts:

## Part I Theory

## Chapter 2. Theoretical model of MEMS cantilever devices

In this study, a semi-classical physical model of the MEMS device with a cantilever structure based on AlGaN/AlN/GaN heterojunction was established using piezotronics theory. The mathematical relationship between the lattice strain of the thin film and the piezoelectric polarization charge intensity in the multilayer heterojunction was deduced through piezoelectric constitutive equation and biaxial stress model. The finite element analysis method of material mechanics is used to calculate the piezoelectric polarization charge intensity of the heterojunction film under different external stresses, and then the self-consistent coupling computational model of the one-dimensional Schrödinger-Poisson coupling equation was used to calculate the modulation characteristics of the external stress on the 2DEG concentration and energy band of the AlGaN/AlN/GaN heterojunction, as well as the electrical properties of the MEMS device. Based on the theoretical model, the new AlGaN/AlN/GaN power MEMS have been designed and fabricated, namely SPD and MPD. This study provides theoretical guidance for the development of new MEMS cantilever devices based on AlGaN/AlN/GaN heterojunctions.

## Part II Manufacturing

### Chapter 3. Manufacturing Technology of Power MEMS Devices

In the Part II, the manufacture of GaN power MEMS devices from epitaxial growth wafers to well-functional devices will be systematically studied. Benefiting from the rapid development of III-V compound semiconductor fabrication and characterization equipment, various complex microstructures including GaN microcantilever structures can now be easily realized by equipment with different functions. This chapter introduced the main nanofabrication and char-

acterization equipment, including epitaxial growth, dry etching, photolithography, thin film deposition, plasma cleaning, Raman spectroscopy, scanning electron microscopy, transmission electron microscopy, etc. I briefly introduced their important role in GaN power MEMS research, as well as the corresponding process design and key parameters.

#### Chapter 4. Process Development and Integration of Power MEMS Devices

In this chapter, I developed the corresponding process parameters and their process integration based on the manufacturing technology and equipment, thus realizing the whole process from GaN wafer to device. The processes in this chapter have been described in detail about the main purpose of the process, the equipment used, and the detailed recipe parameters. Moreover, in order to visualize the fabrication process flow, a corresponding flow chart has been drawn to illustrate the main process steps. Step by step, high-performance GaN HEMTs and GaN power MEMS devices have been successfully fabricated.

### Part III Devices

#### Chapter 5. Strain-controlled power MEMS devices

In this study, we designed a strain modulated power MEMS device (Strain-controlled Power Device, SPD) based on the cantilever structure of AlGaN/AlN/GaN heterojunction, which uses external strain to directly modulate the output power of the device by simulating the reflection process of the human reflex. Based on the piezotronics effect, the piezoelectric polarization charges generated by external strain can modulate the energy band at the AlGaN/AlN/GaN heterojunction, thereby effectively adjusting the 2DEG concentration, and finally controlling the

output current and power density of the SPD. At the same time, similar to the ultimate control ability of the brain in the knee-jerk reflex mechanism, the gate voltage of the SPD can control the output power in a wider range, thus combining the dimensional control advantage of both small-scale external strain control and large-scale programmable gate voltage control, which means that the strain modulation power is programmable. This study not only provides new insights into the interplay of mechanical stimulation and power control, but could also lead to the development of biomimetic smart powered devices that resemble human reflexes.

## Chapter 6. Magnetosensory power MEMS devices.

In this study, we fabricated a magnetic field-regulated power MEMS device (Magnetosensory Power Devices, MPD) by depositing a magnetic thin film on the front end of a cantilevered GaN HEMT based on AlGaN/AlN/GaN heterojunction, which can directly control the output power through an external magnetic field. Moreover, the output power of the MPD has a linear relationship with the external magnetic field, showing good magnetic regulation characteristics. Based on the piezotronics effect, the magnetic force generated by the external magnetic field can generate corresponding piezoelectric polarization charges at the interface of the thin film, which can modulate the energy band of the AlGaN/AlN/GaN heterojunction, thereby effectively adjusting the 2DEG concentration, and finally controlling the output power of the MPD. At the same time, similar to the bio-voltage signal between neuron synapses which effectively regulated the magnitude of neuronal signal in a larger range, the output power is controlled at a larger range by the gate voltage of MPD. Therefore it combines the two-dimensional control advantage. This work not only provides physical electronics insights into the working mechanism of magnetic sensing neurons in the biological sense, but also can promote the development of various neuroelectronic devices.

## **Part I**

## **Theory**

# **Chapter 2**

## **Theoretical Model of Power MEMS Devices**

### **2.1 Polarization effects of III-V nitrides**

III-V nitride semiconductor materials usually exhibit very obvious polarization effects, namely piezoelectric polarization and spontaneous polarization. Due to the lack of inversion symmetry centers in semiconducting nitrides, a prominent piezoelectric polarization effect is exhibited when the lattice is strained along  $<0001>$ . The piezoelectric coefficient in nitrides is almost an order of magnitude larger than many conventional III-V semiconductors [96–99]. The piezoelectric polarization effect has two components, one is lattice strain caused by lattice mismatch between the substrate and the epitaxial layer and the other is thermal strain caused by the difference in thermal expansion coefficient between the substrate and the epitaxial layer. Furthermore, due to the low symmetry of nitrides, there is a spontaneous polarization effect in ideal wurtzite-structured nitrides, which induces intrinsic spontaneously polarized charges at the material surface [100, 101]. Especially when involving the heterojunction interface between two nitride semiconductors with different electronegativities, the spontaneous polarization charge

at the heterojunction interface caused by the spontaneous polarization effect can significantly modulate the heterojunction energy band and optoelectronic properties.

Due to polarization effects in III-V nitride semiconductor materials, there is a high density of polarization charges at the interface of heterojunction devices with significant lattice strain (such as HEMTs), and polarization charges are closely related to the energy band, free carrier distribution and density in the heterojunction. Therefore, polarization effects affect the performance of all nitride-based semiconductor devices, especially HEMTs. Unless using non-polar surfaces (such as a-planes), material polarization effects must be considered in device design. Taking the AlGaN/AlN/GaN heterojunction as an example, as mentioned above, in the absence of external strain, the polarization charge at the interface of the heterojunction has two origins: the piezoelectric polarization charge ( $P_{PE}$ ) caused by lattice mismatch between films, and the spontaneous polarization charge ( $P_{SP}$ ) of the film itself. Generally the spontaneous polarization in the AlGaN/AlN/GaN heterojunction is larger than the piezoelectric polarization in the absence of external strain, and the strain in the heterojunction film decreases when defect-related relaxation occurs, resulting in a weakening of the piezoelectric polarization. These polarized charges are present to varying degrees in all III-V nitride semiconductors unless counteracted by considering lattice symmetry in a particular direction (eg, non-polar surfaces). Since the spontaneous polarization and piezoelectric polarization charges in III-V nitride semiconductor materials can significantly affect the energy band of the heterojunction, thereby changing the optoelectronic properties of the heterojunction, the electrical performance of AlGaN/AlN/GaN MEMS can be effectively modulated by artificially changing the piezoelectric polarization charge in the material [102–104].

The polarization effect depends on the polarity of the crystal. For GaN crystals, the [0001] oriented crystals are called Ga polar crystals, and the [000 $\bar{1}$ ] oriented crystals are called N polar crystals. It is worth noting that polarity is a bulk property of a material, not a surface property. One can imagine a situation in which N-polar GaN is covered by a monolayer of Ga, but the

orientation and polarity of the crystal remain unchanged. Therefore, the polarity of GaN can usually be judged by the following way. When the bond (single bond) along the c-direction of the crystal is from  $Ga^+$  ion to  $N^-$  ion, the polarity is called Ga polarity. Similarly, when the bonds (single bonds) in the c-direction of the crystal are from  $N^-$  ions to  $Ga^+$  ions, the polarity is called N-polarity. Briefly, Ga-polar crystals mean that if the crystal is cut along the c-plane, but only a single bond of the tetrahedral lattice is broken, the surface of the final crystal is a Ga-plane. The opposite is true for N-polar crystals. Studies have shown that the polarity faces of III-V nitride semiconductor materials have a significant impact on heterojunction energy band [105], 2DEG concentration [106], electrical properties [107, 108], short channel effect [109], and light reflection [110], and other optoelectronic properties.

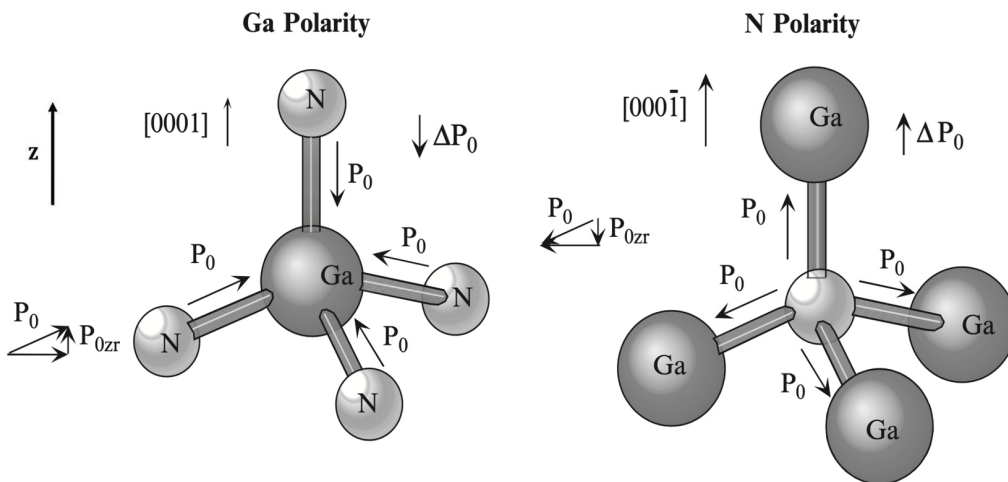


**Fig. 2.1** Ball and stick model of an ideal GaN crystal with Ga and N-polarity in a relaxed state [111]

The effects of polarization due to the low symmetry of the lattice (spontaneous polarization) and the lattice strain of the heterojunction interface (piezoelectric polarization) can be visualized by the simplified ball and stick model. Shown in Figure 2.1 is a ball-and-stick diagram of the tetrahedral lattice between  $Ga$  ions and  $N$  ions in the relaxed Ga-polar and N-polar

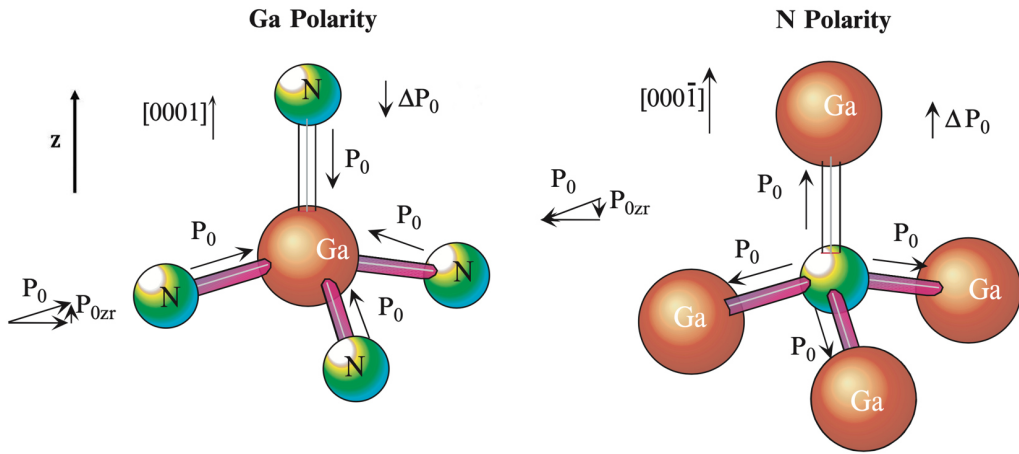


**Fig. 2.2 Ball and stick model of a GaN crystal for both Ga and N polarity with a homogeneous in-plane tensile strain [111]**

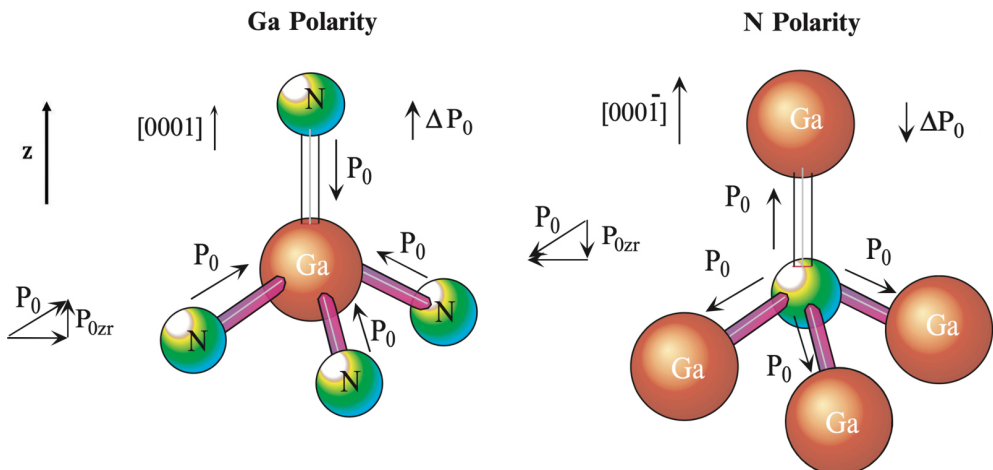


**Fig. 2.3 Ball and stick model of a GaN crystal for both Ga and N polarity with a homogeneous in-plane compressive strain [111]**

GaN lattices, where  $P_0$  denotes the pole between *Ga* ions and *N* ions vectorization. Take the GaN lattice with Ga polarity in the left figure as an example, since the electron cloud of the lattice is closer to the N atom, in the tetrahedral structure, the superposition of the polarization vector  $P_{0zr}$  in the  $+z$  direction of the three bonds of the tetrahedral lattice cannot cancel it out. The polarization vector  $P_0$  in the  $-z$  direction, so the net polarization vector of the Ga-

polar GaN lattice is along the  $-z$  direction. The net polarization phenomenon in this lattice relaxation state is the spontaneous polarization effect. However, when the Ga-polar GaN lattice is under uniform in-plane tensile strain, the accumulated polarization vector in the  $+z$  direction associated with the three bonds of the tetrahedral lattice decreases, thereby enhancing the net polarization vector along the  $-z$  direction, as shown in Figure 2.2. When there is in-plane uniform compressive strain in the Ga-polar GaN lattice, the cumulative polarization vector in the  $+z$  direction related to the three bonds of the tetrahedral lattice will increase, and the GaN lattice exhibits a net polarization vector along the  $+z$  direction, as shown in Figure 2.3. The change of the polarization vector in this external stress state is called the piezoelectric polarization effect, and the change of net polarization vector of the lattice is the result of the combined action of the spontaneous polarization and the piezoelectric polarization. In an N-polar GaN lattice, the same happens, except that the polarization direction is opposite to that of a Ga-polar GaN lattice [111].

## 2.2 Piezoelectric theory of III-V nitrides

### 2.2.1 Piezoelectric constitutive equation

According to the basic theory of piezoelectric effect, the stress-charge form of piezoelectric constitutive equation can be expressed as

$$\begin{cases} \boldsymbol{\sigma} = \mathbf{c}_E \mathbf{S} - \mathbf{e}^T \mathbf{E} \\ \mathbf{D} = \mathbf{e} \mathbf{S} + \mathbf{k} \mathbf{E} \end{cases} \quad (2.1)$$

In this formula,  $\mathbf{E}$  and  $\mathbf{D}$  represent the electric field strength vector and electric displacement vector, and  $\boldsymbol{\sigma}$  is the stress tensor;  $\mathbf{c}_E$  is the elastic coefficient tensor;  $\mathbf{e}$  is the linear piezoelectric coefficient;  $\mathbf{k}$  is the dielectric constant tensor, and  $\mathbf{S}$  is the strain tensor. Among them, the

expression of linear piezoelectric coefficient  $e$  is

$$\mathbf{e} = \begin{bmatrix} e_{11} & e_{12} & e_{13} & e_{14} & e_{15} & e_{16} \\ e_{21} & e_{22} & e_{23} & e_{24} & e_{25} & e_{26} \\ e_{31} & e_{32} & e_{33} & e_{34} & e_{35} & e_{36} \end{bmatrix} \quad (2.2)$$

Next, we start to simplify the theoretical model. First, we only consider the condition of the external electric field  $\mathbf{E} = 0$ . Therefore, Equation 2.1 can be simplified as

$$\begin{cases} \sigma = c_E S \\ \mathbf{D} = \mathbf{e} S \end{cases} \quad (2.3)$$

Since we only need to study the piezoelectric polarization charge-strain relationship, we only take  $\mathbf{D} = \mathbf{e} S$  for discussion, and the thin film materials we study are the III-V group nitride materials AlGaN, AlN and GaN with wurtzite structure. The linear piezoelectric coefficient  $e$  matrix has a special form, and its expansion is written in the matrix form as

$$\begin{bmatrix} D_x \\ D_y \\ D_z \end{bmatrix} = \begin{bmatrix} 0 & 0 & 0 & 0 & e_{15} & 0 \\ 0 & 0 & 0 & e_{24} & 0 & 0 \\ e_{31} & e_{32} & e_{33} & 0 & 0 & 0 \end{bmatrix} \begin{bmatrix} S_{xx} \\ S_{yy} \\ S_{zz} \\ S_{yz} \\ S_{xz} \\ S_{xy} \end{bmatrix} \quad (2.4)$$

where  $e_{31} = e_{32}$ . Since we only study the piezoelectric polarization charge-strain relationship in the  $z$  direction, ie  $D_z$ , from Equation 2.4 we can get

$$\begin{aligned} D_z &= e_{31}S_{xx} + e_{32}S_{yy} + e_{33}S_{zz} \\ &= e_{31}(S_{xx} + S_{yy}) + e_{33}S_{zz} \end{aligned} \quad (2.5)$$

Therefore, the  $z$ -direction electric displacement vector-strain equation of III-V nitride materials is derived from the piezoelectric constitutive equation, where  $S_{xx}$ ,  $S_{yy}$ ,  $S_{zz}$  are the strains of the material in the  $x$ ,  $y$ , and  $z$  directions, respectively.

### 2.2.2 Piezoelectric polarization charge-strain equation

In electromagnetism, the electric displacement vector and electric polarization intensity are defined as:

$$\mathbf{D} = \epsilon_0 \mathbf{E} + \mathbf{P} \quad (2.6)$$

where  $\mathbf{D}$  is the electric displacement vector,  $\epsilon_0$  is the vacuum permittivity,  $\mathbf{E}$  is the electric field strength, and  $\mathbf{P}$  is the electric polarization strength.

Since we only consider the condition of the external electric field  $\mathbf{E} = 0$ , and only consider the electric polarization in the  $z$  direction, Equation 2.6 can be simplified as:

$$D_z = P_z \quad (2.7)$$

Substituting it into Equation 2.5, we finally get the piezoelectric polarization charge-strain equation in the  $z$ -direction of III-V nitride materials:

$$P_z = e_{31} (S_{xx} + S_{yy}) + e_{33} S_{zz} \quad (2.8)$$

Next, we discuss the physical meaning of Equation 2.8 in this study. The electric polarization strength  $\mathbf{P}$  (or electric polarization, or simply polarization) is the vector field that represents the density of permanent electric dipole moment or induced electric dipole moment in the dielectric material, and is a physical quantity characterizing electric dipole moment in a material. In III-V nitride materials, the electric polarization  $\mathbf{P}$  defined by Equation 2.8 can characterize the piezoelectric polarization in the  $z$  direction  $P_z$  induced by strain, so is usually

represented by  $P_{PE}$ , Equation 2.8 is further rewritten for

$$P_{PE} = e_{31} (S_{xx} + S_{yy}) + e_{33} S_{zz} \quad (2.9)$$

So far, we have derived the mathematical equation for the relationship between piezoelectric polarization and strain in the  $z$ -direction of III-V nitride materials. When  $P_{PE} < 0$ , the polarization electric field in the material points to the negative direction of the  $z$ -axis, and is directed from negative charges to positive charges. The distribution of piezoelectric polarization charges is shown in Figure 2.4. Conversely, when  $P_{PE} > 0$ , the polarization electric field in the material points in the positive  $z$ -axis direction, and the distribution of piezoelectric polarization charges is opposite to that in Figure 2.4.

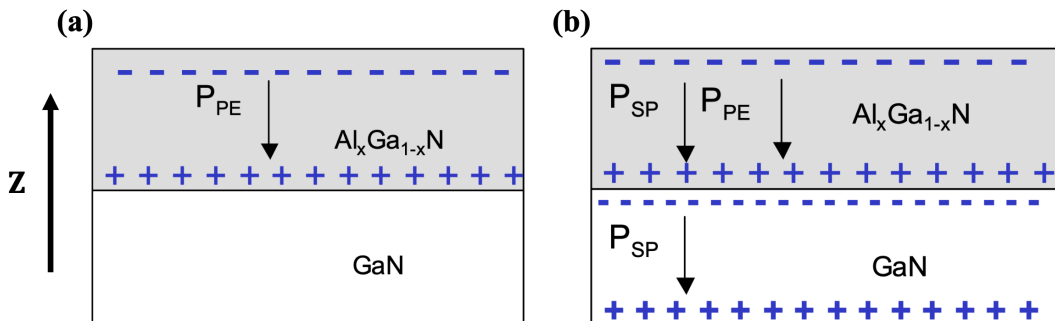


**Fig. 2.4 Piezoelectric polarization charge distribution of group III-V nitride material  $\text{Al}_x\text{Ga}_{1-x}\text{N}$  when  $P_{PE} < 0$ . (a) Spontaneous polarization charge is not considered. (b) Spontaneous polarization charge is considered [112]**

## 2.3 Lattice strain model of AlGaN/AlN/GaN heterojunction

### 2.3.1 Biaxial strain model of thin films

In this section, we study the strains of AlGaN/AlN/GaN heterojunction thin films in the  $x$ ,  $y$ , and  $z$  directions. The thicknesses of the AlGaN, AlN, and GaN films are 30 nm, 1 nm, and 4.3 um, respectively. The thickness of the GaN film is much larger than AlGaN thin film and AlN

thin film, and the GaN material is rigid. Therefore, we can approximately think that the GaN thin film is a rigid substrate material, and use the biaxial stress model to perform strain analysis on the AlGaN thin film and the AlN thin film, as shown in Figure 2.5. The thickness of the film material is much smaller than that of the rigid substrate, so when the film is subjected to lateral strain, the axial strain of the film can be calculated approximately through the Poisson's ratio of the material:

$$S_z = -\frac{v}{1-v} (S_x + S_y) \quad (2.10)$$

where  $S_x$ ,  $S_y$ ,  $S_z$  are the strains in the  $x$ ,  $y$ , and  $z$  directions, respectively, and  $v$  is the Poisson's ratio of the thin film material.

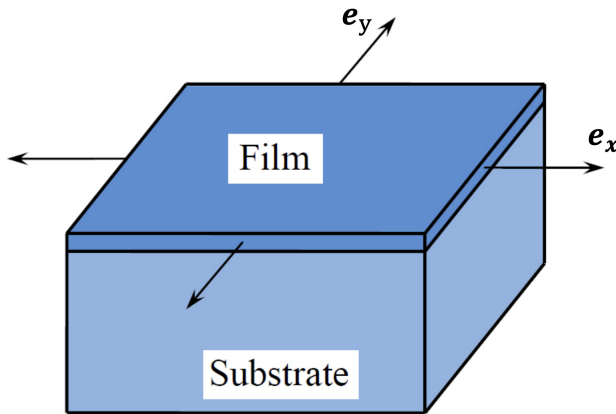


**Fig. 2.5 Schematic diagram of biaxial stress model**

### 2.3.2 Lattice strain in multilayer thin films

Next we investigate the lattice strain of the thin film due to lattice mismatch. Figure 2.6 shows the relationship between the forbidden band width and lattice constant of III-V nitride semiconductors at room temperature, where the lattice constant of AlGaN (30% Al) can be given by Vegard's law [113, 114]:

$$a_{\text{Al}_{0.3}\text{Ga}_{0.7}\text{N}} = 0.3a_{\text{AlN}} + 0.7a_{\text{GaN}} \quad (2.11)$$

We can see that the lattice constants of AlN crystal, AlGaN crystal and GaN crystal are inconsistent, and there is a certain lattice mismatch between them. It is the lattice mismatch between the thin films in the AlGaN/AlN/GaN heterojunction that introduces strain in the films, resulting in the corresponding piezoelectric polarization charge. It is also called lattice strain because this strain is caused by lattice mismatch.

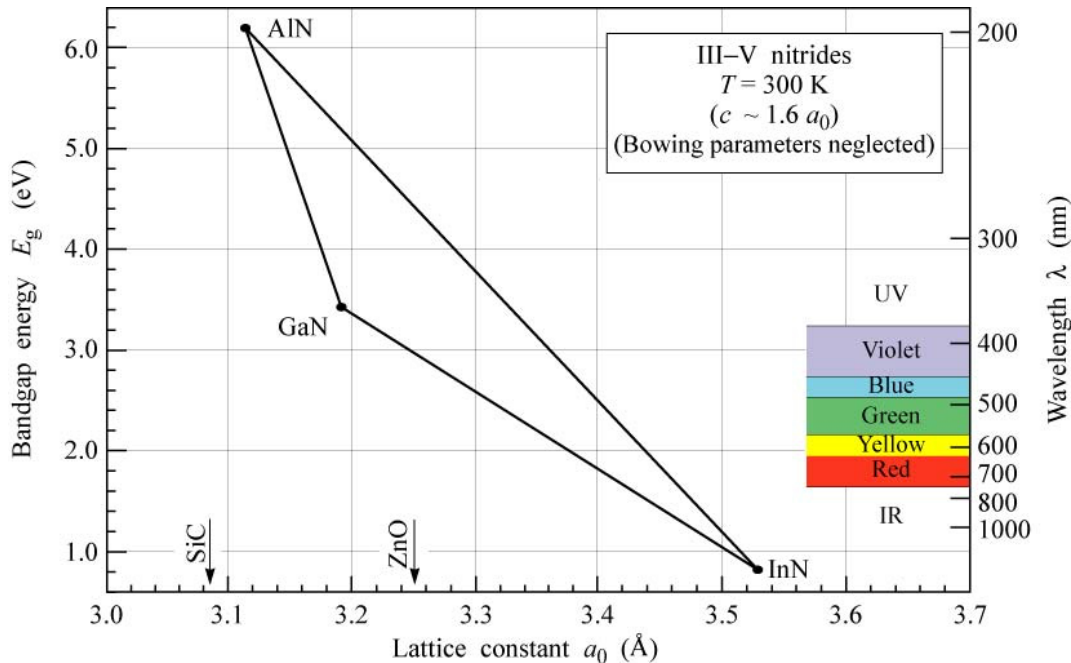


**Fig. 2.6 Bandgap energy versus lattice constant for III-V nitride semiconductors at room temperature**

The lattice strain of the thin film is shown in Figure 2.7. Due to the inconsistency of lattice constants, crystals *A* and *B* have a certain lattice mismatch. When the epitaxial layer is composed of these two crystal materials, under ideal conditions (without considering the lattice-mismatched dislocations) there will be elastic strains between lattices. Usually, since the thickness of the epitaxial substrate is much larger than that of the thin film, we approximately think that the lattice of the substrate does not produce elastic strain, that is, the lattice constant  $a_A$  of the substrate *A* does not change, and the lattice of the thin film *B* undergoes elastic deformation. Thus, the deformed lattice constant  $a_B(epi)$  is equal to the lattice constant  $a_A$  of

the substrate  $A$ , that is,  $a_B(epi) = a_A$ . Then, the lateral lattice strain  $S_B$  of film  $B$  is:

$$\begin{aligned} S_B &= \frac{a_B(epi) - a_B}{a_B} \\ &= \frac{a_A - a_B}{a_B} \end{aligned} \quad (2.12)$$

In the ideal case of no external stress, the lateral  $x$ - and  $y$ -direction lattice strains of film  $B$  are approximately the same, and the  $z$ -direction lattice strain can be obtained according to the biaxial stress model (Equation 2.10).

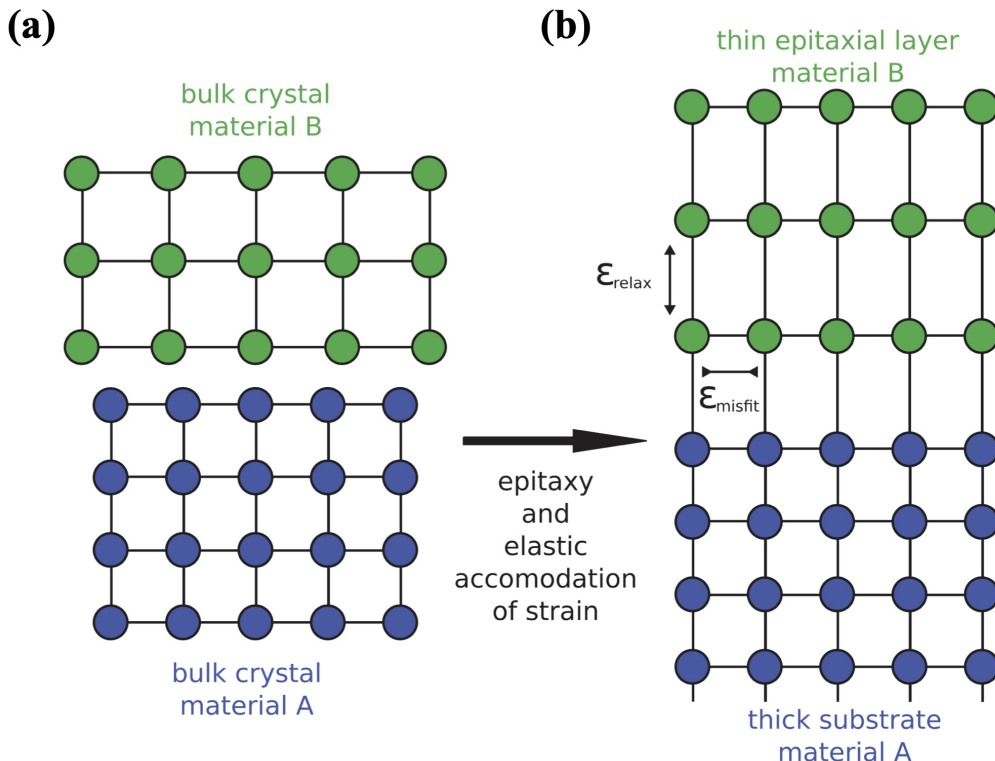


**Fig. 2.7 Lattice strain of the thin films (a) Lattice mismatch between film and substrate material. (b) Purely elastic strain epitaxial layer without misfit dislocations [115]**

Similarly, considering the AlGaN/AlN/GaN heterojunction in this study and the thickness of each layer material (30 nm/1 nm/4.3 um), the thickness of the GaN layer is much larger than that of the AlN film and the AlGaN film. We can approximate that GaN belongs to rigid substrate materials, and AlN and AlGaN belong to thin film materials. This is a structure

consisting of two thin films, as shown in Figure 2.8. It can be seen that since the lattice constants of AlN crystal and AlGaN crystal are both smaller than those of GaN crystal, and the thickness of the GaN layer is much larger than that of the AlN film and the AlGaN film, the AlN film and AlGaN film are both subjected to tensile strain, and the lattice constants after deformation are all equal to lattice constants of GaN crystals.

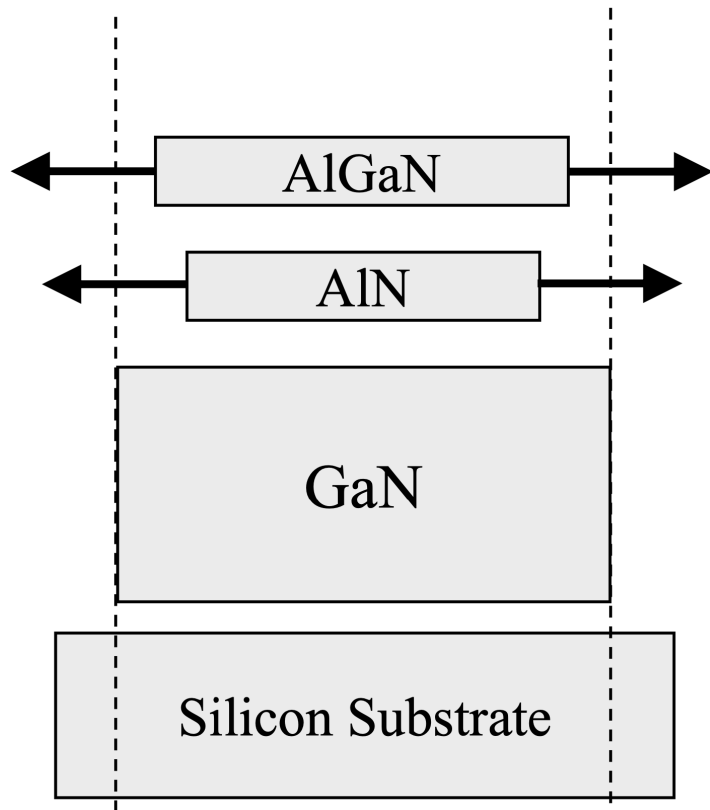


**Fig. 2.8 Thin film structure of AlGaN/AlN/GaN heterostructure**

First we discuss the case where there is no external stress. In this case, the AlN film undergoes tensile elastic strain, and its deformed lattice constant  $a_{AlN}(epi)$  is equal to the lattice constant  $a_{GaN}$  of GaN, that is,  $a_{AlN}(epi) = a_{GaN}$ . Since the thickness of the AlN film is only 1 nm, it can be reasonably approximated that the full lattice strain occurs in the AlN film. So the lattice constant of the AlGaN film after deformation is equal to the lattice constant of the AlN film after the deformation, that is,  $a_{AlGaN}(epi) = a_{AlN}(epi)$ . Finally, we can approximately ex-

press the lateral lattice strain of each layer of AlGaN/AlN/GaN heterojunction without external stress as follows:

$$S_{GaN} = \frac{a_{GaN} - a_{GaN}}{a_{GaN}} = 0 \quad (2.13)$$

$$S_{AlN} = \frac{a_{AlN}(epi) - a_{AlN}}{a_{AlN}} = \frac{a_{GaN} - a_{AlN}}{a_{AlN}} \quad (2.14)$$

$$S_{AlGaN} = \frac{a_{AlGaN}(epi) - a_{AlGaN}}{a_{AlGaN}} = \frac{a_{GaN} - a_{AlGaN}}{a_{AlGaN}} \quad (2.15)$$

In the ideal case of no external stress, the lattice deformations in the  $x$  and  $y$  directions of the AlN film and the AlGaN film are approximately the same, and the lattice strain in the  $z$  direction can be obtained according to the biaxial stress model described in Equation 2.10.

In the presence of external stress, the lattice strain of each layer of AlGaN/AlN/GaN heterojunction will be more complicated. First, the GaN layer will deform laterally and longitudinally under the action of external stress, and the AlN film and AlGaN film will also deform accordingly. In this model, we approximately think that in the case of very weak external stress, each layer of the AlGaN/AlN/GaN heterojunction material still undergoes pure elastic deformation. The lattice constant of the AlN film is still equal to that of the GaN layer, that is, the AlN film is still completely deformed. Therefore the lattice constant of the deformed AlGaN film is still equal to that of the deformed AlN film. The mathematical expression is  $a_{AlN}(starin) = a_{GaN}(starin)$ ,  $a_{AlGaN}(starin) = a_{AlN}(starin)$ . In this way, we can approximately express lateral lattice strain of AlGaN/AlN/GaN heterojunction layers in the presence of external stress:

$$S_{GaN}(strain) = \frac{a_{GaN}(strain) - a_{GaN}}{a_{GaN}} \quad (2.16)$$

$$S_{AlN}(strain) = \frac{a_{AlN}(strain) - a_{AlN}}{a_{AlN}} = \frac{a_{GaN}(strain) - a_{AlN}}{a_{AlN}} \quad (2.17)$$

$$S_{AlGaN}(strain) = \frac{a_{AlGaN}(strain) - a_{AlGaN}}{a_{AlGaN}} = \frac{a_{GaN}(strain) - a_{AlGaN}}{a_{AlGaN}} \quad (2.18)$$

**Table 2.1 Physical parameters of wurtzite structure AlN and GaN**

Parameters	AlN	GaN	Ref
Lattice constant a (nm)	0.311	0.319	[116]
Lattice constant c (nm)	0.498	0.519	[116]
Bandgap $E_g$ (eV)	6.25	3.510	[116]
Effective mass (Electron)	0.32	0.20	[116]
Effective mass (Hole)	3.53	1.56	[117]
Relative permittivity	8.5	10.4	[117]
C11 (GPa)	396	390	[116]
C12 (GPa)	137	145	[116]
C13 (GPa)	108	106	[116]
C33 (GPa)	373	398	[116]
e31 ( $\text{C m}^{-2}$ )	-0.58	-0.452	[111, 118]
e33 ( $\text{C m}^{-2}$ )	1.55	0.818	[111, 118]
e311 ( $\text{C m}^{-2}$ )	5.850	6.185	[119]
e333 ( $\text{C m}^{-2}$ )	-10.750	-8.090	[119]
e133 ( $\text{C m}^{-2}$ )	4.533	1.543	[119]
$P_{sp}$ ( $\text{C m}^{-2}$ )	-0.081	-0.029	[119]

In addition, under the action of external stress, the lattice deformations in the  $x$  and  $y$  directions of the GaN layer, AlN thin film, and AlGaN thin film may be different. Therefore, we can use the finite element analysis method to calculate the strain in the  $x$ ,  $y$  and  $z$  directions of the GaN layer under the action of external stress according to the principles of material mechanics, and then calculate the  $x$  and  $y$  direction lattice constant according to Equation 2.16. On this basis, the lattice strains in the  $x$  and  $y$  directions of the AlN film and the AlGaN film are solved respectively according to Equation 2.17 and Equation 2.18. Finally, the lattice strain in  $z$  direction of the AlN film and the AlGaN film can be solved according to the biaxial stress model.

### 2.3.3 Piezoelectric polarization charge of GaN AlGaN AlN layer

In this subsection, we study the lattice strain of the active region of the cantilevered GaN layer under the action of external stress using the methods of finite element analysis. On this basis, the lattice strain and piezoelectric polarization charge of GaN AlGaN AlN layer can be further obtained.

According to the principles of material mechanics, we can solve the strain of the cantilevered GaN under different external stresses through the methods of finite element analysis. Figure 2.9 shows the deformation of the GaN cantilever under 4 mN external stress simulated by COMSOL Multiphysics 5.1. The length, width, and height of the cantilever are 350  $\mu\text{m}$ , 60  $\mu\text{m}$ , and 4.3  $\mu\text{m}$ , respectively. The Poisson's ratio and Young's modulus of the GaN material are 0.2 [120] and 290 GPa [121, 122] respectively. The external stress is applied to the front half of the cantilever, and we set up a sampling point to extract the strain of the HEMT's active area.

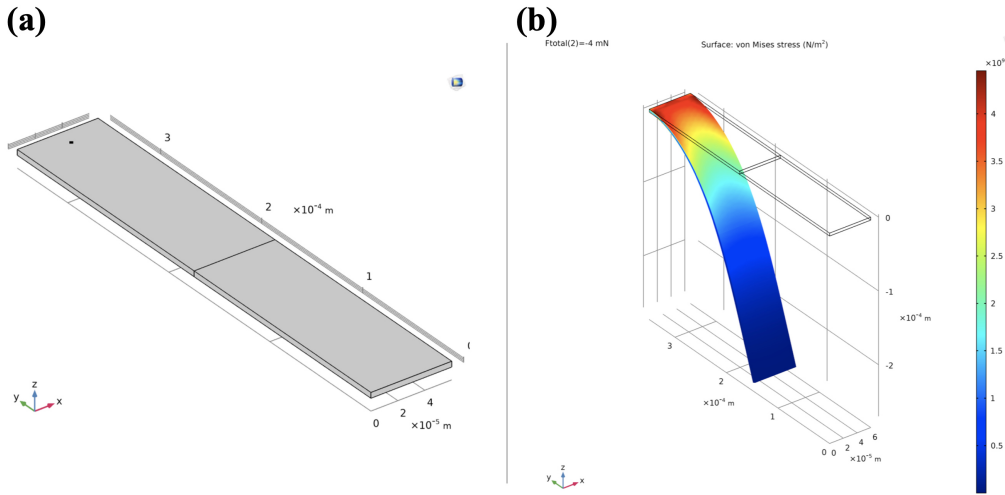


**Fig. 2.9 Finite element analysis of GaN cantilever strain under external stress (a) Structure of the GaN cantilever. (b) Deformation of the GaN cantilever under 4 mN external stress.**

We take the theoretical calculation of the MPD device in chapter 6 in this thesis as an example. Figure 2.9a is a schematic diagram of the structure of the GaN cantilever, which is the same as that of the MPD cantilever. Figure 2.9b shows the Von Mises stress distribution of the GaN cantilever under 4 mN external stress. It can be seen that due to the special structure of the cantilever, the Von Mises stress at the fixed end of the cantilever is much larger than other regions, which is exactly the active region of AlGaN/AlN/GaN heterojunction. So we verify that lattice strain induced by external stress can be enlarged by the cantilever structure. By applying a downward normal force of  $0 \sim 24$  mN to the front half of the cantilever, we calculated the GaN lattice strain in the active region corresponding to different external stresses. The calculation results are shown in Table 2.2. We can clearly see that under the action of external stress, the lattice strain in the  $x$ -direction of the active region is very small and almost negligible, while the lattice strain in the  $y$ -direction and  $z$ -direction is significant. Therefore, through the finite element analysis model of material mechanics, we obtained the GaN's lattice strains in the  $x$ ,  $y$  and  $z$  directions of cantilevered HEMT's active region under different external stresses, namely  $S_{xx}(\text{GaN})$ ,  $S_{yy}(\text{GaN})$  and  $S_{zz}(\text{GaN})$ . On this basis, the piezoelectric

**Table 2.2 Lattice strain of GaN cantilever active region and the corresponding piezoelectric polarization charge density of the films at 0 ~ 24 mN downward force**

F (mN)	Strain tensor,			Piezoelectric polarization charge densities ( $\text{C m}^{-2}$ )		
	$S_{xx}$	$S_{yy}$	$S_{zz}$	$P_{\text{GaN}}^{\text{PE}}$	$P_{\text{AlN}}^{\text{PE}}$	$P_{\text{AlGaN}}^{\text{PE}}$
0	0	0	0	0	-0.0492	-0.0092
-4	-0.0001688	0.0148460	-0.0036991	-0.0097	-0.0637	-0.0200
-8	0.0000291	0.0220201	-0.0055929	-0.0145	-0.0710	-0.0254
-12	0.0001830	0.0268448	-0.0068830	-0.0178	-0.0760	-0.0291
-16	0.0003008	0.0305848	-0.0078887	-0.0204	-0.0798	-0.0320
-20	0.0003956	0.0337095	-0.0087319	-0.0226	-0.0830	-0.0344
-24	0.0004726	0.0363812	-0.0094546	-0.0244	-0.0857	-0.0364

polarization charge densities of GaN ( $P_{\text{GaN}}^{\text{PE}}$ ), AlN ( $P_{\text{AlN}}^{\text{PE}}$ ) and AlGaN ( $P_{\text{AlGaN}}^{\text{PE}}$ ) thin films are further deduced, as shown in Table 2.2.

So far, we have constructed a theoretical model of the piezoelectric polarization charge intensity - external stress relationship ( $P_{\text{PE}} - F$ ) of MEMS devices based on AlGaN/AlN/AlGaN heterojunction cantilever structure. By combining piezoelectric constitutive equations, biaxial stress model and finite element analysis, we can mathematically solve the piezoelectric polarization charge intensities of GaN ( $P_{\text{GaN}}^{\text{PE}}$ ) layer, AlN ( $P_{\text{AlN}}^{\text{PE}}$ ) layer and AlGaN ( $P_{\text{AlGaN}}^{\text{PE}}$ ) layer when the cantilever is subjected to different external stresses  $F$ . The change of the piezoelectric polarization charge intensity  $P_{\text{PE}}$  will affect the electrical properties of the heterojunction. In section 2.4, we will study the modulation properties of the piezoelectric polarization charge intensity  $P_{\text{PE}}$  on the AlGaN/AlN/AlGaN heterojunction energy band, carrier distribution, and 2DEG concentration through a self-consistent coupled computational model.

## 2.4 Self-consistent coupling model of strained AlGaN/AlN/-GaN heterojunction

### 2.4.1 The theoretical equations of the model

The physical model of the energy band of the AlGaN/AlN/GaN heterojunction is a semi-classical model based on the Schrödinger equation and the Poisson's equation. Under the effective mass approximation, the electron subband in the growth direction of the AlGaN/Al-N/GaN heterojunction is the solution of the stationary Schrödinger equation [123]

$$-\frac{\hbar^2}{2} \frac{d}{dx} \left[ \frac{1}{m^*} \frac{d\psi_i(x)}{dx} \right] + [V(x) - E_i] \psi_i(x) = 0 \quad (2.19)$$

where  $m^*$  represents the effective mass of the electron at the edge of the conduction band,  $V(x)$  represents the potential energy,  $E_i$  represents the energy of the  $i$ th subband, and  $\psi_i(x)$  represents the wave function of the  $i$ th subband. Ignoring the non-parabolicity of the conduction band, we assume that  $m^*$  is independent of electron energy, which is isotropic and has abrupt changes at the interface between AlGaN, AlN, and GaN.

The expression for potential energy  $V(x)$  is:

$$V(x) = V_c(x) + V_h(x) + V_{xc}(x) \quad (2.20)$$

where  $V_c(x)$  represents the conduction band edge potential in the form of a step function related to the conduction band shift at the AlGaN/AlN/GaN heterojunction, and  $V_h(x)$  is the Hartree potential induced by electrostatic interactions due to the distribution of mobile and stationary charges.  $V_{xc}(x)$  is the exchange-correlated potential of many-body interactions that are not included in the Hartree potential [124].

$V_h(x)$  is the solution of the Poisson's equation:

$$\frac{d}{dx} \left[ \epsilon(x) \frac{dV_h(x)}{dx} \right] = -q\varphi(x) \quad (2.21)$$

where  $\epsilon(x)$  is the dielectric constant of the material with abrupt changes at the interface between AlGaN, AlN and GaN.  $q$  is the absolute value of the unit charge.

The total charge density distribution  $\varphi(x)$  is given by:

$$\varphi(x) = \sum_{j=t,i,b} \sigma(x)\delta(x - x_j) + p(x) + N_D^+(x) - n(x) - N_A^- \quad (2.22)$$

where  $\sigma(x)$  is the density of polarization charges at the interface between AlGaN, AlN and GaN,  $p(x)$  and  $n(x)$  are the concentrations of holes and free electrons, respectively, and  $N_D^+$  is the donor ion concentration,  $N_A^-$  is the acceptor ion concentration.

According to the electrical neutrality condition, this formula also must be satisfied in the AlGaN/AlN/GaN heterojunction interval:

$$\int_{x_t}^{x_p} \rho(x) dx = 0 \quad (2.23)$$

Written in the form of the sum of all charges:

$$\int_{x_t}^{x_p} [p(x) + N_D^+(x) - n(x) - N_A^-] dx = 0 \quad (2.24)$$

The carrier concentration distribution in the AlGaN/AlN/GaN heterojunction is given by:

$$n(x) = \sum_i n_i |\psi_i(x)|^2 \quad (2.25)$$

where  $n_i$  is the density of electrons in the  $i$ th subband, and usually expressed as a function of effective mass:

$$n_i = \frac{m^* k_B T}{\pi \hbar^2} \ln \left[ 1 + \exp \left( \frac{E_F - E_i}{k_B T} \right) \right] \quad (2.26)$$

$k_B$  and  $T$  are Boltzmann constant and electron temperature, respectively.

The two-dimensional electron gas (2DEG) areal density  $N_e$  is equal to the sum of the electron densities in all the subbands of the heterojunction:

$$N_e = \int_{x_t}^{x_b} n(x) dx = \sum_i n_i \quad (2.27)$$

Next, we study the coupling of the piezoelectric polarization charge intensity  $P_{PE}$  under external strain derived earlier into a self-consistent computational model through the Poisson's equation of Equation 2.21. Due to the non-centrosymmetric wurtzite crystal structure, there are two types of intrinsic polarizations in AlGaN/AlN/GaN heterojunctions [125]: (i) spontaneous polarization existing in AlGaN ( $P_{AlGaN}^{sp}$ ), AlN ( $P_{AlN}^{sp}$ ) and GaN ( $P_{GaN}^{sp}$ ); (ii) piezoelectric polarization due to lattice strain present in GaN ( $P_{GaN}^{PE}$ ), AlN ( $P_{AlN}^{PE}$ ) and AlGaN ( $P_{AlGaN}^{PE}$ ). The density of polarization charges at the interface  $P_{interface}$  of AlGaN, AlN and GaN can be expressed as:

$$P_{Interface} = P_{sp} + P_{PE} + e_{311} S_{\parallel}^2 + e_{333} S_{\perp}^2 + e_{313} S_{\parallel} S_{\perp} \quad (2.28)$$

where  $P_{sp}$  is the spontaneous polarization charge intensity,  $P_{PE}$  is the piezoelectric polarization charge intensity induced by lattice strain, and  $e_{ijk}$  is the nonlinear piezoelectric coefficient.  $S_{\perp}$  and  $S_{\parallel}$  are the lattice strains perpendicular to c-plane and parallel to the c-plane induced by external stress, respectively. In this model, we only consider the piezoelectric polarization effect in the linear case, so Equation 2.28 can be simplified as:

$$P_{Interface} = P_{sp} + P_{PE} \quad (2.29)$$

Equation 2.29 is the polarization charge density in the total charge density distribution of Equation 2.22. The spontaneously polarized charge intensity of AlGaN (30% Al) can be given by Vegard's law [113, 114]:

$$P_{Al_xGa_{1-x}N}^{sp} = x P_{AlN}^{sp} + (1 - x) P_{GaN}^{sp} - b_{Al_xGa_{1-x}N} x(1 - x) \quad (2.30)$$

where  $x$  is the percentage of Al composition in AlGaN and  $b_{Al_xGa_{1-x}N}$  is the bending coefficient of AlGaN [111].

The above are the basic physics equations required to numerically solve the energy band of AlGaN/AlN/GaN heterojunction under external strain [111, 123, 126, 127].

## 2.4.2 A self-consistent numerical method for one-dimensional Schrödinger-Poisson coupling equation

The analytical solution of the Schrödinger-Poisson coupling equation is difficult to derive, so it is usually solved by self-consistent coupling numerical calculation using finite difference or finite element mathematical methods [123, 126], as shown in Figure 2.10. First, we input the potential energy  $V_{in}(x)$  as the initial iteration, and calculate the wave function  $\psi_i(x)$  and the corresponding eigenenergy  $E_i$  using the steady-state Schrödinger wave equation (Equation 2.19), and then use the Equation 2.25 and Equation 2.16 to calculate the electron density  $n_i$  and the carrier concentration distribution  $n(x)$  in the subband. The Hartree potential  $V_h(x)$  is further calculated in the Poisson's equation using the given donor concentration  $N_D^+(x)$ , acceptor concentration  $N_A^-$ , and polarization charge density at the interface  $\sigma(x)$ , and the potential energy  $V_x$  is also calculated according to Equation 2.20. Then We substitute the obtained potential energy  $V_x$  at this time into the steady-state Schrodinger wave equation to find the new wave function  $\psi_i(x)$  and the corresponding eigenenergy  $E_i$ , and to solve the new carrier concentration distribution  $n(x)$ . This new  $n(x)$  together with the donor concentration and acceptor concentration

can be used to calculate the new Hartree potential  $V_h(x)$  and new potential energy  $V_x$  in the Poisson's equation. Compare the newly obtained potential energy  $V_x$  with the previous result, and if it is outside the error range, continue to iterate until convergence is achieved. Finally, the self-consistent solutions of  $V_x$  and  $n(x)$  are used to further determine the energy band diagram and the carrier concentration of the AlGaN/AlN/GaN heterojunction.

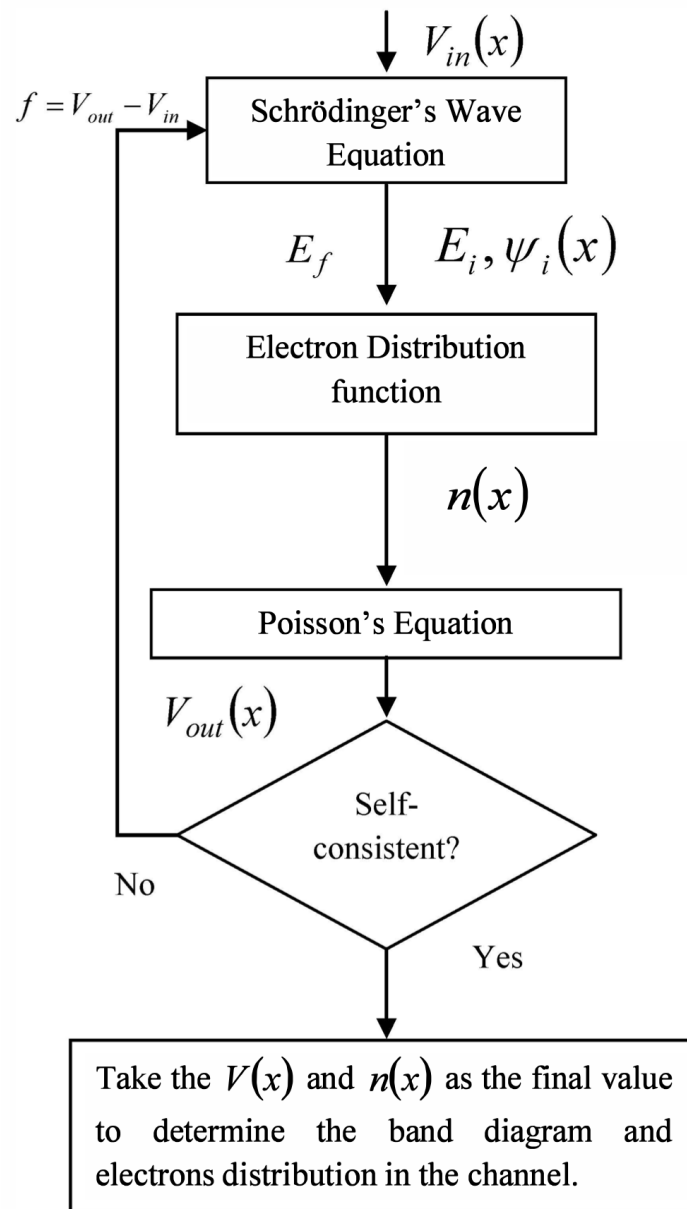


**Fig. 2.10 Iteration process of Schrodinger-Poisson self-consistent calculation [126]**

## 2.5 The framework of theoretical model

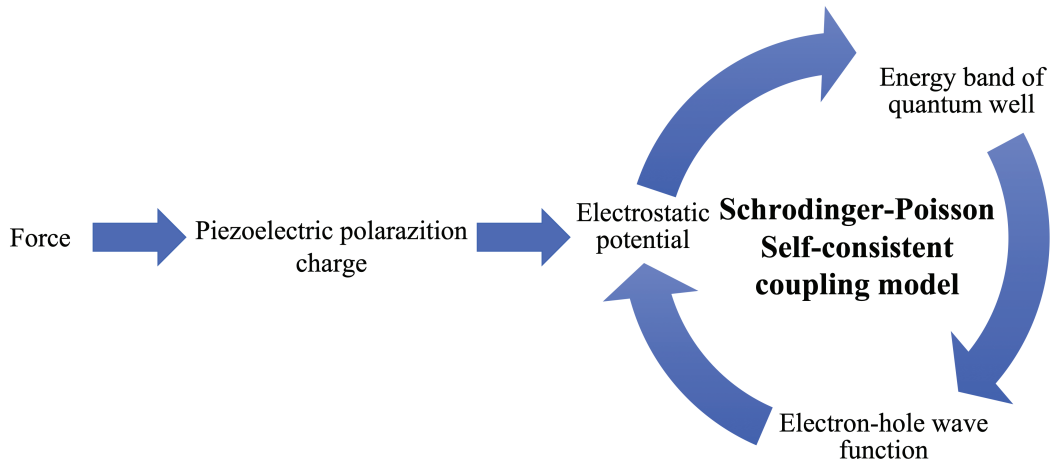


**Fig. 2.11 Framework diagram of the theoretical model**

So far, we have constructed a complete theoretical model of the MEMS device based on the AlGaN/AlN/AlGaN heterojunction cantilever structure. By combining the piezoelectric constitutive equation, the biaxial stress model and the finite element analysis, we deduce the mathematical relationship between the piezoelectric polarization charge intensity and the external stress. Through the self-consistent coupling calculation model of the AlGaN/AlN/GaN heterojunction, we further solved the modulation effect of the piezoelectric polarization charge intensity at the interface on the heterojunction energy band and the electron-hole wave function, thus successfully constructing a semi-classical physical model to explain the regulation mechanism of external stress on the electrical properties of MEMS devices. The overall framework of the theoretical model is shown in Figure 2.11. The piezoelectric polarization charge density at the interface is effectively modulated by external stress, thereby changing the electrostatic field in the AlGaN/AlN/GaN heterojunction, and finally modulating the heterojunction energy band, electron-hole wave function and carrier distribution. This model is an approximate semi-classical physical model with series of simplifications and approximations, which

successfully reveals the modulation characteristics of piezotronics effect on MEMS devices based on AlGaN/AlN/AlGaN heterojunction cantilever structure.

## 2.6 Simulation results of theoretical model

In the above theoretical analysis, we mainly take the theoretical modeling of MEMS under the downward force as an example to illustrate the method. Theoretical modeling and analysis of upward forces is similar. Different from the previous downward stress situation, the upward force on the cantilever weakens the electrical performance of MEMS, that is, the reaction will increase the potential well at the AlN/GaN interface, thereby reducing the concentration of 2DEG. Table 2.3 shows the lattice strain of GaN cantilever active region and the corresponding piezoelectric polarization charge density of the films at  $0 \sim 24$  mN upward force. The corresponding simulation results of MPD is in Figure 2.12.

**Table 2.3 Lattice strain of GaN cantilever active region and the corresponding piezoelectric polarization charge density of the films at  $0 \sim 24$  mN upward force**

F (mN)	Strain tensor,			$S_{zz}$	Piezoelectric polarization charge densities ( $\text{C m}^{-2}$ )		
	$S_{xx}$	$S_{yy}$	$S_{zz}$		$P_{\text{GaN}}^{\text{PE}}$	$P_{\text{AlN}}^{\text{PE}}$	$P_{\text{AlGaN}}^{\text{PE}}$
0	0	0	0	0	0	-0.0492	-0.0092
4	0.0003518	-0.0152836	0.0037110	0.0099	-0.0340	0.0021	
8	0.0002443	-0.0226277	0.0055619	0.0148	-0.0267	0.0076	
12	0.0001342	-0.0274473	0.0067851	0.0180	-0.0219	0.0111	
16	0.0000447	-0.0311016	0.0077137	0.0204	-0.0183	0.0138	
20	-0.0000288	-0.0341114	0.0084785	0.0224	-0.0153	0.0161	
24	-0.0000895	-0.0366690	0.0091278	0.0240	-0.0128	0.0179	

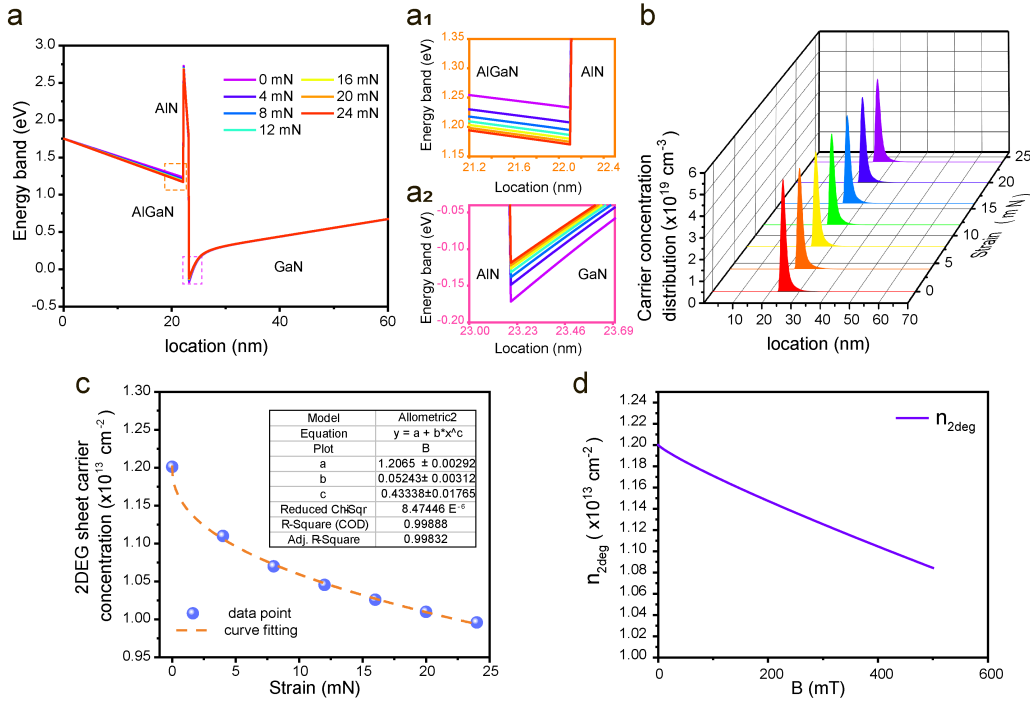


Fig. 2.12 Simulation results of MPD with upward magnetic force

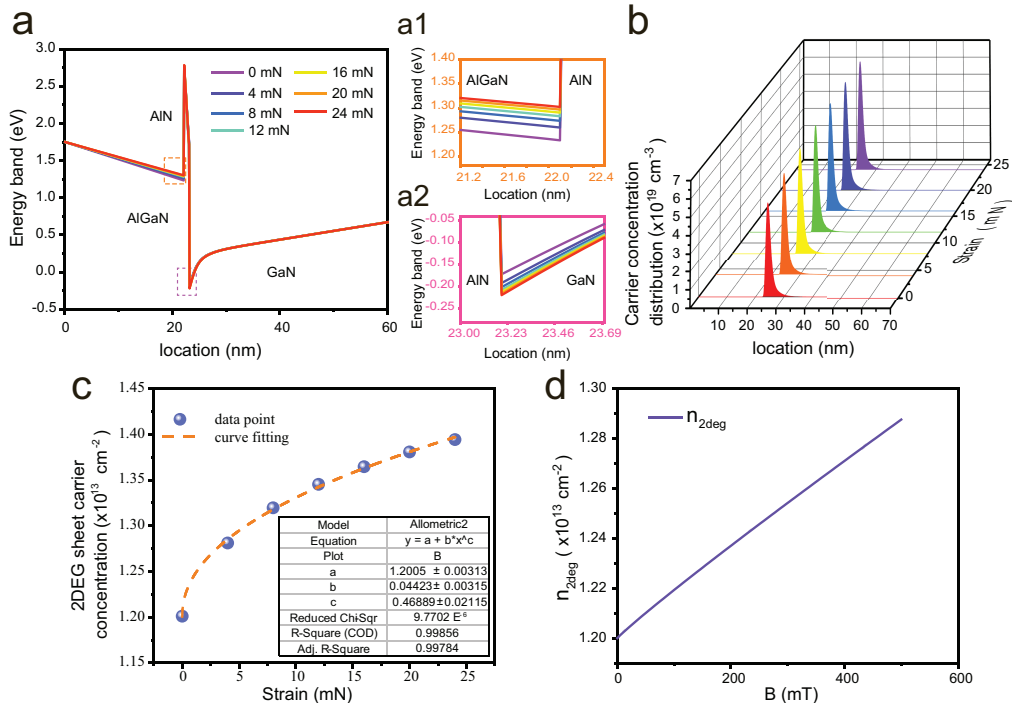
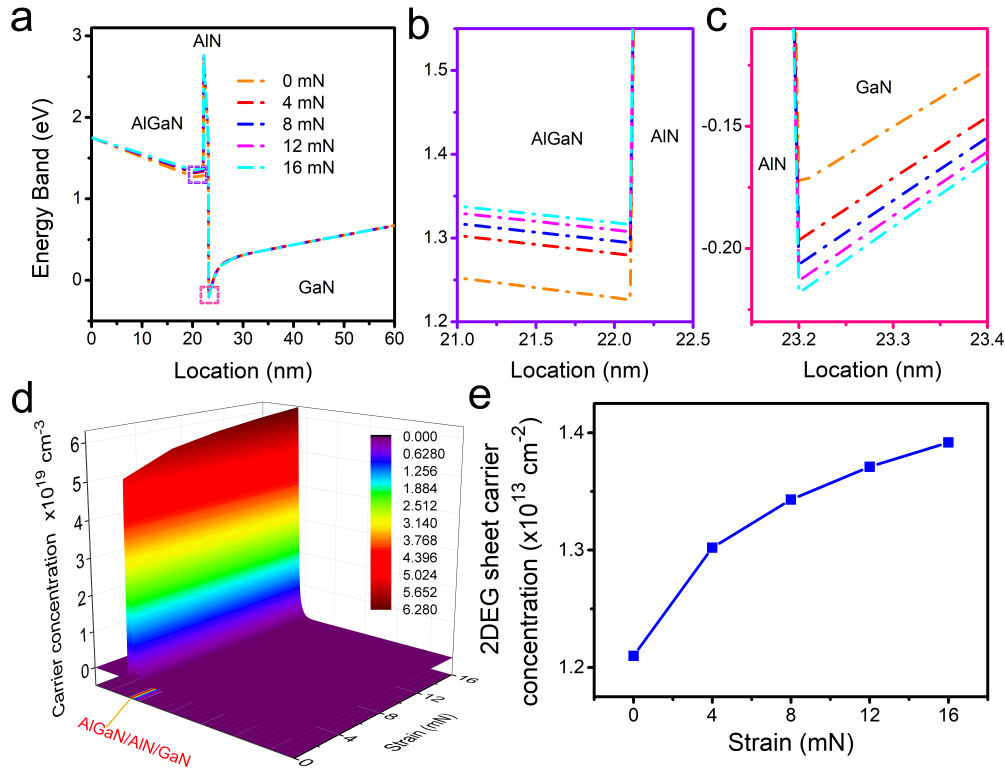


Fig. 2.13 Simulation results of MPD with downward magnetic force



**Fig. 2.14 Simulation results of SPD with downward normal force**

We also present the theoretical simulation results of the SPD and MPD at downward force, as shown in Figure 2.14 and Figure 2.13. The detailed analysis can be found in chapter 5 and chapter 6. By comparing with the experimental test, it can be concluded that the model successfully verifies the experimental results of SPD and MPD, and reveals the physical mechanism of MEMS devices based on AlGaN/AlN/GaN heterojunction cantilever structure.

Furthermore, we use the established model to simulate the energy band and carrier distribution characteristics of MEMS devices with different cantilever lengths under the control of 0 ~ 24 mN downward stress, as shown in Figure 2.15, Figure 2.16 and Figure 2.17. The corresponding cantilever lengths are 400  $\mu\text{m}$ , 450  $\mu\text{m}$  and 500  $\mu\text{m}$ , and the width and thickness are 60  $\mu\text{m}$  and 4.3  $\mu\text{m}$ . In these figures, Figure (a) is the AlGaN/AlN/GaN heterojunction conduction band; Figure (b) is the enlarged conduction band of AlGaN/AlN and AlN/GaN potential

well; Figure (c) is the enlarged conduction band of AlN/GaN potential well; Figure (d) is the carrier concentration distribution; Figure (e) is the two-dimensional electron gas (2DEG) areal density. It can be clearly seen that under the same external stress, the AlN/GaN wells of MEMS devices with cantilever lengths of 450  $\mu\text{m}$  (Figure 2.16c) and 500  $\mu\text{m}$  (Figure 2.17c) are deeper than that of 400  $\mu\text{m}$  (Figure 2.15c). So compared with the MEMS with shorter cantilever, more carriers are bound in the potential well of MEMS with longer cantilever (Figure 2.15d, Figure 2.16d and Figure 2.17d), and the two-dimensional electron gas (2DEG) areal density in the MEMS with cantilever length of 450  $\mu\text{m}$  (Figure 2.16e) and 500  $\mu\text{m}$  (Figure 2.17e) are all higher than that of 400  $\mu\text{m}$  (Figure 2.15e). Based on the theoretical simulation results, we can design cantilevers with different lengths and structures to modulate the MEMS's sensitivity to the external stress response. Therefore, the theoretical model can provide theoretical guidance for the development of MEMS cantilever devices based on AlGaN/AlN/GaN heterojunctions.

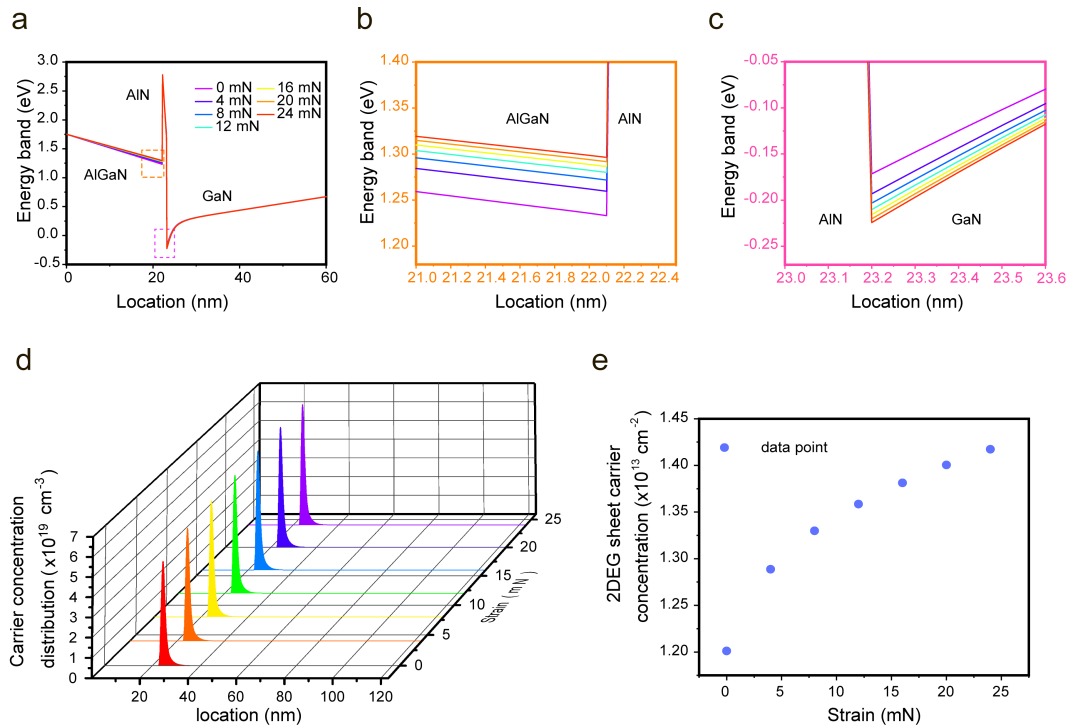


**Fig. 2.15 Simulation results of MEMS with the cantilever length of 400  $\mu\text{m}$  under downward force**

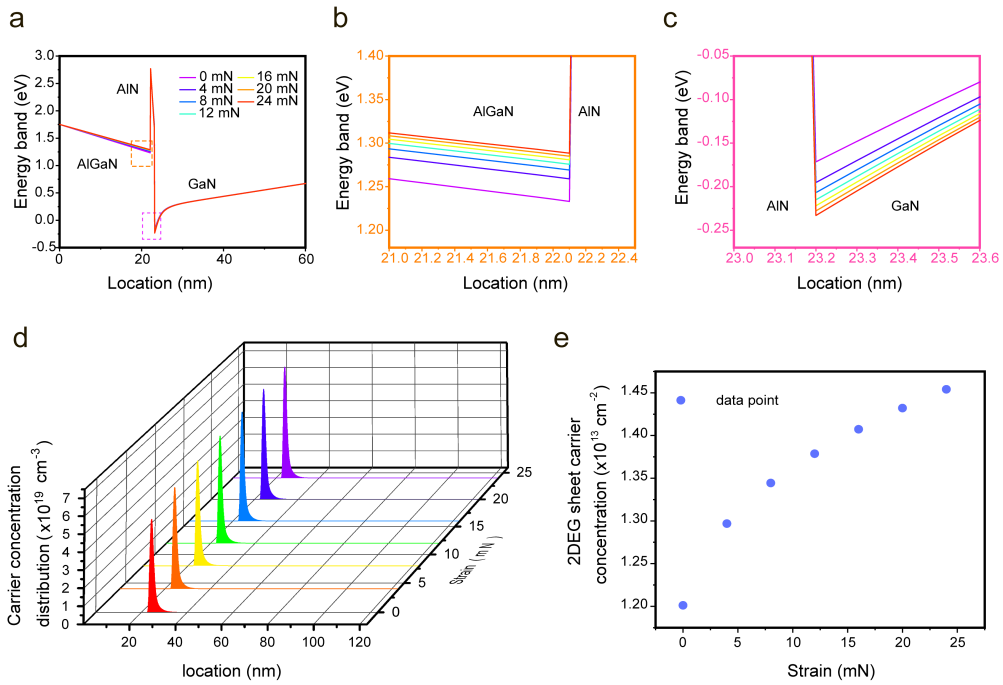


**Fig. 2.16 Simulation results of MEMS with the cantilever length of 450  $\mu\text{m}$  under downward force**

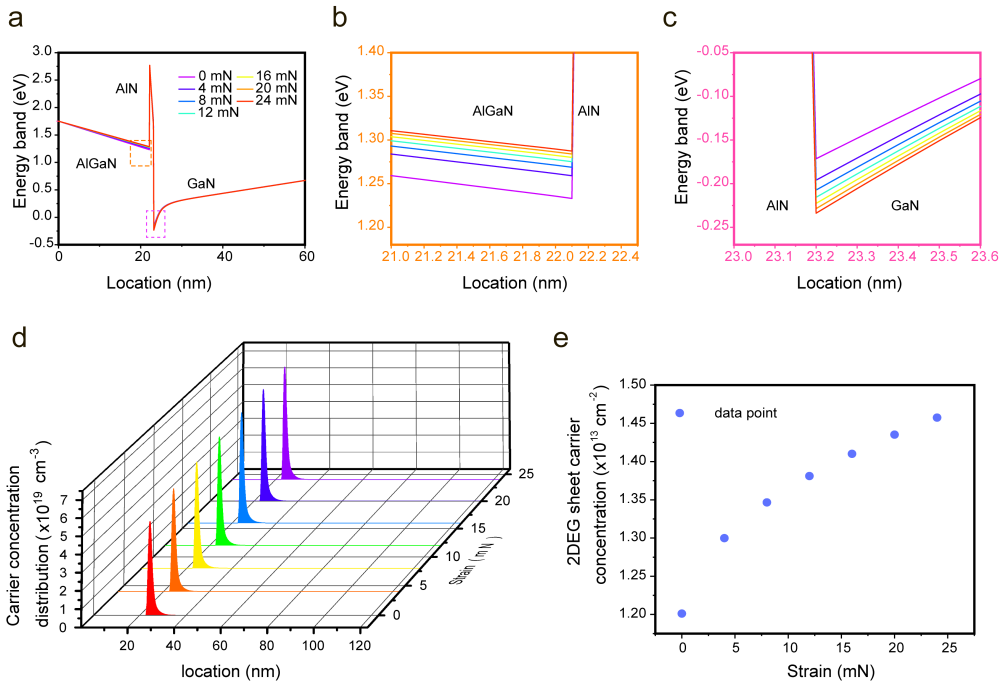


**Fig. 2.17 Simulation results of MEMS with the cantilever length of 500  $\mu\text{m}$  under downward force**

## 2.7 Summary

In this study, a semi-classical physical model of the MEMS device with a cantilever structure based on AlGaN/AlN/GaN heterojunction was established by using piezoelectric theory. The mathematical relationship between the lattice strain and the piezoelectric polarization charge of the multilayer heterojunction film was deduced through piezoelectric constitutive equation and biaxial stress model. Then the finite element analysis method of material mechanics was used to calculate the piezoelectric polarization charge intensity of the heterojunction film under different external stresses, and the one-dimensional Schrödinger-Poisson self-consistent coupling model was used to calculate the modulation characteristics of the external stress on the energy band of the AlGaN/AlN/GaN heterojunction and the electrical properties of the MEMS device. The theoretical results successfully verify the experimental results of the new MEMS devices designed and fabricated in this paper, namely SPD and MPD. The model provides theoretical guidance for the development of novel MEMS cantilever devices based on AlGaN/AlN/GaN heterojunctions.

# **Part II**

# **Manufacturing**

# **Chapter 3**

## **Manufacturing Technology of Power MEMS Devices**

In the Part II, I would systematically study the manufacture of GaN power MEMS devices from epitaxial growth wafers to well-functional devices. Benefiting from the rapid development of III-V compound semiconductor fabrication and characterization equipment, various complex microstructures including GaN microcantilever structures can now be easily realized by equipment devices with different functions. This chapter will introduce the main nanofabrication and characterization equipment, including epitaxial growth, dry etching, photolithography, thin film deposition, plasma cleaning, Raman spectroscopy, scanning electron microscopy, transmission electron microscopy, etc. I would briefly introduce their important role in GaN power MEMS research, as well as the corresponding process design and key parameters. The equipment mentioned in this chapter and later all belong to the micro-nano processing platform of the Chinese Academy of Sciences. The pictures of some of the equipment are from the official website of the equipment manufacturer, and all the models shown here are in one-to-one correspondence with the real objects.

## 3.1 Fabrication techniques

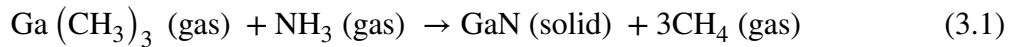
### 3.1.1 GaN-on-Si wafer epitaxial growth



**Fig. 3.1 Aixtron CCS 3×2 MOCVD**

The GaN wafers are typically obtained by epitaxial growth on Si substrates due to the less lattice mismatch. Metal Organic Compound Chemical Vapor Deposition (MOCVD), also known as Metal Organic Vapor Phase Epitaxy (MOVPE) is an important method for preparing nitride semiconductor materials, and it is also the most widely used method in the industry. MOCVD uses organic compounds of group III and group II elements and hydrides of group V and group VI elements as crystal growth source materials, and conducts vapor phase epitaxy on the Si substrate by thermal decomposition reaction to grow various III-V group, II-VI group compound semiconductors and their multicomponent solid solutions.

The growth of nitride crystals is usually carried out in cold-wall or hot-wall reaction chambers under normal or low pressure ( $1 \times 10^1 \sim 1 \times 10^5$  Pa). In the growth of GaN materials, trimethylgallium (TMG) and ammonia gas ( $\text{NH}_3$ ) carried by  $\text{H}_2$  are usually injected into the reaction chamber at the same time, and the reaction gases are transported to the surface of the high-temperature substrate and mixed above. The chemical reaction occurs as follows:



the resulting GaN molecules are deposited on the surface of the Si substrate to form an epitaxial film [24].

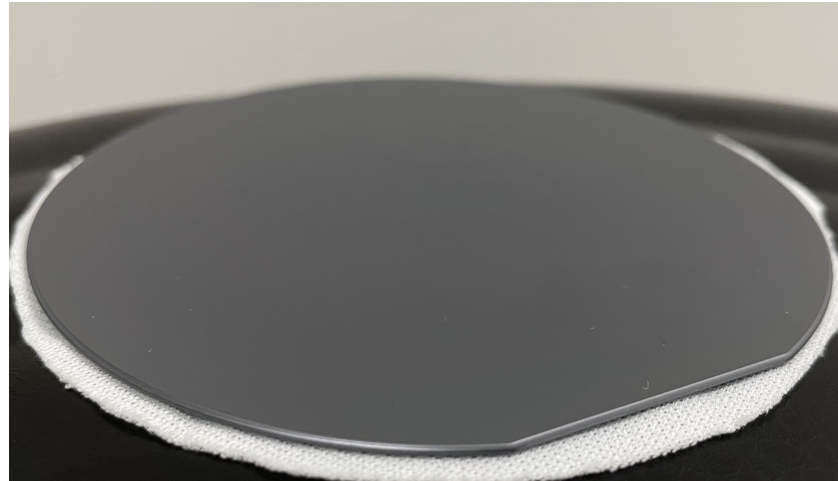


**Fig. 3.2 The 3-inch GaN-on-Si wafer**

In this research, the 3-inch GaN-on-Si wafers have been successfully epitaxially grown on Si(111) substrates using Aixtron CCS 3×2 MOCVD, as shown in Figure 3.2. The total thickness is about 1 mm, including Si(111) substrate, AlN/AlGaN multi-layer buffer layer, unintentionally doped (UID) GaN buffer layer, intrinsic GaN 2DEG channel layer, AlN barrier layer, AlGaN barrier layer and GaN cap layer. The grown wafer exhibits good electrical performance with  $300 \Omega/\text{square}$  sheet resistance,  $1.00 \times 10^{13} \text{ cm}^{-2}$  carrier density,  $2000 \text{ cm}^2/(\text{Vs})$  mobility and 600 V breakdown voltage.

### 3.1.2 Wafer dicing

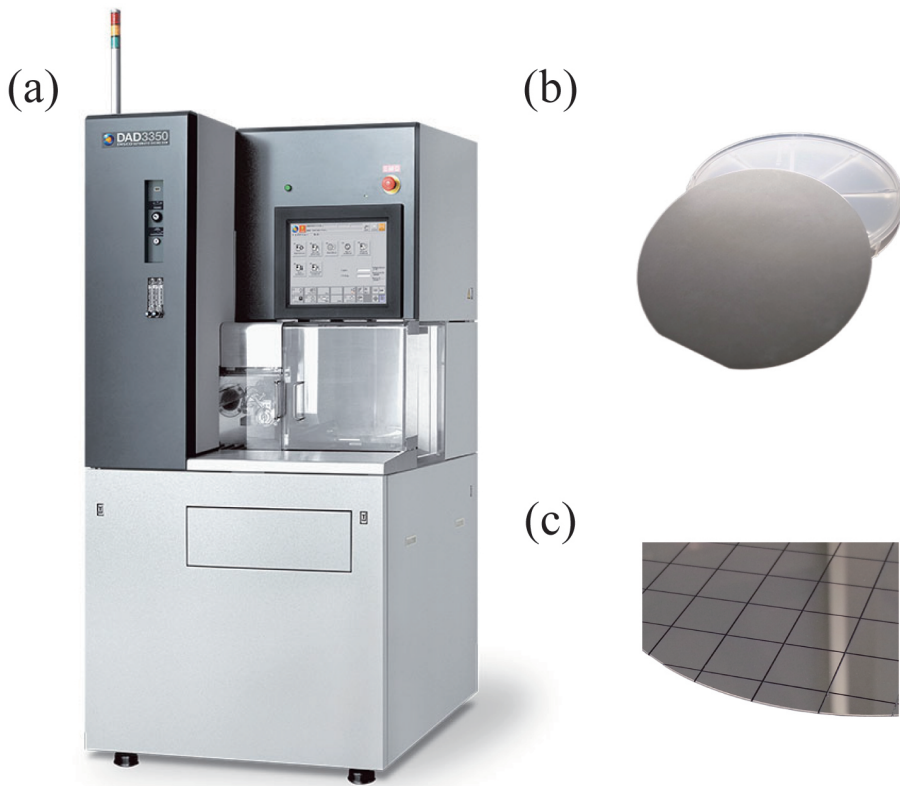


**Fig. 3.3 DISCO DAD3350 automatic dicing saw**

Compound semiconductors, such as GaN and SiC, are difficult to obtain high productivity with slow feed rates when using existing diamond blades for blade cutting, especially as wafer thickness becomes thinner. Therefore, utilizing beneficial characteristics of laser energy, laser cutting has developed as a highly promising method in dicing-grinding service. Laser applications minimize kerf streets, thereby suiting special materials such as GaN or SiC when blade dicing reaches its limits. Further, working with laser technology provides a high degree of flexibility to die forms while offering high processing speed. Laser technology is developing rapidly and the semiconductor industry is taking full advantage of every innovation leap.

In this research, dice of size  $2 \times 2$  mm and  $3 \times 3$  mm have been cut from the grown 3-inch wafers with the DISCO DAD3350 automatic dicing saw.

### 3.1.3 Cleaning technologies

Cleaning procedures are essential steps in semiconductor processing. These are mostly used to remove particles and oxidize organic contaminants. Just a single particle on a wafer is enough to cause a killer defect or excursion that will ultimately lead to device failure. This is because both device reliability and final product yields are directly linked to the cleanliness of a wafer as it passes through the hundreds of patterning, etching, deposition and interconnect process steps. Therefore, the wafer must be strictly cleaned to remove organic and inorganic substances on the surface before the device fabrication process. The precondition of the cleaning process is not to destroy the surface characteristics of the epitaxial wafer. On this basis, the cleaning technologies, including wet cleaning and dry cleaning, are used to effectively remove various residual contaminants and impurities on the surface of the epitaxial wafer.

**Wet cleaning** Some common cleaning solvents include acetone, trichloroethylene, ultrapure water, hydrochloric acid, piranha solution, dilute HF solution and RCA cleaner. The cleaning steps of acetone, trichloroethylene, ultrapure water and hydrochloric acid are simple and will not be repeated. Piranha solution, dilute HF solution, and RCA cleaner are described as follows because of their better cleaning effect and certain dangers during the operation [128–130].

#### 1. Piranha solution

It consists of  $\text{H}_2\text{SO}_4$  (98%) and  $\text{H}_2\text{O}_2$  (30%) in different ratios, and is typically used for removing organic contaminants and stripping photoresists.

#### 2. RCA clean

The RCA clean is a standard set of wafer cleaning steps which need to be performed before high-temperature processing steps (oxidation, diffusion, CVD) of wafers in semiconductor manufacturing. It involves the following chemical processes performed in sequence:

2.1) SC-1: organic clean + particle clean

5 parts of deionized water, 1 part of ammonia water, (29% by weight of NH<sub>3</sub>), and 1 part of aqueous H<sub>2</sub>O<sub>2</sub> (hydrogen peroxide, 30%) at 75 °C or 80 °C typically for 10 minutes. This base-peroxide mixture removes organic residues. Particles are also very effectively removed, even insoluble particles.

2.2) SC-2: ionic clean

6 parts of deionized water, 1 part of aqueous HCl (hydrochloric acid, 37% by weight), and 1 part of aqueous H<sub>2</sub>O<sub>2</sub> (hydrogen peroxide, 30%) at 75 or 80 °C typically for 10 minutes. This treatment effectively removes the remaining traces of metallic (ionic) contaminants.

3. Dilute HF solution

Prepared by diluting 49% HF with dionized water (1:100) at room temperature and can effectively removes the oxide.

In this research, wet cleaning techniques have been applied to wafer cleaning, residual photoresist removal, silicone oil cleaning, organic and particle contamination removal.

**Dry cleaning** Plasma technology is often characterized as a "dry" cleaning process, using ionized gases in vacuum chambers to remove all organic matter from the surface of the semiconductors through the use of an ionized gas called plasma. Plasma is an ionized gas capable of conducting electricity and absorbing energy from an electrical supply. Man-made plasma is generally created in a low-pressure environment. When a gas absorbs electrical energy, its temperature increases causing the ions to vibrate faster and "scrub"



**Fig. 3.4 PVA TePla IoN 40 plasma cleaner**

a surface. This is generally performed in a vacuum chamber utilizing oxygen and/or argon gas and is an effective way to clean without using hazardous solvents. In contrast to chemically-based wet technologies, which have their role in removing thicker contaminants in the micron range, plasma deals with contamination in the nanometer range on substrate and wafer surfaces.

In this research, PVA TePla IoN 40 plasma cleaner is mainly used to remove residual photoresist and organic cleaning solutions by generating oxygen ions.

Cleaning technologies are crucial steps in the semiconductor manufacturing process and directly affects the performance and reliability of the device. In the process integration of chapter 4, a large number of cleaning processes can be found between lithography, etching, deposition, etc. They connect all processes as an indispensable intermediate link. The purpose of the cleaning process is to remove the residual influence of the previous process to the greatest extent on the premise of retaining the previous process results, and to provide a good operating environment for the subsequent process.

### 3.1.4 Photolithography

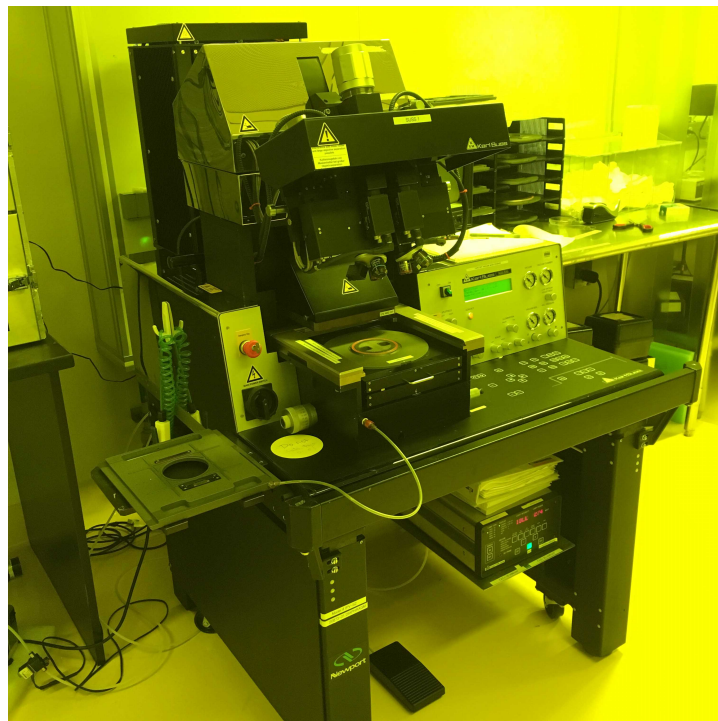


**Fig. 3.5 SUSS MA6 mask aligner designed for high-resolution photolithography**

Photolithography is an optical means of transferring a pattern on a substrate. It uses light to produce minutely patterned thin films of suitable materials over a substrate to protect selected areas of it during subsequent etching, deposition, or implantation operations. Typically, ultraviolet light is used to transfer a geometric design from an optical mask to a light-sensitive chemical (photoresist) coated on the substrate. The photoresist either breaks down or hardens where it is exposed to light. The patterned film is then created by removing the softer parts of the coating with appropriate solvents.

The photolithography process is divided into positive photoresist and negative photoresist according to the type of photoresist. A negative photoresist is a type of photoresist in which the portion of the photoresist that is exposed to light becomes insoluble to the photoresist developer. The unexposed portion of the photoresist is dissolved by the photoresist developer.

Whereas, a positive photoresist is a type of photoresist in which the portion of the photoresist that is exposed to light becomes soluble to the photoresist developer. The unexposed portion of the photoresist remains insoluble to the photoresist developer.

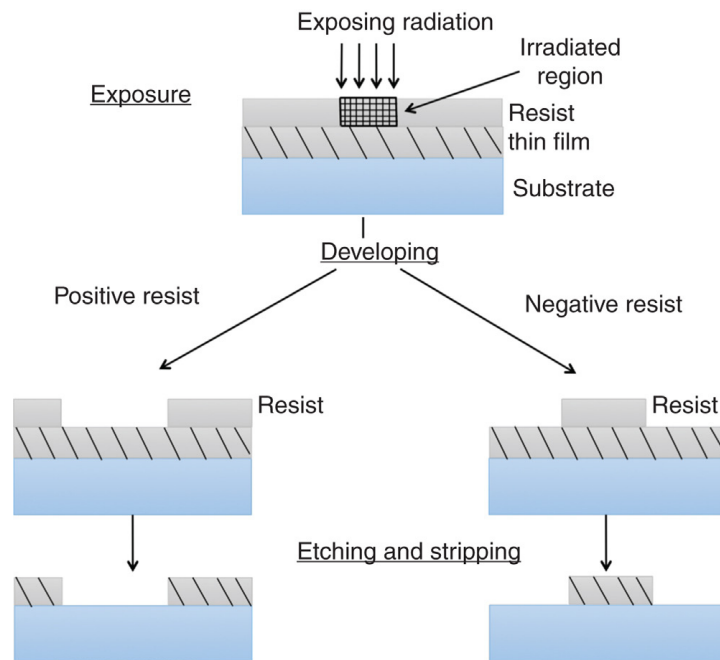


**Fig. 3.6 The schematic diagram showing the process of photolithography [131]**

In this research, the SUSS MA6 mask aligner designed for high-resolution photolithography at the micrometer scale has been applied to transfer patterns from mask to wafer, including mesa patterns, electrode patterns, cantilever patterns, etc.

### 3.1.5 Thin film deposition

Thin Film deposition is the technology of applying a very thin film of material - between a few nanometers to about 100 micrometers, or the thickness of a few atoms – onto a "substrate" surface to be coated, or onto a previously deposited coating to form layers. Thin Film deposition is usually divided into two broad categories - chemical deposition and physical vapor deposition coating systems. Chemical deposition is that a volatile fluid precursor produces a chemical change on a surface leaving a chemically deposited coating, such as chemical vapor deposition

(CVD). Physical vapor deposition (PVD) refers to a wide range of technologies where a material is released from a source and deposited on a substrate using mechanical, electromechanical or thermodynamic processes. The two most common techniques of physical vapor deposition are thermal evaporation and sputtering.

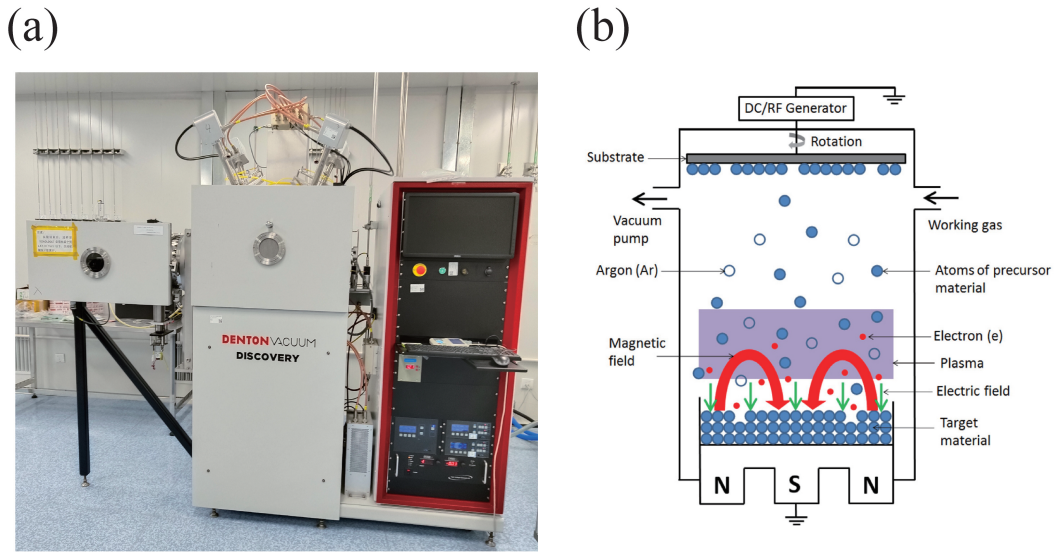


**Fig. 3.7 Denton Discovery 635 magnetron sputtering system**

**Magnetron sputtering** Sputter deposition is a physical vapor deposition (PVD) method of thin film deposited by sputtering. The general sputtering method can be used to prepare a variety of materials such as metals, semiconductors, insulators, etc., and has the advantages of simple equipment, easy control, large coating area, and strong adhesion. Sputtering sources often employ magnetrons that utilize strong electric and magnetic fields to confine charged plasma particles close to the surface of the sputter target. In a magnetic field, electrons follow helical paths around magnetic field lines, undergoing more ionizing collisions with gaseous neutrals near the target surface than would otherwise occur. The sputter gas is typically an inert gas such as argon. The plasma can also be sustained at a lower pressure this way. The certain target atoms near the surface gain sufficient momentum for outward motion and are sputtered out of the target and the

sputtered atoms are neutrally charged and so are unaffected by the magnetic trap. These sputtered atoms deposit onto the surface of the sample to form thin films.

Magnetron sputtering includes direct current (DC) magnetron sputtering and radio frequency (RF) magnetron sputtering, each has a different working principle and application objects. The main advantage of RF magnetron sputtering over DC magnetron sputtering is that it does not require the target as an electrode be electrically conductive. Therefore, any material can be sputter-deposited theoretically using RF magnetron sputtering. Magnetron sputtering is advantageous as it doesn't require evaporation or melting of source materials, allowing for exotic material experimentation and novel coating film applications. Sputter deposition is excellent for materials with high melting points that cannot be evaporated. It can achieve denser coatings than evaporation and is perfect for metallic or insulating coatings with specific optical or electrical properties.

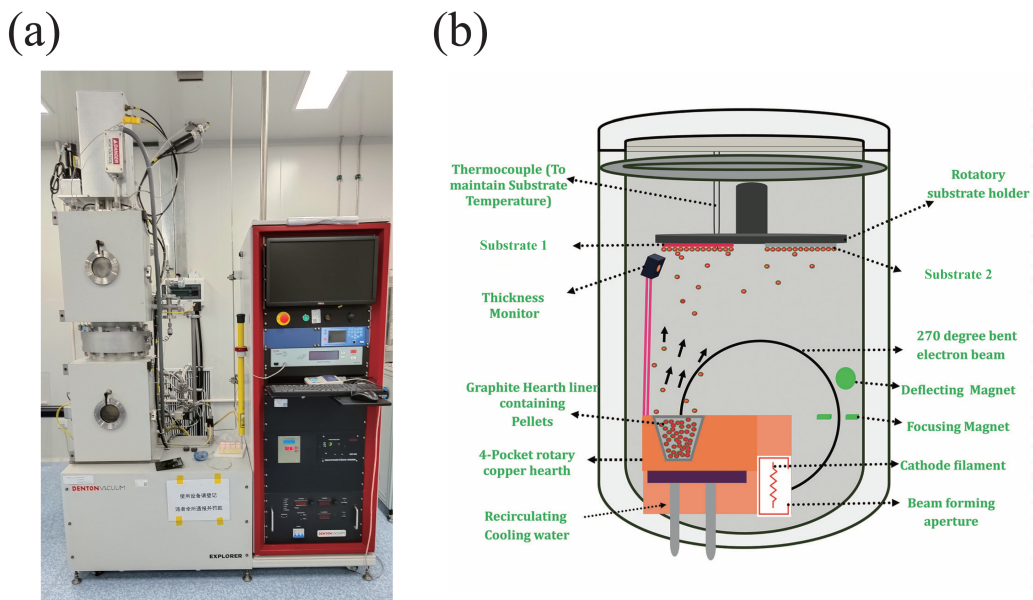


**Fig. 3.8 Denton Vacuum Explore 14 electron beam evaporation system**

**Electron beam evaporation** E-beam (electron beam) evaporation is a thermal evaporation process. E-beam evaporation provides for the direct transfer of a larger amount of en-

ergy into the source material, enabling the evaporation of metal and dielectric materials with very high melting temperatures, such as gold and silicon dioxide, respectively. In e-beam evaporation, the evaporation material can be placed directly in a water-cooled copper hearth or into a crucible and heated by a focused electron beam. Electron beams can be generated by thermionic emission, field electron emission or the anodic arc method. The generated electron beam is accelerated to a high kinetic energy and directed towards the evaporation material. The thermal energy that is produced heats up the evaporation material causing it to melt or sublime. Once temperature and vacuum level are sufficiently high, vapor will result from the melt or solid. The resulting vapor can then deposits on the substrate to form the required thin film

The deposition rate in this process can be as low as 1 nm per minute to as high as few micrometers per minute. The material utilization efficiency is high relative to other methods, and the process offers structural and morphological control of films, as well as the very high deposition rate. E-Beam evaporation are also advantageous for polymeric coating due to its simplicity and flexibility. E-Beam coatings also process in a more rapid fashion in a batch scenario as compared to Magnetron Sputtered coatings which make them ideal for high-volume commercial applications. E-Beam evaporation work for a wide variety of materials, including those with higher melting points that cannot undergo thermal evaporation, deliver better step coverage than sputtering or chemical vapor deposition (CVD), and offers a higher material utilization efficiency and higher deposition rates than sputtering.

In this research, the Denton Discovery 635 magnetron sputtering system has been applied to deposit the magnetic thin film  $(\text{Fe}_{90}\text{Co}_{10})_{78}\text{Si}_{12}\text{B}_{10}$  in MPD, and the Denton Vacuum Explore 14 electron beam evaporation system has been used to deposit the ohmic and Schottky contact metals in both SPD and MPD, including Ti, Al, Au and Ni.

### 3.1.6 Dry etching

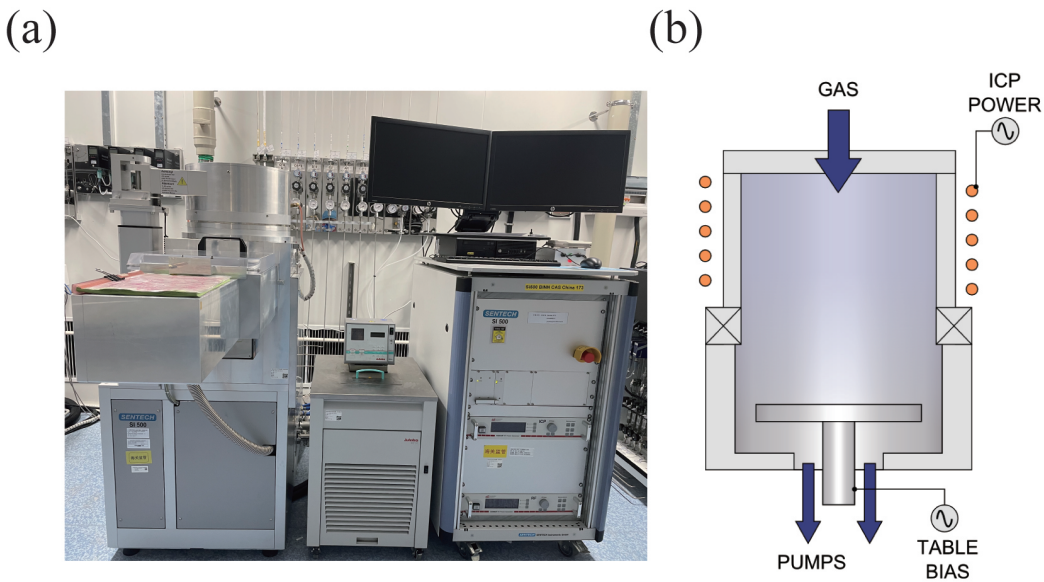


**Fig. 3.9 SENTECH SI 500 inductively coupled plasma reactive ion etching**

ICP RIE etching is an advanced technique designed to deliver high etching rates, high selectivity and low damage processing. The gases are introduced above an inductive coil, placed around a ceramic tube. RF is applied to both the coil and chuck to create a plasma. The substrate is placed on the RF-powered chuck, and the wafer takes on potential which accelerates etching species extracted from plasma toward the etched surface. The introduction of different gases can produce different chemical reactions, thereby achieving the purpose of effectively etching different materials. Usually,  $SF_6/Ar/O_2$  gas is used to etch Si and its compound materials, while  $BCl_3/Cl_2/Ar$  gas is widely used to etch GaN and its compound materials. The etching rate can be effectively adjusted by the etching power. This technology combines chemical reaction and ion-induced etching to achieve a high degree of process flexibility.

In this research, SENTECH SI 500 ICP-RIE plays an important role in the mesa isolation and cantilever structure fabrication process. Especially in the preparation of the cantilever structure, by combining the process design of anisotropic etching of GaN and isotropic etching

of Si, the cantilevered power MEMS devices with good uniformity and excellent performance has been successfully prepared. It can be determined that ICP-RIE process is the core process technology in the research of GaN power MEMS devices.

### 3.1.7 Rapid thermal processing



**Fig. 3.10 LABSYS RTP-1200 rapid thermal processing system**

Rapid thermal processing (RTP) is a semiconductor manufacturing process which heats silicon wafers to temperatures exceeding 1,000°C for not more than a few seconds. During cooling wafer temperatures must be brought down slowly to prevent dislocations and wafer breakage due to thermal shock. Such rapid heating rates are often attained by high-intensity lamps or lasers. These processes are used for a wide variety of applications in semiconductor manufacturing including dopant activation, thermal oxidation, metal reflow, silicide and barrier metal formation, chemical vapor deposition, and other steps in semiconductor manufacturing.

In this research, LABSYS RTP-1200 RTP is mainly used for ohmic contact formation in AlGaN/GaN HEMTs, and the most commonly used ohmic contact metal composition is Ti/Al/Ni/Au (from surface to bottom).

## 3.2 Characterization techniques

### 3.2.1 Semiconductor parameter analyzer

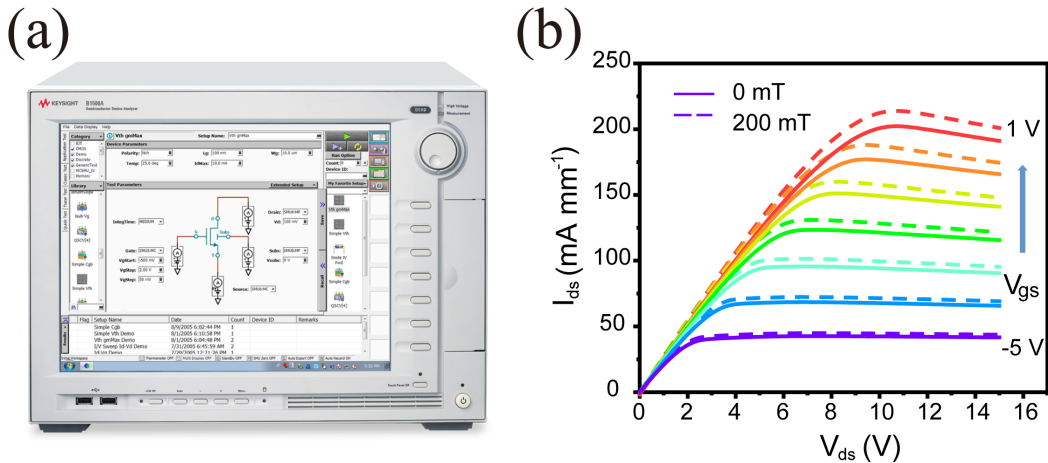


**Fig. 3.11 Keysight B1500A semiconductor device parameter analyzer and I-V characteristics of MPD under external magnetic field modulation**

A semiconductor parameter analyzer is an all-in-one unit designed to discover the characteristics of semiconductor devices such as diodes, transistors, and thyristors. Based on an oscilloscope, the device also contains voltage and current sources that can be used to stimulate the device under test. The function is to apply a swept (automatically continuously varying with time) voltage to the terminals of the device under test and measure the amount of current that the device permits to flow at each voltage. This V-I (voltage versus current) graph is displayed on an oscilloscope screen. Configuration includes the maximum voltage applied, the polarity of the voltage applied (including the automatic application of both positive and negative polarities), and the resistance inserted in series with the device. The main terminal voltage can often be swept up to several thousand volts, with load currents of tens of amps available at lower voltages.

For two terminal devices such as diodes, the parameter analyzer can display all of the interesting parameters such as the diode's forward voltage, reverse leakage current, reverse breakdown voltage, and so on. For three-terminal devices such as transistors and FETs also use a connection to the control terminal of the device being tested, and the control terminal current or voltage is stepped. By sweeping the voltage through the configured range of main terminal voltages, for each voltage step of the control signal, a group of I-V curves is generated automatically. The parameter analyzers can characterize the electrical characterization of the transistors, diodes, resistors and capacitors that make up semiconductors.

In this research, the Keysight B1500A semiconductor device parameter analyzer has been widely used to test the electrical properties of AlGaN/GaN HEMTs and power MEMS devices, especially the I-V characteristics under external stimulus.

### 3.2.2 Scanning electron microscopy (SEM)



**Fig. 3.12 FEI Nova Nano SEM 450 field-emission scanning electron microscopy**

A scanning electron microscopy (SEM) is a type of electron microscope that produces images of a sample by scanning the surface with a focused beam of electrons. The electrons interact with atoms in the sample, producing various signals that contain information about the surface topography and composition of the sample. The signals used by a SEM to produce an image result from interactions of the electron beam with atoms at various depths within the sample. Various types of signals are produced including secondary electrons (SE), reflected or back-scattered electrons (BSE), and transmitted electrons. The electron beam is scanned in a raster scan pattern, and the position of the beam is combined with the intensity of the detected signal to produce an image. Due to the very narrow electron beam, SEM micrographs have a large depth of field yielding a characteristic three-dimensional appearance useful for understanding the surface structure of a sample. There is a wide range of magnifications, from about 10 times to more than 500,000 times, about 250 times the magnification limit of the best light microscopes. Some SEMs can achieve resolutions better than 1 nanometer [132].

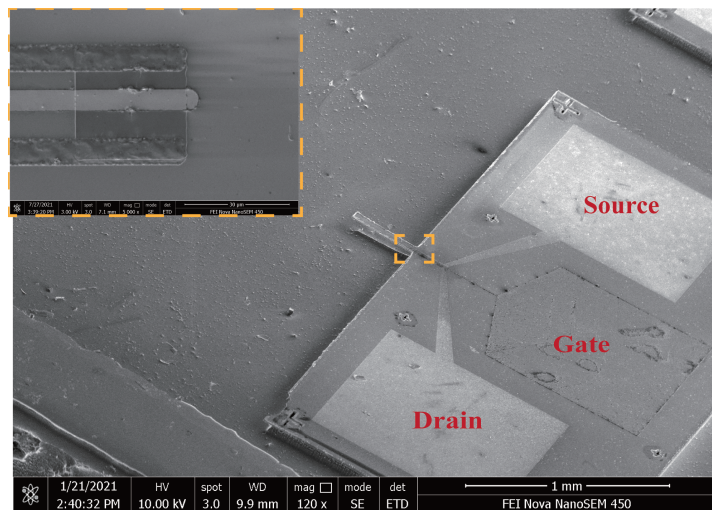


**Fig. 3.13 SEM image of fabricated GaN power MEMS devices**

In this research, FEI Nova Nano SEM 450 field-emission SEM can effectively obtain the topographic features of MEMS devices during fabrication, especially when dry-etching can-

tilever structures. The accurate grasp of the topographic features greatly improves the efficiency of process development.

### 3.2.3 Transmission electron microscopy (TEM)



**Fig. 3.14 FEI Tecnai F20 cryo-transmission electron microscope**

Transmission electron microscopy (TEM) is a microscopy technique in which a beam of electrons is transmitted through a specimen to form an image. An image is formed from the interaction of the electrons with the sample as the beam is transmitted through the specimen. The image is then magnified and focused onto an imaging device. Transmission electron microscopes are capable of imaging at a significantly higher resolution than light microscopes, owing to the smaller de Broglie wavelength of electrons. This enables the instrument to capture fine detail—even as small as a single column of atoms, which is thousands of times smaller than a resolvable object seen in a light microscope. What this means is that a TEM is capable

of returning an extraordinary variety of nanometer- and atomic-resolution information, in ideal cases revealing not only where all the atoms are but what kinds of atoms they are and how they are bonded to each other. Transmission electron microscopy is a major analytical method in the physical, chemical and biological sciences and is widely used in materials science, nanotechnology and semiconductor research.

The main difference between SEM and TEM is that SEM creates an image by detecting reflected or knocked-off electrons, while TEM uses transmitted electrons (electrons that are passing through the sample) to create an image. The magnifications that TEMs offer are much higher compared to SEMs. TEM can magnify the samples by more than 50 million times, while for the SEM, this is limited to 1-2 million times. As a result, TEM offers valuable information on the inner structure of the sample, such as crystal structure, morphology and stress state information, while SEM provides information on the sample's surface and its composition.

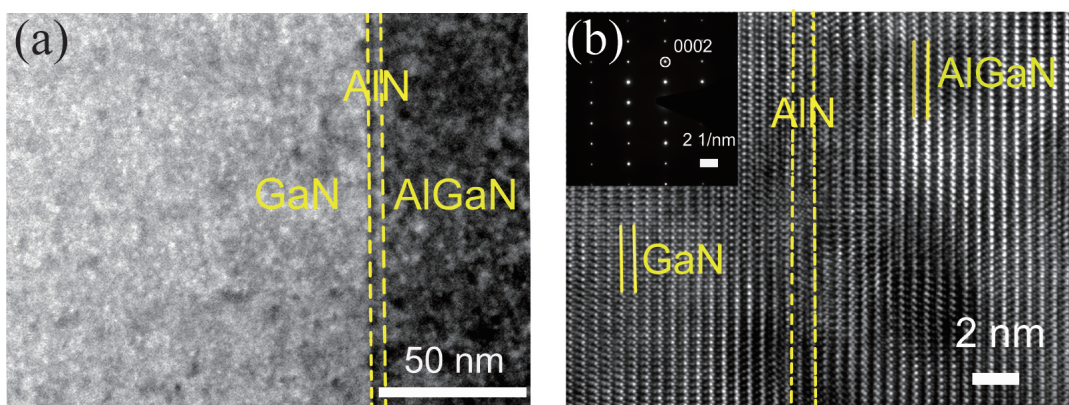


**Fig. 3.15 High-resolution TEM image acquired from the AlGaN/AlN/GaN hetero-stacks**

In this research, FEI Tecnai F20 TEM has been used to characterize the lattice orientation, lattice constants and the dislocation defects of GaN, AlN, AlGaN layer.

### 3.2.4 Energy dispersive X-ray spectroscopy (EDX)

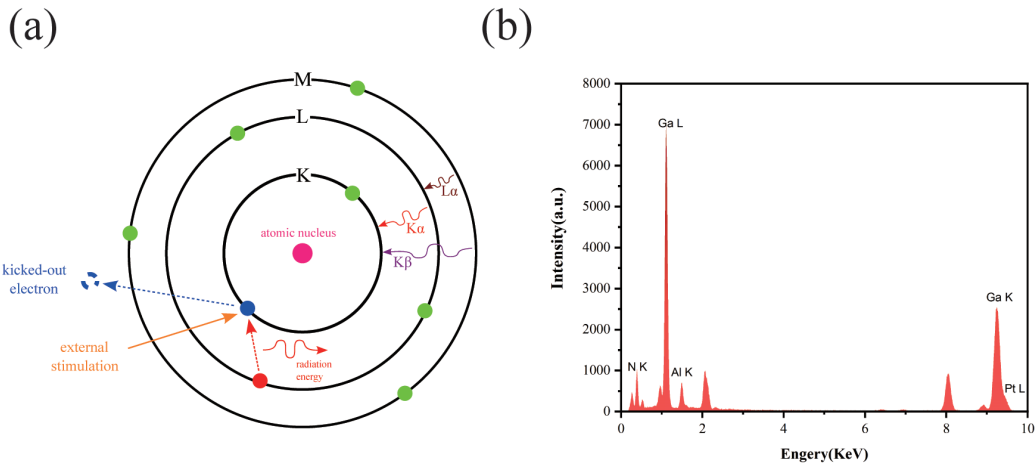


**Fig. 3.16 Principle of EDX and elemental composition of AlGaN/GaN HEMT characterized by EDX**

Energy-dispersive X-ray spectroscopy (EDS, EDX, EDXS or XEDS), is an analytical technique used for the elemental analysis or chemical characterization of a sample. It relies on the interaction of some source of X-ray excitation and a sample. Its characterization capabilities are due in large part to the fundamental principle that each element has a unique atomic structure allowing a unique set of peaks on its electromagnetic emission spectrum. A beam of electrons is focused into the sample to stimulate the emission of characteristic X-rays from a specimen. At rest, an atom within the sample contains ground state (or unexcited) electrons in discrete energy levels or electron shells bound to the nucleus. The incident beam may excite an electron in an inner shell, ejecting it from the shell while creating an electron-hole where the electron was. An electron from an outer, higher-energy shell then fills the hole, and the difference in energy between the higher-energy shell and the lower-energy shell may be released in the form of an X-ray. The number and energy of the X-rays emitted from a specimen can be measured by an energy-dispersive spectrometer. As the energies of the X-rays are characteristic of the

difference in energy between the two shells and of the atomic structure of the emitting element, EDS allows the elemental composition of the specimen to be measured [133].

In this research, the EDX equipment is integrated into the transmission electron microscopy equipment to characterize the elemental composition and distribution of AlGaN/GaN HEMTs.

### 3.2.5 High-resolution X-ray diffraction (HRXRD)

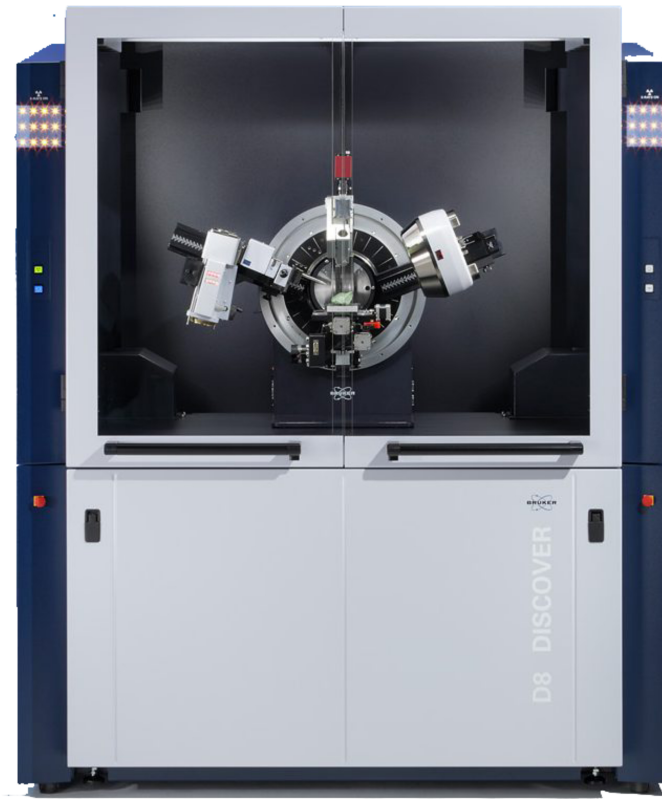


**Fig. 3.17 Bruker D8 DISCOVER high-resolution X-ray diffraction**

Most of today's modern semiconductor device structures are epitaxially grown from the gas phase onto a substrate made from silicon, silicon-germanium, III-V and II-VI compounds. These films are nearly-perfect crystalline films containing a relatively low dislocation density. Film properties are largely determined by their compositional and structural parameters. Information such as layer thickness, composition, strain, relaxation and structural quality is obtained

by measuring rocking curves and reciprocal space maps using high-resolution X-ray diffraction (HR-XRD). The spatial distribution of defects can also be visualized by X-ray diffraction imaging methods.

The working principle behind HRXRD is Bragg's law, which states that when the x-ray incident onto a crystal surface with an angle of incidence it will reflect back with a same angle of scattering. When the path difference is equal to a whole number of wavelength, a constructive interference will occur. The path difference is the separation between the crystal planes that caused the reflection. The crystalline structure causes a beam of incident X-rays to diffract into many specific directions. By measuring the angles and intensities of these diffracted beams, HRXRD can be used to analyze the thickness, composition, and strain state of epitaxial single-crystal thin films, and can also measure the density of defects in epitaxial layers by FWHM of Bragg reflections obtained in the direction perpendicular to the diffraction vector.

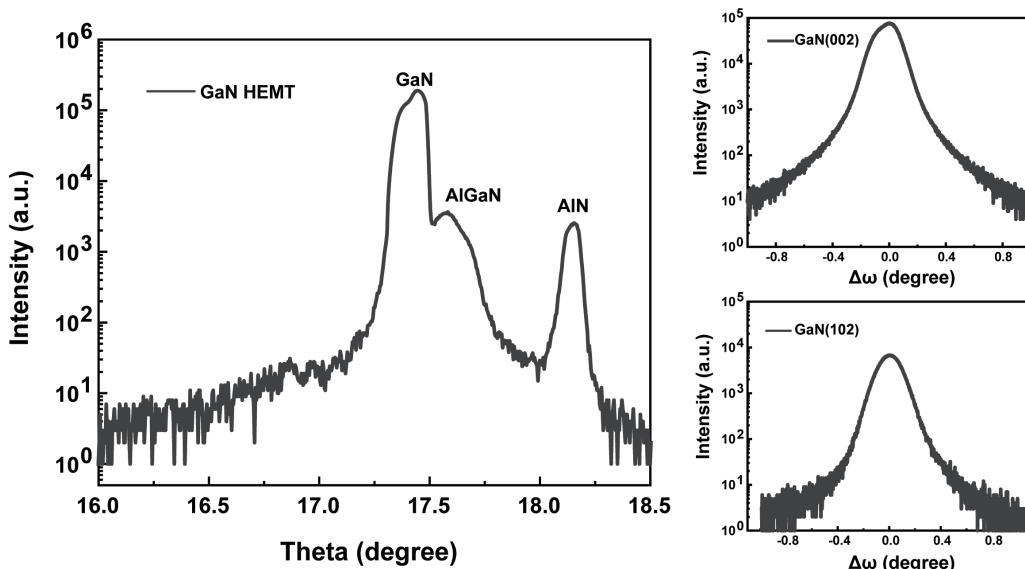


**Fig. 3.18 The X-ray diffraction spectra of GaN HEMT**

In this research, Bruker D8 DISCOVER HR-XRD has been used to measure the composition, defects and thickness of GaN Wafer.

### 3.2.6 Raman spectroscopy



**Fig. 3.19 HORIBA LabRAM HR Evolution Raman spectroscopy**

Raman scattering is an extremely powerful contactless tool which allows non-destructive and quantitative microanalysis of structural and electrical properties of semiconductor materials. This technique is very useful since the Raman signal is very sensitive to the microstructural state of the sample and other local environments, therefore giving information on the structure of the material on the scale of a few lattice constants.

Raman is a light scattering technique, whereby a molecule scatters incident light from a high-intensity laser light source. Most of the scattered light is at the same wavelength as the laser source and does not provide useful information – this is called Rayleigh Scattering. However, a small amount of light (typically 0.0000001%) is scattered at different wavelengths, which depend on the chemical structure of the analyte – this is called Raman Scattering. Raman signal is a function of the electron-phonon interaction, i.e. lattice vibration. A Raman spectrum features a number of peaks, showing the intensity and wavelength position of the Raman scattered light. Each peak corresponds to a specific lattice vibration. Raman spec-

troscopy probes the chemical structure of a material and provides information about chemical structure and identity, phase and polymorphism, intrinsic stress/strain and contamination and impurity [134].

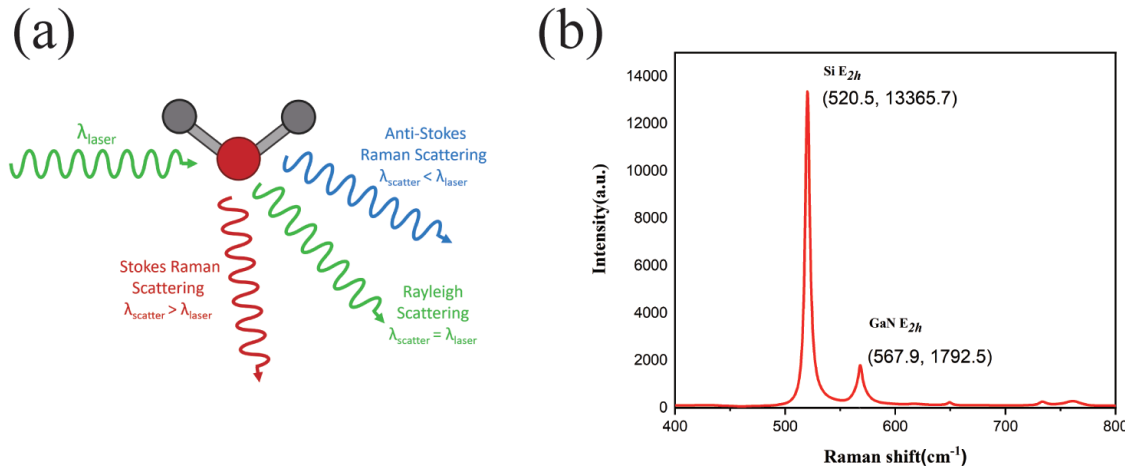


**Fig. 3.20 Principle of Raman spectroscopy and Raman spectroscopy of GaN-on-Si wafers**

In this research, changes in the intrinsic lattice strain between AlGaN, AlN, and GaN layers during the fabrication of MEMS devices can be detected by HORIBA LabRAM HR Evolution Raman spectroscopy, which would greatly affects the material properties and electrical properties of MEMS devices.

### 3.3 Summary

In this chapter, a brief overview of the semiconductor fabrication and characterization equipment used in the manufacturing of GaN power MEMS is given. The equipment is briefly classified according to different functions such as deposition, etching, lithography, etc., and the specific models of the equipment, the basic working principle and the main use in this research are described. The independent processes of these devices with different functions are integrated to complete the preparation of GaN power MEMS, which becomes the basis of process integration in chapter 4.

## **Chapter 4**

# **Process Development and Integration of Power MEMS Devices**

In this chapter, I would develop the corresponding fabrication process parameters and their process integration based on the manufacturing technology and equipment in Chapter Three, thus realizing the whole process from GaN wafer to device. In order to simplify the expression of the process and clarify the steps of the process, this chapter uses different codes to represent the different steps and their meanings. For example MESA.3) indicates that this process is the third step in the mesa preparation process, and [AE-N] indicates the alignment and exposure of negative photoresist. The process that first appears in this chapter would be described in detail about the main purpose of the process, the equipment used, and the detailed recipe parameters and shorthand code, while the same process in the following steps is only represented by the shorthand code. I've listed every step without omission based on shorthand code. Moreover, in order to visualize the fabrication process flow, a corresponding flow chart has been drawn to illustrate the main process steps.

## 4.1 Process flow and recipe

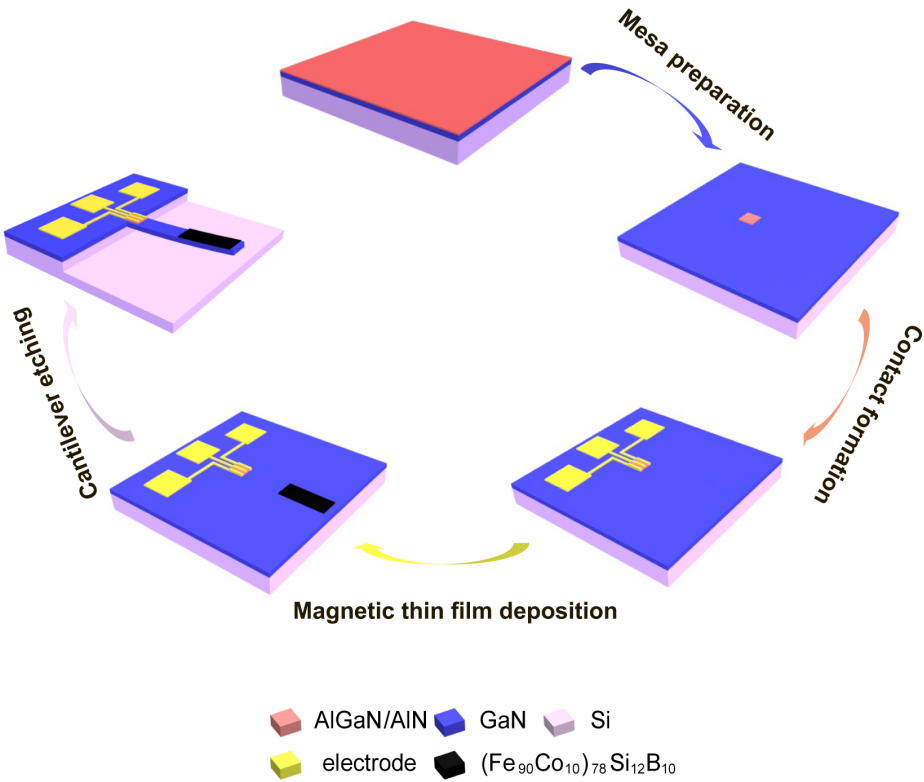


**Fig. 4.1 The schematic diagram of process flow**

The fabrication process flow chart of GaN power MEMS is shown in the Figure 4.1, which can be roughly divided into four main steps. The first step is mesa isolation, and the device is isolated by ICP etching. The second step is to deposit the source, drain and gate metal electrodes to realize the HEMT device. The third step is the deposition of the magnetic thin film at the front end of the cantilever (there is no such step for the SPD device). The fourth step is to etch the cantilever structure. The realization of each step is inseparable from the pattern transfer of photomask, so Figure 4.2 shows the layout (drawn with AutoCAD) during the fabrication. The specific steps will be described in detail in the subsections.



**Fig. 4.2 Layout of GaN power MEMS devices**

### 4.1.1 Wafer growth



**Fig. 4.3 GaN-on-SiC wafer hetero-epitaxial structure**

The epitaxial growth of GaN wafer is a fundamental step in the research of group III nitride semiconductors. Due to the difficulty in obtaining large-scale and high-quality GaN bulk substrates, GaN epitaxial layers are still mainly grown on foreign substrates. The most widely used are sapphire, SiC, and Si, which have a large lattice mismatch with GaN. To address this problem, Amano et al. developed a two-step growth method in 1986. The AlN nucleation layer is first grown at low temperature, and then raised to high temperature to grow GaN layer, which greatly improves the quality of the GaN epitaxial layer [135]. In 1989, Akasaki et al. systematically studied and improved the two-step method, first using low temperature to deposit AlN or GaN as a buffer layer, and then desired GaN material is grown on the buffer layer in a high temperature environment [136].

The hetero-expitaxial structure of 3-inch GaN-on-Si wafer is shown in Figure 4.3. From bottom to top are 1 mm Si(111) substrate, 3.5 ~ 4  $\mu$ m AlN/AlGaN multi-layer buffer layer, 400 ~ 600 nm unintentionally doped (UID) GaN buffer layer, 300 nm intrinsic GaN 2DEG channel layer, 1 nm AlN barrier layer, 20 nm AlGaN barrier layer and 2 nm GaN cap layer.

The lattice mismatch between the Si substrate and the GaN 2DEG channel layer is alleviated by different Al composition of the AlN/AlGaN buffer layer, and the lattice mismatch between the AlN/AlGaN layer and the GaN 2DEG channel layer is further adjusted by the UID GaN buffer layer. The grown wafer exhibits good electrical performance with  $300 \Omega/\text{square sheet}$  resistance,  $1.00 \times 10^{13} \text{ cm}^{-2}$  carrier density,  $2000 \text{ cm}^2/(\text{Vs})$  mobility and  $600 \text{ V}$  breakdown voltage.

#### 4.1.2 Pre-processing

During pre-processing, the dice of size  $2 \times 2 \text{ mm}$  and  $3 \times 3 \text{ mm}$  firstly have been cut from the grown 3-inch wafers with the DISCO DAD3350 automatic dicing saw. Because there are a lot of particles and organic contaminants on the surface of the cut dice, the dice would be then strictly cleaned by cleaning technologies. The recipe is listed here:

**PRE.1)** Wafer dicing [WD].

**PRE.2)** A complete RCA cleaning process ( $\times 1$  time) [WET-RCA].

**PRE.3)** Piranha solution with the  $\text{H}_2\text{SO}_4$  (98%) and  $\text{H}_2\text{O}_2$  (30%) in 7:3 ratios, sonicated for 10 minutes ( $\times 1$  time) [WET-PA].

**PRE.4)** Sonicate in acetone solution for 5 minutes ( $\times 3$  times) [WET-ACE].

**PRE.5)** Sonicate in ethanol solution for 5 minutes ( $\times 3$  times) [WET-ETH].

**PRE.6)** Sonicate in deionized water for 5 minutes ( $\times 3$  times) [WET-DIW].

**PRE.7)** Sonicate in hydrochloric acid for 5 minutes ( $\times 3$  times) [WET-HC].

**PRE.8)** [WET-DIW]

**PRE.9)** Nitrogen gas drying [GD-N].

**PRE.10)** Dry cleaning in PVA TePla IoN 40 plasma cleaner with 80 sccm Oxygen gas and 100 W power for 1 min ( $\times$  1 time) [DC-OX].

### 4.1.3 Mesa preparation

In order to isolate different devices on a single die, mesa isolation, often referred to as active area isolation, is required. We first transfer the active area pattern from photomask to dice by photolithography, and then etch the mesa by ICP-RIE. The size of the active area is  $34 \times 34 \mu\text{m}^2$ , and the photomask is prepared as shown in the Figure 4.4, where the cross pattern marks are mainly used for subsequent overlay alignment. The main steps are as follows:

#### MESA.1) Photoresist coating

Spin coating SUN-9i negative photoresist produced by Suntific Material (Weifang), Ltd. The rotation speed is 500 rpm/min for the first 8 seconds and 5000 rpm/min for the last 40 seconds [PC-N].

#### MESA.2) Post-apply bake

After coating, the resulting resist film will contain between 20% ~ 40% by weight solvent. The post-apply bake process, also called a soft-bake or a pre-bake, involves drying the photoresist after spin coating by removing this excess solvent. The main reason for reducing the solvent content is to stabilize the photoresist film [137]. In this process, the post-apply baking recipe is 110 °C for 60 seconds [PAB-N].

#### MESA.3) Alignment and exposure



**Fig. 4.4 Photomask of active area**

Align and exposure with SUSS MA6 mask aligner, and exposure parameters are as follows: Process: Lithography, Exposure time: 30 seconds, Alignment gap: 50 um, Contact type: Soft, WEC type: Cont, WEC-offset: OFF [AE-N].

#### MESA.4) Post-exposure bake

Post-exposure bake is one method of reducing the standing wave effect [137]. The recipe is 140 °C for 60 seconds [PEB-N].

#### MESA.5) Development

Once exposed, the photoresist must be developed. The aqueous and tetramethyl ammonium hydroxide (TMAH) are commonly used as developers. Development is undoubtedly one of the most critical steps in the photoresist process. The characteristics of the resist-developer interactions determine to a large extent the shape of the photoresist profile and, more importantly, the linewidth control [137]. The development recipe is to first stir and soak in developer solution SUN-238D produced by Suntific Material (Weifang), Ltd for 40 seconds, and then stir and soak in deionized water for 20 seconds [DEV-N].

#### MESA.6) [GD-N]

**MESA.7) [DC-OX]****MESA.8) ICP-RIE etching**

In order to isolate the mesa, all epitaxial layers above the AlN/AlGaN multi-layer buffer layer except the active area must be removed, including UID GaN buffer layer, intrinsic GaN 2DEG channel layer, AlN barrier layer, AlGaN barrier layer and GaN cap layer. The total etching thickness is about 1000 nm. The etching process has been performed with SENTECH SI 500 ICP-RIE and the etching recipe is as follows: Etching gas:  $\text{BCl}_3/\text{Cl}_2/\text{O}_2$  (10/32/5 sccm), Etching power: 550 W, RF power: 100 W. The etching rate is 200 nm/min, and the total etching time is 10 minutes [DE-MESA].

**MESA.9) [WET-ACE]****MESA.10) [WET-ETH]****MESA.11) [WET-DIW]****MESA.12) [GD-N]****MESA.12) [DC-OX]**

#### **4.1.4 Metal-semiconductors contact formation**

After the isolation of the active region, the next step begins to prepare the gate Schottky contact and the source-drain ohmic contact. The source-drain ohmic contact would be prepared first, with an area of  $6 \times 34 \text{ } \mu\text{m}^2$ . By depositing Ti, Al, Ni, Au metals in sequence and undergoing rapid thermal annealing, a good ohmic contact has been formed on the GaN surface. The Schottky contacts are then further formed by depositing Ni and Au, with an area of  $5 \times 34 \text{ } \mu\text{m}^2$ . The prepared gate contact has good control performance on electrons in the channel. For the convenience of subsequent electrical tests, the photomask of the contact also includes a pad with a much larger area (about  $1000 \times 1000 \text{ } \mu\text{m}^2$ ).

**CTC.1) [PC-N]**

**CTC.2) [PAB-N]**

**CTC.3) [AE-N]**

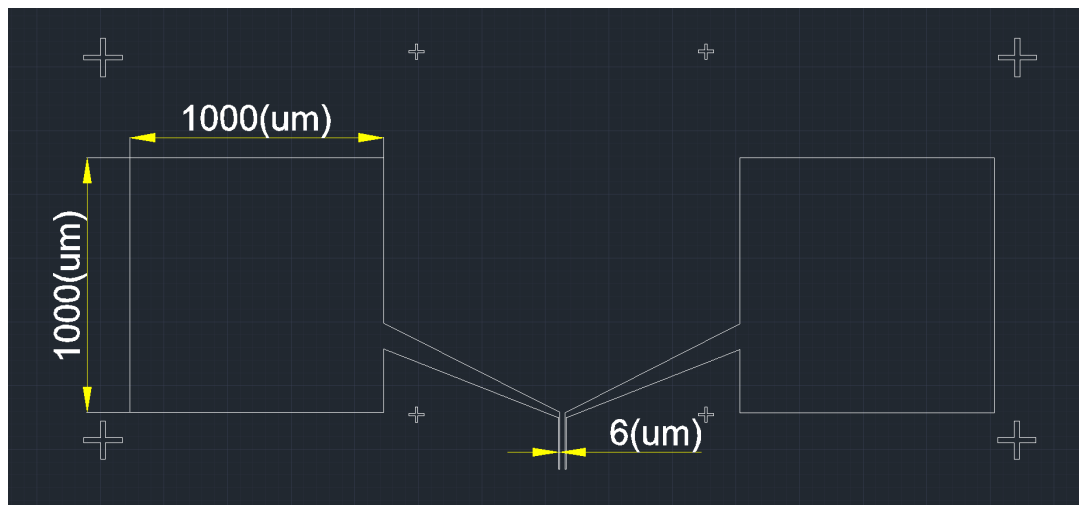


**Fig. 4.5 Photomask of source and drain contact**

**CTC.4) [PEB-N]**

**CTC.5) [DEV-N]**

**CTC.6) [GD-N]**

**CTC.7) [DC-OX]**

**CTC.8) Source-drain metal deposition**

The source-drain contact metal is Ti, Al, Ni, Au. Ti is a barrier metal and must have a work function (3.95 eV) that approximates the affinity potential of GaN (4.11 eV), and therefore is the most widely used barrier metal. Al is a commonly used capping layer, its work function is 4.25 eV, and it can also promote the solid-phase chemical reaction between N atoms and the barrier metal Ti. Ni acts as a diffusion barrier metal, preventing the interdiffusion of the cap layer metal Au and the barrier layer metal Al to the surface

of the GaN material. Au is a stable, low-resistance noble metal ideal for use as a cap layer metal.

In this research, from the bottom (GaN surface) to the top, Ti with a thickness of 20 nm, Al with a thickness of 120 nm, Ni with a thickness of 45 nm, and Au with a thickness of 55 nm have been deposited using Denton Vacuum Explore 14 E-beam evaporation system at deposition rates of 0.5 Å/s, 1 Å/s, 0.5 Å/s and 0.5 Å/s, respectively [DEP-SD].

**CTC.9) [WET-ACE]**

**CTC.10) [WET-ETH]**

**CTC.11) [WET-DIW]**

**CTC.12) [GD-N]**

**CTC.13) [DC-OX]**

**CTC.14) Rapid thermal processing**

Rapid thermal processing (RTP) of the deposited Ti, Al, Ni, Au metal is necessary in order to form an ohmic contact. In this work, rapid thermal annealing at 850 °C for 30 seconds has been performed using a LABSYS RTP-1200 rapid thermal processing system [RTP-OHM].

**CTC.15) [WET-ACE]**

**CTC.16) [WET-ETH]**

**CTC.17) [WET-DIW]**

**CTC.18) [GD-N]**

**CTC.19) [DC-OX]**

**CTC.20) [PC-N]**

**CTC.21) [PAB-N]**

**CTC.22) [AE-N]**

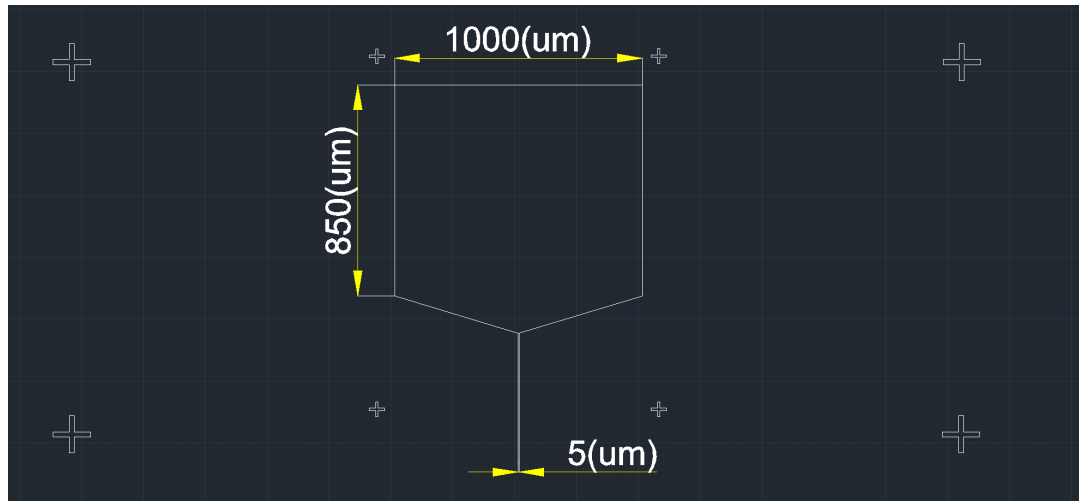


**Fig. 4.6 Photomask of gate contact**

**CTC.23) [PEB-N]**

**CTC.24) [DEV-N]**

**CTC.25) [GD-N]**

**CTC.26) [DC-OX]**

**CTC.27) Gate metal deposition**

The gate contact metal is Ni, Au from the bottom (GaN surface) to the top. Ni with a thickness of 80 nm, and Au with a thickness of 50 nm have been successively deposited using Denton Vacuum Explore 14 E-beam evaporation system at deposition rates of 0.5 Å/s and 0.5 Å/s, respectively [DEP-G].

**CTC.28) [WET-ACE]**

**CTC.29) [WET-ETH]**

**CTC.30) [WET-DIW]**

**CTC.31) [GD-N]**

**CTC.32) [DC-OX]**

Until now, I have prepared an AlGaN/AlN/GaN HEMT device on GaN-on-Si wafer. The active region is  $34 \times 34 \text{ um}^2$ , the gate is a Ti/Au Schottky contact with a width of 5 um, and the source and drain are Ti/Al/Ni/Au ohmic contact with a width of 6 um. The electrical characteristics of HEMT are shown in the Figure 4.7. It can be seen from the figure that HEMT exhibits good Schottky contacts on the gate and ohmic contacts on the source and drain (Figure 4.7c,d). Based on the good electrical contact performance, the output characteristics ( $I_{ds} - V_{ds}$ ) of HEMT have excellent gate control capabilities, as shown in Figure 4.7a. Therefore, the output current exhibits good linearity at low source-drain bias ( $V_{ds}$ ) voltage, and then as the bias voltage further increases, the output current reaches saturation. HEMT can achieve stable large current output in the saturation region, and can be effectively controlled at various gate voltage  $V_{gs}$  from  $-7 \text{ V}$  to  $1 \text{ V}$ . The maximum current density at  $1 \text{ V}$  gate voltage reaches  $304 \text{ mA mm}^{-1}$ , and the maximum transconductance reaches  $42.4 \text{ mS mm}^{-1}$ , showing excellent electrical performance. Moreover, the gate leakage current and source-drain leakage current of HEMT are also within a reasonable range (Figure 4.7e,f).

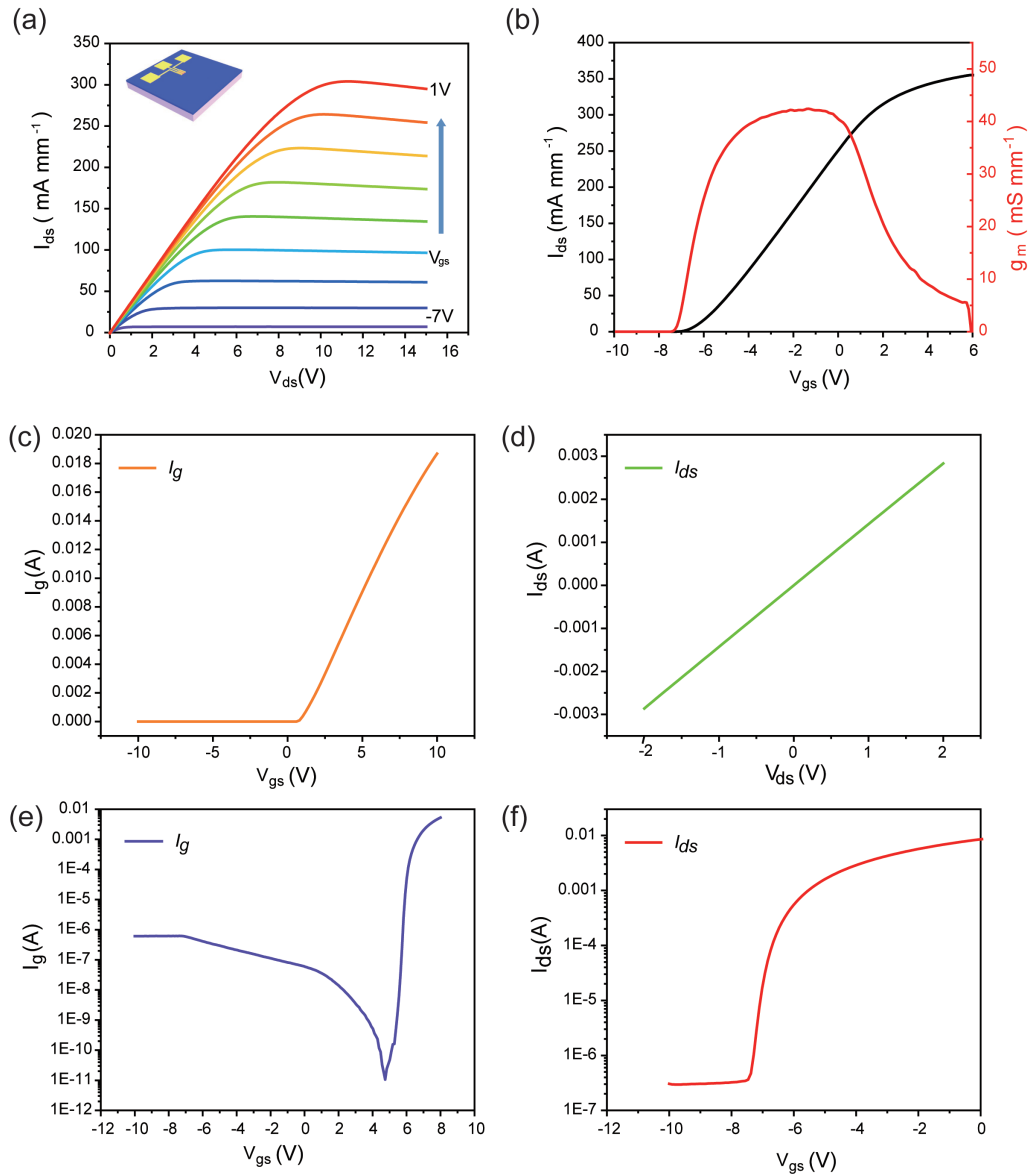


**Fig. 4.7 Electrical performance of fabricated AlGaN/AlN/GaN HEMTs**

#### 4.1.5 Magnetic thin film deposition (For MPD)

Before the preparation of cantilever, there is one more process which is unique to MPD. This process aims to deposit a magnetic thin film on the top half of the cantilever, which can generate magnetic forces in different directions at the front of the cantilever under the action of external

magnetic field. The size of the mask is  $175 \times 60 \text{ }\mu\text{m}^2$ , and it is located in the front half of the cantilever, where the size of the cantilever is  $350 \times 60 \text{ }\mu\text{m}^2$ .

**MAG.1) [PC-N]**

**MAG.2) [PAB-N]**

**MAG.3) [AE-N]**

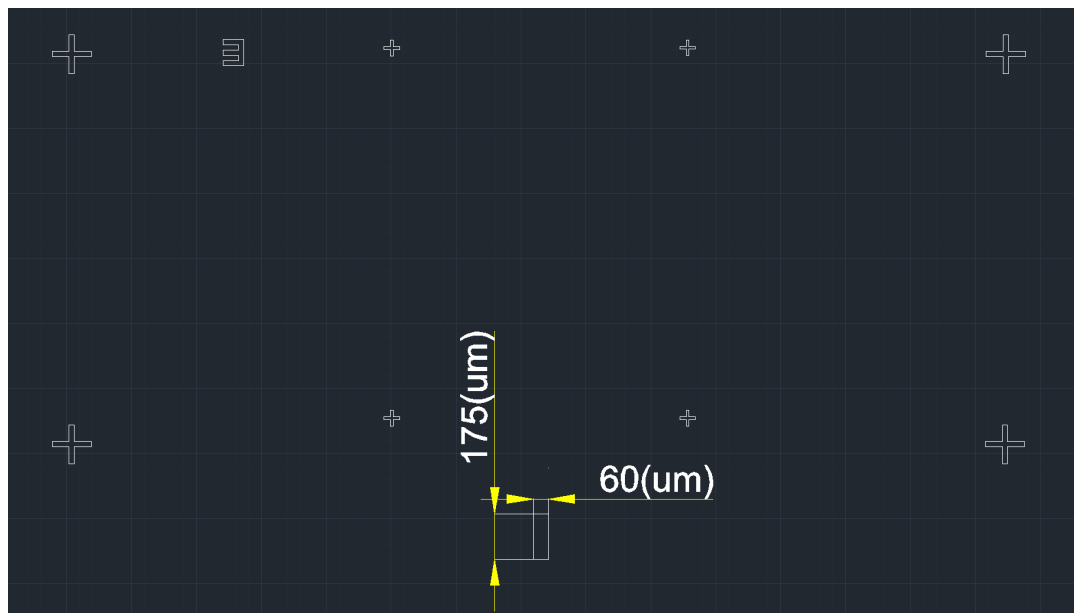


**Fig. 4.8 Photomask of magnetic film**

**MAG.4) [PEB-N]**

**MAG.5) [DEV-N]**

**MAG.6) [GD-N]**

**MAG.7) [DC-OX]**

**MAG.8 Magnetic thin film deposition**

The Denton Discovery 635 magnetron sputtering system has been applied to deposit 500 nm thick magnetic thin film  $(\text{Fe}_{90}\text{Co}_{10})_{78}\text{Si}_{12}\text{B}_{10}$ . The recipe is as follow: DC

sputtering, Gas: Ar 135 sccm, Power: 400 W, Pressure: 7.2 mtorr. The deposition rate is 15 nm/min, and the deposition time is 33.3 min [DEP-MAG].

**MAG.9) [WET-ACE]**

**MAG.10) [WET-ETH]**

**MAG.11) [WET-DIW]**

**MAG.12) [GD-N]**

**MAG.13) [DC-OX]**

#### **4.1.6 GaN cantilever preparation**

Finally, the ICP-based dry etching has been performed by combining the anisotropic/isotropic etching to fabricate the cantilever. The main steps of the etching process are as follows: Step 1: anisotropic etching of photoresist patterned GaN (thickness: 5 µm). Step 2: isotropic etching of Si to release the cantilever. The manufactured cantilever has dimensions of 350 × 60 × 5 µm<sup>3</sup>. For the final fabricated MEMS devices, the SPD has only a single cantilever, while the MPD has a cantilever with a magnetic thin film in the front half end.

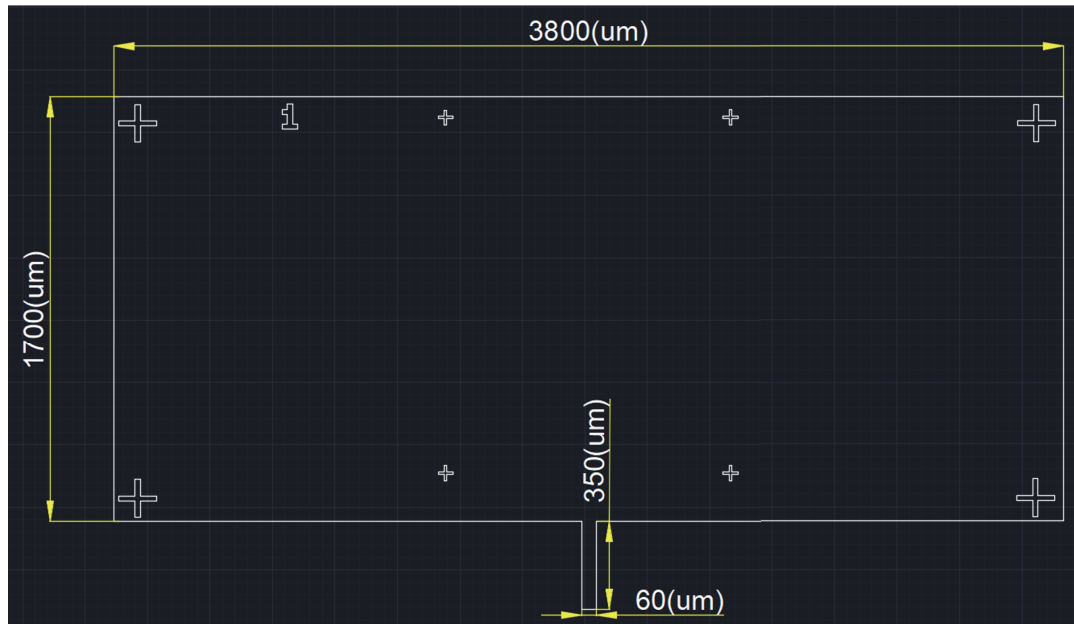
**CAN.1) Photoresist coating**

Spin coating AZ4620 positive photoresist produced by Suntific Material (Weifang), Ltd. The rotation speed is 500 rpm/min for the first 8 seconds and 3500 rpm/min for the last 60 seconds [PC-P].

**CAN.2) Post-apply bake**

The pre-baking recipe is 95 °C for 3 minutes [PAB-P].

**CAN.3) [PC-P]**

**CAN.4) [PAB-P]****CAN.5) Alignment and exposure****Fig. 4.9 Photomask of GaN cantilever**

Align and exposure with SUSS MA6 mask aligner, and exposure parameters are as follows: Process: Lithography, Exposure time: 54 seconds, Alignment gap: 30  $\mu\text{m}$ , Contact type: Soft, WEC type: Cont, WEC-offset: OFF [AE-P].

**CAN.6) Development**

The developing recipe is firstly immersed in a 3:1 solvent of deionized water and developer solution AZ-400K produced by Santaifu Materials (Weifang), Ltd, and then stirred and immersed in deionized water. The time needs to be determined in real time according to the real-time observation of the optical microscope (about 4 ~ 5 min) [DEV-P].

**CAN.7) [GD-N]****CAN.8) [DC-OX]**

**CAN.9) ICP-RIE etching**

To fabricate the cantilever, an anisotropic etching must first be performed to etch the GaN, AlN and AlGaN layers, and then an isotropic etching of Si must be performed to release the cantilever. The etching process is performed with SENTECH SI 500 ICP-RIE. Firstly, the GaN etching recipe is as follows: Etching gas:  $\text{BCl}_3/\text{Cl}_2/\text{Ar}$  (10/32/5 sccm), Etching power: 550 W, RF power: 100 W. The etching rate is 200 nm/min, and the total etching time is 25 min. Secondly, the Si etching recipe is as follows: Etching gas:  $\text{SF}_6/\text{O}_2/\text{Ar}$  (30/5/10 sccm), Etching power: 800 W, RF power: 50 W. The lateral etching rate is 2  $\mu\text{m}/\text{min}$ , and the total etching time is 25 min [DE-CAN].

**CAN.10) [DC-OX]**

In this section, I have successfully prepared the GaN power MEMS devices with cantilever structure. The electrical characteristics of MPD are shown in the Figure 4.10. MPD exhibits electrical properties similar to HEMT. However, compared with HEMT, the current of MPD under the bias voltage of 10 V is reduced by  $60.5 \text{ mA mm}^{-1}$ . The gate leakage current and source-drain leakage current of MPD are also slightly larger than HEMT, as shown in Figure 4.10e,f. Furthermore, the transfer ( $I_{ds} - V_{gs}$ ) characteristics of the MPD at  $V_{ds} = 10 \text{ V}$  has also been measured. The maximum transconductance ( $g_{m,max}$ ) of MPD is  $32.9 \text{ mS mm}^{-1}$  (Figure 4.10b), while the value for the HEMT can reach  $42.4 \text{ mS mm}^{-1}$  (Figure 4.7b). Therefore, the transconductance performance of MPD is also slightly lower than HEMT due to the performance degradation caused by dry etching process.

It can be concluded that, compared with the HEMT device before etching, the performance of the MPD device is reduced by about 30%. This is because the long-term ICP etching weakens the contact performance of the electrode, and the removal of the Si substrate releases the lattice strain of AlGaN/AlN/GaN heterojunction. This is also because the dry etching process has caused damage to the lattice structure of the material. The performance degradation of MEMS devices before and after etching is discussed in detail in the next subsection.

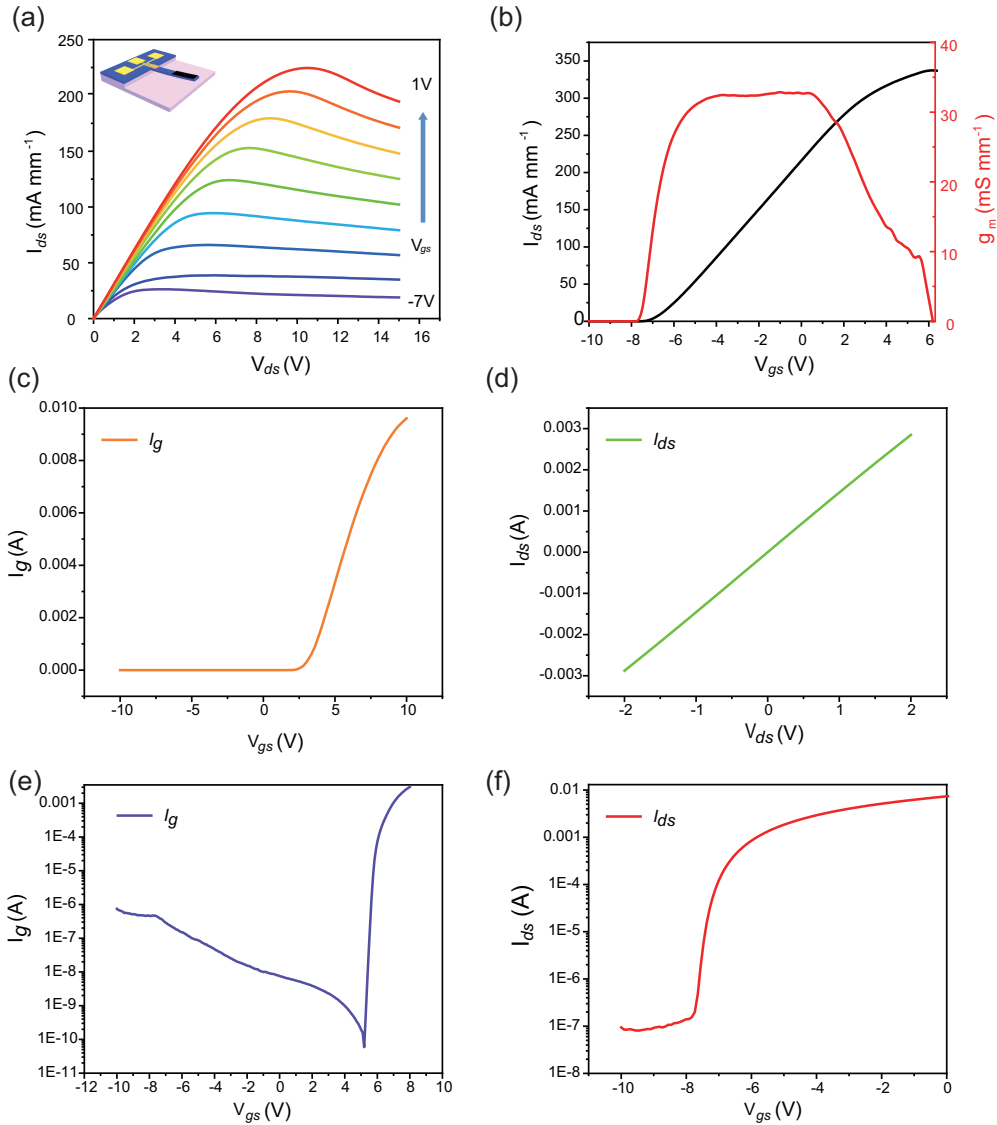


**Fig. 4.10 Electrical performance of fabricated MPD**

## 4.2 Mechanisms of process-induced performance degradation

This section briefly discusses the physical mechanisms of MEMS device performance degradation before and after the ICP-RIE etching process. By means of Raman spectroscopy and

literature review, the effects of lattice strain release and introduction of lattice defects during the cantilever fabrication process on device performance have been revealed respectively.

#### 4.2.1 Lattice strain relief and piezoelectric effect

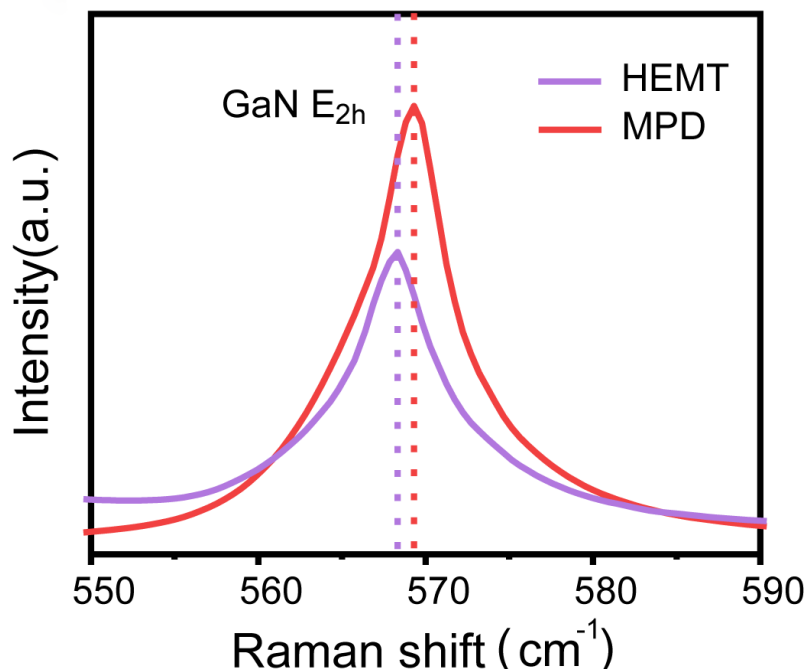


**Fig. 4.11 Raman spectroscopy of fabricated HEMT and MPD**

In order to reveal the physical mechanism of process-induced performance loss, the Raman spectroscopy tests on both HEMT and MPD at room temperature have been performed to explain the influence of the ICP dry etching process on the electrical performance of MEMS, as shown in Figure 4.11. It exhibits that the  $E_{2h}$  phonon mode of MPD shows a blue shift from  $568.31\text{ cm}^{-1}$  to  $569.33\text{ cm}^{-1}$  compared with the HEMT, which reveals that the dry etching process releases the silicon substrate and relaxes the tensile strain of the GaN layer [138, 29]. The relationship between the biaxial stress and the shift of the Raman phonon frequency is

shown in Equation 4.1

$$\sigma_a = \frac{\Delta\omega}{K_{RS}^{E2(high)}} \quad (4.1)$$

where  $\sigma_a$  is the in-plane biaxial stress,  $\Delta\omega$  is the shift of the Raman phonon frequency, and  $K_{RS}^{E2(high)}$  is the Raman biaxial stress conversion factor. We can obtain that the tensile strain of the GaN epitaxial layer is reduced by 352 MPa compared with that on the Si substrate [139]. According to the piezoelectric effect, the removal of the Si substrate partially releases the lattice strain of the GaN layer, thereby changing the piezoelectric polarization charge of the GaN layer, adjusting the energy band of the heterostructure, and finally reducing the density of 2DEG in the AlGaN/AlN/GaN heterojunction.

#### 4.2.2 Lattice defects and Schottky contact degradation

In addition, a large number of lattice defects have also been introduced during the dry etching process, which reduces the electrical performance of MPD to a certain extent [140–142]. Moreover, it has been reported that the ICP etching could introduce lattice defects and surface state to the AlGaN/AlN/GaN heterojunction and massive damage to contact electrode, which will form electron trap levels. This will result in the increase of ideality factor and the leakage current, thereby significantly reducing the gate control ability [143–146]. Last but not least, the etching of the Si substrate under the cantilever will also greatly weaken the heat dissipation in the active area. All these effects enhance the self-heating effect of the MEMS device, thus impairing the output current performance [147–149].

In summary, ICP dry etching could inevitably degrade the performance of MEMS during the preparation of the cantilever. Comparing the performance of MPD and HEMT, it can be concluded that due to the ICP etching process in the cantilever fabrication process, the electrical performance of MPD has been degraded to a certain extent compared to HEMT devices. It has shown that this performance degradation is unavoidable in the process of fabricating cantilever

structures using the ICP process, but we have improved the performance degradation during cantilever fabrication through process optimization. Compared to the electrical performance of SPD in chapter 5, the electrical performance of MPD in chapter 6 has been greatly improved, which is detailed in the process optimization subsection.

## 4.3 Process optimization

Since the successful preparation of SPD, the huge performance loss of SPD before and after etching has been the biggest process problem. How to significantly improve the performance of MEMS devices in the preparation of MPD has become the primary issue. After persistent experiments and analysis, I finally succeeded in finding a process optimization method that greatly improves the performance of MEMS devices. The core idea is how to protect the active area and electrode contacts of MEMS during long-time cantilever ICP-RIE etching. Therefore, starting with photoresist coating and ICP-RIE etching, two complementary optimized processes have been developed.

### 4.3.1 Positive photoresist double coating process

In this process, we need to choose a suitable photoresist as the etching mask for the cantilever and increase the withstanding time during the ICP etching. Because the ICP etching time of cantilever is so long that the ordinary photoresist mask can not withstand, here I choose AZ4620 positive photoresist produced by Suntific Material (Weifang), Ltd. Moreover, photoresist needs to be thick or hard enough to be used as an etching mask. There could be two main methods here. One method is to spin coat the photoresist twice to increase the thickness of the photoresist, and the other one is to harden the photoresist in some ways. I choose the first method here, and maybe explore the second method in the future. The first spin coating velocity is 3500 rpm/min, and the coating time is one minute. After post-apply bake for 3 min-

utes at 95 °C, the thickness of photoresist is about 9  $\mu\text{m}$ . Then spin coat at 3500 rpm/min for another one minute and bake for 3 minutes at 95 °C again. The total thickness of photoresist is about 18  $\mu\text{m}$  now, and is thick enough to withstand long-time ICP etching.

### 4.3.2 GaN cantilever ICP-RIE etching process

In this process, how to maximize the withstanding time of photoresist during the ICP etching process is the most important issue. Since plasma etching will generate extremely high heat which will greatly reduce the hardness of the photoresist, it is necessary to apply silicone oil to the bottom of the wafer before etching to enhance heat dissipation. Furthermore, it is significant to carefully control the chamber temperature. Through the alternate etching steps of short-time etching and long-time cooling, the temperature in the chamber is maintained at no more than 10 °C.

The etching condition of the cantilever can be judged by optical microscope and SEM, and the judgment method of optical microscope is more convenient and has been introduced here. Because the band gap of GaN, AlN, and AlGaN is larger than the energy of visible light, AlGaN, AlN, and GaN are all transparent and we can directly observe the Si substrate through an optical microscope. When etching Si isotropically, we can observe the real-time situation of lateral etching of Si under the GaN cantilever, and judge the etching process of the cantilever in real time.

These optimized processes have successfully realized cantilever structure MEMS devices with excellent electrical performance, which has become the most important process in the fabrication of GaN power MEMS devices.

## **4.4 Summary**

In this chapter, I use the processing equipment described in chapter 3 to introduce the fabrication process and process flow of GaN power MEMS devices in detail. There are six main parts in the preparation process, and a total of about eighty specific steps. The purpose, recipe, and precautions of each process are briefly described. The description of repetitive processes is simplified by means of process integration, and therefore the logical structure of the fabrication process is highlighted. More importantly, the physical mechanism and process optimization of performance degradation during MEMS device fabrication are analyzed. As a result, high-performance GaN HEMTs and GaN power MEMS devices have been successfully fabricated.

# **Part III**

# **Devices**

# **Chapter 5**

## **Strain-Controlled Power Devices**

### **5.1 Background and motivation**

With the rapid development of artificial intelligence (AI), innovative science and technologies are emerging, such as the intelligent robots and autonomous driving technologies [150, 151], which have greatly changed our lives. In the process of researching novel MEMS devices for emerging AI applications, nature has provided us with many inspiring examples [152, 153]. In recent years, with the increasing maturity of biomimicry research, researchers are developing biomimetic smart devices or systems [154, 155], such as electronic skins [156], electronic noses [157], cochlear implants [158, 159], prosthetics [160], and artificial larynx [161]. As an important part of emerging AI smart devices, the research on biomimetic MEMS devices integrating "perception" - "thinking" - "execution" has also developed rapidly, and researchers have developed novel biomimetic MEMS vector hydrophones [162], bionic MEMS electronic stethoscope [163], high-resolution ocean turbulence sensor based on MEMS bionic structure [164], and MEMS based on biological sensory system for bionic human [165] and so on, which has greatly promoted the development of new smart MEMS devices in the era of artificial intelligence.

In practical applications, conventional sensor-actuator systems (eg, pressure sensors) typically employ sensing elements and varistors to convert mechanical signals (eg, displacement, velocity, and acceleration) into electrical signals (eg, voltage and current) ). However, the conversion process inevitably requires complex circuit modules, including analog-to-digital (A/D) or digital-to-analog (D/A) converters, strong/weak current isolation, and CPU control. To date, AI systems have been primarily programming-based and rely on computer-controlled electronics, known as unsupervised systems. In addition, some complex AI systems still rely on human judgment and decision-making during operation, which are called supervised systems. It has been a long-standing challenge to design and fabricate power devices that can achieve real-time unsupervised/supervised responses to changes in the external environment in AI systems. With the rapid development of driverless and intelligent robot technology, AI devices in self-driving cars and robot attitude balance control need to be able to control the output power in real time in a fast-response manner according to external stimuli. Therefore, in the future practical application of AI technology, new power MEMS devices that can directly modulate the output power by external stimuli under unsupervised/supervised conditions are highly desired. Driven by this challenge, combined with recent research advances in biomimicry, researchers have attempted to draw inspiration from biology to develop new smart power MEMS devices.

In the traditional field of power electronics, III-V wide-bandgap semiconductor materials with both semiconductor and piezoelectric properties have very broad application prospects. Among them, AlGaN/AlN/GaN high electron mobility transistor (HEMT) has become an important power component in switching elements due to its high carrier density, high electron mobility and large breakdown electric field [166, 167]. Based on the piezoelectric properties of the AlGaN/AlN/GaN heterojunction, the piezoelectric polarization charges generated at the interface due to lattice strain can significantly modulate the concentration of two-dimensional electron gas (2DEG) in the potential well. In recent years, some research teams have reported that strain-induced piezoelectric polarization charges in HEMT can be introduced at the local

interface through the action of external stress, thereby further modulating 2DEG concentration and electrical transport properties. This coupling effect of semiconductor and piezoelectric properties is called the piezotronics effect, which has been widely used in the research of nanowires [168], sensors [169] and HEMTs [33]. In this study, we designed a cantilever HEMT device based on AlGaN/AlN/GaN heterojunction inspired by the bionic research on the reflection mechanism of the human body. Real-time control of the electrical conductivity and output power of the device by external excitation is realized, and a novel strain-regulated power MEMS device is fabricated.

In this chapter, we design a strain modulated power MEMS device (Strain-controlled Power Device, SPD), which uses external strain to modulate the output power of the device by simulating the reflection process of the human body. As shown in Figure 5.1a, when the thigh muscles of the knee receive external stimulation, action potentials in sensory neurons are sent to the gray matter of the spinal cord. Sensory neurons in the spinal cord make direct synaptic connections with motor neurons. If the signal is strong enough, the action potential of the motor neuron can be triggered, causing the knee-jerk reflex. In addition, the knee jerk reflex is a spinal reflex that is centered in the spinal cord but still regulated by the higher central nervous system (brain) [170]. Figure 5.1b shows the schematic diagram of the SPD, which has a high sensitivity response to external stress due to the design of the cantilever structure, and a high output power due to the excellent electrical properties of the HEMT device based on the AlGaN/AlN/GaN heterojunction. The external stress applied to the end of the cantilever in SPD can simulate the mechanical stimulation of human body reflex, and the output power of the SPD can be controlled by inputting the mechanical stimulation. In the actual application process of the device, the external stress can significantly modulate the output power within a certain amplitude, and the gate voltage can ultimately control the output power value in a large range, which means that the working mechanism of the strain-modulated power is programmable. This work not only provides new insights into novel MEMS devices that directly control out-

put power based on mechanical stimulation, but could also facilitate the development of smart power MEMS devices similar to human body reflexes. SPD has broad application prospects in various fields such as autonomous driving, robot control system and human-machine interface.

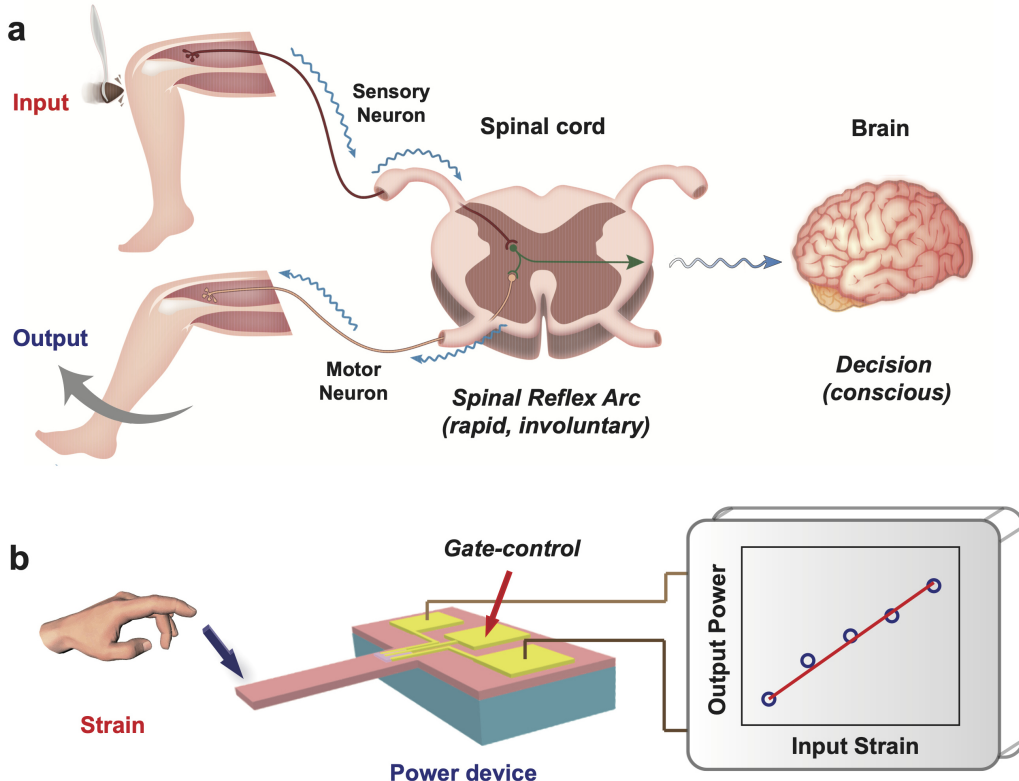


**Fig. 5.1** Concept of strain-controlled power device (SPD) as inspired by human reflex

## 5.2 Design and preparation

### 5.2.1 Device structure and characterization

The SPD is designed by using the AlGaN/AlN/GaN heterojunction in a cantilever architecture, as schematically shown in Table 5.1 and Figure 5.3a. The enlarged part is the schematic cross-section of the AlGaN/AlN/GaN heterostructure. The thicknesses of AlGaN, AlN, and GaN layers are 30 nm, 1 nm and 4.3 um, respectively. The detailed fabrication process is described

in the subsection 5.2.2. The cantilever-based structure of the as-fabricated SPD is clearly shown in the scanning electron microscopy (SEM) images of Figure 5.3b. And the inset illustrates the geometry of gate and source-drain contacts.

**Table 5.1 Structure parameters of the HEMT and SPD**

SPD design	Material	Length (um)	Width (um)	Thickness (nm)
Cantilever	GaN	350	50	5000
HEMT	AlGaN/AlN/GaN	27	27	30/1/4300

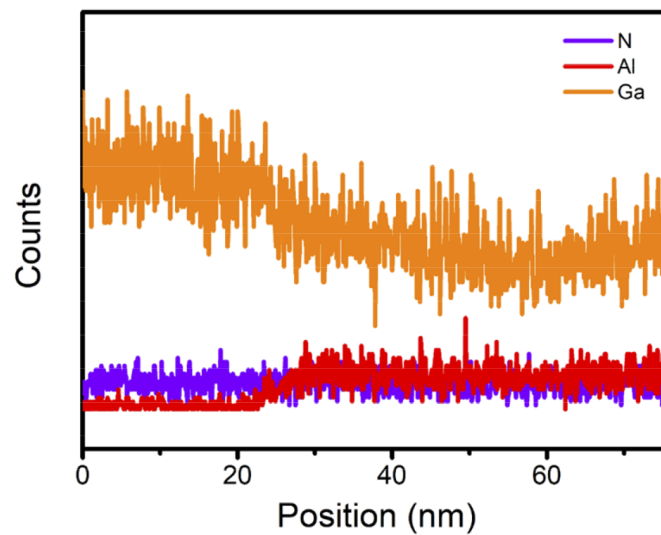


**Fig. 5.2 EDX line profiles for the element of Ga (orange), Al (red), and N (purple)**

The high-angle annular dark-field scanning transmission electron microscopy (HAADF-STEM) images (Figure 5.3c) exhibit the AlGaN/AlN/GaN heterostructure. Furthermore, the energy-dispersive X-ray spectroscopy (EDX) elemental mapping (Figure 5.3c) confirms the existence and corresponding distributions of the elements of Ga, Al, and N. The detailed structural information of the AlGaN/AlN/GaN heterostructure is investigated by high-resolution

transmission electron microscopy (HRTEM) and selected area electron diffraction (SEAD) (inset of Figure 5.3d). The interfaces atoms of AlGaN/AlN and AlN/GaN are uniform and sharp without apparent boundary defects or dislocations. The layers of GaN, AlN, and AlGaN can be easily identified, corresponding to the (0002) plane. Additionally, the corresponding line profile extracted from EDX mapping is presented in Figure 5.2, confirming the variation of chemical compositions.

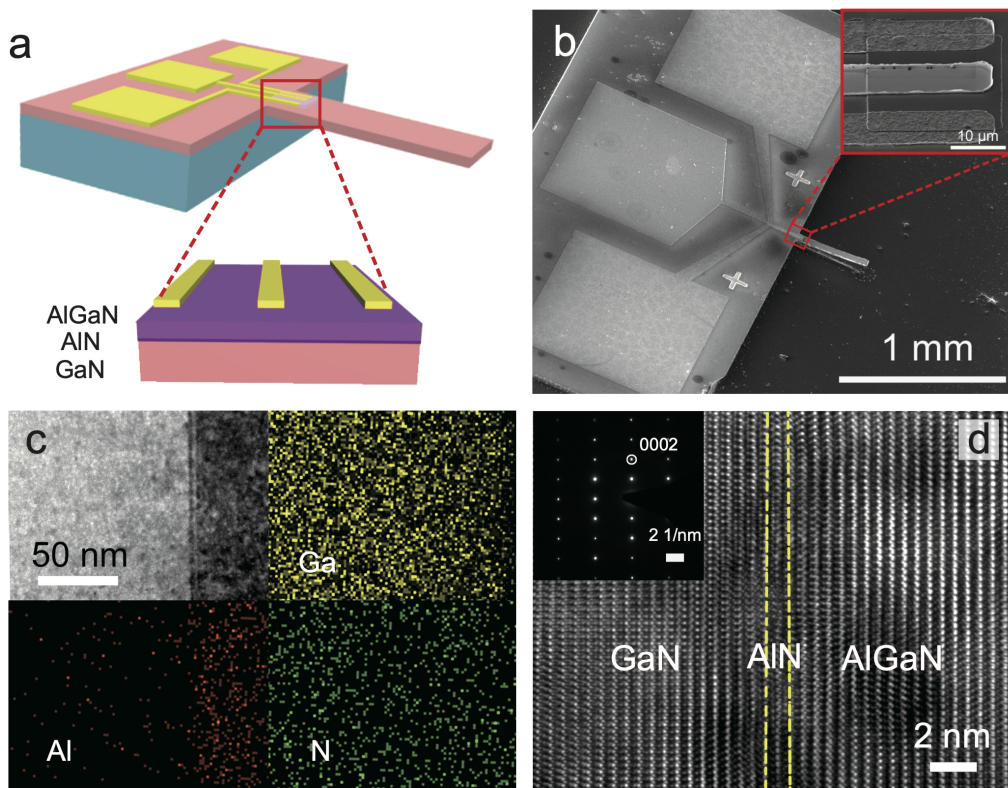


**Fig. 5.3 Structure and material characterizations of the SPD. (a) Schematic illustration and (b) SEM image of the SPD. (c) Cross-sectional HAADF-STEM image and the EDX element mapping, as well as the (d) TEM image of the AlGaN/AlN/GaN hetero-stacks.**

### 5.2.2 Fabrication processes

We develop a fully dry etching process by using the inductively coupled plasma etching (ICP) to fabricate the GaN-based cantilever, and the details of the ICP-based dry etching steps are

schematically shown in Figure 5.4. The two key procedures are illustrated as follows: (i) trenches are fabricated by anisotropic etching of GaN/Si (Figure 5.4b). The photoresist patterned GaN thin film (thickness: 5  $\mu\text{m}$ ) was completed etched by using the anisotropic etching recipe ( $\text{BCl}_3/\text{Cl}_2/\text{Ar}$ : 10/32/5 sccm; Power: 550 W; Process time: 20 min); (ii) the cantilever structure is laterally released by isotropic etching of Si (Figure 5.4c). The cantilever structure was fabricated with the isotropic etching recipe ( $\text{SF}_6/\text{O}_2/\text{Ar}$ : 30/5/10 sccm; Power: 800 W; Process time: 25 min). The manufactured cantilever had dimensions of  $350 \times 50 \times 5 \mu\text{m}^3$ , with the embedded HEMT had a mesa dimension of  $27 \times 27 \mu\text{m}^2$  and a gate length of 5  $\mu\text{m}$ . The anisotropic / isotropic etching steps can be easily controlled by simply adjusting the etching recipe (e.g., gas mixture, power, and time). The presented fully dry etching process has many unique advantages including precise control, well-aligned shape, less-contaminated, and easily-integrated into Si-based circuits.

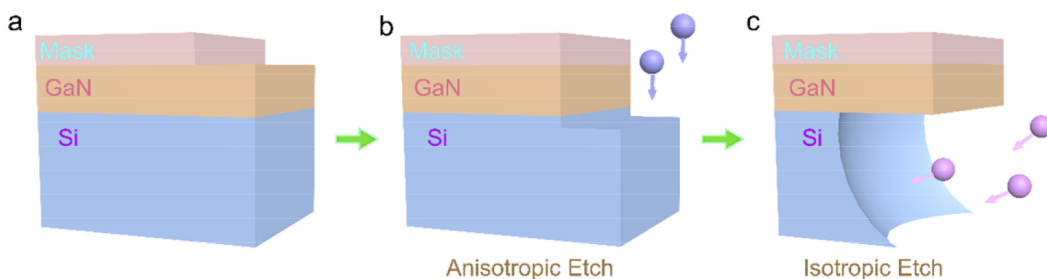


**Fig. 5.4 Etching process flow chart of the SPD. (a) Patterning the cantilever with positive photo resist. (b) Fabricating a trench by anisotropic etching of GaN/Si. (c) Releasing the cantilever structure by isotropic etching of Si.**

The SPD was fabricated using III-Nitride epitaxial layers by metal-organic chemical vapor deposition (MOCVD) on Si substrate (111) with the 2DEG sheet density of  $8 \times 10^{12} \sim 1 \times 10^{13} \text{ cm}^{-2}$ . The epitaxial layer structure consists of AlGaN (30 nm, 30% Al) / AlN (1 nm) / GaN (4.3  $\mu\text{m}$ ) / AlGaN buffer layer / Si substrate. The mesa and cantilever patterns were etched using an inductively coupled plasma etching system (ICP, SENTECH SI 500) etch process based on  $\text{BCl}_3/\text{Cl}_2/\text{Ar}$  and  $\text{SF}_6/\text{O}_2/\text{Ar}$ . Ti/Al/Ni/Au (20 nm / 120 nm / 45 nm / 55 nm) metal stack depo-

sition was evaporated using electron beam evaporation system (Denton Vacuum Explore 14) and annealed at 850 °C in N<sub>2</sub> environment for 30 s to form an ohmic contact using a rapid thermal processing system (LABSYS RTP-1200). Ni/Au (80 nm / 50 nm) was evaporated for gate metallization to form Schottky contacts. Finally, the ICP-based dry etching was performed by combining the anisotropic/isotropic etching to release the cantilever, as schematically illustrated in Figure 5.4. The fabrication process flow is detailed in Figure 5.5.

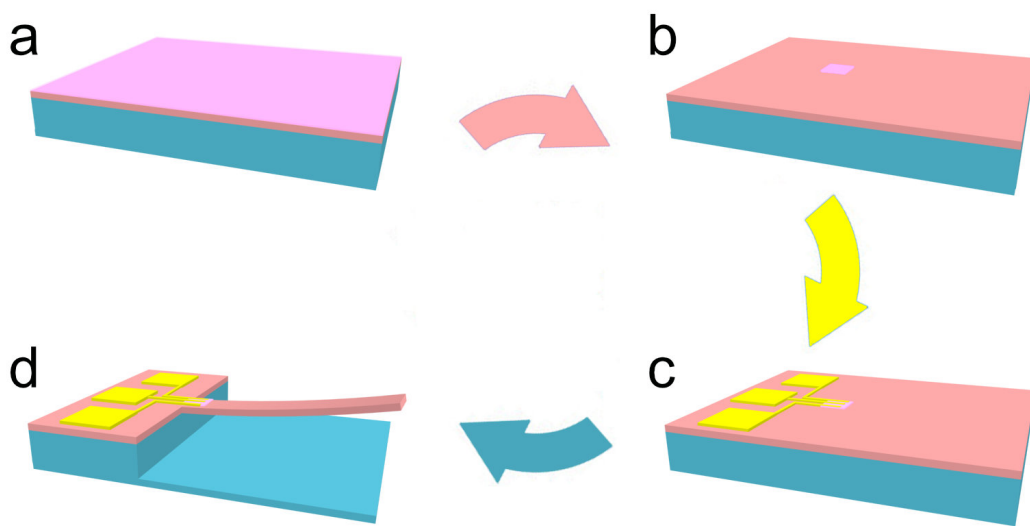


**Fig. 5.5 Fabrication process flow chart of the SPD. (a) A diced chip with AlGaN/AlN/GaN epilayers grown on Si substrate. (b) The mesa etching of AlGaN, AlN and GaN by ICP. (c) Deposition of Ohmic contact and Schottky contact. (d) Cantilever preparation by ICP etching.**

## 5.3 Device performance

### 5.3.1 Electrical performance

The measured contact characteristics of the source-drain contact and gate contact of the SPD and the HEMT are shown in Figure 5.7a, b and Figure 5.6a, b, respectively. Both the SPD and the HEMT exhibit typical Ohmic and Schottky contacts. Based on the suitable contacts,

the output characteristics ( $I_{ds}$ - $V_{ds}$ ) of the SPD and the HEMT show good capability of gate-control, as respectively shown in Figure 5.8a and Figure 5.6c. The output characteristics show a distinct linear region at a low source-drain bias ( $V_{ds}$ ), and then the drain current approaches saturation with further increasing of the drain bias. Large output currents are achieved in both SPD and HEMT and can be effectively controlled at various  $V_{gs}$  of  $-5$  V to  $1$  V. When compared to the HEMT, the SPD shows a reduced current of  $60$  mA mm $^{-1}$  at  $10$  V because of its suffering from strain partial release and more dry etching process. Furthermore, the transfer ( $I_{ds}$ - $V_{gs}$ ) characteristics of the SPD and the HEMT at  $V_{ds} = 6$  V are shown in Figure 5.8b and Figure 5.6d, respectively. The maximum transconductance ( $g_{m,max}$ ) of  $7.5$  mS mm $^{-1}$  is measured in the SPD (Figure 5.8b), while the value for the HEMT can reach  $52$  mS mm $^{-1}$  (Figure 5.6d).

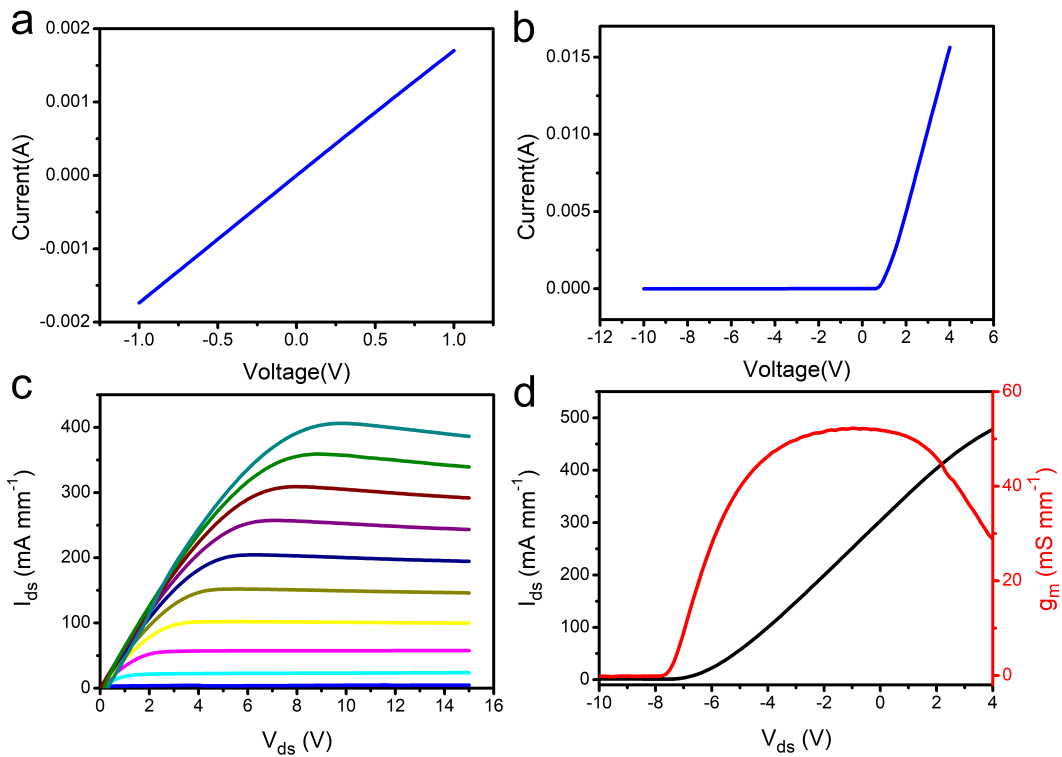


**Fig. 5.6 Electrical performance of the HEMT. (a) Ohmic contact characteristics. (b) Schottky contact characteristics. (c) Output characteristics. (d) Transfer characteristics**

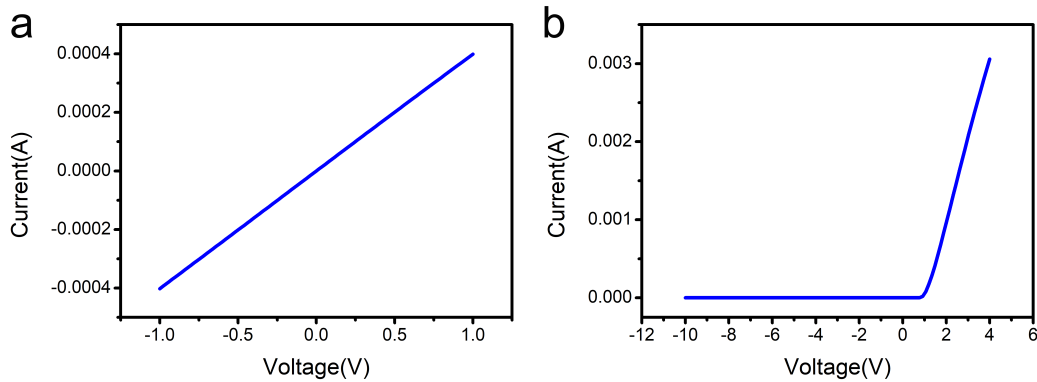


**Fig. 5.7 Contact characterizations of the SPD (a) Ohmic contact curve. (b) Schottky contact curves.**

To further investigate the reason for the degradation of SPD performance before and after etching, we measured the micro-Raman spectra of SPD and HEMT at room temperature (Figure 5.8c). It can be seen that the  $E_{2h}$  phonon mode peak of GaN in SPD shows a blue-shift of Raman phonon frequency from 566.8 to 569.2  $\text{cm}^{-1}$  compared to HEMT. It revealed that the ICP etching process during the fabrication of the cantilever induces tensile strain relaxation of the GaN layer [138], which is due to the lattice mismatch between the III-V nitride and the silicon substrate. The lattice constant of GaN typically is 3.189 Å, while Si has a lattice constant of 5.43 Å, which results in severe tensile strain in the GaN layer [171]. Due to the strong piezoelectric effect of III-V nitrides, lattice strain can generate corresponding piezoelectric polarization charges at the interface of the GaN layer, thereby modulating the energy band structure of the AlGaN/AlN/GaN heterojunction, and ultimately affecting the carrier concentration and other electrical properties in heterojunctions. Therefore, when the Si substrate is removed by an isotropic etching process, the tensile strain of the GaN layer is partially released [139], which significantly weakens the piezoelectric polarization charge density and reduces the 2DEG concentration in AlGaN/AlN/GaN interface [36]. On the other hand, since the ICP etching time is as long as 45 minutes in the cantilever fabrication process, the long etching time will introduce a large number of defects in the SPD lattice [140–142, 172, 145], thus re-

ducing the electrode contact performance in the SPD active area. It will also degrade the final electrical performance to some extent. Therefore, how to protect the SPD during the long-time etching process is the key to improve the device performance. In the process of MPD device preparation in chapter 6, we propose a method of applying multi-layer photoresist to further protect the active area of MPD device during the etching process, and the experimental results show that the device performance of MPD has been significantly improved. The relevant discussion will be expanded in chapter 6.

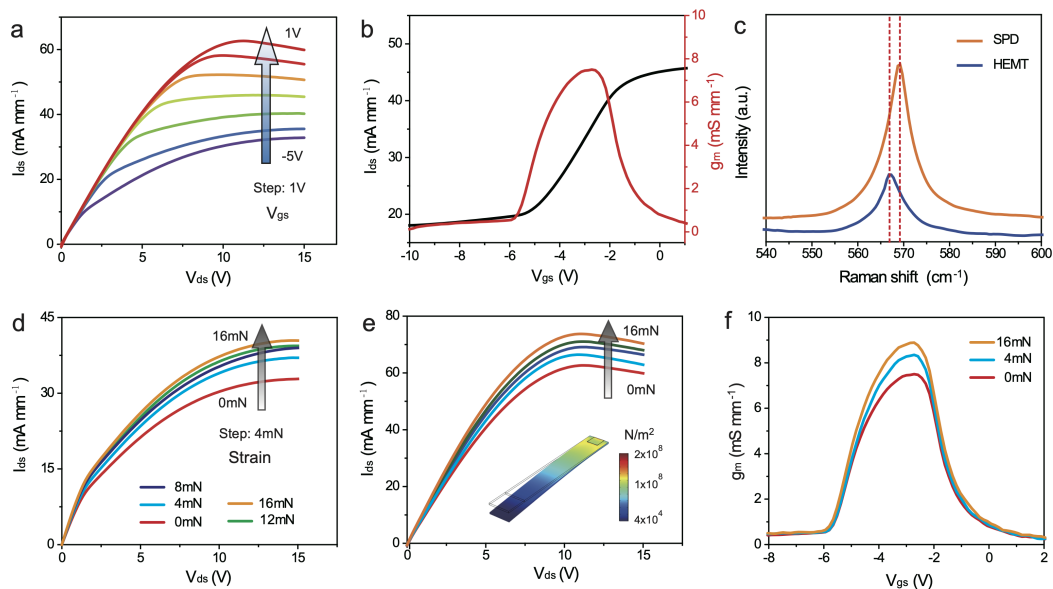


**Fig. 5.8 Electrical performance of the SPD.** (a) Output characteristics. (b) Transfer characteristics. (c) Spatial Raman spectra of the AlGaN/AlN/GaN heterostructures before (HEMT) and after (SPD) dry-etching. (d), (e) Output characteristics under external strain from 0 ~ 16 mN, with the gate voltage  $V_{gs}$  of (d) -5 V and (e) 1 V, respectively. The inset of (e) illustrates the strain distribution of the SPD under an external strain of 16 mN. (f) The transconductance under various external strain.

### 5.3.2 Strain-power modulation performance

Based on the piezotronics effect, the output power of the SPD can be effectively modulated by external mechanical stimulus in real time. The external strain is loaded on the free-end of the

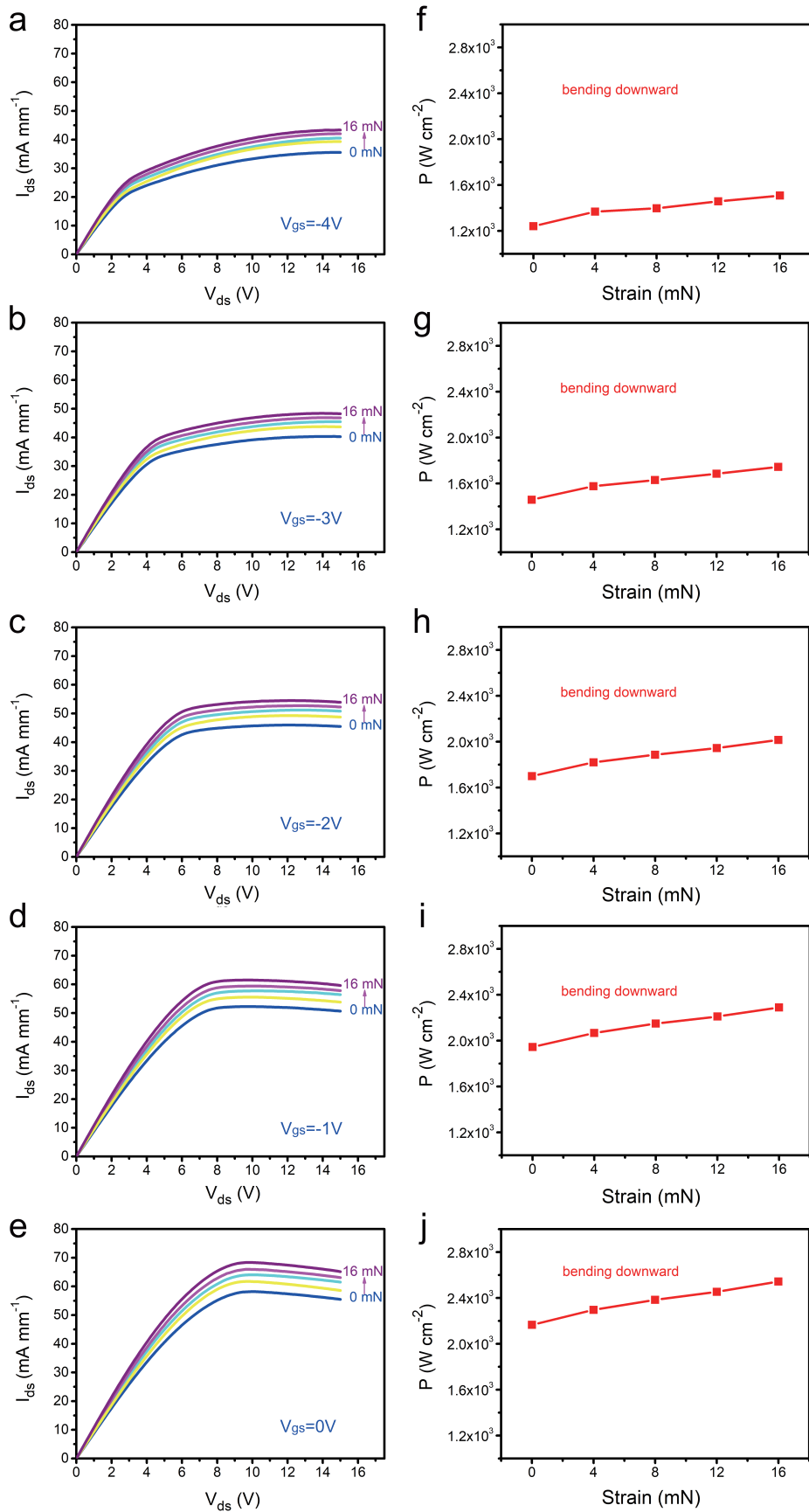


**Fig. 5.9 Strain-controlled output power characteristics at various gate voltage**

cantilever by using a probe needle loaded along the c-axis direction. An increase in in-plane tensile strain occurs in the AlGaN/AlN/GaN heterostructure. The deflection depth of the cantilever can be tuned by the probe needle in the controllable/reproducible manners. And the loaded strain can be calculated with material mechanics equations. And thus, the normal force increases from 0 to 16 mN as the deflection depth of the cantilever increases from 0 to 20  $\mu\text{m}$ .

In order to further understand the strain effect on the output characteristics of the SPD, different external strains are loaded on the free-end of the cantilever. It can be clearly observed that the  $I_{ds}$ - $V_{ds}$  curves show up-shifts to some degrees according to the increasing of the strain, which are both shown in Figure 5.8d, e. It means a direct and effective output power modulation by a weak mechanical stimulus. As applying an external strain along c-axis, a piezo-potential is generated, resulting in the change of 2DEG and thus modulating electron transport. It should be noted that the SPD is a high-power device capable of directly controlling electricity rather than a strain sensor.

In addition, the output current response to the external strain is also effectively modulated by the  $V_{gs}$ . The controllable capabilities of various  $V_{gs}$  ( $-5 \text{ V} \sim 1 \text{ V}$ ) under strains of  $0 \sim 16 \text{ mN}$  are presented in Figure 5.8d, e and Figure 5.9a–e, respectively. It can be clearly seen that a progressively higher modulation of current density is directly controlled at a  $V_{gs}$  of 1 V with the same strain. When the cantilever is subjected to an external strain, the output current density of the cantilever increases, both in the linear region or the saturation region. The saturated current at  $V_{ds} = 15 \text{ V}$  reaches  $40.43 \text{ mA mm}^{-1}$  under the maximum applied pressure (or strain of 16 mN) compared to the SPD without strain ( $32.83 \text{ mA mm}^{-1}$  at  $V_{gs} = -5 \text{ V}$ ). In contrast, the output current can be reached  $70.36 \text{ mA mm}^{-1}$  compared to the SPD without strain ( $59.87 \text{ mA mm}^{-1}$ ) at  $V_{gs} = 1 \text{ V}$ . It indicates that the SPD sensitivity is programmable. The inset of Figure 5.8e illustrates the strain distribution of the SPD under an external strain of 16 mN, which is simulated by COMSOL Multiphysics. Besides, the transconductance of the SPD at different applied external strain is displayed in Figure 5.8f. The transconductance shows an in-

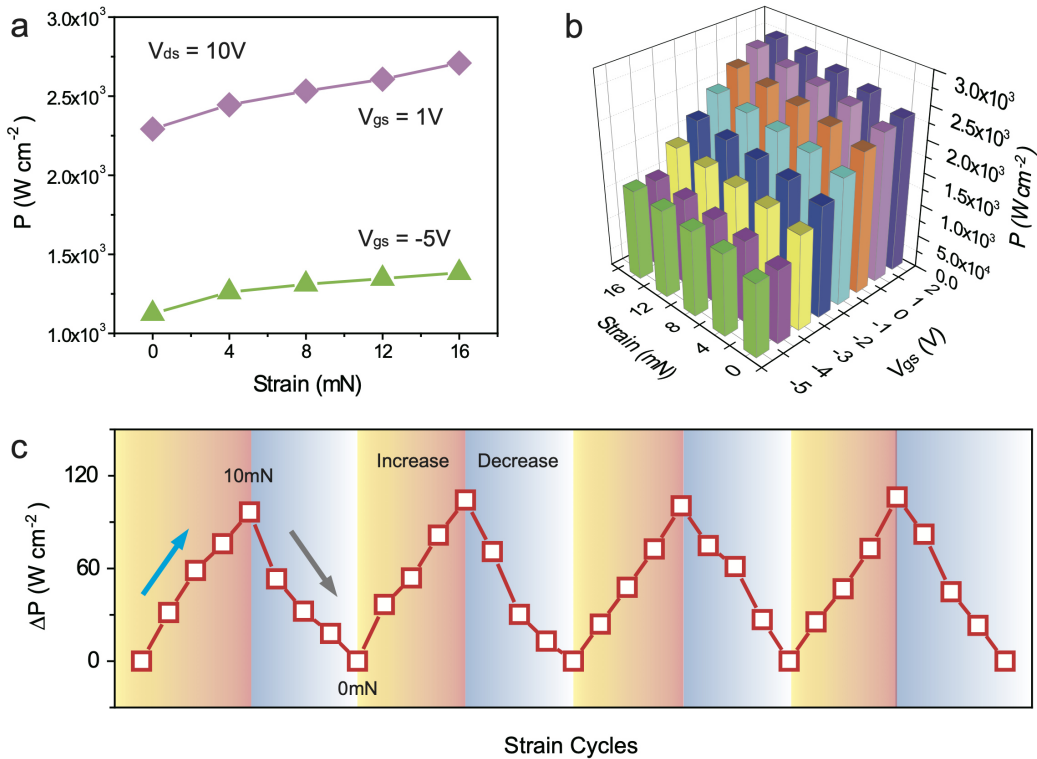


**Fig. 5.10 Strain-controlled output power characteristics of SPD. (a)** Output power density under external strain from 0 to 16 mN at  $V_{\text{gs}} = -5\text{V}$  and  $V_{\text{gs}} = 1\text{V}$ . **(b)** 3D plots illustrating the relationship between the output power density and the input strain or gate voltage. **(c)** Reproducible procedures of loading or unloading strain ( $0 \sim 10) in response to the relative output power density in cyclic tests.$

-crease with the increasing of applied external strain, indicating that the gate has an increasingly stronger capability to control the channel current. Therefore, it proves that the piezotronics effect, i.e., strain-controlled behavior, can effectively modulate the output characteristics of the SPD.

The output power modulation of the SPD is further discussed. Figure 5.10a shows the relationship between output power density and different strain. The output power density dependence on the applied strain can be obtained by employing strain-controlled output characteristics. More specifically, the output power density shows an increase with the applied strain ( $0 \sim 16), as a result of the increasing of the additional electrons and concentrations of$

2DEG suffering from in-plane tensile strain. The maximum output power density of the SPD can reach  $1.39 \times 10^3 \text{ W cm}^{-2}$  and  $2.72 \times 10^3 \text{ W cm}^{-2}$ , respectively, in response to the  $V_{gs}$  of  $-5 \text{ V}$  and  $1 \text{ V}$  under the strain of  $16 \text{ mN}$ . Furthermore, the output power level can also be tuned at the different  $V_{gs}$ , as shown in Figure 5.10a, b, and Figure 5.9f–j. Upon the strain of  $16 \text{ mN}$ , the relative output power density increases up to  $1.51, 1.74, 2.02, 2.29$ , and  $2.54 \times 10^3 \text{ W cm}^{-2}$ , respectively, at different  $V_{gs}$  (Figure 5.9f–j). To check the sensitivity of the output power under various  $V_{gs}$ , and the  $V_{gs}$  sweeps are systematically conducted. The relationships of the output power characteristics of the SPD on the external strain and the  $V_{gs}$  are all shown in Figure 5.10b, illustrating that the output power intensity rapidly increases as the external compressive strain increases. It is due to the increase in 2DEG density with external strain, leading to a significant piezoelectric effect. The results also show that the output power variations are sensitive to the continuous increase of gate voltage in the SPD (Figure 5.10b). It means that the  $V_{gs}$  can significantly change the sensitivity of the output power to external strain. Similar to human reflexes, external stimuli (e.g., strain) can induce knee reflex (analogy to output power

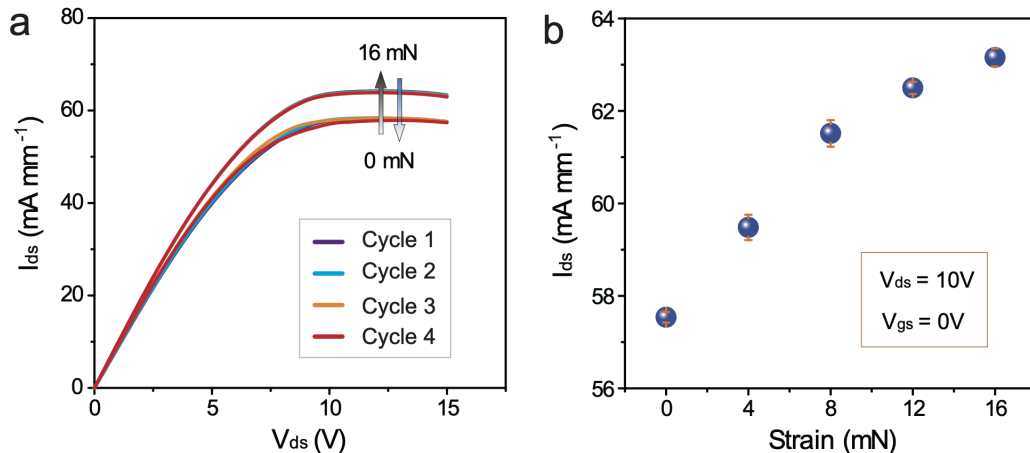


**Fig. 5.11 Reproducible strain-dependent analysis of the SPD. (a) Output characteristics in four consecutive cycles as the load and release of strain (0 /sim 16 mN). (b) Statistical variation measured at  $V_{ds} = 10 \text{ V}$ ,  $V_{gs} = 0 \text{ V}$  under external strain of  $0 \sim 16 \text{ mN}$ .**

changes). Moreover, the brain (gate) reserves the ultimate control over knee reflex. Besides, the reproducible procedures of loading or unloading multiple strains in response to the relative output power density of the SPD are shown in Figure 5.10c in cyclic tests, showing very good stable and repeatable performance for the strain-controlled devices.

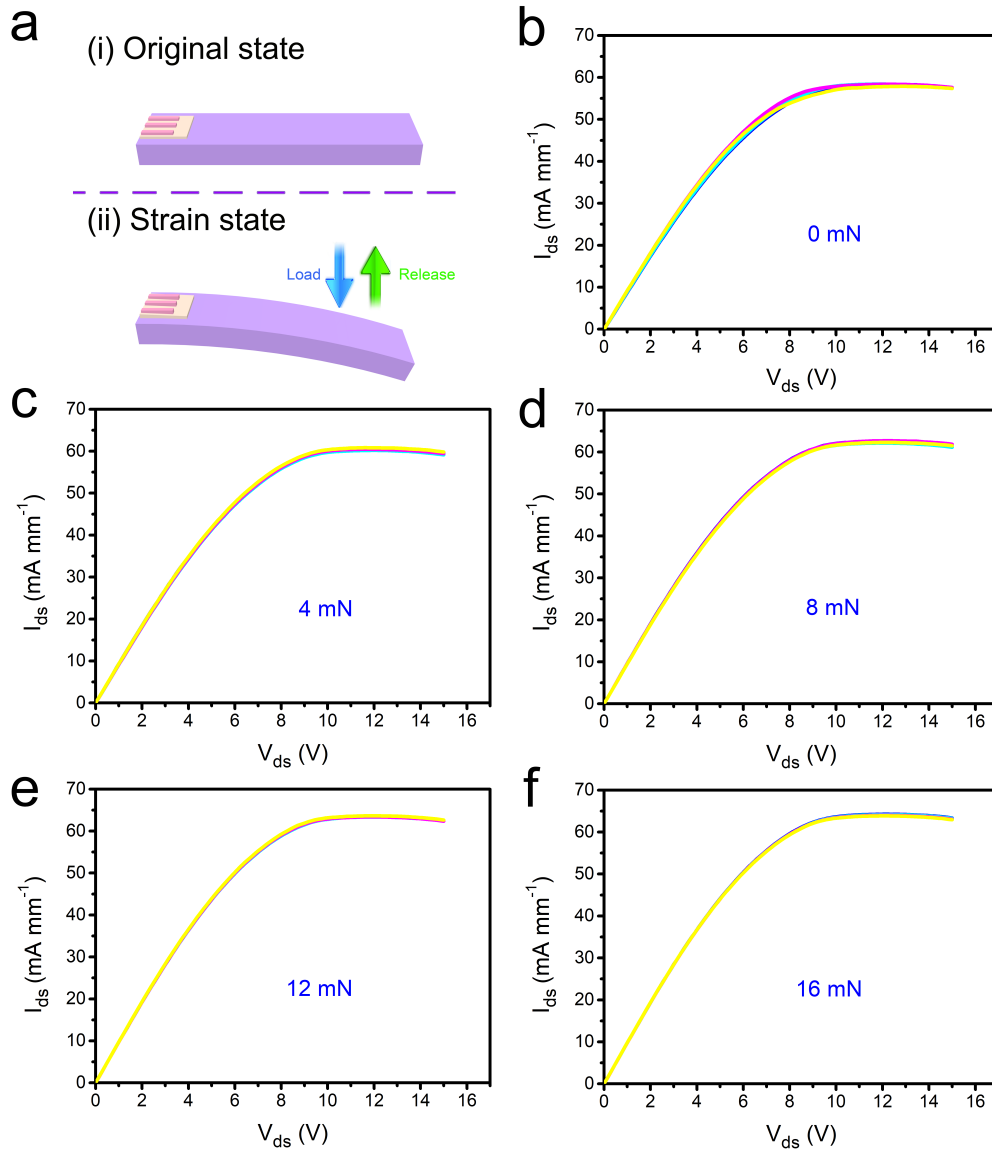


**Fig. 5.12 The reproducibility under external strain. (a) Schematic illustration of the external strain program (load and release). Output characteristics to various strain of (b) 0 mN, (c) 4 mN, (d) 8 mN, (e) 12 mN and (f) 16 mN at  $V_{ds}=0$  V, respectively.**

To further investigate the reproducibility of the SPD under external strain, the output currents can be obtained with the same batch sample after repeated loading/releasing strains (0, 4, 8, 12, and 16 mN) at a  $V_{gs}$  of 0 V. The strain-dependent output current curves and the statistical variation are shown in Figure 5.11a, b, respectively. Highly stability and repeatability of the SPD are clearly observed under each external strain (Figure 5.12). In addition, there is no obvious hysteresis in the strain response procedures, as shown in Figure 5.11a. With the accretion of strain (0 ~ 16 mN), the output current of the SPD shows a positive correlation (Figure 5.11b). And the standard deviations under each strain (0, 4, 8, 12, and 16 mN) are calculated as 0.11%, 0.27%, 0.29%, 0.13%, 0.19%, respectively. The SPD exhibits good reproducibility under the external strain stimuli, which is very suitable for strain-controlled power electronics.

## 5.4 Working mechanism

In this section we discuss the working mechanism of SPD, use the semi-classical physical model established in chapter 2 to demonstrate our experimental results and draw theoretical guidance for performance improvement. The analysis of the working principle of SPD is based on the piezotronics effect, that is, the coupling effect of the piezoelectric effect and the semiconductor properties existing in the III-V nitride AlGaN/AlN/GaN heterojunction. Because of the general piezoelectric polarization and spontaneous polarization effects in III-V nitrides, tensile and compressive strains of the lattice will generate corresponding piezoelectric polarization charges at the interface, thereby changing the net polarization charge density at the interface. In AlGaN/AlN/GaN heterojunctions, the change in the net polarization charge density at the interface affects the energy band of the heterojunction, which in turn affects a range of electrical properties. In the structural design of SPD, by introducing a cantilever structure, we amplify the strain effect of external stress on the lattice, thereby amplifying the modu-

lation characteristics of external stress on the output current and output power of SPD, and successfully fabricated a MEMS device with strain-controlled power. The calculation results are shown in Table 5.2 and Figure 5.13, respectively.

**Table 5.2 The calculated result for  $n_{2deg}$ -strain relationship under the external force**

Strain (mN)	2DEG Concentration ( $\times 10^{13} \text{ cm}^{-2}$ )
0	1.2099
4	1.3021
8	1.3431
12	1.3711
16	1.3918

The calculated conduction band ( $E_c$ ) of the AlGaN/AlN/GaN heterostructure is shown in Figure 5.13a. And the enlarged  $E_c$  of the AlGaN/AlN and AlN/GaN heterojunctions are shown in Figure 5.13b, c, respectively. It is obvious that, as the increase of compressive strain on the cantilever, the  $E_c$  of AlGaN is lifted up while the  $E_c$  of GaN is lowered down, which will deepen the potential well of the AlN/GaN heterojunction. Owing to the reformation of  $E_c$ , the distribution of carrier concentration is calculated and, as a result, varies with external strains (Figure 5.13d). It can be found that the peak value of carrier concentration increases with strain, indicating that more electrons are confined in the AlGaN/ AlN/GaN potential well. By virtue of the semiconductor physics theory, the 2DEG sheet carrier concentration under various strains is obtained by integrating the carrier concentration distribution along the c-axis. Figure 5.13e shows that the 2DEG sheet carrier concentration has an increase with the loading strains ranging from 0 to 16 mN, which contributes to the strain-responding output characteristics and power densities consequently. The calculated result for the relationships between 2DEG concentration and external force are listed in Table 5.2. The calculated 2DEG sheet

carrier concentrations qualitatively match well with the experimental results (Figure 5.12b), where the  $I_{ds}$  is proportional to the 2DEG concentration.

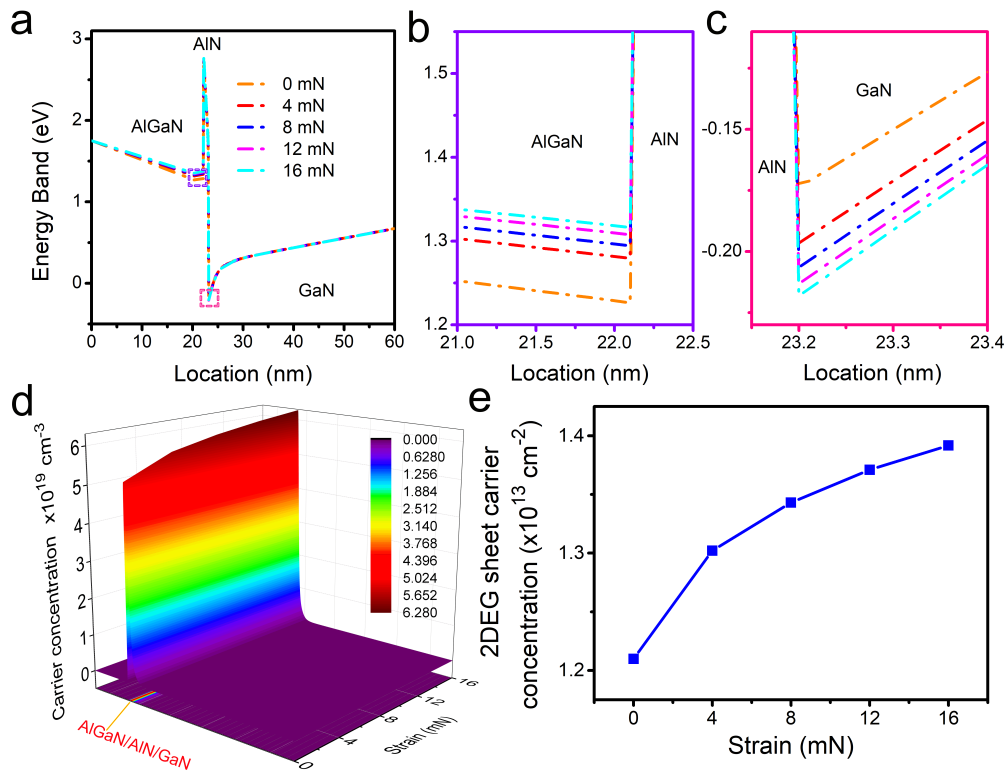


**Fig. 5.13 The calculated energy band and 2DEG concentration in AlGaN/AlN/GaN heterojunction under external strains. (a) The conduction band under external strains. The enlarged conduction band of the AlGaN/AlN (b) and AlN/GaN (c). (d) The carrier concentration distribution and the 2DEG concentration (e) under external strains.**

## 5.5 Summary

In this chapter, we present a bio-inspired strain-controlled power MEMS device based on the piezotronics effect which could directly control output power density with the mechanical stimuli. Ultra-high values of output power density ( $\times 10^{13} \text{ W cm}^{-2}$ ) control under a weak force (mN) control are achieved. The output power density of the SPD increases to  $2.72 \times 10^3 \text{ W cm}^{-2}$  under an external strain of 16 mN, which also exhibits a good sensitivity. The strain-induced

piezoelectric polarization charge can contribute to modifying the conduction band distribution at the local AlGaN/AlN/GaN heterojunction, and effectively adjust the concentration of 2DEG to tune/control the output current and power density of the SPD. In analogy to the ultimate control capability of the brain in the biological model, the gate voltage bias of the SPD can directly control the output power. This structure combines the advantages of high output power density and programmable gate-control response of AlGaN/AlN/GaN heterojunction HEMT by using the piezoelectric effect of flexible GaN-based cantilevers. The SPD will be very suitable for future AI applications including but not limited to autopilot, intelligent robots, and human-machine interface technologies.

# **Chapter 6**

## **Magnetosensory Power Devices**

### **6.1 Background and motivation**

Biological studies have suggested that a variety of animals have the ability to perceive the geomagnetic field, including insects [173], amphibians [174], reptiles [175], fish [176], and birds [177]. Migratory birds, for instance, have been suggested to not only orient themselves by sensing the inclination of the field [178], but also may deduce their location by discerning minute local variations in the geomagnetic field [179, 180]. Driven by the ongoing rapid advance of artificial intelligence (AI), neuroscience, and bionics, the development of bionic smart devices has made significant progress, such as the bionic eye [181], artificial synapse network [182], bionic artificial nerve [183], bionic skins [184], etc. The biophysical mechanisms that underlie magnetoreception in nature would be an appealing source from which inspiration can be drawn to develop magnetosensory power devices for interactive electronics [185, 186]. Traditional magnetic sensors have been proposed as a way to interact with objects in a touchless manner and move beyond conventional tactile interactions. Such sensors have been applied to magnetosensitive e-skins [187] and wearable magnetic sensors [188]. However, due to their discrete design and low output power density, these magnetic sensors can usually only be used as sensing devices, and therefore require bulky analog amplifiers as actuators, which are difficult to

be applied as interactive electronic systems with high integration and high power density. The demand for operating power of new intelligent bionic devices has promoted the cross-study of magnetosensory power devices, thereby realizing the integrated interactive electronic system of non-contact sensing and execution.

As the important representative of the power semiconductor materials, III-nitride compound semiconductor materials have important application prospects in the fields of power electronics [189], due to the high carrier density, high electron mobility, and wide bandgap. More significantly, III-nitrides show obvious spontaneous and piezoelectric polarization, which accounts well for the modulation of the energy band profile and two-dimensional electron gas (2DEG) concentration in the heterojunction [190, 25, 23]. Based on coupling effects of semiconductor characteristics and piezoelectric characteristics, the piezotronics effect can be observed in III-nitrides [26, 7, 27], and it opens a window to strain-regulated nanowires [29, 13], LEDs [30–32], and HEMTs [34, 29, 191], especially in the artificial intelligence devices [191, 192].

Here, we present a bioinspired magnetosensory power device (MPD) that can demonstrate large output power control with the emulation of magnetoreception in nature. The MPD is based on a cantilever-structured AlGaN/AlN/GaN HEMT device integrated with a high magnetic film  $(\text{Fe}_{90}\text{Co}_{10})_{78}\text{Si}_{12}\text{B}_{10}$ . The cantilever structure of the MPD is an ingenious design that can help to amplify the sensitivity of the output current/power in response to the change of external magnetic field. It is observed that MPD has a sensitive magnetic field-power modulation response. Meanwhile, the gate voltage of the MPD can finally control the operating point of the output power, indicating the robust and programmable characteristics of the MPD. According to the experiment and simulation results, the modulation relationship between the output power of the MPD and the external magnetic field is quasi-linear, showing excellent output power control characteristics with magnetic field. This work not only provides bioinspired device insights into the mechanism of magnetoreception, but also promotes the development of

high power interactive electronic and AI smart devices. It can be expected that MPD will have excellent application prospects in interactive electronics, artificial intelligence, and robotics.

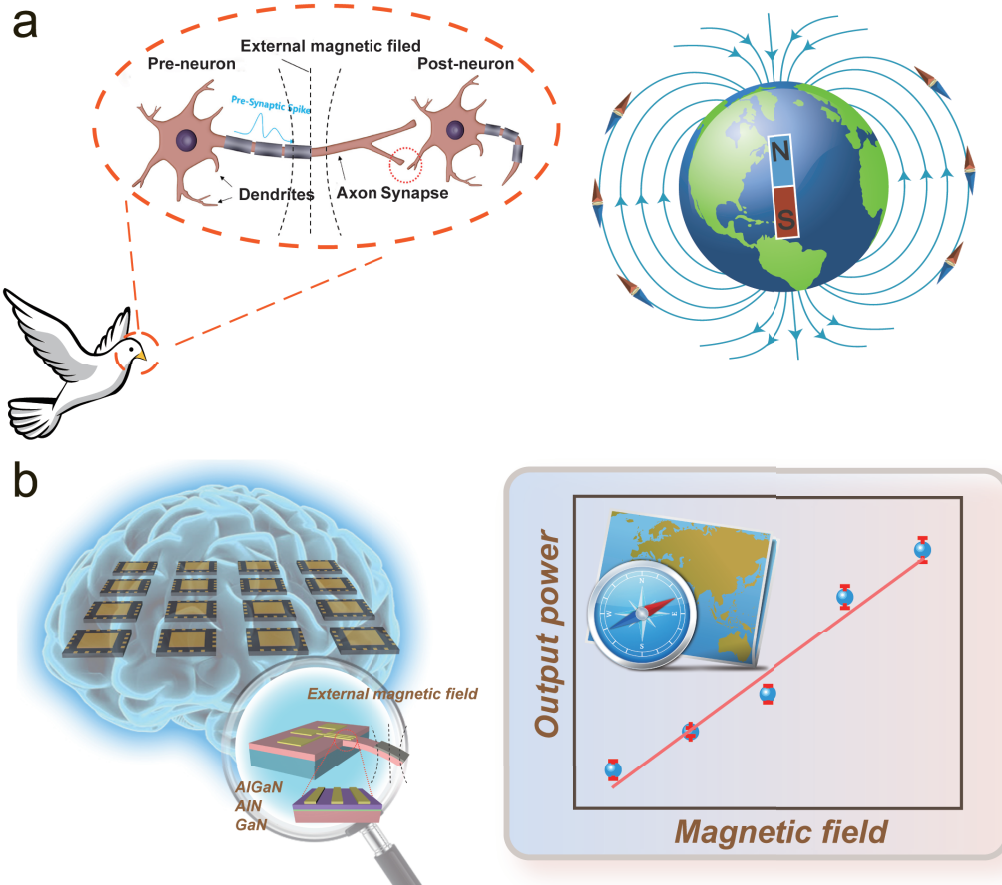


**Fig. 6.1 Illustration of the magnetosensory power device (MPD) inspired by magnetoreception in birds. (a) Schematic diagram of the birds' navigation and orientation through the geomagnetic field. (b) Schematic diagram of the MPD.**

The magnetoreception in nature has fascinated scientists due to its unique biological and bionic characteristics. For example, pigeons can locate themselves and determine directions by sensing the geomagnetic field. Figure 6.1 illustrates the magnetoreception in birds and bioinspired magnetosensory power device (MPD). The external magnetic field applied to the MPD can mimic the mechanism of magnetoreception to control the output current and power with the external magnetic field stimulus. The geomagnetic sense of the biological model

of birds is schematically displayed in Figure 6.1a. Under the action of geomagnetic field, the current signals of neurons between synapses in birds can be significantly modulated for location and orientation [193].

## 6.2 Design and preparation

### 6.2.1 Device structure and characterization

Figure 6.1b shows the schematic diagram of the cantilever-based magnetosensory power device MPD. The designed MPD is based on the cantilever-structured AlGaN/GaN high-electron-mobility transistor (HEMT), in which a magnetic thin film  $(\text{Fe}_{90}\text{Co}_{10})_{78}\text{Si}_{12}\text{B}_{10}$  is deposited on the front end of the cantilever. The enlarged part is the schematic cross-section of the AlGaN/GaN HEMT, where from top to bottom are AlGaN, AlN, GaN, and Si substrate. The thicknesses of AlGaN, AlN, and GaN layers are 30 nm, 1 nm, and 4.3  $\mu\text{m}$ , respectively, and the active region of MPD is  $34 \times 34 \mu\text{m}^2$ . The structural parameters of HEMT and MPD are detailed in Table 6.1. It can be clearly seen that MPD has a more complex cantilever structure with a magnetic film deposited compared to traditional HEMT on AlGaN/AlN/GaN epitaxial wafers. When the MPD senses an external magnetic field, the magnetic force on the magnetic film at the front end of the cantilever will cause bending strain on the active region of the MPD. Based on the piezotronics effect, the bending strain of the active region will induce piezoelectric polarization charges in the AlGaN, AlN, and GaN layers, thereby adjusting the AlGaN/AlN/GaN heterojunction energy band and 2DEG concentration, and finally modulating the output current and power of MPD. Therefore, the MPD manifests effective power modulation characteristics under the stimulation of external magnetic field, realizing high-power interactive electronics with non-contact sensing and control.

**Table 6.1 Structural parameters of HEMT and MPD**

MPD design	Material	Length (μm)	Width (μm)	Thickness (nm)
Cantilever	GaN	350	60	4300
Magnetic film	$(\text{Fe}_{90}\text{Co}_{10})_{78}\text{Si}_{12}\text{B}_{10}$	175	60	500
HEMT	AlGaN/AlN/GaN	34	34	30/1/4300

The fabrication process of MPD is shown in Figure 6.2a. We first prepare the HEMT device on the AlGaN/AlN/GaN epitaxial wafer, then deposit a magnetic film  $(\text{Fe}_{90}\text{Co}_{10})_{78}\text{Si}_{12}\text{B}_{10}$  in the front end of the active region, and finally released the cantilever structure of GaN. To fabricate the GaN-based cantilever, we perform a fully dry etching process by using inductively coupled plasma etching (ICP) [138]. We first remove GaN layer by anisotropic etching of GaN, and the cantilever structure is laterally released by isotropic etching of Si. The dry etching process has its own unique advantages, such as precise controllability, patterning, and good repeatability. By simply adjusting the etching time and recipe, we can manufacture the cantilever-based structure MPD under precise control, which is of great significance for the integrated MEMS application of MPD. The main fabrication process can be briefly divided into four steps shown in Figure 6.2a. Step 1: (a1) Initial Si-based AlGaN/AlN/GaN epitaxial layer; Step 2: (a2) The mesa isolation etching of AlGaN, AlN, and GaN by ICP; Step 3: (a3) Electron beam deposition to prepare Ohmic contact and Schottky contact electrodes, as well as magnetic film; Step 4: (a4) The released cantilever by ICP. The device fabrication process is also detailed in the subsection 6.2.2. The scanning electron microscopy (SEM) image and the inset optical picture taken by CCD camera of Figure 6.2b clearly displays the manufactured MPD, from which the complete cantilever structure and the HEMT device can be easily observed. The active region is located at the junction between the end of the cantilever

and the substrate, and therefore bears the greatest bending strain under the action of external stress, which induces piezoelectric polarization charges in the AlGaN/AlN/GaN interface and modulates the output power of the MPD. The high-resolution TEM image acquired from the AlGaN/AlN/GaN hetero-stacks is displayed in Figure 6.2c. It is clearly shown that the interface atoms of AlGaN/AlN and AlN/GaN are uniform and sharp without apparent boundary defects or dislocations, and the layers of GaN, AlN, and AlGaN can be easily identified.

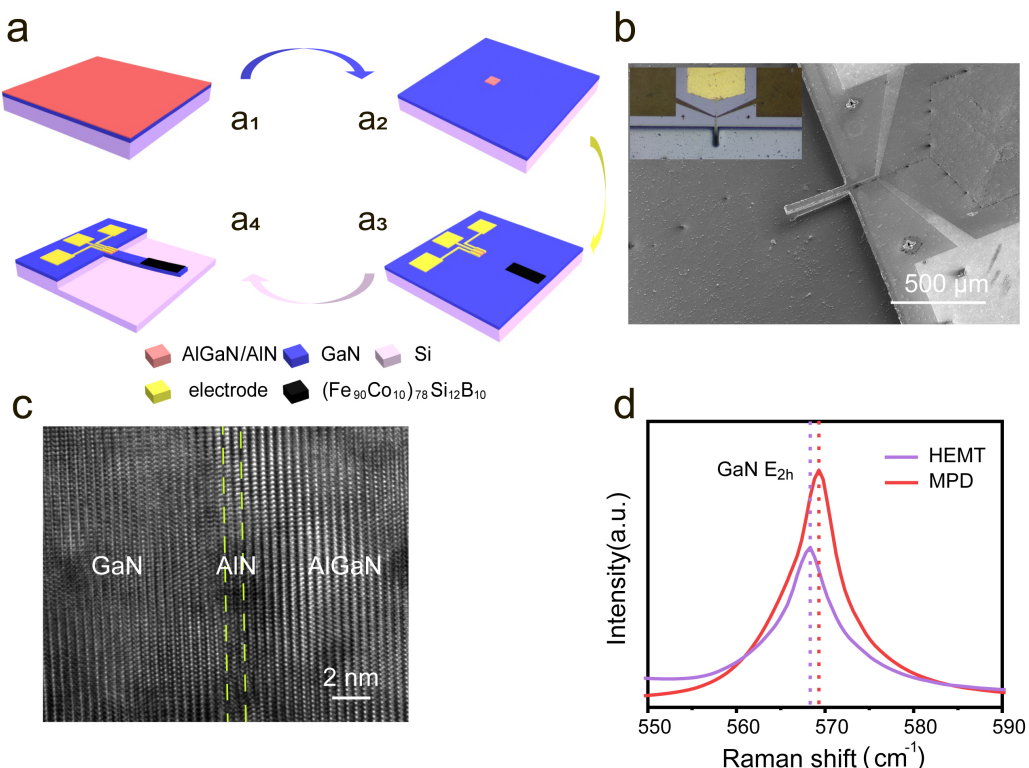


**Fig. 6.2 The fabrication process and characterization of MPD.** (a) The fabrication flow chart. (b) The SEM and CCD image. (c) The TEM image acquired from the AlGaN/AlN/GaN hetero-stacks. (d) The micro-Raman spectra of the AlGaN/AlN/GaN heterostructures before (HEMT) and after (MPD) dry-etching.

The Raman spectroscopy tests on both HEMT and MPD at room temperature have been performed to reveal the influence of the ICP dry etching process on the electrical performance of MPD, as shown in Figure 6.2d. The MPD exhibits that the  $E_{2h}$  phonon mode of GaN shows a blue shift from  $568.31\text{ cm}^{-1}$  to  $569.33\text{ cm}^{-1}$  compared with the HEMT, which reveals that

the dry etching process releases the silicon substrate and relaxes the tensile strain of the GaN layer [138, 29]. The alleviation of the tensile strain of the GaN layer will partially weaken the piezoelectric polarization effect of the GaN layer, thereby reducing the 2DEG concentration in the AlGaN/AlN/GaN heterojunction. The relationship between the biaxial stress and the shift of the Raman phonon frequency is shown in Equation 6.1.

$$\sigma_a = \frac{\Delta\omega}{K_{RS}^{E2(high)}} \quad (6.1)$$

where  $\sigma_a$  is the in-plane biaxial stress,  $\Delta\omega$  is the shift of the Raman phonon frequency, and  $K_{RS}^{E2(high)}$  is the Raman biaxial stress conversion factor. We can obtain that the tensile stress of the GaN epitaxial layer is reduced by 352 MPa compared with that on the Si substrate [139]. In addition, lattice defects have also been introduced during the dry etching process, which reduces the electrical performance of MPD to a certain extent [140–142]. Therefore, ICP dry etching will inevitably degrade the performance of MPD during the preparation of the cantilever. Comparing the performance of MPD and HEMT in Figure 6.4, it can be concluded that due to the ICP etching process in the cantilever fabrication process, the electrical properties of MPD are degraded to a certain extent compared to HEMT devices. Literature studies have shown that this performance degradation is unavoidable in the process of fabricating cantilever structures using the ICP process, but we have improved the performance degradation during cantilever fabrication through process optimization. Compared to the electrical properties of SPD in chapter 5, the electrical performance of MPD has been greatly improved, which is detailed in the fabrication process subsection.

Figure 6.3a illustrates the EDX line profiles for the element of Ga (red), Al (green), and N (purple) and energy-dispersive X-ray spectroscopy (EDS) element mapping including Ga, Al, and N acquired from the AlGaN/AlN/GaN hetero-stacks, which evidently displays the Al-GaN/AlN/GaN heterostructure and confirms the chemical element composition. The high-

resolution TEM image acquired from the AlGaN/AlN/GaN hetero-stacks is displayed in Figure 6.3b. It is clearly shown that the interface atoms of AlGaN/AlN and AlN/GaN are uniform and sharp without apparent boundary defects or dislocations, and the layers of GaN, AlN, and AlGaN can be easily identified.

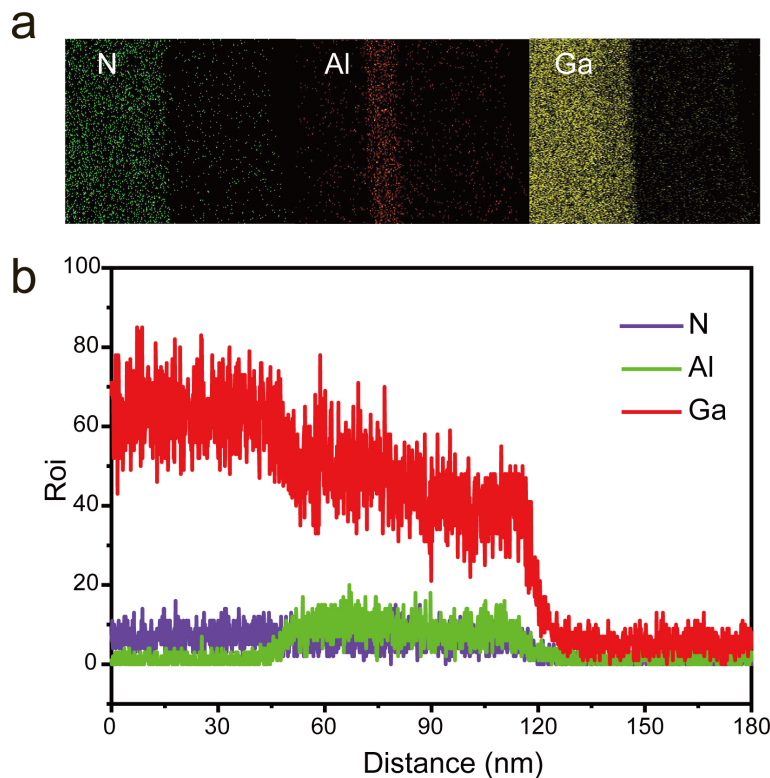


**Fig. 6.3** The EDX line profiles for the element of Ga (red), Al (green), and N (purple) and energy-dispersive X-ray spectroscopy (EDS) element mapping including Ga, Al, and N acquired from the AlGaN/AlN/GaN hetero-stacks.

### 6.2.2 Fabrication processes

The MPD was fabricated with III-Nitride epitaxial layers by metal-organic chemical vapor deposition (MOCVD) on Si substrate (111). The epitaxial layer structure consists of AlGaN (30 nm, 30% Al) / AlN (1 nm) / GaN (4.3  $\mu$ m) / AlGaN buffer layer / Si substrate. The mesa was etched using an inductively coupled plasma etching system (ICP, SENTECH SI 500)

etch process based on  $\text{BCl}_3/\text{Cl}_2/\text{Ar}$ . In order to form the ohmic contact and Schottky contact,  $\text{Ti}/\text{Al}/\text{Ni}/\text{Au}$  (20 nm / 120 nm / 45 nm / 55 nm) metal stack deposition was evaporated using an electron beam evaporation system (Denton Vacuum Explore 14) and annealed at 900 °C in  $\text{N}_2$  environment for 30 s using a rapid thermal processing system (LABSYS RTP-1200), and  $\text{Ni}/\text{Au}$  (80 nm / 50 nm) was evaporated for gate metallization respectively. Then the magnetic film  $(\text{Fe}_{90}\text{Co}_{10})_{78}\text{Si}_{12}\text{B}_{10}$  (500 nm) was deposited by magnetron sputtering (Denton Discovery 635). Finally, the ICP-based dry etching was performed by combining the anisotropic/isotropic etching to fabricate the cantilever using an inductively coupled plasma etching system (ICP, SENTECH SI 500). The main steps of the etching process of the cantilever structure based on ICP dry etching are as follows: Step 1: anisotropic etching of GaN. The photoresist patterned GaN thin film (thickness: 5  $\mu\text{m}$ ) is completely etched with the anisotropic etching recipe ( $\text{BCl}_3/\text{Cl}_2/\text{Ar}$ : 10/32/5 sccm; Power: 550 W; Process time: 30 min). Step 2: isotropic etching of Si. The cantilever structure is fabricated with the isotropic etching recipe ( $\text{SF}_6/\text{O}_2/\text{Ar}$ : 30/5/10 sccm; Power: 800 W; Process time: 25 min). The manufactured cantilever had dimensions of  $350 \times 60 \times 5 \mu\text{m}^3$ , with the embedded HEMT had a mesa dimension of  $34 \times 34 \mu\text{m}^2$  and a gate length of 5  $\mu\text{m}$ .

It is worth noting that a significant performance degradation before and after cantilever etching was observed during the preparation of SPD in chapter 5, which is because the long-term ICP etching introduces a large number of lattice defects. As a result, the electrical conductivity and electrode contact performance of the SPD is greatly reduced. So if the active area of the device can be more effectively protected during prolonged ICP etching, the electrical performance of the device will be significantly improved. In the process of preparing the cantilever structure of MPD in this study, the thickness of the photoresist as the anti-etching mask layer is significantly increased by applying multiple layers of positive photoresist. The UV exposure and development parameters of the photoresist under the corresponding thickness have been explored through the experimental process, therefore a mask layer with high etching

resistance with a complete pattern has been successfully prepared. The experimental results show that the high etch-resistance mask layer composed of multi-layer photoresist effectively protects the active area of the device, and the performance degradation of MPD before and after cantilever etching is greatly improved. Compared with unetched HEMT, when  $V_{gs} = 0$  V and  $V_{ds} = 10$  V, the saturated output current of MPD is only reduced by  $67 \text{ mA mm}^{-1}$ , while the saturated output current of SPD under the same conditions is reduced by  $250 \text{ mA mm}^{-1}$ . Therefore, by applying photoresist in multiple layers, we have successfully improved the fabrication process of cantilever MEMS devices based on AlGaN/AlN/GaN heterojunctions, and explored a new process method for the preparation of higher performance cantilever MEMS devices in the future.

## 6.3 Device performance

### 6.3.1 Electrical performance

The electrical characteristics of HEMT (before the dry-etching for the cantilever structure) and manufactured MPD are shown in Figure 6.4. Based on the good electrical contact performance, the output characteristics ( $I_{ds}$ - $V_{ds}$ ) of both HEMT and MPD have excellent gate control capabilities, as shown in Figure 6.4a,c, respectively. It is clearly shown that the output current shows good linearity at low source-drain bias ( $V_{ds}$ ) voltage, and then as the bias voltage further increases, the output current reaches saturation. Both HEMT and MPD can achieve stable large output current above  $200 \text{ mA mm}^{-1}$  in the saturation region, and can be effectively controlled at various gate voltage ( $V_{gs}$ ) from -7 V to 1 V. Compared with HEMT, the saturated output current of MPD under the source-drain bias voltage of 10 V drops from  $264 \text{ mA mm}^{-1}$  to  $197 \text{ mA mm}^{-1}$ . Furthermore, we measure the transfer ( $I_{ds}$ - $V_{gs}$ ) characteristics of the HEMT and the MPD at  $V_{ds} = 10$  V, as shown in Figure 6.4b,d, respectively. The maximum transconductance ( $g_{m,max}$ ) of HEMT is  $42.4 \text{ mA mm}^{-1}$  (Figure 6.4b), while the value for the MPD reduces

to  $32.9 \text{ mA mm}^{-1}$  (Figure 6.4d). The transconductance performance of MPD is also slightly lower than HEMT. The reduction in the output current and transconductance of the MPD can be attributed to the dry etching process, which inevitably leads to stress release and lattice defects in the GaN layer.

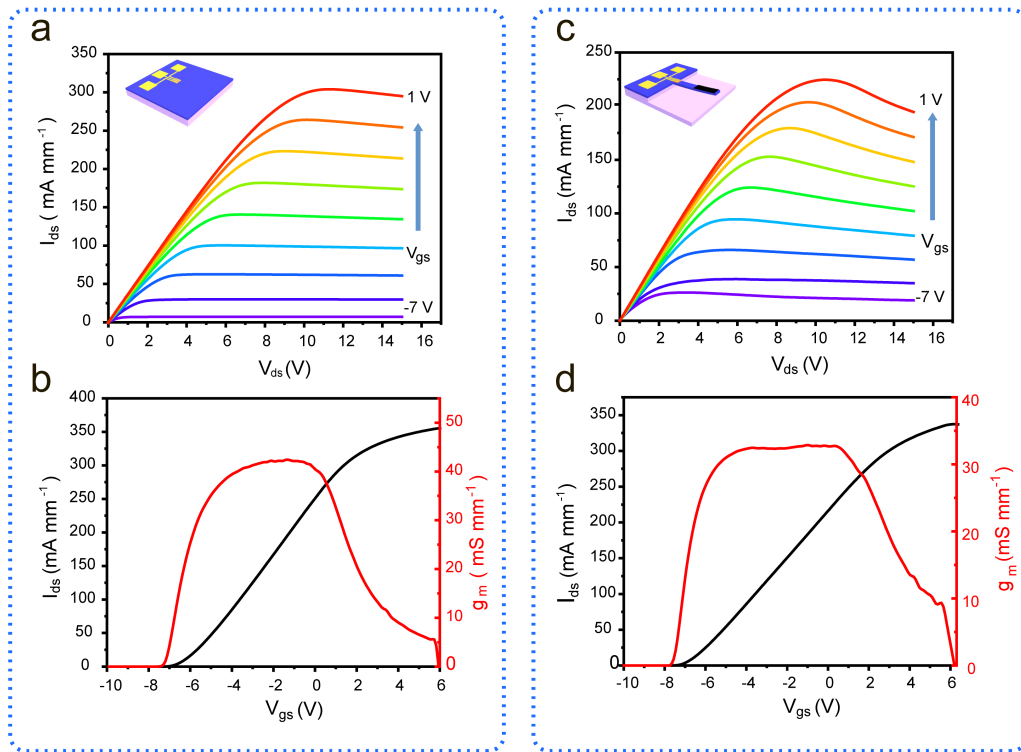


**Fig. 6.4 Electrical characteristics of the HEMT (before etching) and the as-fabricated MPD. Output ( $I_{ds}$ - $V_{ds}$ ) characteristics of the (a) HEMT and (c) MPD. Transfer ( $I_{ds}$ - $V_{gs}$ ) characteristics of the (b) HEMT and (d) MPD measured.**

Both HEMT and MPD exhibit good Schottky contacts on the gate and Ohmic contacts on the source and drain (Figure 6.5a,b). However, the Schottky contact performance of MPD is slightly worse than that of HEMT, which is caused by the lattice defects introduced by the ICP process [144, 143] and the enhanced self-heating effect after etching [147–149]. It can be concluded that due to the dry etching process, the electrical performance of MPD is slightly lower than that of HEMT, but it still has excellent output characteristics and transfer charac-

teristics. The leakage current characteristics of HEMT and MPD are shown in Figure 6.5c,d, respectively. It is clearly shown that the ICP process does not significantly increase the leakage current of the device. The SPD maintains substantially the same leakage current characteristics as the HEMT.

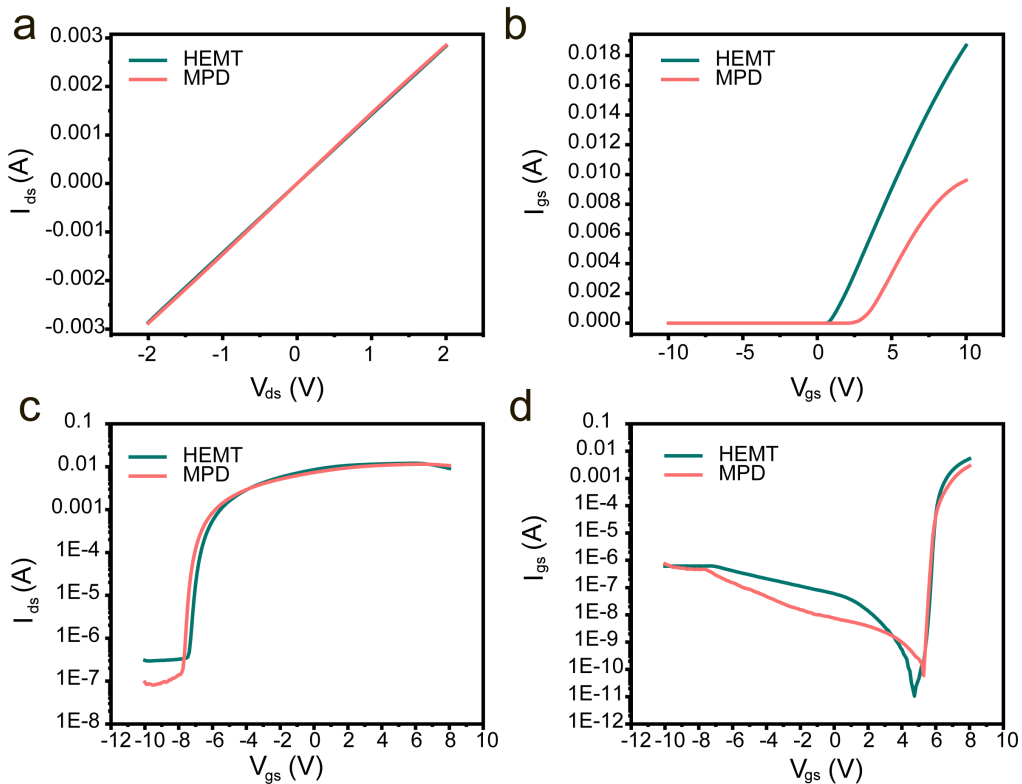


**Fig. 6.5 The contact and leakage current characteristics of HEMT and MPD** (a) The source-drain Ohmic contact and (b) gate Schottky contact characteristics. (c) The  $I_{ds}$  –  $V_{gs}$  characteristics and (d) gate leakage currents characteristics.

### 6.3.2 Magnetic field-power modulation performance

Different magnetic fields are applied to the MPD under various gate voltages to mimic the magnetoreception. The modulation characteristics of the external magnetic field on the output current and power of the MPD are systematically discussed. In this study, we design an

energized solenoid to generate a uniform controllable magnetic field, and in order to enhance the magnetic field inside the energized solenoid, we design a correspondingly sized iron core. According to the Biot-Savart law, the magnetic field inside a long energized solenoid can be approximately regarded as a uniform magnetic field. By changing the current of the energized solenoid and calibrating with a magnetic field detector, the magnetic field acting on the MPD can be accurately controlled. We put the MPD inside the energized solenoid and change the input current of the solenoid to generate the magnetic fields of 0 mT, 100 mT, 200 mT, 300 mT, and 400 mT, respectively. The source-drain voltage  $V_{ds}$  and the gate-source voltage  $V_{gs}$  are used to measure the output characteristics and transfer characteristics of the MPD under different external magnetic fields.

Figure 6.6a illustrates the strain distribution of the MPD under an external magnetic field of 400 mT, which is simulated by COMSOL Multiphysics and the magnetic force on the MPD cantilever is in the negative z direction. It clearly shows that due to the design of the cantilever structure, the active region of the MPD bears the strain under the action of the magnetic field, thereby enhancing the piezotronics effect and increasing the modulation of the output power by the magnetic field. Figure 4b displays the output characteristics of the MPD under an external magnetic field of 200 mT, with the gate voltage  $V_{gs}$  ranging from -5 V to 1 V at a step of 1 V. Under the same magnetic field, the modulation effect of the current density becomes more significant with the increase of  $V_{gs}$ , which means that the output current response to the external magnetic field is effectively modulated by the gate voltage.

In addition, the output current of the MPD can also be effectively modulated by an external magnetic field. Figure 6.6c illustrates the output characteristics of MPD under various external magnetic fields when  $V_{gs} = -5$  V. As the magnetic field increases, the output current density of the MPD increases in both the linear and saturation regions. At  $V_{gs} = -5$  V and  $V_{ds} = 15$  V,

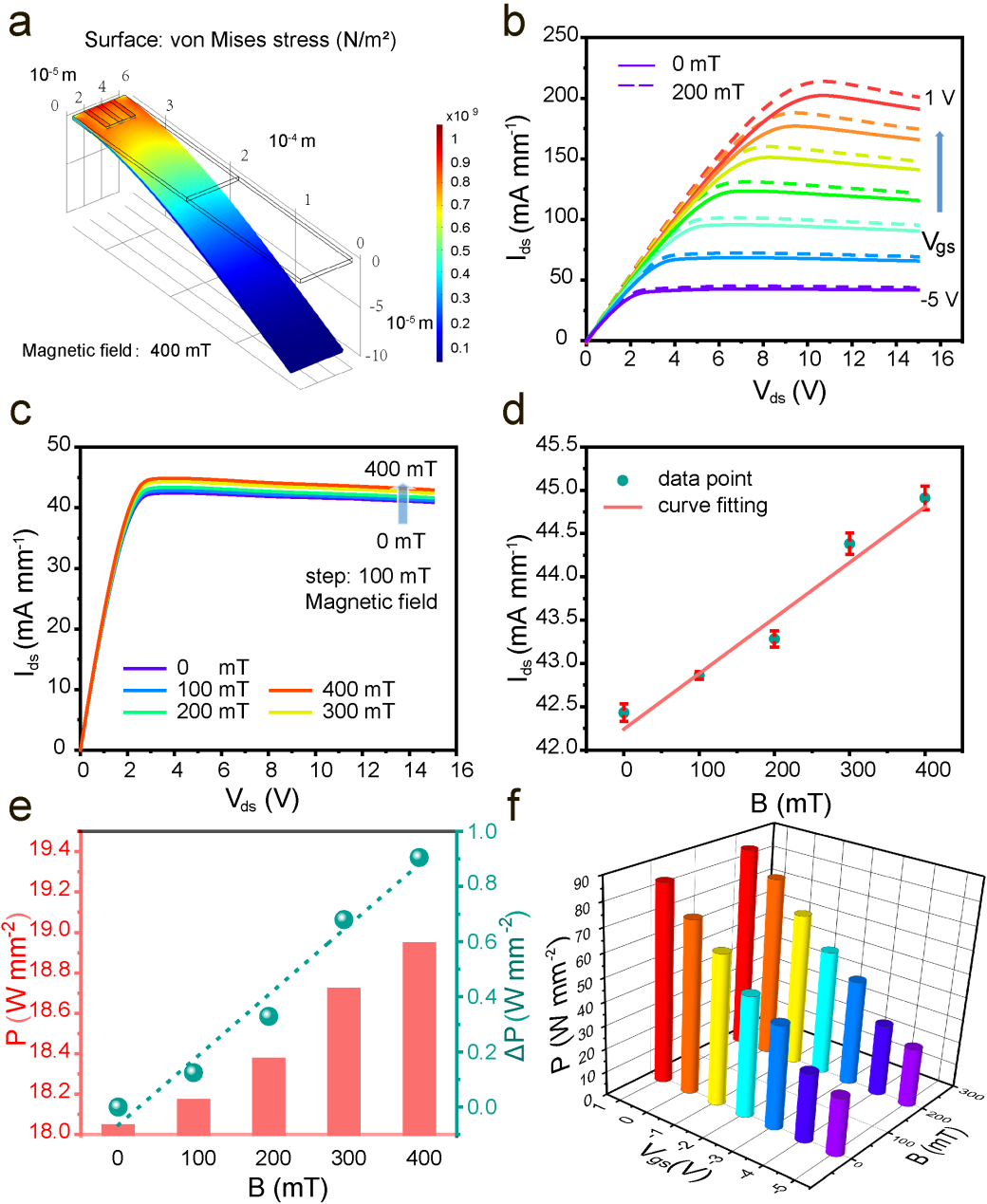


**Fig. 6.6 The magnetic field-power modulation characteristics of MPD.** (a) The strain distribution under the magnetic field of 400 mT. (b) Output characteristics under the magnetic field of 200 mT. (c) Output characteristics under the magnetic field with  $0 \sim 400$  mT at  $V_{gs} = -5$  V. (d) The curve fitting of the saturation output current in (c) under the magnetic field at  $V_{ds} = 15$  V,  $V_{gs} = -5$  V. (e) Output power density plots under the magnetic field with  $0 \sim 400$  mT at  $V_{gs} = -5$  V. (f) 3D plots illustrating the relationship between the output power density and the magnetic field or gate voltage.

when the magnetic field increases from 0 to 400 mT, the saturation current of the MPD increases from 40.90 to 42.94 mA mm<sup>-1</sup>. This shows that the output current of MPD can be effectively adjusted by the magnetic field, which can mimic the magnetoreception mechanism of neuron synapses. Moreover, the saturation output current of MPD under the 0 ~ 400 mT magnetic field at  $V_{ds}= 15$  V in Figure 4c is selected, and the fitting curve is also obtained, as shown in Figure 6.6d. It is clearly shown that the saturation output current of the MPD has a quasi-linear relationship with the external magnetic field, indicating that the MPD has excellent magnetic field-current modulation performance.

Figure 6.6e illustrates the output power at  $V_{gs} = -5$  V and  $V_{ds} = 15$  V under the modulation of magnetic field from 0 to 400 mT. It is clearly shown that the output power density ( $P$ ) of MPD increases from 18.04 to 18.94 W mm<sup>-2</sup>, and the changes in output power density ( $\Delta P$ ) increase quasi-linearly with the increase of the external magnetic field. Furthermore, the magnetic field-power modulation characteristics under different gate voltages are systematically measured, as shown in Figure 6.6f. The output power density shows an increase with the external magnetic field, as a result of the increase of 2DEG concentrations caused by piezotronic effect. Upon the magnetic field of 200 mT, the maximum output power density of the MPD increases up to 25.1, 30.5, 45.1, 53.6, 65.3, 77.0, 85.8 W mm<sup>-2</sup>, respectively, in response to the  $V_{gs}$  various from -5 V to 1 V. It means that the  $V_{gs}$  can significantly change the sensitivity of the output power to the external magnetic field. It can be concluded that MPD has an ultra-high-output power density, and it can drive external execution devices of different power levels according to the gate voltage after detecting the change of magnetic field, which can be applied as interactive electronics that integrates sensing and execution functions.

In the next subsection, we will study the physical mechanism by which the external magnetic field modulates the output current and power of the MPD, especially the most unique linear relationship compared to SPD. We will further calculate the output characteristics of MPD under the rotating magnetic field to make predictions for further research.

## 6.4 Working mechanism

Due to the non-centrosymmetric crystal structure of wurtzite group III-nitride materials, there are spontaneous polarization charges on the surface of the material. Meanwhile, the lattice mismatch between AlGaN, AlN, and GaN films also induces piezoelectric polarization charges at the interface. Studies have shown that the spontaneous polarization charge and piezoelectric polarization charge at the interface jointly modulates the energy band and electrical properties of the AlGaN/AlN/GaN heterojunction [190, 194]. Based on the principle of piezotronics effect, when an external strain is applied to the HEMT device along the c-axis, the piezoelectric polarization charges at the interface are significantly regulated, thereby adjusting the energy band profile and 2DEG concentration of the AlGaN/AlN/GaN heterojunction, and finally modulating the electrical properties of the HEMT devices. Since a magnetic film is deposited on the front half of the cantilever of the MPD, the external magnetic field can generate a magnetic force at the front end of the cantilever, thereby inducing piezoelectric polarization charges and modulating the output current of the MPD. The external magnetic force is loaded on the front half of the cantilever by using an electric solenoid with an iron core, which can generate a magnetic field along the c-axis direction. The loaded magnetic force can be calculated using the Equation 6.3. As the magnetic field increases from 0 to 400 mT, the normal force on the cantilever increases from 0 to 0.67 mN, which exists in both the  $+z$  and  $-z$  directions. Resulting from the magnetic force introduced by the external magnetic field on the magnetic film, the output current and power of the MPD can be effectively modulated in real time through external magnetic field stimulation.

We first study the case where the normal force generated by the magnetic field is in the  $+z$  direction. In order to rationalize our experimental results and reveal the in-depth modulation mechanism of the piezotronics effect on the output characteristics of the MPD, a self-consistent numerical calculation model based on the Schrödinger, Poisson, and Piezoelectric Constitu-

tive equations has been fully developed to simulate the modulation of energy band profile and 2DEG concentration under external strains [195, 196, 34] through the methods described in chapter 2, as shown in Figure 6.7. Figure 6.7a presents the calculated conduction band ( $E_c$ ) of AlGaN/AlN/GaN heterojunction, and the enlarged  $E_c$  of the AlGaN/AlN and AlN/GaN heterojunction are shown in Figure 6.7a1, a2, respectively. As the strain on the cantilever increases (from 0 to 24 mN), the  $E_c$  of AlGaN is lowered down while the Ec of GaN is lifted upward, which shallow the potential well of AlN/GaN heterojunction. Therefore, the carrier concentration distribution of the heterojunction is significantly reduced, as shown in Figure 6.7b. It is clearly shown that the peak value of carrier concentration decreases with strain, indicating that less electrons are confined in the AlN/GaN potential well. According to the theory of semiconductor physics, the 2DEG sheet carrier concentration under different strains can be obtained by integrating the carrier concentration distribution along the c-axis, resulting in Figure 6.7c. It illustrates that the 2DEG sheet carrier concentration decreases rapidly with external strains (over a range of 0 to 24 mN).

We further simulated the device performance when the magnetic force on the MPD cantilever is in the  $+z$  direction. The calculated 2DEG concentration under various magnetic field (Table 6.2) and the fitting result (Table 6.3) shows that the 2DEG concentration is about 0.5 power of external strain in our strain range and can be expressed as

$$n_{2deg} = 1.2 - 0.05 \times F^{0.43} \quad (6.2)$$

Where  $F$  is magnetic force, the unit is mN,  $n_{2deg}$  is 2DEG concentration, the unit is  $\times 10^{13}$   $\text{cm}^{-2}$ . Furthermore, based on the magnetic force formula obtained from Maxwell's equation, the strain displays a square relationship with the magnetic field.

$$F = \frac{B^2 A_m}{2\epsilon_0} = 4.2 \times B^2 \quad (6.3)$$

**Table 6.2 The calculated result for  $n_{2deg}$ -strain relationship under the magnetic force in +z direction**

Strain (mN)	2DEG Concentration ( $\times 10^{13} \text{ cm}^{-2}$ )
0	1.2011
4	1.1112
8	1.0712
12	1.0455
16	1.026
20	1.0099
24	0.9963

**Table 6.3 The fitting curve of the calculated  $n_{2deg}$ -strain relationships under the magnetic force in +z direction**

Model	Allometric2
Equation	$y = a + b \times x^c$
a	$1.20165 \pm 0.00292$
b	$-0.05243 \pm 0.00312$
c	$0.43338 \pm 0.01765$
Reduced Chi-Sqr	8.47446E-6
R-Square (COD)	0.99888
Adj. R-Square	0.99832

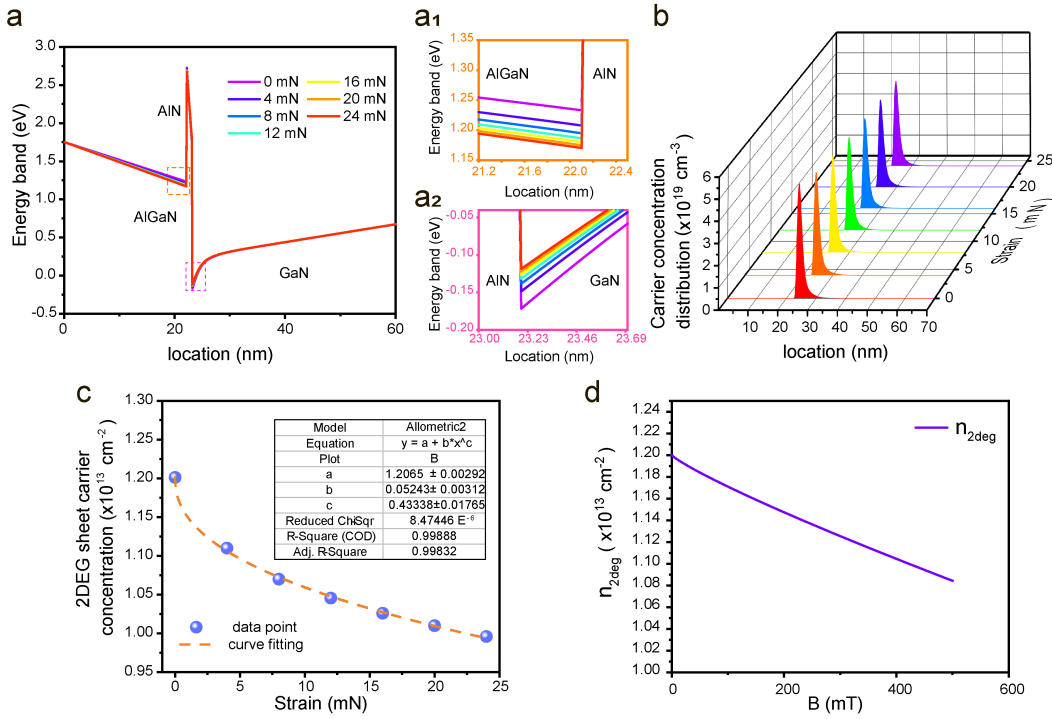


**Fig. 6.7 The calculated energy band and 2DEG concentration n AlGaN/AlN/GaN heterojunction under magnetic force in  $+z$  direction. (a) The conduction band under external strains. (b) The carrier concentration distribution and the 2DEG concentration (c) under external strains, as well as the fitting curve. (d) The 2DEG concentration under magnetic force in  $+z$  direction.**

where  $\epsilon_0$  is vacuum permeability with the unit  $\text{H m}^{-1}$ ,  $B$  is external magnetic field with the unit T,  $A_m$  is the area of magnetic film with the unit  $\text{m}^2$ . Hence, combining these two equations, we have eventually derived the linear relationship between 2DEG concentration ( $n_{2deg}$ ) and external magnetic field ( $B$ ).

$$n_{2deg} = 1.2 - 0.21 \times B^{0.86} \quad (6.4)$$

The curve of the Equation 6.4 is shown in Figure 6.7d. It clearly shows that when the magnetic field increases from 0 to 400 mT, the 2DEG concentration decreases quasi-linearly with the external magnetic field. By virtue of semiconductor theory, the source-drain current of AlGaN/GaN HEMT is proportional to the 2DEG concentration. Therefore, we can conclude that

the source-drain current and output power are quasi-linearly related to the external magnetic field.

We then study the case where the normal force generated by the magnetic field is in the  $-z$  direction, which is exactly the experimental condition in this study. The self-consistent calculation result is displayed in Figure 6.8 and Table 6.4. It is clearly shown that as the strain on the cantilever increases (from 0 to 24 mN), the  $E_c$  of AlGaN is lifted upward while the Ec of GaN is lowered down, which deepen the potential well of AlN/GaN heterojunction (Figure 6.8a). Therefore, the carrier concentration distribution of the heterojunction is significantly increased, as shown in Figure 6.8b. It is clearly shown that the peak value of carrier concentration increases with strain, indicating that more electrons are confined in the AlN/GaN potential well. According to the theory of semiconductor physics, the 2DEG sheet carrier concentration under different strains can be obtained by integrating the carrier concentration distribution along the c-axis, resulting in Figure 6.8c. It illustrates that the 2DEG sheet carrier concentration increases rapidly with external strains (over a range of 0 to 24 mN).

In order to further explain the quasi-linear modulation relationship of external magnetic field ( $B$ ) to source-drain current ( $I_{ds}$ ) and changes of output power density ( $\Delta P$ ), we also perform a curve-fitting on the calculated 2DEG sheet carrier concentration in Figure 6.8c. The fitting result (Table 6.5) shows that the 2DEG concentration is about 0.5 power of external strain in our strain range and can be expressed as

$$n_{2deg} = 1.2 + 0.04 \times F^{0.47} \quad (6.5)$$

Combing the equation with the Equation 6.3, we have eventually derived the linear relationship between 2DEG concentration ( $n_{2deg}$ ) and external magnetic field ( $B$ ).

$$n_{2deg} = 1.2 + 0.168 \times B^{0.94} \quad (6.6)$$

**Table 6.4 The calculated result for  $n_{2deg}$ -strain relationship under the magnetic force in  $-z$  direction**

Strain (mN)	2DEG Concentration ( $\times 10^{13} \text{ cm}^{-2}$ )
0	1.2011
4	1.2811
8	1.3196
12	1.3452
16	1.3645
20	1.3806
24	1.3941

**Table 6.5 The fitting curve of the calculated  $n_{2deg}$ -strain relationships under the magnetic force in  $-z$  direction**

Model	Allometric2
Equation	$y = a + b \times x^c$
a	$1.2005 \pm 0.00313$
b	$0.04423 \pm 0.00315$
c	$0.46889 \pm 0.02115$
Reduced Chi-Sqr	9.7702E-6
R-Square (COD)	0.99856
Adj. R-Square	0.99784

The curve of the Equation 6.6 is shown in Figure 6.8d. It clearly shows that when the magnetic field increases from 0 to 400 mN, the 2DEG concentration increases quasi-linearly with the external magnetic field. Therefore, the source-drain current of AlGaN/GaN HEMT is proportional to the 2DEG concentration and we can conclude that the source-drain current and output power are quasi-linearly related to the external magnetic field. The theoretical model agrees well with the experimental result.

The 2DEG sheet carrier concentration when the MPD rotates at different angles under 0–400 mT magnetic fields have also been further simulated to imitate the mechanism that birds orient themselves by sensing the angle and magnitude of the geomagnetic field. The formula under the magnetic force in the  $+z$  direction and  $-z$  direction are derived in Equation 6.7 and Equation 6.8, respectively.

$$n_{2deg} = 1.2 - 0.21 \times B^{0.86} \times \cos\left(\frac{(\theta - 180)\pi}{180}\right) \quad (6.7)$$

$$n_{2deg} = 1.2 + 0.168 \times B^{0.94} \times \cos\left(\frac{\theta\pi}{180}\right) \quad (6.8)$$

where  $\theta$  is the rotation angle.

The curve has been shown in Figure 6.8e. It clearly illustrates that the 2DEG concentration of MPD has an approximately sinusoidal relationship with the rotation angle, and its maximum value increases significantly with the increase of the magnetic field. Therefore, it can be concluded that the output current and power of MPD show a sinusoidal relationship with the angle of the magnetic field, and a linear relationship with the magnitude of the magnetic field when sensing different external magnetic fields. This indicates that the output current and power of MPD can be effectively modulated by the angle and magnitude of the magnetic field, showing excellent orientation and sensing capabilities.

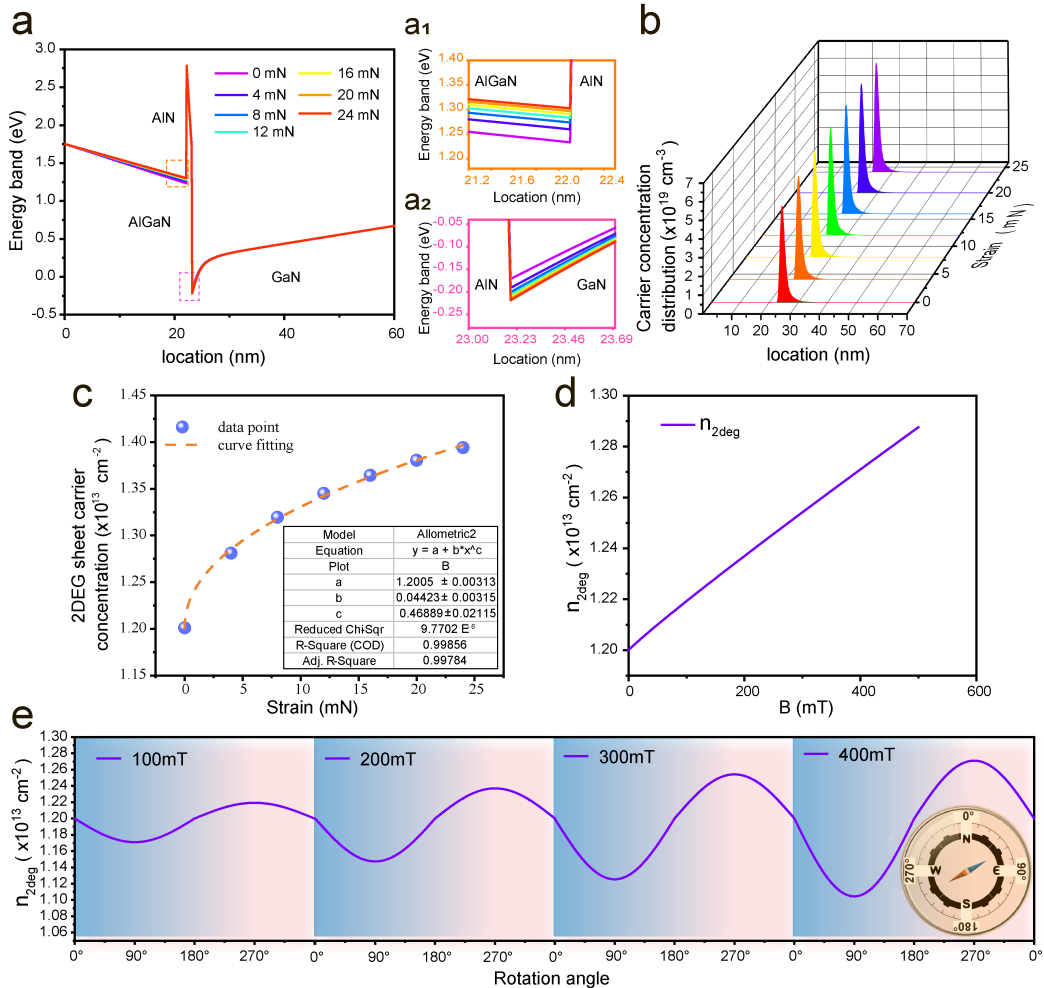


**Fig. 6.8** The calculated energy band and 2DEG concentration in AlGaN/AlN/GaN heterojunction under magnetic force in  $-z$  direction and rotation. (a) The conduction band under external strain. (b) The carrier concentration distribution and the 2DEG concentration (c) under external strains, as well as the fitting curve. (d) The 2DEG concentration under magnetic force in  $-z$  direction. (e) The 2DEG concentration of SPD at different rotation angles under  $0 \sim 400$  mT magnetic fields.

## 6.5 Summary

In summary, we demonstrate a magnetosensory power device that can utilize external magnetic field to modulate the output power of the device by the emulation of magnetoreception in nature. Based on the piezotronic effect, the strain-induced piezoelectric polarization charges

can modify the energy band profile of the local AlGaN/AlN/GaN heterojunction, and effectively adjust the 2DEG concentration to tune/control the output power of the MPD. Due to the design of the magnetic cantilever of the MPD, the external magnetic field can introduce a normal compressive strain at the front end of the cantilever, thereby triggering piezotronics effect. Under the action of the external magnetic field of  $0 \sim 400$  mT, when the gate voltage is -5 V, the saturation output power density of MPD increases quasi-linearly from  $18.04 \text{ W mm}^{-2}$  to  $18.94 \text{ W mm}^{-2}$ , showing good magnetic field-power modulation characteristics. Meanwhile, the gate voltage of MPD can control the working point of the output power in a larger range. The maximum output power density of MPD can reach  $85.8 \text{ W mm}^{-2}$  at 1 V gate voltage under 200 mT magnetic field, thereby realizing the two-dimensional control of the output power by the external magnetic field and the gate voltage. This work not only provides insights into interactive electronics that integrate sensing and control functionalities, but also promotes the development of bionic AI smart devices, especially in applications of very large scale integration (VLSI) systems that mimic neurobiological architectures present in the nervous system [197, 198].

# **Chapter 7**

## **Discussion and Outlook**

### **7.1 Conclusions**

This thesis systematically studies the theoretical modeling and fabrication of III-V nitride power MEMS devices based on the piezotronics effect. We established a semi-classical physical model of the MEMS cantilever device based on AlGaN/AlN/GaN heterojunction, and fabricated a strain-controlled power MEMS device (SPD) and a magnetic field-controlled power MEMS device (MPD), thus providing a theoretical framework and novel device structure for the research of power MEMS devices based on AlGaN/AlN/GaN heterojunctions. The main conclusions of this thesis are as follows:

1. Theoretical model of power MEMS devices

In this study, a semi-classical physical model of a MEMS cantilever device based on AlGaN/AlN/GaN heterojunction was established according to piezotronics effect. Combined with piezoelectric constitutive equation, biaxial stress model, finite element analysis of GaN cantilever material mechanics, and self-consistent coupling model of one-dimensional Schrödinger-Poisson equation, the modulation characteristics of external stress on the energy band of AlGaN/AlN/GaN heterojunction and the electrical trans-

port properties of MEMS devices are calculated, which provides a theoretical basis for the development of SPD and MPD, as well as the theoretical guidance for the development of new power MEMS devices based on AlGaN/AlN/GaN heterojunction cantilever structures.

## 2. Manufacturing of power MEMS devices

In the study, the manufacture of GaN power MEMS devices from epitaxial growth wafers to well-functional devices have been systematically studied. We introduced the main nanofabrication and characterization equipment, including epitaxial growth, dry etching, photolithography, thin film deposition, plasma cleaning, Raman spectroscopy, scanning electron microscopy, transmission electron microscopy, etc, and briefly introduced their important role in GaN power MEMS research, as well as the corresponding process design and key parameters. Furthermore, we developed the corresponding process parameters and their process integration, thus realizing the whole process from GaN wafer to well-functional GaN power MEMS device.

## 3. Strain-controlled power MEMS devices

In this study, we propose a strain-regulated power MEMS device (SPD) inspired by the human knee-jerk reflex mechanism. This is a new type of MEMS device based on the cantilever structure of AlGaN/AlN/GaN heterojunction, which can directly control the output power density through external mechanical stimulation, realizing ultra-high output power density under weak force (mN) control ( $\times \text{W mm}^{-2}$ ). The maximum output power density of the SPD increases from  $2.30 \times 10^3 \text{ W mm}^{-2}$  to  $2.72 \times 10^3 \text{ W mm}^{-2}$  under external strain of  $0 \sim 16 \text{ mN}$ , showing good response sensitivity. At the same time, similar to the ultimate control ability of the brain in the knee-jerk reflex mechanism, the

gate voltage of the SPD can control the output power in a wider range, thus combining the two-dimensional control advantage of both small-scale external strain control and large-scale programmable gate voltage control. SPD is well suited for future AI applications including but not limited to autopilots, intelligent robotics and human-machine interface technologies.

#### 4. Magnetosensory power MEMS devices

In this study, by depositing a magnetic thin film on the front half of the cantilever of the SPD, the magnetic field-regulated power MEMS device was fabricated. This is a new type of power MEMS device based on the cantilever structure of AlGaN/AlN/GaN heterojunction, which can directly control the output power through an external magnetic field, realizing a high output power density ( $85.8 \text{ W mm}^{-2}$ ) under the control of the magnetic field (mT). Under the action of the external magnetic field of  $0 \sim 400 \text{ mT}$ , when the gate voltage is -5 V, the saturation output power density of MPD increases quasi-linearly from  $18.04 \text{ W mm}^{-2}$  to  $18.94 \text{ W mm}^{-2}$ , showing good magnetic field-power modulation characteristics. At the same time, similar to the voltage signal between neuron synapses that ultimately determines the size of neuron current, the gate voltage of MPD can regulate the output power in a wider range, so it combines two-dimensional control advantage of small-scale external magnetic field control and large-scale programmable gate control. This work not only provides physical electronics insights into the working mechanism of magnetic sensing neurons in the biological sense, but also promote the development of various neuroelectronic devices.

## 7.2 Future work

### 1. Improvement of MEMS fabrication process

Develop new micro-nano processing technology to improve the electrical properties of MEMS devices based on AlGaN/AlN/GaN heterojunction cantilever structures. In the follow-up research, the Si substrate of MEMS devices needs to be removed, and the MEMS devices can be transferred to flexible substrates to further fabricate flexible power MEMS devices, which can be applied to wearable electronic devices and robots in the future.

## 2. Optimization of the theoretical model

The semi-classical physical model established in this thesis takes many approximations when analyzing the strain in the MEMS active region. The sampling point setting of the finite element analysis of COMSOL Multiphysics approximates that the active area is uniformly strained. In the follow-up research, the non-uniform strain of the MEMS active region needs to be mathematically analyzed to establish a more complete theoretical model.

## 3. In-depth analysis of physical mechanisms

Since the bending strain of the non-centrosymmetric GaN will also produce the flexoelectric effect, this study can be further extended to the deep research of the bending strain and the flexoelectric effect of the power MEMS device based on the cantilever structure of AlGaN/AlN/GaN heterojunction. By combining the principles of piezoelectric effect and flexoelectric effect, the physical mechanisms of MEMS devices with cantilever structure can be studied more deeply [199–205].

# Bibliography

- [1] Douglas A Skoog, F James Holler, and Stanley R Crouch. *Principles of Instrumental Analysis*. Cengage Learning, 2017.
- [2] Curie Jacques and Curie Pierre. Development, via compression, of electric polarization in hemihedral crystals with inclined faces. *Bull. Soc. Minéralogique Fr*, 3:90–3, 1880.
- [3] Woldemar Voigt. *Lehrbuch der Kristallphysik:(mit Ausschluss der Kristalloptik)*, volume 34. BG Teubner, 1910.
- [4] Neil A Downie. *Exploding Disk Cannons, Slimemobiles, and 32 Other Projects for Saturday Science*. JHU Press, 2006.
- [5] Zhong Lin Wang. Nanopiezotronics. *Advanced Materials*, 19(6):889–892, 2007.
- [6] Wenzhuo Wu and Zhong Lin Wang. Piezotronics and piezo-phototronics for adaptive electronics and optoelectronics. *Nature Reviews Materials*, 1(7):1–17, 2016.
- [7] Zhong Lin Wang, Wenzhuo Wu, and Christian Falconi. Piezotronics and piezo-phototronics with third-generation semiconductors. *MRS Bulletin*, 43(12):922–927, 2018.
- [8] Ronan Hinchet, Usman Khan, Christian Falconi, and Sang-Woo Kim. Piezoelectric properties in two-dimensional materials: Simulations and experiments. *Materials Today*, 21(6):611–630, 2018.
- [9] Weiguo Hu, Kourosh Kalantar-Zadeh, Kapil Gupta, and Chuan-Pu Liu. Piezotronic materials and large-scale piezotronics array devices. *MRS Bulletin*, 43(12):936–940, 2018.
- [10] Zhen Guo, Haixi Pan, Chuanyu Li, Lili Zhang, Shuai Yan, Wei Zhang, Jia Yao, Yuguang Tang, Hongbo Yang, Yihui Wu, et al. Dynamic carrier transport modulation for constructing advanced devices with improved performance by piezotronic and

- piezo-phototronic effects: a brief review. *Semiconductor Science and Technology*, 32(8):083001, 2017.
- [11] Jun Xin, Yanqing Zheng, and Erwei Shi. Piezoelectricity of zinc-blende and wurtzite structure binary compounds. *Applied Physics Letters*, 91(11):112902, 2007.
- [12] Zhong Lin Wang. *Piezotronics and Piezo-phototronics*, volume 24. Springer, 2012.
- [13] Zhong Lin Wang and Jinhui Song. Piezoelectric nanogenerators based on zinc oxide nanowire arrays. *Science*, 312(5771):242–246, 2006.
- [14] Xudong Wang, Jun Zhou, Jinhui Song, Jin Liu, Ningsheng Xu, and Zhong L Wang. Piezoelectric field effect transistor and nanoforce sensor based on a single ZnO nanowire. *Nano Letters*, 6(12):2768–2772, 2006.
- [15] J Hsin He, Cheng L Hsin, Jin Liu, Lih J Chen, and Zhong L Wang. Piezoelectric gated diode of a single ZnO nanowire. *Advanced Materials*, 19(6):781–784, 2007.
- [16] Jun Zhou, Yudong Gu, Peng Fei, Wenjie Mai, Yifan Gao, Rusen Yang, Gang Bao, and Zhong Lin Wang. Flexible piezotronic strain sensor. *Nano letters*, 8(9):3035–3040, 2008.
- [17] Peng Fei, Ping-Hung Yeh, Jun Zhou, Sheng Xu, Yifan Gao, Jinhui Song, Yudong Gu, Yanyi Huang, and Zhong Lin Wang. Piezoelectric potential gated field-effect transistor based on a free-standing ZnO wire. *Nano Letters*, 9(10):3435–3439, 2009.
- [18] Weihua Liu, Minbaek Lee, Lei Ding, Jie Liu, and Zhong Lin Wang. Piezopotential gated nanowire- nanotube hybrid field-effect transistor. *Nano Letters*, 10(8):3084–3089, 2010.
- [19] Wenzhuo Wu, Yaguang Wei, and Zhong Lin Wang. Strain-gated piezotronic logic nanodevices. *Advanced Materials*, 22(42):4711–4715, 2010.
- [20] Wenzhuo Wu and Zhong Lin Wang. Piezotronic nanowire-based resistive switches as programmable electromechanical memories. *Nano Letters*, 11(7):2779–2785, 2011.
- [21] ES Hellman. The polarity of GaN: a critical review. *Materials Research Society Internet Journal of Nitride Semiconductor Research*, 3, 1998.
- [22] Fabio Sacconi, A Di Carlo, P Lugli, and H Morkoc. Spontaneous and piezoelectric polarization effects on the output characteristics of AlGaN/GaN heterojunction modulation doped FETs. *IEEE Transactions on Electron Devices*, 48(3):450–457, 2001.

- [23] ET Yu, XZ Dang, PM Asbeck, SS Lau, and GJ Sullivan. Spontaneous and piezoelectric polarization effects in III–V nitride heterostructures. *Journal of Vacuum Science & Technology B: Microelectronics and Nanometer Structures Processing, Measurement, and Phenomena*, 17(4):1742–1749, 1999.
- [24] Yue Hao, Jin Feng Zhang, and Jin Cheng Zhang. *Nitride Wide Bandgap Semiconductor Material and Electronic Devices*. CRC Press, 2016.
- [25] Debdeep Jena, John Simon, Albert Wang, Yu Cao, Kevin Goodman, Jai Verma, Satyaki Ganguly, Guowang Li, Kamal Karda, Vladimir Protasenko, et al. Polarization-engineering in group III-nitride heterostructures: New opportunities for device design. *Physica Status Solidi (a)*, 208(7):1511–1516, 2011.
- [26] Caofeng Pan, Junyi Zhai, and Zhong Lin Wang. Piezotronics and piezo-phototronics of third generation semiconductor nanowires. *Chemical Reviews*, 119(15):9303–9359, 2019.
- [27] Wei Sha, Jicai Zhang, Shuxin Tan, Xiangdong Luo, and Weiguo Hu. III-nitride piezotronic/piezo-phototronic materials and devices. *Journal of Physics D: Applied Physics*, 52(21):213003, 2019.
- [28] LL Lev, IO Maiboroda, M-A Husanu, ES Grichuk, NK Chumakov, IS Ezubchenko, IA Chernykh, X Wang, B Tobler, T Schmitt, et al. k-space imaging of anisotropic 2D electron gas in GaN/GaAlN high-electron-mobility transistor heterostructures. *Nature Communications*, 9(1):1–9, 2018.
- [29] Xingfu Wang, Ruomeng Yu, Chunyan Jiang, Weiguo Hu, Wenzhuo Wu, Yong Ding, Wenbo Peng, Shutu Li, and Zhong Lin Wang. Piezotronic effect modulated heterojunction electron gas in AlGaN/AlN/GaN heterostructure microwire. *Advanced Materials*, 28(33):7234–7242, 2016.
- [30] Xin Huang, Chunhua Du, Yongli Zhou, Chunyan Jiang, Xiong Pu, Wei Liu, Weiguo Hu, Hong Chen, and Zhong Lin Wang. Piezo-phototronic effect in a quantum well structure. *Acs Nano*, 10(5):5145–5152, 2016.
- [31] Ting Liu, Ding Li, Hai Hu, Xin Huang, Zhenfu Zhao, Wei Sha, Chunyan Jiang, Chunhua Du, Mengmeng Liu, Xiong Pu, et al. Piezo-phototronic effect in InGaN/GaN semi-floating micro-disk LED arrays. *Nano Energy*, 67:104218, 2020.

- [32] Qi Guo, Ding Li, Qilin Hua, Keyu Ji, Wenhong Sun, Weiguo Hu, and Zhong Lin Wang. Enhanced heat dissipation in gallium nitride-based light-emitting diodes by piezo-phototronic effect. *Nano Letters*, 21(9):4062–4070, 2021.
- [33] Ting Liu, Chunyan Jiang, Xin Huang, Chunhua Du, Zhenfu Zhao, Liang Jing, Xiaolong Li, Shichao Han, Jiangman Sun, Xiong Pu, et al. Electrical transportation and piezotronic-effect modulation in AlGaN/GaN MOS HEMTs and unpassivated HEMTs. *Nano Energy*, 39:53–59, 2017.
- [34] Chunyan Jiang, Ting Liu, Chunhua Du, Xin Huang, Mengmeng Liu, Zhenfu Zhao, Linxuan Li, Xiong Pu, Junyi Zhai, Weiguo Hu, et al. Piezotronic effect tuned AlGaN/GaN high electron mobility transistor. *Nanotechnology*, 28(45):455203, 2017.
- [35] Jiyuan Zhu, Xingyu Zhou, Liang Jing, Qilin Hua, Weiguo Hu, and Zhong Lin Wang. Piezotronic effect modulated flexible AlGaN/GaN high-electron-mobility transistors. *ACS Nano*, 13(11):13161–13168, 2019.
- [36] O Ambacher, J Smart, JR Shealy, NG Weimann, K Chu, M Murphy, WJ Schaff, LF Eastman, R Dimitrov, L Wittmer, et al. Two-dimensional electron gases induced by spontaneous and piezoelectric polarization charges in N-and Ga-face AlGaN/GaN heterostructures. *Journal of Applied Physics*, 85(6):3222–3233, 1999.
- [37] Ting Liu. *Flexible (Photoelectric) Electronic Devices*. PhD thesis, University of Chinese Academy of Sciences, 2018.
- [38] Jiyuan Zhu. Research on GaN-based flexible electronic devices. Master’s thesis, University of Chinese Academy of Sciences, 2020.
- [39] Sergey Edward Lyshevski. *Nano-and Micro-Electromechanical Systems: Fundamentals of Nano-and Microengineering*. CRC Press, 2018.
- [40] Tai-Ran Hsu. *MEMS and Microsystems: Design and Manufacture*. McGrae Hill, 2002.
- [41] Julian W Gardner, Vijay K Varadan, and Osama O Awadelkarim. *Microsensors, MEMS, and Smart Devices*. John Wiley & Sons, Inc., 2003.
- [42] Volker Cimalla, CC Röhlig, V Lebedev, Oliver Ambacher, Katja Tonisch, Florentina Niebelshütz, Klemens Brueckner, and Matthias A Hein. AlGaN/GaN based heterostructures for MEMS and NEMS applications. In *Solid State Phenomena*, volume 159, pages 27–38. Trans Tech Publ, 2010.

- [43] Gastone Ciuti, Leonardo Ricotti, Arianna Menciassi, and Paolo Dario. MEMS sensor technologies for human centred applications in healthcare, physical activities, safety and environmental sensing: A review on research activities in Italy. *Sensors*, 15(3):6441–6468, 2015.
- [44] Tomohide Yabuki and Osamu Nakabeppu. Heat transfer mechanisms in isolated bubble boiling of water observed with MEMS sensor. *International Journal of Heat and Mass Transfer*, 76:286–297, 2014.
- [45] Xiaodong Wang, Baoqing Li, Zhixiong Xiao, Sang Hwui Lee, Harry Roman, Onofrio L Russo, Ken K Chin, and Kenneth R Farmer. An ultra-sensitive optical MEMS sensor for partial discharge detection. *Journal of Micromechanics and Microengineering*, 15(3):521, 2004.
- [46] Farbod Khoshnoud and Clarence W de Silva. Recent advances in MEMS sensor technology–biomedical applications. *IEEE Instrumentation & Measurement Magazine*, 15(1):8–14, 2012.
- [47] Farbod Khoshnoud and Clarence W de Silva. Recent advances in MEMS sensor technology-mechanical applications. *IEEE Instrumentation & Measurement Magazine*, 15(2):14–24, 2012.
- [48] AGP Kottapalli, CW Tan, M Olfatnia, JM Miao, G Barbastathis, and M Triantafyllou. A liquid crystal polymer membrane MEMS sensor for flow rate and flow direction sensing applications. *Journal of Micromechanics and Microengineering*, 21(8):085006, 2011.
- [49] Luis J Fernandez, Remco J Wiegerink, Jakob Flokstra, J Sese, HV Jansen, and M El-wenspoek. A capacitive RF power sensor based on MEMS technology. *Journal of Micromechanics and Microengineering*, 16(7):1099, 2006.
- [50] Massimo Donelli and Jacopo Iannacci. Exploitation of RF-MEMS switches for the design of broadband modulated scattering technique wireless sensors. *IEEE Antennas and Wireless Propagation Letters*, 18(1):44–48, 2018.
- [51] Chengkuo Lee and Jer-Liang Andrew Yeh. Development and evolution of MOEMS technology in variable optical attenuators. *Journal of Micro/Nanolithography, MEMS, and MOEMS*, 7(2):021003, 2008.
- [52] Jacopo Iannacci. Internet of things (IoT); internet of everything (IoE); tactile internet; 5G–A (not so evanescent) unifying vision empowered by EH-MEMS (energy harvesting

- MEMS) and RF-MEMS (radio frequency MEMS). *Sensors and Actuators A: Physical*, 272:187–198, 2018.
- [53] Pavel Davidson, Jani Hautamäki, and Jussi Collin. Using low-cost MEMS 3d accelerometer and one gyro to assist GPS based car navigation system. In *Proceedings of 15th Saint Petersburg International Conference on Integrated Navigation Systems (May 2008)*, 2008.
- [54] Jiri Marek. Automotive MEMS sensors—trends and applications. In *Proceedings of 2011 International Symposium on VLSI Technology, Systems and Applications*, pages 1–2. IEEE, 2011.
- [55] Dominik Berndt, Josef Muggli, Franz Wittwer, Christoph Langer, Stephan Heinrich, Thorsten Knittel, and Rupert Schreiner. MEMS-based thermal conductivity sensor for hydrogen gas detection in automotive applications. *Sensors and Actuators A: Physical*, 305:111670, 2020.
- [56] Paddy French, Gijs Krijnen, and Fred Roozeboom. Precision in harsh environments. *Microsystems & Nanoengineering*, 2(1):1–12, 2016.
- [57] Mina Rais-Zadeh, Vikrant Jayant Gokhale, Azadeh Ansari, Marc Faucher, Didier Théron, Yvon Cordier, and Lionel Buchaillot. Gallium nitride as an electromechanical material. *Journal of Microelectromechanical Systems*, 23(6):1252–1271, 2014.
- [58] R Tabrizian, M Rais-Zadeh, and F Ayazi. Effect of phonon interactions on limiting the fQ product of micromechanical resonators. In *TRANSDUCERS 2009-2009 International Solid-State Sensors, Actuators and Microsystems Conference*, pages 2131–2134. IEEE, 2009.
- [59] So Karmann, R Helbig, and RA Stein. Piezoelectric properties and elastic constants of 4H and 6H SiC at temperatures 4–320 K. *Journal of Applied Physics*, 66(8):3922–3924, 1989.
- [60] Michael S Shur. *Handbook Series on Semiconductor Parameters*, volume 1. World Scientific, 1996.
- [61] Michael Shur, Sergey L Rumyantsev, et al. *SiC Materials and Devices*, volume 1. World Scientific, 2006.
- [62] Sadao Adachi. *Physical Properties of III-V Semiconductor Compounds*. John Wiley & Sons, 1992.

- [63] Sadao Adachi. *GaAs and Related Materials: Bulk Semiconducting and Superlattice Properties*. World Scientific, 1994.
- [64] Qiang Zou, Donald Lee, Frank Bi, Richard Ruby, Martha Small, Steve Ortiz, Yury Oshmyansky, and Jyrki Kaitila. High coupling coefficient temperature compensated FBAR resonator for oscillator application with wide pulling range. In *2010 IEEE International Frequency Control Symposium*, pages 646–651. IEEE, 2010.
- [65] Vikrant J Gokhale and Mina Rais-Zadeh. Phonon-electron interactions in piezoelectric semiconductor bulk acoustic wave resonators. *Scientific Reports*, 4(1):1–10, 2014.
- [66] Vikrant J Gokhale, Yonghyun Shim, and Mina Rais-Zadeh. Observation of the acoustoelectric effect in gallium nitride micromechanical bulk acoustic filters. In *2010 IEEE International Frequency Control Symposium*, pages 524–529. IEEE, 2010.
- [67] VJ Gokhale, J Roberts, and M Rais-Zadeh. High performance bulk mode gallium nitride resonators and filters. In *2011 16th International Solid-State Sensors, Actuators and Microsystems Conference*, pages 926–929. IEEE, 2011.
- [68] Laura C Popa and Dana Weinstein. L-band lamb mode resonators in gallium nitride MMIC technology. In *2014 IEEE international frequency control symposium (FCS)*, pages 1–4. IEEE, 2014.
- [69] Robert P Strittmatter. *Development of Micro-electromechanical Systems in Gallium Nitride*. California Institute of Technology, 2004.
- [70] V Cimalla, Joerg Pezoldt, and Oliver Ambacher. Group III nitride and SiC based MEMS and NEMS: materials properties, technology and applications. *Journal of Physics D: Applied Physics*, 40(20):6386, 2007.
- [71] KL Ekinci and ML Roukes. Nanoelectromechanical systems. *Review of Scientific Instruments*, 76(6):061101, 2005.
- [72] M Kuball, François Demangeot, J Frandon, MA Renucci, N Grandjean, and O Briot. Thermal stability of GaN investigated by raman scattering. *MRS Online Proceedings Library*, 537, 1998.
- [73] ICimalla, F Will, K Tonisch, M Niebelshütz, V Cimalla, V Lebedev, G Kittler, M Himmerlich, S Krischok, JA Schaefer, et al. AlGaN/GaN biosensor—effect of device processing steps on the surface properties and biocompatibility. *Sensors and Actuators B: Chemical*, 123(2):740–748, 2007.

- [74] S Tadigadapa and K Mateti. Piezoelectric MEMS sensors: state-of-the-art and perspectives. *Measurement Science and technology*, 20(9):092001, 2009.
- [75] M Eickhoff, J Schalwig, G Steinhoff, O Weidemann, L Görgens, R Neuberger, M Hermann, B Baur, G Müller, O Ambacher, et al. Electronics and sensors based on pyroelectric AlGaN/GaN heterostructures—part B: Sensor applications. *Physica Status Solidi (c)*, (6):1908–1918, 2003.
- [76] SJ Pearton, BS Kang, Suku Kim, F Ren, BP Gila, CR Abernathy, Jenshan Lin, and SNG Chu. GaN-based diodes and transistors for chemical, gas, biological and pressure sensing. *Journal of Physics: Condensed Matter*, 16(29):R961, 2004.
- [77] KH Chen, HW Wang, BS Kang, CY Chang, YL Wang, TP Lele, F Ren, SJ Pearton, A Dabiran, A Osinsky, et al. Low Hg (II) ion concentration electrical detection with AlGaN/GaN high electron mobility transistors. *Sensors and Actuators B: Chemical*, 134(2):386–389, 2008.
- [78] CY Chang, BS Kang, HT Wang, F Ren, YL Wang, SJ Pearton, DM Dennis, JW Johnson, P Rajagopal, JC Roberts, et al. CO<sub>2</sub> detection using polyethylenimine/starch functionalized AlGaN/GaN high electron mobility transistors. *Applied Physics Letters*, 92(23):232102, 2008.
- [79] Zhibo Guo, Lai Wang, Zhibiao Hao, and Yi Luo. pH sensor based on an AlGaN/GaN HEMT structure. *Procedia Engineering*, 27:693–697, 2012.
- [80] Byoung Sam Kang, Fan Ren, Lin Wang, Charles Lofton, Weihong W Tan, SJ Pearton, Al Dabiran, A Osinsky, and PP Chow. Electrical detection of immobilized proteins with ungated AlGaN/GaN high-electron-mobility transistors. *Applied Physics Letters*, 87(2):023508, 2005.
- [81] Takuya Kokawa, Taketomo Sato, Hideki Hasegawa, and Tamotsu Hashizume. Liquid-phase sensors using open-gate AlGaN/GaN high electron mobility transistor structure. *Journal of Vacuum Science & Technology B: Microelectronics and Nanometer Structures Processing, Measurement, and Phenomena*, 24(4):1972–1976, 2006.
- [82] BS Kang, J Kim, S Jang, F Ren, JW Johnson, RJ Therrien, P Rajagopal, JC Roberts, EL Piner, KJ Linthicum, et al. Capacitance pressure sensor based on GaN high-electron-mobility transistor-on-Si membrane. *Applied Physics Letters*, 86(25):253502, 2005.

- [83] Jianwen Sun, Dong Hu, Zewen Liu, Luke M Middelburg, Sten Vollebregt, Pasqualina M Sarro, and Guoqi Zhang. Low power AlGaN/GaN MEMS pressure sensor for high vacuum application. *Sensors and Actuators A: Physical*, 314:112217, 2020.
- [84] T Zimmermann, M Neuburger, P Benkart, FJ Hernández-Guillén, C Pietzka, M Kunze, I Daumiller, A Dadgar, A Krost, and E Kohn. Piezoelectric GaN sensor structures. *IEEE Electron Device Letters*, 27(5):309–312, 2006.
- [85] Irina Khmyrova and Elena Shestakova. Multi-cantilever HEMT-based resonant sensor. In *2009 IEEE International Conference on Microwaves, Communications, Antennas and Electronics Systems*, pages 1–4. IEEE, 2009.
- [86] S Vittoz, L Rufer, G Rehder, U Heinle, and P Benkart. Analytical and numerical modelling of AlGaN/GaN/AlN heterostructure based cantilevers for mechanical sensing in harsh environments. *Sensors and Actuators A: Physical*, 172(1):27–34, 2011.
- [87] Azadeh Ansari and Mina Rais-Zadeh. A thickness-mode AlGaN/GaN resonant body high electron mobility transistor. *IEEE Transactions on Electron Devices*, 61(4):1006–1013, 2014.
- [88] Azadeh Ansari, Vikrant J Gokhale, John Roberts, and Mina Rais-Zadeh. Monolithic integration of GaN-based micromechanical resonators and HEMTs for timing applications. In *2012 International Electron Devices Meeting*, pages 15–5. IEEE, 2012.
- [89] Indu Sarangadharan, Abiral Regmi, Yen-Wen Chen, Chen-Pin Hsu, Pei-chi Chen, Wen-Hsin Chang, Geng-Yen Lee, Jen-Inn Chyi, Shu-Chu Shiesh, Gwo-Bin Lee, et al. High sensitivity cardiac troponin I detection in physiological environment using AlGaN/GaN high electron mobility transistor (HEMT) biosensors. *Biosensors and Bioelectronics*, 100:282–289, 2018.
- [90] Christian A Zorman and Rocco J Parro. Micro-and nanomechanical structures for silicon carbide MEMS and NEMS. *Physica Status Solidi (b)*, 245(7):1404–1424, 2008.
- [91] K Brueckner, F Niebelshuetz, Katja Tonisch, Ch Foerster, Volker Cimalla, R Stephan, Joerg Pezoldt, Thomas Stauden, Oliver Ambacher, and MA Hein. Micro-and nano-electromechanical resonators based on SiC and group III-nitrides for sensor applications. *Physica Status Solidi (a)*, 208(2):357–376, 2011.
- [92] Takehiro Yamada, Yuto Ando, Hirotaka Watanabe, Yuta Furusawa, Atsushi Tanaka, Manato Deki, Shugo Nitta, Yoshio Honda, Jun Suda, and Hiroshi Amano. Fabrication

- of GaN cantilever on GaN substrate by photo-electrochemical etching. *Applied Physics Express*, 14(3):036505, 2021.
- [93] S Davies, TS Huang, MH Gass, AJ Papworth, TB Joyce, and PR Chalker. Fabrication of GaN cantilevers on silicon substrates for microelectromechanical devices. *Applied Physics Letters*, 84(14):2566–2568, 2004.
- [94] Jian An Lv, Zhen Chuan Yang, Gui Zheng Yan, Yong Cai, Bao Shun Zhang, and Kevin J Chen. Characterization of AlGaN/GaN cantilevers fabricated with deep-release techniques. In *Key Engineering Materials*, volume 483, pages 14–17. Trans Tech Publ, 2011.
- [95] JN Lv, ZC Yang, GZ Yan, Y Cai, BS Zhang, and KJ Chen. Characterization of GaN cantilevers fabricated with GaN-on-silicon platform. In *2011 IEEE 24th International Conference on Micro Electro Mechanical Systems*, pages 388–391. IEEE, 2011.
- [96] Alexei Bykhovski, Boris Gelmont, and Michael Shur. The influence of the strain-induced electric field on the charge distribution in GaN-AlN-GaN structure. *Journal of Applied Physics*, 74(11):6734–6739, 1993.
- [97] AD Bykhovski, BL Gelmont, and MS Shur. Elastic strain relaxation and piezoeffect in GaN-AlN, GaN-AlGaN and GaN-InGaN superlattices. *Journal of Applied Physics*, 81(9):6332–6338, 1997.
- [98] John G Gualtieri, John A Kosinski, and Arthur Ballato. Piezoelectric materials for acoustic wave applications. *IEEE Transactions on Ultrasonics, Ferroelectrics, and Frequency Control*, 41(1):53–59, 1994.
- [99] GD O’Clock Jr and MT Duffy. Acoustic surface wave properties of epitaxially grown aluminum nitride and gallium nitride on sapphire. *Applied Physics Letters*, 23(2):55–56, 1973.
- [100] Raffaele Resta. Macroscopic polarization in crystalline dielectrics: the geometric phase approach. *Reviews of Modern Physics*, 66(3):899, 1994.
- [101] RD King-Smith and David Vanderbilt. Theory of polarization of crystalline solids. *Physical Review B*, 47(3):1651, 1993.
- [102] Hyeongnam Kim, Digbijoy Nath, Siddharth Rajan, and Wu Lu. Polarization-engineered Ga-face gan-based heterostructures for normally-off heterostructure field-effect transistors. *Journal of Electronic Materials*, 42(1):10–14, 2013.

- [103] Debdeep Jena, John Simon, Albert Wang, Yu Cao, Kevin Goodman, Jai Verma, Satyaki Ganguly, Guowang Li, Kamal Karda, Vladimir Protasenko, et al. Polarization-engineering in group III-nitride heterostructures: New opportunities for device design. *Physica Status Solidi (a)*, 208(7):1511–1516, 2011.
- [104] Sumit Verma, Sajad A Loan, and Abdullah G Alharbi. Polarization engineered enhancement mode GaN HEMT: Design and investigation. *Superlattices and Microstructures*, 119:181–193, 2018.
- [105] Ho Won Jang, Jung-Hee Lee, and Jong-Lam Lee. Characterization of band bendings on Ga-face and N-face GaN films grown by metalorganic chemical-vapor deposition. *Applied Physics Letters*, 80(21):3955–3957, 2002.
- [106] R Dimitrov, M Murphy, J Smart, W Schaff, JR Shealy, LF Eastman, O Ambacher, and M Stutzmann. Two-dimensional electron gases in Ga-face and N-face AlGaN/GaN heterostructures grown by plasma-induced molecular beam epitaxy and metalorganic chemical vapor deposition on sapphire. *Journal of Applied Physics*, 87(7):3375–3380, 2000.
- [107] Diego Guerra, Marco Saraniti, Nicolas Faralli, David K Ferry, Stephen M Goodnick, and Fabio Alessio Marino. Comparison of N- and Ga-face GaN HEMTs through cellular Monte Carlo simulations. *IEEE Transactions on Electron Devices*, 57(12):3348–3354, 2010.
- [108] R Dimitrov, A Mitchell, L Wittmer, O Ambacher, M Stutzmann, J Hilsenbeck, and W Rieger. Comparison of N-face and Ga-face AlGaN/GaN-based high electron mobility transistors grown by plasma-induced molecular beam epitaxy. *Japanese Journal of Applied Physics*, 38(9R):4962, 1999.
- [109] Pil Sung Park and Siddharth Rajan. Simulation of short-channel effects in N- and Ga-polar AlGaN/GaN HEMTs. *IEEE Transactions on Electron Devices*, 58(3):704–708, 2011.
- [110] C Buchheim, AT Winzer, R Goldhahn, G Gobsch, O Ambacher, A Link, M Eickhoff, and M Stutzmann. Photoreflectance studies of (Al) Ga- and N-face AlGaN/GaN heterostructures. *Thin Solid Films*, 450(1):155–158, 2004.
- [111] Hadis Morkoc and Jacob Leach. Polarization in GaN based heterostructures and heterojunction field effect transistors (HFETs). In *Polarization Effects in Semiconductors: From Ab Initio Theory to Device Applications*, pages 373–466. Springer, 2008.

- [112] Ramakrishna Vetur. *Polarization Induced 2DEG in Aluminum Gallium Nitride/Gallium Nitride HEMTs: On the Origin, DC and Transient Characterization*. PhD thesis, University of California, Santa Barbara, 2000.
- [113] Lars Vegard. Die konstitution der mischkristalle und die raumfüllung der atome. *Zeitschrift für Physik*, 5(1):17–26, 1921.
- [114] Alan R Denton and Neil W Ashcroft. Vegard’s law. *Physical Review A*, 43(6):3161, 1991.
- [115] Michał Łopuszyński and Jacek A Majewski. Ordering in ternary nitride semiconducting alloys. *Physical Review B*, 85(3):035211, 2012.
- [116] I Vurgaftman and JR n Meyer. Band parameters for nitrogen-containing semiconductors. *Journal of Applied Physics*, 94(6):3675–3696, 2003.
- [117] Fabio Bernardini, Vincenzo Fiorentini, and David Vanderbilt. Spontaneous polarization and piezoelectric constants of III-V nitrides. *Physical Review B*, 56(16):R10024, 1997.
- [118] Lorin E Stevens. *Thermo-Piezo-Electro-Mechanical Simulation of AlGaN (Aluminum Gallium Nitride)/GaN (Gallium Nitride) High Electron Mobility Transistors*. Utah State University, 2013.
- [119] Joydeep Pal, Geoffrey Tse, Vesel Haxha, Max A Migliorato, and Stanko Tomić. Second-order piezoelectricity in wurtzite III-N semiconductors. *Physical Review B*, 84(8):085211, 2011.
- [120] Hongbo Qin, Xinghe Luan, Chuang Feng, Daoguo Yang, and Guoqi Zhang. Mechanical, thermodynamic and electronic properties of wurtzite and zinc-blende GaN crystals. *Materials*, 10(12):1419, 2017.
- [121] Achraf Ben Amar, Marc Faucher, Virginie Brandli, Yvon Cordier, and Didier Théron. Young’s modulus extraction of epitaxial heterostructure AlGaN/GaN for MEMS application. *Physica Status Solidi (a)*, 211(7):1655–1659, 2014.
- [122] Roman Nowak, M Pessa, M Saganuma, M Leszczynski, I Grzegory, S Porowski, and F Yoshida. Elastic and plastic properties of GaN determined by nano-indentation of bulk crystal. *Applied Physics Letters*, 75(14):2070–2072, 1999.
- [123] TR Lenka and AK Panda. Self-consistent subband calculations of Al<sub>x</sub>Ga<sub>1-x</sub>N/(AlN)/GaN-based high electron mobility transistor. In *Advanced Materials Research*, volume 159, pages 342–347. Trans Tech Publ, 2011.

- [124] Kyu-Seok Lee, Doo-Hyeb Yoon, Sung-Bum Bae, Mi-Ran Park, and Gil-Ho Kim. Self-consistent subband calculations of AlGaN/GaN single heterojunctions. *ETRI Journal*, 24(4):270–279, 2002.
- [125] O Ambacher, J Smart, JR Shealy, NG Weimann, K Chu, M Murphy, WJ Schaff, LF Eastman, R Dimitrov, L Wittmer, et al. Two-dimensional electron gases induced by spontaneous and piezoelectric polarization charges in N- and Ga-face AlGaN/GaN heterostructures. *Journal of Applied Physics*, 85(6):3222–3233, 1999.
- [126] TR Lenka, GN Dash, and AK Panda. 2DEG transport characteristics by self-consistent subband calculations of schrödinger and poisson equations in InAlN/GaN HEMT. In *2014 IEEE 9th Nanotechnology Materials and Devices Conference (NMDC)*, pages 124–127. IEEE, 2014.
- [127] Chunyan Jiang. *Applications of Piezotronics and Piezophotonics in Gallium Nitride Based Devices*. PhD thesis, University of Chinese Academy of Sciences, 2018.
- [128] Karen Reinhardt and Werner Kern. *Handbook of Silicon Wafer Cleaning Technology*. William Andrew, 2018.
- [129] SW King, JP Barnak, MD Bremser, KM Tracy, C Ronning, RF Davis, and RJ Nemanich. Cleaning of AlN and GaN surfaces. *Journal of Applied Physics*, 84(9):5248–5260, 1998.
- [130] Yukihiko Tsuji, Tsukuru Katsuyama1 Akinobu Teramoto, Yasuyuki Shirai, Shigetoshi Sugawa, and Tadahiro Ohmi. Wet cleaning process for GaN surface at room temperature.
- [131] Mangey Ram and J Paulo Davim. *Advanced Applications in Manufacturing Engineering*. Woodhead Publishing, 2018.
- [132] Ludwig Reimer. *Scanning Electron Microscopy: physics of image formation and microanalysis*. IOP Publishing, 2000.
- [133] Joseph I Goldstein, Dale E Newbury, Joseph R Michael, Nicholas WM Ritchie, John Henry J Scott, and David C Joy. *Scanning Electron Microscopy and X-ray Microanalysis*. Springer, 2017.
- [134] Ewen Smith and Geoffrey Dent. *Modern Raman Spectroscopy: a practical approach*. John Wiley & Sons, 2019.

- [135] Hiroshi Amano, N Sawaki, I Akasaki, and Y Toyoda. Metalorganic vapor phase epitaxial growth of a high quality GaN film using an AlN buffer layer. *Applied Physics Letters*, 48(5):353–355, 1986.
- [136] Isamu Akasaki, Hiroshi Amano, Yasuo Koide, Kazumasa Hiramatsu, and Nobuhiko Sawaki. Effects of ain buffer layer on crystallographic structure and on electrical and optical properties of GaN and Ga<sub>1-x</sub>Al<sub>x</sub>N ( $0 < x \leq 0.4$ ) films grown on sapphire substrate by MOVPE. *Journal of Crystal Growth*, 98(1-2):209–219, 1989.
- [137] Chris Mack. *Fundamental Principles of Optical Lithography: the science of microfabrication*. John Wiley & Sons, 2008.
- [138] Ming Yang, Zhaojun Lin, Jingtao Zhao, Yutang Wang, Zhiyuan Li, Yuanjie Lv, and Zhihong Feng. Influence of sapphire substrate thickness on the characteristics of Al-GaN/AlN/GaN heterostructure field-effect transistors. *Superlattices and Microstructures*, 85:43–49, 2015.
- [139] Sukwon Choi, Eric Heller, Donald Dorsey, Ramakrishna Vetury, and Samuel Graham. Analysis of the residual stress distribution in AlGaN/GaN high electron mobility transistors. *Journal of Applied Physics*, 113(9):093510, 2013.
- [140] Julien Ladroue, Aline Meritan, Mohamed Boufnichel, Philippe Lefaucheux, Pierre Ranson, and Remi Dussart. Deep GaN etching by inductively coupled plasma and induced surface defects. *Journal of Vacuum Science & Technology A: Vacuum, Surfaces, and Films*, 28(5):1226–1233, 2010.
- [141] SJ Pearton, RJ Shul, and Fan Ren. A review of dry etching of GaN and related materials. *Materials Research Society Internet Journal of Nitride Semiconductor Research*, 5(1), 2000.
- [142] Kuo-Chin Huang, Wen-How Lan, and Kai Feng Huang. Inductively coupled plasma reactive ion etching-induced GaN defect studied by Schottky current transport analysis. *Japanese Journal of Applied Physics*, 43(1R):82, 2004.
- [143] XA Cao, AP Zhang, GT Dang, F Ren, SJ Pearton, RJ Shul, and L Zhang. Schottky diode measurements of dry etch damage in n- and p-type GaN. *Journal of Vacuum Science & Technology A: Vacuum, Surfaces, and Films*, 18(4):1144–1148, 2000.
- [144] Kyoung Jin Choi, Ho Wan Jang, and Jong-Lam Lee. Observation of inductively coupled-plasma-induced damage on n-type GaN using deep-level transient spectroscopy. *Applied Physics Letters*, 82(8):1233–1235, 2003.

- [145] Chao-Yi Fang, Weng-Jung Huang, Edward Yi Chang, Chia-Feng Lin, and Ming-Shiann Feng. Etching damages on AlGaN, GaN and InGaN caused by hybrid inductively coupled plasma etch and photoenhanced chemical wet etch by Schottky contact characterizations. *Japanese Journal of Applied Physics*, 42(7R):4207, 2003.
- [146] Jie Liu, Chong Wang, Qian Feng, Jincheng Zhang, Yue Hao, Yan Yang, and Xin Gong. Influence of ICP induced damage in n-type GaN on Ni/Au Schottky contact characteristics. *Semiconductor Technology*, 32(1):40–42, 81, 1 2007.
- [147] Li-Yuan Yang, Yue Hao, Xiao-Hua Ma, Jin-Cheng Zhang, Cai-Yuan Pan, Ji-Gang Ma, Kai Zhang, and Ping Ma. High temperature characteristics of AlGaN/GaN high electron mobility transistors. *Chinese Physics B*, 20(11):117302, 2011.
- [148] Ali Hajjiah, Asmaa Alkhabbaz, Hussein Badran, and Ivan Gordon. The effect of temperature on the forward bias electrical characteristics of both pure ni and oxidized Ni/Au Schottky contacts on n-type GaN: A case study. *Results in Physics*, 19:103656, 2020.
- [149] G Greco, S Di Franco, F Iucolano, F Giannazzo, and F Roccaforte. Temperature dependence of the I–V characteristics of Ni/Au Schottky contacts to AlGaN/GaN heterostructures grown on Si substrates. *Physica Status Solidi (a)*, 214(9):1600764, 2017.
- [150] Robin R Murphy. *Introduction to AI Robotics*. MIT Press, 2019.
- [151] Murat Dikmen and Catherine M Burns. Autonomous driving in the real world: Experiences with tesla autopilot and summon. pages 225–228. Association for Computing Machinery, 2016.
- [152] Owies M Wani, Hao Zeng, and Arri Priimagi. A light-driven artificial flytrap. *Nature Communications*, 8(1):1–7, 2017.
- [153] Yu Zhao, Fuji Sakai, Lu Su, Yijiang Liu, Kongchang Wei, Guosong Chen, and Ming Jiang. Progressive macromolecular self-assembly: From biomimetic chemistry to bio-inspired materials. *Advanced Materials*, 25(37):5215–5256, 2013.
- [154] Remi Geiger, Vincent Ménoret, Guillaume Stern, Nassim Zahzam, Patrick Cheinet, Baptiste Battelier, André Villing, Frédéric Moron, Michel Lours, Yannick Bidel, et al. Detecting inertial effects with airborne matter-wave interferometry. *Nature Communications*, 2(1):1–7, 2011.
- [155] Honggu Chun and Taek Dong Chung. Iontronics. *Annual Review of Analytical Chemistry*, 8:441–462, 2015.

- [156] Sigurd Wagner, Stéphanie P Lacour, Joyelle Jones, I Hsu Pai-hui, James C Sturm, Teng Li, and Zhigang Suo. Electronic skin: architecture and components. *Physica E: Low-dimensional Systems and Nanostructures*, 25(2-3):326–334, 2004.
- [157] Frank Röck, Nicolae Barsan, and Udo Weimar. Electronic nose: current status and future trends. *Chemical Reviews*, 108(2):705–725, 2008.
- [158] Christina L Runge, Fang Du, and Yi Hu. Improved speech perception in cochlear implant users with interleaved high-rate pulse trains. *Otology & Neurotology*, 39(5):e319–e324, 2018.
- [159] Sandy MS Choi, Eddie CM Wong, and Bradley McPherson. Aided cortical auditory evoked measures with cochlear implantees: the challenge of stimulus artefacts. *Hearing, Balance and Communication*, 17(3):229–238, 2019.
- [160] CM Light and PH Chappell. Development of a lightweight and adaptable multiple-axis hand prosthesis. *Medical Engineering & Physics*, 22(10):679–684, 2000.
- [161] Louis D Lowry. Artificial larynges: A review and development of a prototype self-contained intra-oral artificial larynx. *The Laryngoscope*, 91(8):1332–1355, 1981.
- [162] Chenyang Xue, Shang Chen, Wendong Zhang, Binzhen Zhang, Guojun Zhang, and Hui Qiao. Design, fabrication, and preliminary characterization of a novel MEMS bionic vector hydrophone. *Microelectronics Journal*, 38(10-11):1021–1026, 2007.
- [163] Sicun Duan, Weidong Wang, Sai Zhang, Xi Yang, Yu Zhang, and Guojun Zhang. A bionic MEMS electronic stethoscope with double-sided diaphragm packaging. *IEEE Access*, 9:27122–27129, 2021.
- [164] Wenjun Zhang, Congcong Hao, Zengxing Zhang, Shasha Yang, Jiali Peng, Bin Wu, Xiaobin Xue, Junbin Zang, Xu Chen, Hua Yang, et al. Vector high-resolution marine turbulence sensor based on a MEMS bionic cilium-shaped structure. *IEEE Sensors Journal*, 21(7):8741–8750, 2020.
- [165] Salmah B Karman, Mark O MacQueen, Tina R Matin, S Zaleha M Diah, Jeanette Mueller, Jumril Yunas, Teresa Makaruk, and Ille C Gebeshuber. *On the way to the bionic man: A novel approach to MEMS based on biological sensory systems*, volume 254. Trans Tech Publ, 2011.
- [166] L Shen, S Heikman, B Moran, R Coffie, N-Q Zhang, D Buttari, IP Smorchkova, S Keller, SP DenBaars, and UK Mishra. AlGaN/AlN/GaN high-power microwave HEMT. *IEEE Electron Device Letters*, 22(10):457–459, 2001.

- [167] N-Q Zhang, S Keller, Giacinta Parish, S Heikman, SP DenBaars, and UK Mishra. High breakdown GaN HEMT with overlapping gate structure. *IEEE Electron Device Letters*, 21(9):421–423, 2000.
- [168] Zhenfu Zhao, Xiong Pu, Changbao Han, Chunhua Du, Linxuan Li, Chunyan Jiang, Weiguo Hu, and Zhong Lin Wang. Piezotronic effect in polarity-controlled GaN nanowires. *Acs Nano*, 9(8):8578–8583, 2015.
- [169] Qilin Hua, Junlu Sun, Haitao Liu, Xiao Cui, Keyu Ji, Wenbin Guo, Caofeng Pan, Weiguo Hu, and Zhong Lin Wang. Flexible GaN microwire-based piezotronic sensory memory device. *Nano Energy*, 78:105312, 2020.
- [170] Robert B Daroff and Michael J Aminoff. *Encyclopedia of the Neurological Sciences*. Academic Press, 2014.
- [171] Jianpeng Cheng, Xuelin Yang, Ling Sang, Lei Guo, Anqi Hu, Fujun Xu, Ning Tang, Xinqiang Wang, and Bo Shen. High mobility algan/gan heterostructures grown on Si substrates using a large lattice-mismatch induced stress control technology. *Applied Physics Letters*, 106(14):142106, 2015.
- [172] Wen-How Lan, Kuo-Chin Huang, and Kai Feng Huang. ICP-induced defects in GaN characterized by capacitance analysis. *Solid-State Electronics*, 50(11-12):1677–1681, 2006.
- [173] David Dreyer, Barrie Frost, Henrik Mouritsen, Anja Günther, Ken Green, Mary Whitehouse, Sönke Johnsen, Stanley Heinze, and Eric Warrant. The earth’s magnetic field and visual landmarks steer migratory flight behavior in the nocturnal australian bogong moth. *Current Biology*, 28(13):2160–2166, 2018.
- [174] JH Fischer, MJ Freake, SC Borland, and JB Phillips. Evidence for the use of magnetic map information by an amphibian. *Animal Behaviour*, 62(1):1–10, 2001.
- [175] Francisco J Diego-Rasilla, Valentín Pérez-Mellado, and Ana Pérez-Cembranos. Spontaneous magnetic alignment behaviour in free-living lizards. *The Science of Nature*, 104(3):1–12, 2017.
- [176] Lewis C Naisbett-Jones, Nathan F Putman, Michelle M Scanlan, David LG Noakes, and Kenneth J Lohmann. Magnetoreception in fishes: the effect of magnetic pulses on orientation of juvenile pacific salmon. *Journal of Experimental Biology*, 223(10):jeb222091, 2020.

- [177] Klaus-Peter Ossenkopp and Raphael Barbeito. Bird orientation and the geomagnetic field: A review. *Neuroscience & Biobehavioral Reviews*, 2(4):255–270, 1978.
- [178] Thorsten Ritz, Salih Adem, and Klaus Schulten. A model for photoreceptor-based magnetoreception in birds. *Biophysical Journal*, 78(2):707–718, 2000.
- [179] Dmitry Kishkinev, Nikita Chernetsov, Alexander Pakhomov, Dominik Heyers, and Henrik Mouritsen. Eurasian reed warblers compensate for virtual magnetic displacement. *Current Biology*, 25(19):R822–R824, 2015.
- [180] Henrik Mouritsen and Thorsten Ritz. Magnetoreception and its use in bird navigation. *Current Opinion in Neurobiology*, 15(4):406–414, 2005.
- [181] Jong Min Ong and Lyndon da Cruz. The bionic eye: a review. *Clinical & Experimental Ophthalmology*, 40(1):6–17, 2012.
- [182] Li Qiang Zhu, Chang Jin Wan, Li Qiang Guo, Yi Shi, and Qing Wan. Artificial synapse network on inorganic proton conductor for neuromorphic systems. *Nature Communications*, 5(1):1–7, 2014.
- [183] Xinqin Liao, Weitao Song, Xiangyu Zhang, Chaoqun Yan, Tianliang Li, Hongliang Ren, Cunzhi Liu, Yongtian Wang, and Yuanjin Zheng. A bioinspired analogous nerve towards artificial intelligence. *Nature Communications*, 11(1):1–9, 2020.
- [184] Yue Cao, Yu Jun Tan, Si Li, Wang Wei Lee, Hongchen Guo, Yongqing Cai, Chao Wang, and Benjamin C-K Tee. Self-healing electronic skins for aquatic environments. *Nature Electronics*, 2(2):75–82, 2019.
- [185] Gilbert Santiago Cañón Bermúdez, Hagen Fuchs, Lothar Bischoff, Jürgen Fassbender, and Denys Makarov. Electronic-skin compasses for geomagnetic field-driven artificial magnetoreception and interactive electronics. *Nature Electronics*, 1(11):589–595, 2018.
- [186] Pavlo Makushko, Eduardo Sergio Oliveros Mata, Gilbert Santiago Cañón Bermúdez, Mariam Hassan, Sara Laureti, Christian Rinaldi, Federico Fagiani, Gianni Barucca, Natalia Schmidt, Yevhen Zabila, et al. Flexible magnetoreceptor with tunable intrinsic logic for on-skin touchless human-machine interfaces. *Advanced Functional Materials*, 31(25):2101089, 2021.
- [187] Gilbert Santiago Cañón Bermúdez, Dmitriy D Karnaushenko, Daniil Karnaushenko, Ana Lebanov, Lothar Bischoff, Martin Kaltenbrunner, Jürgen Fassbender, Oliver G

- Schmidt, and Denys Makarov. Magnetosensitive e-skins with directional perception for augmented reality. *Science Advances*, 4(1):eaao2623, 2018.
- [188] Michael Melzer, Jens Ingolf Mönch, Denys Makarov, Yevhen Zabila, Gilbert Santiago Cañón Bermúdez, Daniil Karnaushenko, Stefan Baunack, Falk Bahr, Chenglin Yan, Martin Kaltenbrunner, et al. Wearable magnetic field sensors for flexible electronics. *Advanced Materials*, 27(7):1274–1280, 2015.
- [189] Tetsuzo Ueda. Gan power devices: Current status and future challenges. *Japanese Journal of Applied Physics*, 58(SC):SC0804, 2019.
- [190] Oliver Ambacher, B Foutz, Joseph Smart, JR Shealy, NG Weimann, K Chu, M Murphy, AJ Sierakowski, WJ Schaff, LF Eastman, et al. Two dimensional electron gases induced by spontaneous and piezoelectric polarization in undoped and doped AlGaN/GaN heterostructures. *Journal of Applied Physics*, 87(1):334–344, 2000.
- [191] Qilin Hua, Xiao Cui, Keyu Ji, Bingjun Wang, and Weiguo Hu. Piezotronics enabled artificial intelligence systems. *Journal of Physics: Materials*, 4(2):022003, 2021.
- [192] Sönke Johnsen and Kenneth J Lohmann. The physics and neurobiology of magnetoreception. *Nature Reviews Neuroscience*, 6(9):703–712, 2005.
- [193] Shuo Zhang, Bei Ma, Xingyu Zhou, Qilin Hua, Jian Gong, Ting Liu, Xiao Cui, Jiyuan Zhu, Wenbin Guo, Liang Jing, et al. Strain-controlled power devices as inspired by human reflex. *Nature Communications*, 11(1):1–9, 2020.
- [194] AE Romanov, TJ Baker, S Nakamura, JS Speck, and ERATO/JST UCSB Group. Strain-induced polarization in wurtzite III-nitride semipolar layers. *Journal of Applied Physics*, 100(2):023522, 2006.
- [195] B Jogai. Free electron distribution in AlGaN/GaN heterojunction field-effect transistors. *Journal of Applied Physics*, 91(6):3721–3729, 2002.
- [196] I-H Tan, GL Snider, LD Chang, and EL Hu. A self-consistent solution of schrödinger-poisson equations using a nonuniform mesh. *Journal of Applied Physics*, 68(8):4071–4076, 1990.
- [197] Carver Mead. Neuromorphic electronic systems. *Proceedings of the IEEE*, 78(10):1629–1636, 1990.
- [198] Steve Furber. Large-scale neuromorphic computing systems. *Journal of Neural Engineering*, 13(5):051001, 2016.

- [199] Umesh Kumar Bhaskar, Nirupam Banerjee, Amir Abdollahi, Zhe Wang, Darrell G Schlom, Guus Rijnders, and Gustau Catalan. A flexoelectric microelectromechanical system on silicon. *Nature Nanotechnology*, 11(3):263–266, 2016.
- [200] PV Yudin and AK Tagantsev. Fundamentals of flexoelectricity in solids. *Nanotechnology*, 24(43):432001, 2013.
- [201] Pavlo Zubko, Gustau Catalan, and Alexander K Tagantsev. Flexoelectric effect in solids. *Annual Review of Materials Research*, 43:387–421, 2013.
- [202] Z Yan and LY Jiang. Flexoelectric effect on the electroelastic responses of bending piezoelectric nanobeams. *Journal of Applied Physics*, 113(19):194102, 2013.
- [203] Longlong Shu, Renhong Liang, Zhenggang Rao, Linfeng Fei, Shanming Ke, and Yu Wang. Flexoelectric materials and their related applications: A focused review. *Journal of Advanced Ceramics*, 8(2):153–173, 2019.
- [204] Junyi Zhai, Yong Qin, and Zhong Lin Wang. Flexoelectronics of centrosymmetric semiconductors. *Strain*, 1:2.
- [205] Longfei Wang, Shuhai Liu, Xiaolong Feng, Chunli Zhang, Laipan Zhu, Junyi Zhai, Yong Qin, and Zhong Lin Wang. Flexoelectronics of centrosymmetric semiconductors. *Nature Nanotechnology*, 15(8):661–667, 2020.

# Appendix A

## Publication Titles

1. **Xingyu Zhou**, Qilin Hua, Wei Sha, Jiyuan Zhu, Ting Liu, Chunyan Jiang, Qi Guo, Liang Jing, Chunhua Du, Junyi Zhai, Weiguo Hu, Zhong Lin Wang. Magnetosensory power devices based on AlGaN/GaN heterojunctions for interactive electronics. *Advanced Electronic Materials*, 2023,
  - <https://onlinelibrary.wiley.com/doi/full/10.1002aelm.202200941>
2. Shuo Zhang‡, Bei Ma‡, **Xingyu Zhou‡** (‡ co-first authors), Qilin Hua, Jian Gong, Ting Liu, Xiao Cui, Jiyuan Zhu, Wenbin Guo, Liang Jing, Weiguo Hu, Zhong Lin Wang. Strain-controlled power devices as inspired by human reflex. *Nature Communications*, 2020, 11(1): 1-9.
  - <https://www.nature.com/articles/s41467-019-14234-7>
3. Jiyuan Zhu‡, **Xingyu Zhou‡** (‡ co-first authors), Liang Jing, Qilin Hua, Weiguo Hu, Zhong Lin Wang. Piezotronic effect modulated flexible AlGaN/GaN high-electron-mobility transistors. *ACS Nano*, 2019, 13(11): 13161-13168.
  - <https://pubs.acs.org/doi/abs/10.1021/acsnano.9b05999>

# Magnetosensory Power Devices Based on AlGaN/GaN Heterojunctions for Interactive Electronics

Xingyu Zhou, Qilin Hua, Wei Sha, Jiyuan Zhu, Ting Liu, Chunyan Jiang, Qi Guo, Liang Jing, Chunhua Du, Junyi Zhai,\* Weiguo Hu,\* and Zhong Lin Wang\*

The advances in biological magnetoreception and microelectronics have promoted the vigorous development of interactive electronic devices capable of noncontact interaction and control via magnetic fields. Here, a magnetosensory power device (MPD) that integrates a magnetic film ( $(\text{Fe}_{90}\text{Co}_{10})_{78}\text{Si}_{12}\text{B}_{10}$ ) unit into a cantilever-structured AlGaN/GaN-based high-electron-mobility-transistor is presented. The MPD is capable to not only sense external magnetic field, but also control device output power with the emulation of magnetoreception. Specifically, the device can achieve significant control of output power density (18.04 to 18.94 W mm<sup>-2</sup>) quasi-linearly with magnetic field stimuli (0–400 mT) at a gate bias of –5 V. In addition, the maximum output power density of the MPD can reach 85.8 W mm<sup>-2</sup> when a gate bias of 1 V is applied. The simulation and experimental results show that MPD has excellent orientation and magnetic field sensing functions under 0–400 mT magnetic fields. With the intelligent capabilities of magnetic sense and output power control, such interactive electronic devices will have broad application prospects in the fields of artificial intelligence, advanced robotics, and human-machine interfaces.

## 1. Introduction

Biological studies have suggested that a variety of animals have the ability to perceive the geomagnetic field, including insects,<sup>[1]</sup> amphibians,<sup>[2]</sup> reptiles,<sup>[3]</sup> fish,<sup>[4]</sup> and birds.<sup>[5]</sup> Migratory birds, for instance, have been suggested to not only orient themselves by sensing the inclination of the field,<sup>[6]</sup> but also may deduce their location by discerning minute local variations in the geomagnetic field.<sup>[7,8]</sup> Driven by the ongoing rapid advance of artificial intelligence (AI), neuroscience, and bionics, the development of bionic smart devices has made significant progress, such as the bionic eye,<sup>[9]</sup> artificial synapse network,<sup>[10]</sup> bionic artificial nerve,<sup>[11]</sup> bionic skins,<sup>[12]</sup> etc. The biomimetic applications of magnetoreception in nature would be an appealing source from which inspiration can be drawn to develop magnetosensory

X. Zhou, Q. Hua, W. Sha, C. Jiang, Q. Guo, L. Jing, J. Zhai,  
 W. Hu, Z. L. Wang  
 CAS Center for Excellence in Nanoscience  
 Beijing Key Laboratory of Micro-nano Energy and Sensor  
 Beijing Institute of Nanoenergy and Nanosystems  
 Chinese Academy of Sciences  
 Beijing 101400, China  
 E-mail: jy়zai@binn.cas.cn; huweiguo@binn.cas.cn;  
 zhong.wang@mse.gatech.edu

X. Zhou, Q. Hua, W. Sha, C. Jiang, Q. Guo, L. Jing, J. Zhai,  
 W. Hu, Z. L. Wang  
 School of Nanoscience and Technology  
 University of Chinese Academy of Sciences  
 Beijing 100049, China

J. Zhu  
 State Key Laboratory of ASIC and System  
 School of Microelectronics  
 Fudan University  
 Shanghai 200433, China

 The ORCID identification number(s) for the author(s) of this article can be found under <https://doi.org/10.1002/aelm.202200941>.

© 2023 The Authors. Advanced Electronic Materials published by Wiley-VCH GmbH. This is an open access article under the terms of the Creative Commons Attribution License, which permits use, distribution and reproduction in any medium, provided the original work is properly cited.

DOI: [10.1002/aelm.202200941](https://doi.org/10.1002/aelm.202200941)

T. Liu  
 College of Mathematics and Physics  
 Beijing University of Chemical Technology  
 Beijing 100029, China

C. Du  
 Key Laboratory for Renewable Energy  
 Beijing Key Laboratory for New Energy Materials and Devices  
 Beijing National Laboratory for Condensed Matter Physics  
 Institute of Physics  
 Chinese Academy of Science  
 Beijing 100190, China

J. Zhai, W. Hu, Z. L. Wang  
 Research Center for Optoelectronic Materials and Devices  
 School of Physical Science and Technology  
 Guangxi University  
 Nanning 530004, China

Z. L. Wang  
 School of Materials Science and Engineering  
 Georgia Institute of Technology  
 Atlanta, GA 30332-0245, USA

## ARTICLE

<https://doi.org/10.1038/s41467-019-14234-7>

OPEN

# Strain-controlled power devices as inspired by human reflex

Shuo Zhang<sup>1,2,7</sup>, Bei Ma<sup>3,7</sup>, Xingyu Zhou<sup>1,2,7</sup>, Qilin Hua<sup>1,2\*</sup>, Jian Gong<sup>4</sup>, Ting Liu<sup>1,2</sup>, Xiao Cui<sup>1,2</sup>, Jiyuan Zhu<sup>1,2</sup>, Wenbin Guo<sup>1,2</sup>, Liang Jing<sup>1,2</sup>, Weiguo Hu<sup>1,2,5\*</sup> & Zhong Lin Wang<sup>1,2,5,6\*</sup>

Bioinspired electronics are rapidly promoting advances in artificial intelligence. Emerging AI applications, e.g., autopilot and robotics, increasingly spur the development of power devices with new forms. Here, we present a strain-controlled power device that can directly modulate the output power responses to external strain at a rapid speed, as inspired by human reflex. By using the cantilever-structured AlGaN/AlN/GaN-based high electron mobility transistor, the device can control significant output power modulation ( $2.30\text{--}2.72 \times 10^3 \text{ W cm}^{-2}$ ) with weak mechanical stimuli (0–16 mN) at a gate bias of 1 V. We further demonstrate the acceleration-feedback-controlled power application, and prove that the output power can be effectively adjusted at real-time in response to acceleration changes, i.e.,  $\Delta P$  of  $72.78\text{--}132.89 \text{ W cm}^{-2}$  at an acceleration of 1–5 G at a supply voltage of 15 V. Looking forward, the device will have great significance in a wide range of AI applications, including autopilot, robotics, and human-machine interfaces.

<sup>1</sup>CAS Center for Excellence in Nanoscience, Beijing Key Laboratory of Micro-nano Energy and Sensor, Beijing Institute of Nanoenergy and Nanosystems, Chinese Academy of Sciences, Beijing 100083, China. <sup>2</sup>School of Nanoscience and Technology, University of Chinese Academy of Sciences, Beijing 100049, P. R. China. <sup>3</sup>Graduate School of Electrical and Electronic Engineering, Chiba University, Chiba 263-8522, Japan. <sup>4</sup>Estuarine and Coastal Environment Research Center, Chinese Research Academy of Environmental Sciences, Beijing 100012, P. R. China. <sup>5</sup>Center on Nanoenergy Research, School of Physical Science and Technology, Guangxi University, Nanning 530004, China. <sup>6</sup>School of Materials Science and Engineering, Georgia Institute of Technology, Atlanta, GA 30332-0245, USA. <sup>7</sup>These authors contributed equally: Shuo Zhang, Bei Ma, Xingyu Zhou. \*email: [huaqilin@binn.cas.cn](mailto:huaqilin@binn.cas.cn); [huweiguo@binn.cas.cn](mailto:huweiguo@binn.cas.cn); [zhong.wang@mse.gatech.edu](mailto:zhong.wang@mse.gatech.edu)

# Piezotronic Effect Modulated Flexible AlGaN/GaN High-Electron-Mobility Transistors

Jiyuan Zhu,<sup>†,‡,§</sup> Xingyu Zhou,<sup>†,‡,§</sup> Liang Jing,<sup>†,‡</sup> Qilin Hua,<sup>†,‡,§</sup> Weiguo Hu,<sup>\*,†,‡,§,||</sup> and Zhong Lin Wang<sup>\*,†,‡,§,||</sup>

<sup>†</sup>CAS Center for Excellence in Nanoscience, Beijing Key Laboratory of Micro-Nano Energy and Sensor, Beijing Institute of Nanoenergy and Nanosystems, Chinese Academy of Sciences, Beijing 100083, China

<sup>‡</sup>School of Nanoscience and Technology, University of Chinese Academy of Sciences, Beijing 100049, China

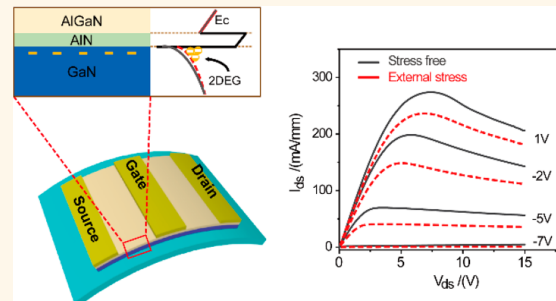
<sup>§</sup>Center on Nanoenergy Research, School of Physical Science and Technology, Guangxi University, Nanning 530004, China

<sup>||</sup>School of Materials Science and Engineering, Georgia Institute of Technology, Atlanta, Georgia 30332-0245, United States

## Supporting Information

**ABSTRACT:** Flexible electronic technology has attracted great attention due to its wide range of potential applications in the fields of healthcare, robotics, and artificial intelligence, etc. In this work, we have successfully fabricated flexible AlGaN/GaN high-electron-mobility transistors (HEMTs) arrays through a low-damage and wafer-scale substrate transfer technology from a rigid Si substrate. The flexible AlGaN/GaN HEMTs have excellent electrical performances with the  $I_{d,max}$  achieving 290 mA/mm at  $V_{gs} = +2$  V and the  $g_{m,max}$  reaching to 40 mS/mm. The piezotronic effect provides a different freedom to optimize device performances, and flexible HEMTs can endure the larger mechanical distortions. Based on the piezotronic effect, we applied an external stress to significantly modulate the electrical performances of flexible HEMTs. The piezotronic effect modulated flexible AlGaN/GaN HEMTs exhibit great potential in human-machine interface, intelligent microinductor systems, and active sensors, etc, and introduce an opportunity to sensing or feedback external mechanical stimuli and so on.

**KEYWORDS:** AlGaN/GaN high-electron-mobility transistors, flexible substrate, piezotronic effect, two-dimensional electron gas, wafer-scale



In recent years, flexible electronic technology has shown a rapid development trend,<sup>1</sup> opening a wide range of potential applications for energy harvesting, medical healthcare, consumer electronics, robotics, etc.<sup>2</sup> Thanks to the high saturation drift velocity, high sheet carrier concentration, wide band gap, and excellent frequency characteristics,<sup>3</sup> AlGaN/GaN high-electron-mobility transistors (HEMTs) are the best candidates for radio frequency (RF), microwave devices and power devices and so on.<sup>4</sup> The flexible HEMTs are expected to satisfy the urgent requirements of the wireless communication and electrical supply in flexible electronics. However, due to the limitation of growth kinetics, AlGaN/GaN HEMTs are usually fabricated on rigid substrates such as Si, sapphire, or SiC, thus they cannot be applied to nonplanar environments and are hard to deform. The substrate transfer technology has received a lot of attention and rapid developments, and some flexible AlGaN/GaN HEMTs have been fabricated with various substrate transfer technologies, for example, a mechanical lapping and etching,<sup>5</sup> a sacrificial 2D

boron nitride layer,<sup>6</sup> and a xenon difluoride etching.<sup>7</sup> Alleviating the devices performances degradation on flexible substrates is still a significant issue. In addition, flexible substrates provide some different functions such as flexible structures, stretchable structures, and curved conformal installations, which induce complex stress distribution to greatly affect the electrical characteristics.<sup>8</sup>

The piezotronic effect proposed by Z. L. Wang utilizes piezoelectric polarization charge to change the energy band structure at the interface or junction to control carrier transport.<sup>9–12</sup> III-nitrides are ideal piezotronic materials and have wide industrial applications. The AlGaN and GaN have strong spontaneous polarization and piezoelectric polarization, resulting in a strong polarization electric field in the AlGaN/

Received: July 30, 2019

Accepted: October 21, 2019

Published: October 21, 2019

## **Appendix B**

### **Micro/Nano-fabrication Equipment**

Inductively Coupled Plasma Etching	SENTECH SI 500
E-Beam Evaporation	Denton Vacuum Explore 14
Rapid Thermal Processing	LABSYS RTP-1200
Magnetron Sputtering	Denton Discovery 635
Photolithography	SUSS MA6
Raman Spectroscopy	HORIBA LabRAM HR Evolution
X-ray Diffraction	Bruker D8 DISCOVER
Semiconductor Device Parameter Analyzer	Keysight B1500
Scanning Electron Microscopy	FEI Nova Nano SEM 450
Focused Ion Beam	FEI Helios NanoLab 600i
Transmission Electron Microscope	TECNAI F20
Metal-organic Chemical Vapor Deposition	Aixtron CCS 3×2 MOCVD
Atomic force microscopy	Asylum Research MFP-3D-SA-DV
Plasma Cleaner	PVA TePla IoN 40

# **Appendix C**

## **MATLAB Code for Theoretical Model**

### **Guidence**

This MATLAB code is the programming realization of the theoretical model developed in chapter 2. It consists of main program (Main.m), parameter subprogram (Parameter.m), Fermi level subprogram (Fermi\_level.m), Poisson equation subprogram (Poisson.m), Schrodinger equation subprogram (Schrodinger.m), device structure subprogram (Structure.m), and piezo-electric polarization charge subprogram (Polaration.m). Given the strain states obtained from COMSOL Multiphysics, the corresponding polarization charge can be calculated by the polarization charge subprogram and substituted into the structure subprogram. The structure subprogram defines the heterostructure of AlGaN/AlN/GaN, and can be modified according to the designed device structure. Finally, the corresponding energy band, carrier distribution and 2DEG concentration can be solved through the main program.

Here only main program (Main.m) is attached for reference. All intellectual property rights reserved. Any request for full program for academic research is warmly welcome, and could contact me via email xingyu.zhou.phd@gmail.com.

## MATLAB M Files

### Main.m

```

1 clear all;
2 % main function
3
4 %parameters
5 global m0          % electron mass (Unit:kg)
6 global h           % Planck's constant (unit:J*s)
7 global h1          % Planck's constant (unit:J*s)
8 global Kb          % Boltzmann constant (Unit:eV/K)
9 global pi          % pi
10 global eps0        % vacuum dielectric constant (Unit:F/m)
11 global e           % electron charge (Unit:C)
12 global ev          % ev to J (unit:J/ev)
13 global T           % room temperature (Unit:K)
14 global N           % Mesh number
15 global L           % Well structure (unit:m)
16 global dz          % Step lenth (unit:m)
17 global me          % Electron effecive mass distribution
18 global mhh         % hole effecive mass
19 global Ed          % Donor ionization energy distribution (Unit:eV)
20 global eps          % dielectric constant (Unit:F/m)
21 global Esf3         % Material-3 surface potential (Unit:eV)
22 global miu;        % Sheet polarizition charge(unit:C/m^2)
23 global A           % Schrodinger Matrix
24 global Psi          % Wavefunction
25 global Psi_0        % Origin Wavefunction
26 global Ei          % eigenergy (Unit:eV)
27 global Psi1         % 1st Wavefunction
28 global Ei1          % 1st eigenergy (Unit:eV)
29 global na          % Free electron sheet concentration (Unit: 1/m^2)
30 global n           % Free electron distribution (unit:1/m^3)
31 global n_j_sum     % Total Free electron concentration (Unit: 1/m^2)
32 global Nd          % ionized donor concentration (unit:1/m^3)
33 global Nd_sum      % Total ionized donor concentration (unit:1/m^2)
34 global Nd0_sum     % Total donor concentration (unit:1/m^2)

```

---

```

35 global Esd3      % Material-3 surface donor state ionization energy (Unit:eV)
36 global Esa3      % Material-3 acceptor donor state ionization energy (Unit:eV)
37 global Esf3      % Material-3 surface potential (Unit:eV)
38 global Nsd0      % surface donor state concentration (unit:1/m^2)
39 global Nsa0      % surface acceptor state concentration (unit:1/m^2)
40 global Nsd      % surface donor state concentration (unit:1/m^3)
41 global Nsa      % surface donor state concentration (unit:1/m^3)
42 global ro       % Total charge concentration (unit:1/m^2)
43 global sum_ro    % Square Total charge concentration (unit:1/m^3)
44 global Charge    % Total charge distribution (unit:C^2/m/ev)
45 global aB       % Effective Bohr radius
46 global rs       % the ratio of the mean electron distance to the effective Bohr radius
47 global C        % Poisson Matrix
48 global Vex      % local exchange potential
49 global V        % total potential
50 global Nd0
51 global na_j
52 global n_j
53
54 % load parameter
55 Parameter;
56 global Interlayer % Interlayer width (unit:m)
57 global Rms        % surface RMS (unit:m)
58 global ii
59 for ii=3:3;
60     Interlayer(ii) = (ii-1)*4.9816e-10;
61     Structure;
62     results = num2str((ii-1)/2);
63     HEFT = strcat('HEFT', results, '.txt'); % output file name
64
65 % original iteration value
66 global V_0
67 global V_1
68 global Fermi;
69 global Standard
70
71 % Conduction band
72 global Ec        % Conduction band
73 global Ec0       % Oringin conduction band
74 global Ei_c      % eigenergy (Unit:eV)

```

```

75 global Psi1_c      % 1st Wavefunction
76 global Ei1_c       % 1st eigenenergy (Unit:eV)
77 global Psi_c        % Free electron distribution
78 global VH           % Hatree pontential
79 global Iteration   % Iteration time
80 global V_dif        % Force difference (eV)
81
82 V_0 = Ec0-Ec0;
83 V_1 = Ec0;
84 Iteration = 0;
85 while max(abs(V_1-V_0)) > Standard
86     Iteration = Iteration + 1;
87     V_1 = 0.01*V_1 + (1-0.01)*V_0;          %0.01 relaxation factor
88     V_0 = V_1;
89     V = V_0;
90     m = me;
91     Psi = Schrodinger(m,V);
92     Fermi = V(1) - Esf3;
93     Fermi_level(Fermi);
94     VH = Poisson;
95     V_1 = Ec0 - VH + Vex;
96     V_dif(Iteration) = max(abs(V_1-V_0));
97     if Iteration >= 800;
98         break;
99     end
100 end
101 Ec = V_1 - 0.5*Fermi;
102 Ei_c = Ei- Fermi;
103 Psi_c = Psi;
104 Psi1_c = Psi1;
105
106 % electron concentration at each layer
107 global Interface1 % interface-1 mesh number
108 global Interface2 % interface-2 mesh number
109 global dz          % Step lenth (unit:m)
110 global n           % Free electron concentration (Unit: 1/m^3)
111 global n_per        % Different layer electron concentration percent (Unit: 1/m^3)
112 global FWHM         % FWHM of electron (Unit: m)
113
114 n_AlGaN(ii) = sum(n(1:Interface1-1-Rms/dz))/sum(n)*100;

```

```
115 n_AlN(ii) = sum(n(Interface1-Rms/dz:Interface2+Rms/dz))/sum(n)*100;
116 n_GaN(ii) = sum(n(Interface2+1+Rms/dz:N+1))/sum(n)*100;
117
118 %FWHM of electron distribution
119 for i=1:N+1;
120     if n(i) >= mean(n);
121         FWHM_1(i) = 1;
122     else
123         FWHM_1(i) = 0;
124     end
125 end
126
127 FWHM(ii) = sum(FWHM_1)*dz*1e10; %unit :A
128
129 % Graph output
130 figure (1);
131 plot(1:N+1,Ec);
132 hold on;
133 title ('energy bend')
134
135 figure (2);
136 plot(1:N+1,Psi1_c);
137 grid on;
138 title ('electron wavefunction');
139
140 figure (3);
141 subplot (4,1,1);
142 plot(1:N+1,VH);
143 grid on;
144 title('hartree force');
145 subplot (4,1,2);
146 plot(1:N+1,Nd);
147 grid on;
148 title('donor concentration');
149 subplot (4,1,3);
150 plot(1:N+1,n);
151 grid on;
152 title('carrier concentration');
153 subplot (4,1,4);
154 plot(1:N+1,ro);
```

```
155 grid on;
156 title('sheet charge concentration')
157
158 figure(4)
159 plot(1:N+1,ro);
160 grid on;
161 hold on;
162 title('sheet charge concentration')
163
164 %txt output
165 fid=fopen(HEFT,'at');
166 fprintf(fid,'%s\t %f\t %s\t \n','ALN depth(A)', Interlayer(ii)*1e10);
167 fprintf(fid,'%s\t %g\t %s\t %f\t \n','2DEG sheet carrier density:',sum(n*dz), 'FWHM(A):',
168 FWHM(ii));
169 fprintf(fid,'%s\t %f\t %s\t %f\t %s\t %f\t \n', 'AlGaN-electron:',n_AlGaN, 'AlN-electron:',
170 n_AlN, 'GaN-electron:', n_GaN);
171 fprintf(fid,'%s\t %f\t \n', 'Iteration:', Iteration);
172 fprintf(fid,'%s\t %f\t \n', 'Fermi level:', Fermi);
173 fprintf(fid,'%s\t %s\t %s\t \n', 'depth(A):', 'Ec:', 'carrier concentration:');
174 iiii = 1:N+1;
175 Out = [iiii',Ec',n]';
176 fprintf(fid,'%3.0f\t %4.5f\t %g\t \n', Out);
177 fclose(fid);
178 end
```

# Index

- Active region, 27, 47, 48, 56, 92, 94, 98, 107, 121, 134, 135, 143
- AlGaN/AlN/GaN heterojunction, 13, 27–31, 34, 40, 42, 43, 45, 48–55, 58, 61, 103, 106, 112–115, 120, 127, 134, 137, 140, 146, 147
- Back-scattered electrons (BSE), 79
- Biaxial stress model, 29, 41, 43, 45, 47, 49, 55, 61, 105, 137
- Bionic, 111, 113, 131, 133
- Bragg’s law, 84
- Cantilever, 20, 26–31, 47–49, 55, 56, 58–61, 63, 71, 75, 76, 80, 99, 101–103, 105–108, 113–118, 120, 121, 123, 127–130, 132, 134–137, 139–141, 143–147, 150, 154–158
- Carrier
- concentration, 51, 53, 54, 59, 91, 120, 128, 147, 150, 152
- distribution, 15, 34, 49, 51, 55, 58, 59, 128, 147, 150
- Channel, 8, 21, 65, 91, 94, 124
- Cleaning
- dry cleaning, 67, 68, 92
- plasma cleaning, 30, 63, 69
- RCA cleaning, 68, 91
- wet cleaning, 67, 68, 91
- Conduction band, 50, 58, 128, 130, 147
- Contact
- Ohmic contact, 74, 94, 96, 98, 118, 135, 139, 141
- Schottky contact, 4–6, 8, 74, 94, 97, 98, 118, 135, 139, 141
- Crystal, 1–4, 10–12, 26, 34, 35, 42, 44, 52, 64, 65, 84, 146
- Current

- drain current, 16, 22, 119, 121–123, 125–127, 140–144  
leakage current, 98, 103, 142
- Deformation, 12, 42, 44, 45, 47
- Degradation, 17, 103, 104, 106, 120, 137, 139
- Deionized water, 68, 91, 93, 102
- Deposition  
chemical vapor deposition (CVD), 71  
electron beam evaporation, 73, 118, 139  
magnetron sputtering, 72, 73, 100, 139  
physical vapor deposition (PVD), 72
- Developer solution, 93, 102
- Dice, 66, 91, 92
- Elastic  
coefficient, 37  
deformation, 42, 45  
strain, 42, 44
- Electric  
dipole moment, 3, 12, 39  
displacement vector, 37, 39  
field, 4, 11, 37–39, 112  
polarization strength, 39
- Electrical  
conductivity, 14, 113
- neutrality condition, 51
- Electrode, 21, 71, 103, 106, 107, 121
- Electron mobility, 12, 65, 91, 112, 132
- Electronegativity, 11, 33
- Electrostatic  
field, 55  
interactions, 50
- Energy band, 4, 6, 8, 12, 14, 15, 27, 29–31, 34, 49, 50, 53–55, 58, 106, 120, 132, 134, 146
- Energy-dispersive X-ray spectroscopy (EDX), 82, 115, 137
- Epitaxial  
growth, 25, 29, 30, 63–65, 90  
layer, 15, 33, 42, 106, 117, 138
- Etching  
anisotropic etching, 75, 101, 103, 117, 135, 139  
dry etching, 30, 63, 103, 105, 106, 116, 119, 135–137, 139, 141  
isotropic etching, 76, 101, 103, 117, 120, 135, 139
- Fabrication process, 30, 63, 87, 90–92, 94–96, 98, 99, 101–104, 106–109, 114, 118, 135, 140

- Finite element analysis, 29, 47–49, 55, 61, 121, 143
- Hartree potential, 50, 53, 54
- HEMT, 14–16, 21, 23, 30, 31, 34, 48, 98, 103, 105, 106, 112, 119, 120, 132, 134–136, 140, 146, 149, 152
- Heterojunction electron gas (HEG), 13, 14
- High-resolution X-ray diffraction (HRXRD), 84
- Hydrochloric acid, 67, 68, 91
- Hydrofluoric acid, 67, 68
- Hydrogen peroxide, 68
- In-plane biaxial stress, 106
- Inductively coupled plasma (ICP), 25, 75, 94, 101, 103, 104, 106–108, 116, 117, 135, 137, 139
- Interactive electronic, 131, 132, 154
- Interface, 3–8, 12, 15, 20, 21, 31, 33–35, 50–53, 56, 112, 120, 127, 136
- Lattice constant, 41, 42, 44, 45, 47, 81, 85, 120
- defects, 105, 106, 120, 139, 141
- deformation, 45, 47
- mismatch, 12, 33, 34, 41, 42, 64, 90, 120, 146
- strain, 12, 29, 33–35, 41–43, 45, 47, 48, 52, 56, 61, 103, 105, 106, 112, 120, 127
- Magnetic field, 20, 28, 31, 100, 132, 134, 142, 143, 145, 149, 150, 152
- force, 27, 31, 134, 143, 146
- thin film, 31, 99, 100, 132, 134, 135, 146
- Magnetoreception, 133, 142, 145
- Magnitosensory power MEMS devices (MPD), 28, 29, 31, 48, 56, 58, 99, 103–107, 131–154
- MEMS, 14, 17–25, 27–30, 34, 49, 56, 58, 59, 61, 63, 101, 103, 106, 107, 109, 113
- Mesa isolation, 92, 94, 135
- MOCVD, 64, 117, 138
- Modulation, 6, 8, 9, 12, 14, 15, 17, 20, 27–31, 49, 55, 56, 61, 124, 128, 132, 142
- Nitride, 10, 12, 13, 19, 20, 22, 23, 25, 27, 28, 33–35, 39–41, 64, 117, 120, 132, 138, 146

- Output  
current, 16, 27, 31, 98, 106, 119, 123, 127, 128, 134, 140, 143  
power, 28, 30, 31, 113, 123, 124, 128, 132, 134, 145, 150, 152
- Photolithography, 30, 63, 70, 92
- Photomask, 89, 92–95, 97, 100, 102
- Photoresist, 67–71, 92–95, 97, 99–102, 107, 117, 139
- Physical  
framework, 27, 55  
mechanism, 55, 58, 104, 105, 127, 145
- Piezoelectric  
coefficient, 1, 33, 37, 38, 52  
constitutive equation, 29, 37, 39, 49, 55, 61  
effect, 1, 2, 4, 8, 12, 14, 20, 22, 37, 106, 112, 120, 125, 127  
polarization, 12, 33–35, 37, 39, 40, 52, 127, 132  
polarization charge, 4–8, 12, 14, 15, 27, 29–31, 34, 38–40, 47, 49, 52, 55, 56, 61, 106, 112, 120, 127, 134, 136, 146  
potential, 2, 4, 6, 8, 9, 20
- Piezotronics, 2, 4, 6–10, 12–17, 27, 29–31, 56, 113, 121, 124, 127, 132, 134, 143, 145, 146, 155
- Piranha solution, 67, 91
- Poisson's  
equation, 50–54  
ratio, 41, 47
- Polarization  
charge, 3, 12, 34, 51–53  
effect, 11, 12, 33, 34  
electric field, 40  
engineering, 12  
vector, 36, 37
- Post-apply bake, 92, 101, 107
- Post-exposure bake, 93
- Potential  
energy, 50, 53, 54  
well, 12, 58, 59, 112, 128, 147, 150
- Raman  
biaxial stress conversion factor, 106, 137  
phonon frequency, 106, 120, 137  
scattering, 85  
spectroscopy, 30, 63, 86, 104, 136
- Rapid thermal  
annealing (RTA), 94, 96

- processing (RTP), 76, 96, 118, 139
- Rayleigh scattering, 85
- Resonant body transistor (RBT), 20
- Scanning electron microscopy (SEM), 27, 30, 63, 79, 108, 115, 135
- Schrödinger equation, 50
- Schrödinger-Poisson coupling equation, 29, 53
- Secondary electrons (SE), 79
- Self-consistent computational model, 29, 49, 52, 53, 55
- Self-heating effect, 106
- Semiconductor parameter analyzer, 77
- Spontaneous polarization, 11, 12, 33–35, 37, 52, 127, 132, 146
- Strain, 4–6, 8, 12, 14–17, 19, 21, 27, 28, 30, 31, 33, 34, 37–42, 47, 52, 53, 113, 119, 128, 143, 146
- Strain-controlled power MEMS devices (SPD), 28–31, 58, 107, 111–130, 137, 139, 140, 142, 145
- Substrate, 16, 21, 26, 33, 41–43, 64, 65, 70–72, 103, 106, 108, 117, 120, 136
- Surface, 4, 11, 12, 20, 33, 34, 67, 69, 73, 91, 94, 96, 146
- Thin film, 25, 29–31, 38, 40–43, 47, 49, 63, 70, 99, 117
- Transconductance, 16, 21, 98, 103, 119, 140
- Transmission electron microscopy (TEM), 30, 63, 80, 115, 138
- Transmitted electrons, 79
- Two-dimensional electron gas (2DEG), 12, 15, 20–22, 27, 29–31, 49, 52, 56, 59, 65, 91, 94, 106, 113, 117, 120, 123, 125, 128, 129, 132, 134, 137, 145–152
- Vacuum permittivity, 39
- Vegard’s law, 41, 53
- Voltage
- breakdown voltage, 65, 91
  - gate voltage, 8, 9, 16, 31, 98, 113, 125, 130, 132, 140, 142, 143, 145, 154
  - gate-source voltage, 143
  - source-drain voltage, 140, 143
- Von Mises stress, 48
- Wafer, 27, 29, 30, 63–65, 67, 68, 90, 98, 108
- Wurtzite, 2, 10, 11, 33, 38, 52, 146
- Young’s modulus, 19, 47